Leiva Casemiro Oliveira Antonio Marcus Nogueira Lima Carsten Thirstrup Helmut Franz Neff

Surface Plasmon Resonance Sensors A Materials Guide to Design and Optimization



SpringerBriefs in Physics

Editorial Board

Egor Babaev, University of Massachusetts, Massachusetts, USA Malcolm Bremer, University of Bristol, Bristol, UK Xavier Calmet, University of Sussex, Brighton, UK Francesca Di Lodovico, Queen Mary University of London, London, UK Maarten Hoogerland, University of Auckland, Auckland, New Zealand Eric Le Ru, Victoria University of Wellington, Wellington, New Zealand Hans-Joachim Lewerenz, California Institute of Technology, Pasadena, USA James M. Overduin, Towson University, Towson, USA Vesselin Petkov, Concordia University, Concordia, Canada Charles H.-T. Wang, University of Aberdeen, Aberdeen, UK Andrew Whitaker, Queen's University Belfast, Belfast, UK

More information about this series at http://www.springer.com/series/8902

Leiva Casemiro Oliveira Antonio Marcus Nogueira Lima Carsten Thirstrup · Helmut Franz Neff

Surface Plasmon Resonance Sensors

A Materials Guide to Design and Optimization



Leiva Casemiro Oliveira
Department of Electrical
Engineering (DEE)
Federal University of Campina
Grande (UFCG)
Campina Grande
Brazil

Antonio Marcus Nogueira Lima Department of Electrical Engineering (DEE) Federal University of Campina Grande (UFCG) Campina Grande Brazil Carsten Thirstrup
Danish National Metrology Institute
Kongens Lyngby
Denmark

Helmut Franz Neff
Department of Electrical
Engineering (DEE)
Federal University of Campina
Grande (UFCG)
Campina Grande
Brazil

ISSN 2191-5423 SpringerBriefs in Physics ISBN 978-3-319-14925-7 DOI 10.1007/978-3-319-14926-4 ISSN 2191-5431 (electronic)

ISBN 978-3-319-14926-4 (eBook)

Library of Congress Control Number: 2015931530

Springer Cham Heidelberg New York Dordrecht London © The Author(s) 2015

This work is subject to copyright. All rights are reserved by the Publisher, whether the whole or part of the material is concerned, specifically the rights of translation, reprinting, reuse of illustrations, recitation, broadcasting, reproduction on microfilms or in any other physical way, and transmission or information storage and retrieval, electronic adaptation, computer software, or by similar or dissimilar methodology now known or hereafter developed.

The use of general descriptive names, registered names, trademarks, service marks, etc. in this publication does not imply, even in the absence of a specific statement, that such names are exempt from the relevant protective laws and regulations and therefore free for general use.

The publisher, the authors and the editors are safe to assume that the advice and information in this book are believed to be true and accurate at the date of publication. Neither the publisher nor the authors or the editors give a warranty, express or implied, with respect to the material contained herein or for any errors or omissions that may have been made.

Printed on acid-free paper

Springer International Publishing AG Switzerland is part of Springer Science+Business Media (www.springer.com)

This book is gratefully dedicated to all of our family members. It also represents a token of a strong and fruitful Brazilian-German-Danish friendship that has been cultivated for several years.

Preface

An introductory lecture on surface plasmons often begins by showing the audience a photograph of a Lycurgus cup dating back to the fourth-century Roman period. The spectacular cup exhibits a most impressive change in colour from red to green depending on whether light shines from behind or from the front. Colloidal nanoparticles of gold and silver had been dispersed in the glass of the cup and their strong interaction with visible light due to localized surface plasmons is responsible for the fascinating colour effect. It is a challenge for scientists to understand how the Romans were able to make this cup; whether they could control the colour effect by design or whether it was more or less made by chance.

Surface plasmons exhibit many other fascinating properties, which attract the interest of scientists in many different fields, including electrochemistry, artificial photosynthesis, plasmon mediated chemical nanoparticle growth, catalysis, photothermal cancer therapy, telecommunications, scanning tunnelling and surface plasmon microscopy, optical sensing and in particular optical bio-sensing. This book focuses mainly but not exclusively on the latter topic, and it is intended to be used as a materials guide in the design of surface plasmon sensors, but it may also serve as an inspiration for people in other fields.

The book is a result of a study of the parameters that affect the surface plasmon response. The important parameters are the choice of metal for the thin film or the nanoparticle, the choice of dielectric substrate materials, the choice of liquid analyte, sizes and configurations. Properties of a large number of metals have been collected from the periodic table, including traditional noble metals like gold and silver, noble transition metals of the platinum group like osmium and rhodium, alkali metals like lithium, and transition metals like molybdenum and tantalum, and other common metals. In addition, a few examples of surface plasmon responses of alloys and superlattices have been included. Three different types of surface plasmons are examined: (1) a propagating surface-plasmon in a metal thin film between two dielectrics, where one dielectric is a substrate material in which the surface plasmon is excited by light and the other layer is a liquid analyte causing the sensor response; (2) a propagating long-range surface plasmon in a metal thin film between two dielectrics, but further comprising an additional dielectric layer situated

viii Preface

between the substrate and the liquid analyte enabling the propagation of an antisymmetric surface plasmon mode with a long propagating length; and (3) a localized surface plasmon in a metal nanoparticle.

The analysis of the surface plasmon sensor response covers three different interrogation modes: (a) the angular interrogation mode, where the wavelength is fixed and the response is monitored as a function of the incident angle of the light (excluded for nanoparticles), (b) the wavelength interrogation mode, where the angle of incidence of light is fixed and the sensor response is monitored as a function of wavelength and (c) the intensity interrogation mode where both the angle and the wavelength are fixed and solely the intensity is monitored. The latter interrogation mode is only briefly treated in this book, because it is obviously less sensitive than the other methods, but it may be relevant for analysis of large arrays of sensor elements in surface plasmon resonance imaging of, for example, twodimensional arrays of sensor elements. The book starts with an introduction to surface plasmons and surface plasmon resonance sensors followed by a sensor design guide and descriptions of modelling the surface resonance response for propagating surface plasmons and localized surface plasmons. These topics are covered in Chaps. 1–5. For a number of materials systems and surface plasmon configurations as described above, detailed surface plasmon response analyses are presented in Chaps. 6-12. Finally, the results of the analyses are summarized in Chap. 13 by a table and concluding remarks are presented. It is the hope of the authors that the book will inspire scientists from several other fields beyond biosensing and that it can help in introducing new materials and/or configurations for surface plasmons, going beyond those based on gold and silver, whose effects have already fascinated people for centuries.

Campina Grande, Paraíba, Brazil, October 2014 Campina Grande, Paraíba, Brazil Lyngby, Denmark Campina Grande, Paraíba, Brazil Leiva Casemiro Oliveira Antonio Marcus Nogueira Lima Carsten Thirstrup Helmut Franz Neff

Acknowledgments

Much of the SP-sensor technology discussed in this book was developed over 10 years ago at VIR Biosensor A/S, located in Taastrup, Denmark. Many of our former colleagues there, especially Weiyong Zong, Martin Borre and Ulli Ruedel, made essential contributions. This book would not have been written without the entrepreneurial courage of Stig Hojberg-Jensen, the founder of VIR A/S. The authors gratefully acknowledge the financial support for many years of CAPES, CNPQ, FINEP and contributions of all the former and current undergraduate and graduate students.

Contents

1		rences	8						
2	-	ical Features of the Surface Plasmon Polariton	11						
	Ketei	rences	14						
3	Phys	ical Features of Surface Plasmon Resonance Sensors	15						
		rence	17						
4	Desig	gn Features of Surface Plasmon Resonance Sensors	19						
	4.1	Propagating Surface Plasmons	19						
	4.2	Localized SP's	24						
	Refe	rences	25						
5	Data Extraction Algorithms								
	5.1	Multilayer Fresnel Analysis for Extended Metal Films	27						
	5.2	Long Range Surface Plasmon Polaritons	29						
	5.3	Localized Surface Plasmon Resonance in Small Particles	30						
	5.4	Partial Differential Equation Formulation	31						
	Refe	rences	32						
6	SPR-	-Sensor Properties of Metal Films and Particles:							
	Free Electron Type Metals								
	6.1	Thin Aluminum Films and Colloidal Particles	33						
		6.1.1 Long Range Surface Plasmon Polaritons							
		(LRSPP-Mode)	36						
		6.1.2 Localized Plasmons in Colloidal Al-Particles							
		(LSPR-Mode)	38						
	6.2	Thin Lithium (Li) Films	39						
	6.3	Thin Magnesium (Mg) Films	43						
	Refe	rences	46						

xii Contents

7	Clas	sical Noble Metals	47
	7.1	Thin Copper (Cu) Films and Colloidal Particles	47
		7.1.1 Long Range Surface Plasmon Polariton	
		(LRSPP-mode)	51
		7.1.2 Localized Plasmons in Colloidal Cu-Particles	
		(LSPR-mode)	51
	7.2	Thin Gold (Au) Films and Colloidal Particles	52
		7.2.1 Long Range Surface Plasmon Polariton	
		(LRSPP-mode)	57
		7.2.2 Localized Plasmons in Colloidal Au-Particles	
		(LSPR-mode)	57
	7.3	Thin Silver (Ag) Films and Colloidal Particles	59
		7.3.1 Long Range Surface Plasmon Polaritons	- 1
		(LRSPP-mode)	64
		7.3.2 Localized Plasmons in Colloidal Ag-Particles	~ ~
	D C	(LSPR-mode)	65
	Refe	rences	68
8	Nobl	le Transition Metals of the Platinum Group	69
o	8.1	Thin Iridium (Ir) Films and Colloidal Particles	69
	0.1	8.1.1 Localized Plasmon in Colloidal Ir-Particles	09
		(LSPR-Mode)	72
	8.2	Thin Osmium (Os) Films and Colloidal Particles	72
	0.2	8.2.1 Long Range Surface Plasmon Polaritons	12
		(LRSPP-Mode)	76
		8.2.2 Properties of Localized Plasmons in Os-Colloidal	70
		Particles	77
	8.3	Thin Palladium (Pd) Films	78
	8.4	Thin Platinum (Pt) Films	81
	0	8.4.1 Properties of Localized Plasmons in Pt-Colloidal	01
		Particles	85
	8.5	Thin Rhodium (Rh) Films	86
	8.6	Thin Ruthenium (Ru) Films	89
		erences	95
9	Com	nmon Transition Metals	97
	9.1	Thin Chromium (Cr) Films	97
	9.2	Thin Cobalt (Co) Films	99
	9.3	Thin Iron (Fe) Films	102
		9.3.1 Properties of Localized Plasmons in Colloidal	
		Fe-Particles	107
		9.3.2 Magneto-Optical Effects	109
	9.4	Thin Molybdenum (Mo) Films	109
	9.5	Thin Nickel (Ni) Films	112

Contents xiii

	9.6	Thin Niobium (Nb) Films	115					
	9.7	Thin Tantalum (Ta) Films	119					
	9.8	Thin Titanium (Ti) Films	123					
	9.9	Thin Tungsten (W) Films	126					
	9.10	Thin Vanadium (V) Films	129					
	9.11	Thin Zirconium (Zr) Films	133					
	Refer	rences	138					
10	Othe	r Common Metals	139					
	10.1	Thin Indium (In) Films	139					
	10.2	Thin Tin (Sn) Films	143					
	10.3	Thin Zinc (Zn) Films	145					
	10.4	Thin Lead (Pb) Films	147					
		10.4.1 Long Range Surface Plasmon Polariton						
		(LRSPP-mode)	151					
		10.4.2 Localized Plasmons in Colloidal Pb-Particles						
		(LSPR-mode)	152					
	10.5	Thin Bismuth (Bi) Films	154					
	Refer	rences	157					
11	SPR	Active Metal-Type Compounds	159					
	11.1	Thin Indium-Tin-Oxide (ITO) Films	159					
	11.2	Thin Titanium-Nitride (TiN) Films	162					
	Refer	rences	168					
12	Artificial Metal-Insulator Multi-layer Structures							
	12.1	Silver-Al ₂ O ₃ -Silver Multilayer Structures	169					
13	Conc	clusions	173					
Glo	ssary		179					
Ind	ex		181					

Chapter 1 Introduction and Background Information

The optically excited surface plasmon resonance (SPR) in thin metal films, also known as the surface plasmon polariton (SPP), is a scientifically and technologically attractive physical phenomenon, utilized in the design of a large variety of physicochemical optical sensors. The collective electronic excitation originates from a coherent, resonant interaction of photons with the free electron system in the metal. Its negatively charged, mobile electrons oscillate at a plasma frequency ω_p against the static background of positively charged metal ions. At the resonance, the angular frequency of an incident electro-magnetic wave corresponds to ω_p . Furthermore, for a thin metal film, confined between two identical or different bulk dielectrics, the plasma resonance at frequency ω_{sp} becomes considerably modified, when compared with the situation in the bulk metal, the single metal-dielectric interface or to small metal particles embedded within a dielectric matrix.

Under certain conditions, the SPP constitutes two modes of an attenuated, TM-polarized electro-magnetic plane wave, expressed as $\mathbf{A}_0 e^{j(\omega t - \mathbf{k} \cdot \mathbf{r})}$. It propagates along the metal-dielectric interfaces, with \mathbf{k} representing the wave vector and \mathbf{r} the space vector, and \mathbf{A}_0 the interfacial field amplitude. Apart from appearance of distinct optical absorption features that may involve co-existing symmetric and anti-symmetric modes, the resonance is also linked to high interfacial electric fields. Attenuation of the propagating SPP-wave caused by a limited lifetime reduces the propagation length to the order of micro-meters or less. Eventually, the spectral or angular variations of the resonance account for the characteristic features of an SPR based optical sensor, commonly associated with its optical responsivity, the related (linear) sensing range and the limit of detection (LOD).

The excitation and propagation of plasma waves in solids, considered as an analogue to those in ionized gases, was established long time ago [1]. The plasmon energy E_{sp} (ω_{sp} , k_{sp}) varies with frequency ω and wave-vector \mathbf{k} , which is known as the plasmon dispersion relation. Originally, the existence of both, bulk and surface plasmons in thin metal sheets was introduced to explain the inelastic scattering characteristics of traversing free electrons [2]. Closed analytical representations of the SP phenomenon were only reported within the classical Drude approximation (DA),

1

and thus were restricted to free electron type metals that exhibit strictly parabolic conduction bands.

Briefly, the DA roughly explains the frequency dependent, complex electrical conductivity of a metal sample as:

$$\sigma\left(\omega\right) = \frac{\sigma_0}{1 + j\omega/\gamma},\tag{1.1}$$

and

$$\sigma_0 = \frac{N\mathbf{e}^2}{m_e \gamma} \tag{1.2}$$

is the dc-value, N is the number of electrons per volume unit, m_e is the effective electron mass, \mathbf{e} is its charge and γ is an attenuation coefficient. At optical frequencies, the complex dielectric constant (CDK) writes as:

$$\varepsilon''(\omega) \approx \left(1 - \frac{\omega_p^2}{\omega^2}\right) + j\left(\gamma \frac{\omega_p^2}{\omega^3}\right),$$
 (1.3)

with the plasma frequency of a bulk sample ω_p given as:

$$\omega_p = \sqrt{\frac{N\mathbf{e}^2}{m_e \varepsilon_0}}.\tag{1.4}$$

Ideally, the reflectivity from the surface approaches unity for the frequency range $\omega < \omega_p$, but drops to rather small values for $\omega > \omega_p$. Both physical quantities, the electrical dc-conductivity σ_0 and the plasma frequency ω_p , scale with N and \sqrt{N} respectively. Hence ω_p -as well as ω_{sp} -should scale with $\sqrt{\sigma_0}$. Nevertheless, the DA is of only limited value for an understanding of the optical properties of real world metals, which require inclusion of electronic band structure effects, particularly interband transitions.

The resonant interaction of surface confined plasmons with light in thin metal films leads to the concept of the surface plasmon polariton. As said above, the optical reflectance differs significantly from the corresponding bulk sample. For a further in-depths exploration of theoretical and experimental aspects, we refer the reader to Refs. [3–20].

The experimental optical SPR set-up typically comprises a multi-layer arrangement, where a thin metal film is embedded between two different or identical layers of an optically transmitting dielectric material. Especially for optical sensor applications, one of the layers is either a polar (water) or non-polar liquid, and it is commonly called "the analyte". A sketch of the corresponding optical arrangement is shown in Fig. 1.1.

A comparison between the CDK of Aluminum, as obtained from a modified version of the DA and experimentally determined values, is depicted in Fig. 1.2

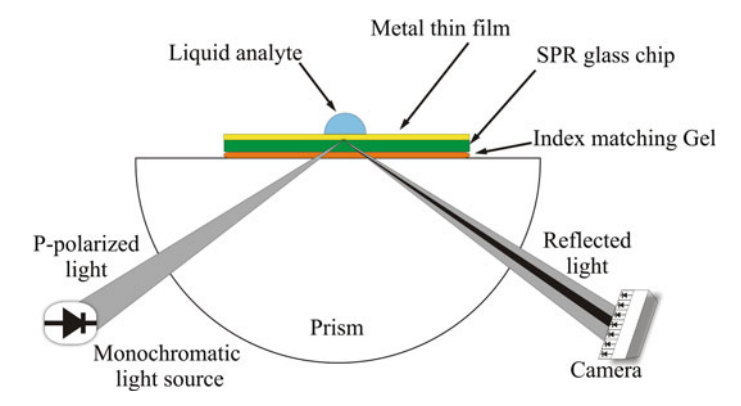


Fig. 1.1 Sketch of a surface plasmon resonance set-up and required components in the Kretschmann configuration in the angular interrogation mode, employing a bulk glass prism and a thin glass chip, attached thereon by an index matching gel for efficient optical coupling

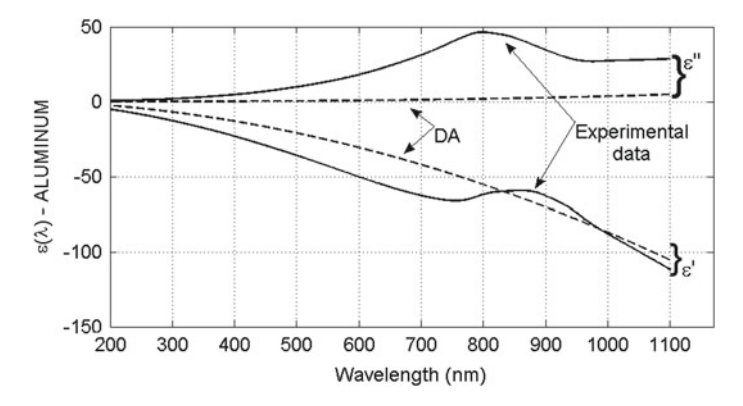


Fig. 1.2 Comparison of the wavelength dependent CDK of Aluminum, obtained from the DA (*broken curves*) with the experimentally determined CDK (*solid curve*)

for optical frequencies, illustrating the limitations of this approximation. Evidently, the complex part ε'' is too small and insufficiently reproduced by the DA, as well as any wavelength dependent features in both, ε' and ε'' that appear at wavelengths around 800 nm.

There are a large number of solid, optically transmitting dielectric substrate materials available. Thin metal films can be placed onto the substrates by means of a suitable deposition method. This can be achieved using thermal or electron beam evaporation in high vacuum, electrolytic deposition, magnetron sputtering, laser ablation or chemical vapor deposition, among numerous other deposition methods. Thermal evaporation of pure metals requires temperatures between the metal melting and boiling points, which usually needs to be sustained over a time span of minutes, and a high vacuum environment. Magnetron sputtering is typically achieved in gas plasma, supported by a magnetic field at low pressure (mTorr range) of

un-reactive noble gases, usually Argon. Quartz microbalance recordings are frequently used to determine the metal film thickness, down to the nanometer scale.

For the noble metals, the lower limit for deposition of homogeneous films is 20–30 nm. Due to an influence of surface scattering of charge carriers, the electrical conductivity of thin, homogeneous metal films is considerably smaller, than those obtained for a thick metal layer. Furthermore, very thin metal films, deposited onto amorphous solid substrates below the critical film thickness and low substrate temperature, tend to nucleate into small and electrically isolated islands. For such inhomogeneous films, thermally activated electrical conduction via tunneling occurs, resulting in a further increase of the electrical resistance. The present Fresnel model still applies to inhomogeneous thin metal films, if the average island size exceeds the SPP-propagation range. For smaller extensions, use of a model for localized SPP's would be required. Whilst the dc-conductivity is rather sensitive to the actual film thickness, the materials specific CDK at optical frequencies remains largely unaffected.

The SPP is observable by various optical configurations. Most commonly, an incident collimated light beam at a pre-selected angle and/or wavelength range is specularly reflected from an optically semi-transparent metal layer, comprising the condition of total internal reflection (TIR). The reflected fraction of the incident radiation is detected by a suitable optical receiver, which is frequently a CMOS or CCD camera, or by a fiber optic spectrometer. Its output signals are processed by suited algorithms for further information extraction. This optical set-up is known as the "Kretschmann configuration". It is widely utilized in the design of commercial instruments. Since it avoids moving optical components, it is suitable for real time monitoring of binding events to a metal surface. Other experimental optical configurations include the "Otto-configuration", and the "grating" based configuration. Both optical configurations are not considered in this report.

Analytically, those optical features originating from the SPP phenomenon can be obtained from a Fresnel analysis in a multi-layer matrix representation. This mathematical treatment requires experimentally determined materials specific dispersion relations for the optical constants of the dielectrics and metals, being selected for the respective materials combinations and wavelength range of interest. The MATLAB software platform has been employed in this book, which efficiently supports the lengthy matrix calculations.

Under certain conditions, multiple excitations may exist, or the width of the resonance would decrease substantially, along with an increased propagation length and life time of the SPP at the interface: this effect is known as the long range surface plasmon polariton (LRSPP), as reported earlier in Ref. [10]. This phenomenon comes into effect for a symmetric dielectric layer configurations, where the CDK of the supporting solid dielectrics with the metal film thereon, is close to the CDK of the analyte solution at the opposite side. Results of the Fresnel analysis are presented for selected metals in Chaps. 6–8.

Furthermore, the phenomenon of localized surface plasmons modes in metal nanoparticles (NP's) has attracted much attention recently. Within the DA, its frequency is defined by

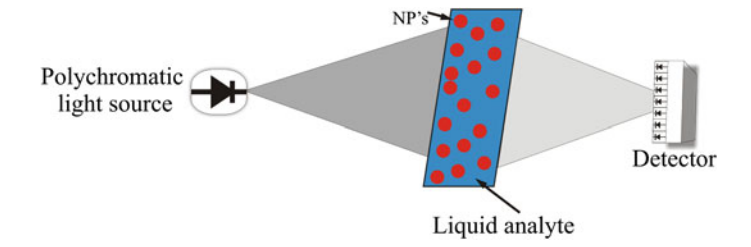


Fig. 1.3 Sketch of an optical transmission set-up for detection of the localized surface plasmon resonance, utilizing nano-particles (NP's) dissolved in a liquid, contained in a glass vessel and optical components

$$\omega_{lsp} = \sqrt{\frac{N\mathbf{e}^2}{3m_e\varepsilon_0}}. (1.5)$$

For an overview, we refer to Refs. [18, 19]. The theoretical model used here, utilizes the Mie light scattering theory, described briefly in Sect. 5.3. Both SP-modes are explored here for a limited number of metals.

A sketch of the experimental arrangement for optical spectroscopy with localized plasmons is shown below in Fig. 1.3.

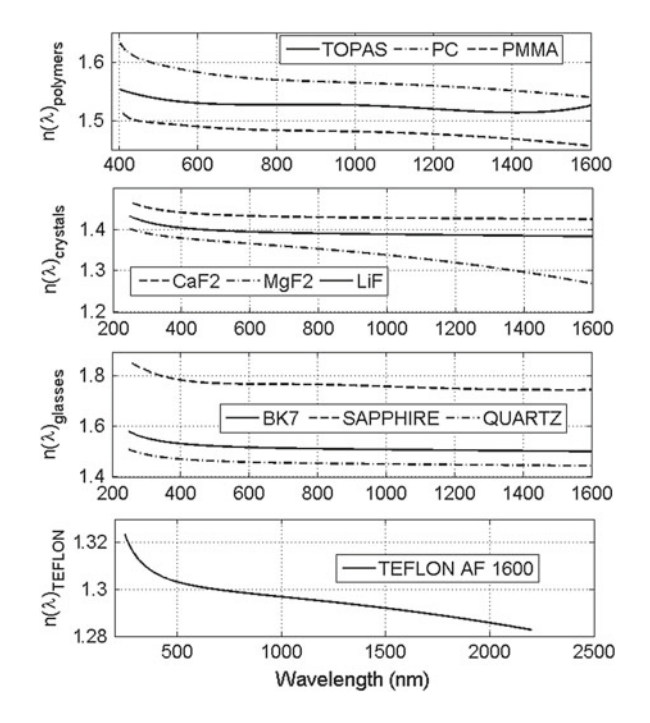
There are established chemical methods for synthesis of colloidal, metal nanoparticles and a variety of nano-particles is already commercially available. The selection of solid dielectrics including amorphous optical polymers, glasses, as well as various crystalline substrate materials is shown below. TOPAS is the trade name for a certain class of cyclo-olefins with exceptionally good optical properties. The material behaves similar to BK7 and is widely used for large volume production of commercial optical products. For simplification, crystalline dielectric substrates are treated here as isotropic. A large variety of metals has been explored by multi-layer Fresnel analysis, as is listed below. Optical materials parameters were taken from Refs. [21–32]. Data fits were made either by polynomial fits or suitable spline representations. The SPR characteristic of the noble metals Au, Ag and Cu is well established, and fully confirmed by experiments, although being restricted to few substrate materials. Here, we present the SPR characteristic of a large variety of common metals, a quasi-metal, a degenerately doped semiconductor and an example of a metal-dielectric superlattice structure (Table 1.1). All are of potential technical interest and can be produced as thin films by established deposition methods, especially magnetron sputter deposition. Native oxide layers-if present—forming upon contact of the individual metal surfaces to air or water, are usually self-limiting in the mono—or few layer range. They therefore do not significantly modify the SPP characteristics.

Figure 1.4 illustrates the dispersion curves, i.e. the variation of the refractive index as function of wavelength λ at ambient temperature for the dielectric substrate

Table 1.1	List of	materials:	active	metals	and	metallic	compounds,	solid	dielectric	substrates,
liquid diele	ectrics									

SPR-active metals and metallic compounds						
1. Aluminium (Al)	11. Lithium (Li)	21. Ruthenium (Ru)				
2. Bismuth (Bi)	12. Lead (Pb)	22. Silver (Ag)				
3. Chromium (Cr)	13. Magnesium (Mg)	23. Tantalum(Ta)				
4. Cobalt (Co)	14. Molybdenum (Mo)	24. Tin (Sn)				
5. Copper (Cu)	15. Nickel (Ni)	25. Titanium (Ti)				
6. Gold (Au)	16. Niobium (Nb)	26. Titaniumnitride (TiN)				
7. Indium (In)	17. Osmium (Os)	27. Tungsten (W)				
8. IndiumTinOxide (ITO)	18. Palladium (Pd)	28. Vanadium (V)				
9. Iridium (Ir)	19. Platinum (Pt)	29. Zinc (Zn)				
10. Iron (Fe)	20. Rhodium (Rh)	30. Zirconium (Zr)				
Solid dielectric substrates						
1. BK7	5. PMMA	9. LiF				
2. Sapphire	6. TOPAS	10. MgF2				
3. Quartz	7. Teflon					
4. PC	8. CaF2					
Liquid dielectrics						
Water and cyclo-Hexane						

Fig. 1.4 Refractive index as function of wavelength for various dielectric substrate materials



materials under consideration. The materials specific coefficients B_N and C_N of the Sellmeier equation, which writes as:

$$n_{\text{MAT}}(\lambda)^2 = 1 + \frac{B_1 \lambda^2}{\lambda^2 - C_1} + \frac{B_2 \lambda^2}{\lambda^2 - C_2} + \frac{B_3 \lambda^2}{\lambda^2 - C_3}$$
 (1.6)

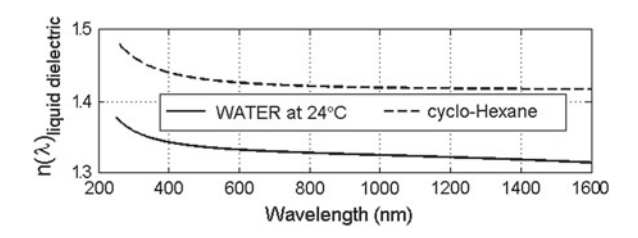
are indicated in Refs. [21–28, 33–35]. In some special cases, higher order polynomials were also employed in the data fitting.

Similarly, the dispersion curves for the two liquid dielectrics at ambient temperature are shown in Fig. 1.5. Lower and upper wavelength limits for all materials are selected to maintain optical transmission >90 %. Water is a versatile solvent used for many organic and in-organic substances, including a large variety of bio-chemicals. Use of an organic solvent is required for those reactive metals that would immediately oxidize on contact with water, without first forming a protective oxide-layer at the surface. Many organic compounds, as well as some bio-chemicals dissolve in cyclo-hexane.

Except the noble metals, metals in contact with water or the ambient atmosphere form thin, frequently compact oxide films at the surface. The oxide layer usually affects the SPR features depending, however, on its actual film thickness. A noticeable deterioration of sensor performance can be avoided, if the oxide layer thickness remains on the order of one or two mono-layers. Films of highly reactive metals, such as the alkaline earth metals, are not stable in contact with water or ambient atmosphere and undergo an exothermic chemical reaction. Hence, use of a non-oxidizing organic solvent as the liquid dielectric is essential.

The present book provides the information, that is needed in the design of an SPR sensor: selection of the optical dielectric substrate and type of metal film, associated input angle or angle range, wavelength or wavelength range, the thickness of the metal film and optimal combinations thereof, where the resonance-or resonances-would occur. Since solid-gas interfaces are rarely employed in SPR-sensor applications, this situation is not included in the present materials evaluation. There are numerous excellent review articles and books published that extensively treat basic physics features of the SPR phenomenon and SPR-sensors. We refer especially to Refs. [7, 8] and the review paper in Ref. [36]. Hence, these aspects are not covered in this report. The information provided here rather supports those researchers and instrumental developers who are planning to build or optimize their own SPR sensor.

Fig. 1.5 Optical dispersion of water and cyclo-hexane at ambient temperature



References

- 1. Langmuir, I.: The effect of space charge and residual gases on thermionic currents in high vacuum. Phys. Rev. **2**, 450–486 (1913)
- Fermi, E.: The Ionization loss of energy in gases and in condensed materials. Phys. Rev. 57, 485–493 (1940)
- 3. Ritchie, R.H.: Plasma losses by fast electrons in thin films. Phys. Rev. 106, 874 (1957)
- Ferrell, R.A.: Predicted radiation of plasma oscillations in metal films. Phys. Rev. 111, 1214 (1958)
- Otto, A.: Excitation of nonradiative surface plasma waves in silver by the method of frustrated total reflection. Z. F. Physik 216, 398 (1968)
- 6. Economou, E.N.: Surface plasmons in thin films. Phys. Rev. 182, 539 (1969)
- 7. Kretschmann, E., Raether, H.: Z. Naturforschung A. 23, 2135 (1968)
- 8. Raether, H.: Surface Plasmons on Smooth and Rough Surfaces and on Gratings. Springer, Berlin (1988)
- Ekinci, Y., Solak, H.H., Loeffler, J.F.: Plasmon resonances of aluminum nanoparticles and nanorods. J. Appl. Phys. 104, 083107 (2008)
- Sarid, D.: Long-range surface-plasma waves on very thin metal films. Phys. Rev. Lett. 47, 1927 (1982)
- Gryczynski, I., Malicka, J., Gryczynski, Z., Nowaczyk, K., Lakowicz, J.R.: Ultraviolet surface plasmon-coupled emission using thin aluminum films. Anal. Chem. 76, 4076–4081 (2004)
- 12. Neff, H., Sass, J.K., Lewerenz, H.J.: A photoemission-into-electrolyte study of surface plasmon excitation on high index faces of silver. Surf. Sci. 143, L356–L362 (1984)
- 13. Neff, H., Sass, J.K., Lewerenz, H.J., Ibach, H.: Photoemission studies of electron localization at very low excess energies. J. Phys. Chem. **84**, 1135 (1980)
- 14. Abelès, F.: Optical properties of very thin films. Thin Solid Films 34, 291 (1976)
- 15. Pettit, R.B., Silcox, J., Vincent, R.: Measurement of surface-plasmon dispersion in oxidized aluminum films. Phys. Rev. B 11, 3116 (1975)
- Tillin, M.J., Sambles, J.R.: A surface plasmon polariton study of the dielectric-constants of reactive metals-aluminium. Thin Solid Films 167, 73–83 (1988)
- 17. Pockrand, L.: Ph.D. thesis, Universitaet Hamburg (1978)
- 18. Mayer, K.M., Hafner, J.: Plasmonics **111**, 3828 (2011)
- 19. Zeng, S., Baillargeat, D., Hod, H.-P., Yong, K.T.: Chem. Soc. Rev. 43, 3426 (2014)
- 20. Dionne, J.A., Sweatlock, L.A., Atwater, H.A., Polman, A.: Phys. Rev. B72, 075405 (2005)
- Kasarova, S.N., Sultanova, N.G., Inov, C.D., Nikolov, I.D.: Analysis of the dispersion of optical plastic materials. Opt. Mater. 29, 1481–1490 (2007)
- SCHOTT, Optical Glass Data Sheet-Catalog. http://www.schott.com/advanced_optics/us/abbe_datasheets/schott_datasheet_all_us.pdf
- Yang, M.K., French, R.H., Tokarsky, E.W.: Optical properties of TeflonAF amorphous fluoropolymers. J. Micro/Nanolith. MEMS MOEMS 3(033010), 1–9 (2008)
- Khanarian, G., Celanese, H.: Optical properties of cyclic olefin copolymers. Opt. Eng. 40(6), 1024–1029 (2001)
- 25. TYDEX: Sapphire refractive index versus wavelength
- Masumura, A., Daimon, M.: Measurement of the refractive index of distilled water from the near-infrared region to the ultraviolet region. Appl. Opt. 46, 18 (2007)
- 27. Malitson, I.H.: Comparison of the refractive index of fused silica. J. Opt. Soc. Am. 55, 1205–1209 (1965)
- 28. Rheims, J., Köser, J., Wriedt, T.: Refractive-index measurements in the near-IR, using an Abbe refractometer. Meas. Sci. Technol. **8**, 601–605 (1997) (cyclo-Hexane)
- Rakic, A.D.: Algorithm for the determination of intrinsic optical constants of metal films: application to aluminum. Appl. Opt. 34(22), 4755–4767 (1995)
- 30. Hagemann, H.-J. et al.: Optical constants from the far infrared to the x-ray region: Mg, Al, Cu, Ag, Au, Bi, C, and Al₂O₃. J. Opt. Soc. Am. **65**(6), 742–744 (1975)

References 9

- 31. Palik, E.D.: Handbook of Optical Constants of Solids. Academic Press, Boston (1985)
- 32. Johnson, P.B., Christy, R.W.: Optical constants of the noble metals. Phys. Rev. B 6(12), 4370–4379 (1972)
- 33. Malitson, I.H.: A Redetermination of some optical properties of calcium fluoride. Appl. Opt. **2**, 1103–1107 (1963)
- 34. Dodge, M.J.: Refractive properties of magnesium fluoride. Appl. Opt. 23, 1980–1985 (1984)
- 35. Lee, H.H.: Refractive index of alkali halides and its wavelength and temperature derivatives. J. Phys. Chem. Ref. Data 5, 329–528 (1976)
- 36. Naik, G.V., Shalaev, V.M., Boltasseva, A.: Alternative plasmonic materials. Beyond gold and silver. Adv. Mater. 25, 3264–3294 (2013)

Chapter 2 Physical Features of the Surface Plasmon Polariton

The surface plasmon resonance is an interfacial many particle phenomenon, where a resonant interaction of free electrons in thin metal films with incoming photons accounts for an angular or spectral precisely defined optical absorption. This feature is used in the design of optical sensors that are able to determine either the refractive index of bulk solutions, or detect presence and/or temporal evolution of optically transparent absorption layers in real time with exceptional accuracy.

The currently best known application area of SPR sensors is linked to biochemical research. The identification of antigen-antibody interactions, enzymatic reactions, drug screening and forensics, the search for new bio-markers, proteomics and numerous other applications are important research topics being addressed. Real time SPR sensing also allows a kinetic analysis of selective binding mechanisms. As a major advantage, SPR sensing technology avoids need for color, fluorescent or radio-active molecular labeling. The surface plasmon resonance also plays a role in the surface enhanced Raman scattering (SERS) process, may support heterogeneous catalysis and the development of novel opto-electronic and magneto-optical devices.

The SPR phenomenon at solid-liquid and solid-gas interfaces is well established for the noble metals including Gold, Copper and Silver. Primarily, since its optical materials properties are well-known, thin films of this class of materials class are easily fabricated by evaporation at elevated temperature, and their surfaces are relatively insensitive to oxidation. Nevertheless, a considerable fraction of common metals-yet rarely considered as potential SPR sensor materials-also exhibits suited electro-optical properties, i.e. sufficiently negative values of the real part of dielectric constant in the visible and near infrared range of the electro-magnetic spectrum. This feature establishes presence and the excitation conditions of SPP's provided, however, that such the films are placed onto and combined with suited dielectric substrate materials. Furthermore, especially by means of magnetron sputter deposition technology in inert atmosphere, thin layers of chemically reactive non-noble metal on various dielectric substrates are readily produced without danger of surface oxidation or bulk oxygen contamination. Cost reduction through replacement of noble metals is a major requirement for large volume production and thus desirable in the design of disposable biochips. A rather large number of optical, geometrical

and materials parameters determines the SPP: incident wavelength and angle range, the substrate and metal film material, its thickness. To achieve optimum optimal SPR sensor performance, all of these parameters must be appropriately selected and adjusted for.

Briefly, existence and position of a surface plasmon resonance within a suited energy/wavelength range is most easily illustrated by the dispersion relations $E(\mathbf{k}) = \hbar \mathbf{k}$ of the exciting photon and the SPP. E is the energy, \hbar is the reduced Planck constant, λ is the incident wavelength and \mathbf{k} is the associated wave-vector. The SPP wave-vector along the interface between a metal film and an adjacent liquid dielectric writes as:

$$k_{spp}(\lambda) = \frac{2\pi}{\lambda} \sqrt{\frac{\varepsilon_{an}(\lambda) \varepsilon_{mr}(\lambda)}{\varepsilon_{an}(\lambda) + \varepsilon_{mr}(\lambda)}}$$
(2.1)

Within the wavelength range of interest, the CDK of the dielectric analyte ε_{an} (λ) remains real. It should be re-called that the refractive index n is related with to the CDK and permeability μ via: $n = \sqrt{\mu \varepsilon}$, but simplifies to $\sqrt{\varepsilon}$, if $\mu \approx 1$. Furthermore, since the dielectric constant ε_{mr} (λ) = ε'_{mr} (λ) + $j\varepsilon''_{mr}$ (λ) of the metal film is a complex quantity, the wave-vector of the SPP also writes in a complex form k_{spp} (λ) = k' (λ) + jk'' (λ). To obtain a scalar representation for the dispersion $E(\mathbf{k}) = \hbar |\mathbf{k}|$ transformation into a solely real expression by means of its complex conjugate k_{spp}^* and calculation of $|\mathbf{k}| = \sqrt{\mathbf{k} \cdot \mathbf{k}^*}$ is beneficial. The outcome of this formal treatment is not obvious, and occasionally leads to unexpected features.

The photon wave-vector for propagation in vacuum is real and writes as:

$$k_{ph} = \frac{2\pi}{\lambda} \tag{2.2}$$

Upon propagation within a non-absorptive dielectric substrate with refractive index n_{MAT} and incident angle θ , the wave-vector component parallel to the metal film writes as

$$k_{ph} = n_{\text{MAT}} \frac{2\pi}{\lambda} \sin\left(\theta\right) \tag{2.3}$$

In case of surface plasmon-photon coupling, both expressions of Eqs. 2.1 and 2.3 match at the resonance wavelength λ_{res} (or λ_R), and the intersection point defines the resonance position for this 3-phase layer system. The outcome is an analytical expression for the refractive index of the liquid bulk analyte n_{an} , as function of a varying resonance angle θ_{res} or θ_R (the Angular Interrogation Mode—AIM), whilst comprising a fixed incident wavelength λ_{res} ,

$$n_{an}(\theta_{res}) = \sqrt{\frac{\varepsilon_{mr}(\lambda_{res}) \left[n_{\text{MAT}}(\lambda_{res}) \sin(\theta_{res})\right]^2}{\varepsilon_{mr}(\lambda_{res}) - \left[n_{\text{MAT}}(\lambda_{res}) \sin(\theta_{res})\right]^2}}$$
(2.4)

Similarly, in the Wavelength Interrogation Mode—WIM, the refractive index of the analyte as function of a varying resonance wavelength λ_{res} at fixed incident angle

 θ_1 , is expressed as:

$$n_{an}(\lambda_{res}) = \sqrt{\frac{\varepsilon_{mr}(\lambda_{res}) n_{\text{MAT}}(\lambda_{res}) \sin(\theta_1)^4}{\left[\varepsilon_{mr}(\lambda_{res}) - n_{\text{MAT}}(\lambda_{res})^2 \sin(\theta_1)^2\right]^2 + \varepsilon_{mr}(\lambda_{res})^2}}$$
(2.5)

These expressions illustrate that the physical function of an SPR-sensor essentially resembles an optical refractometer.

Figure 2.1 illustrates the elementary physical interaction scheme, based on energy-momentum (wave-vector) conservation: the SPP-dispersion $E(k_{spp})$ in case of a free electron type Aluminum metal surface, and its coupling to photons, with dispersion $E(k_{ph})$.

Ideally, $E(k_{ph})$ exhibits a straight line in vacuum (or gas), and is placed outside of the SPP dispersion region. At low k-values, it may bend beneath the $E(k_{spp})$ regime, provided that the light beam propagates within a suitable dielectric substrate that supports the metal film. Under optimum conditions, $E(k_{ph})$ intersects with the SPP-dispersion at a well-defined resonance energy or wavelength, whilst the slopes (or group velocities) comprise $dE(k_{spp})/dk \neq dE(k_{ph})/dk$. Furthermore, due to the dispersion $n_{\text{MAT}}(\lambda)$ within a dielectric, over a large range of k-values, $E(k_{ph})$ is not necessarily a simple straight line.

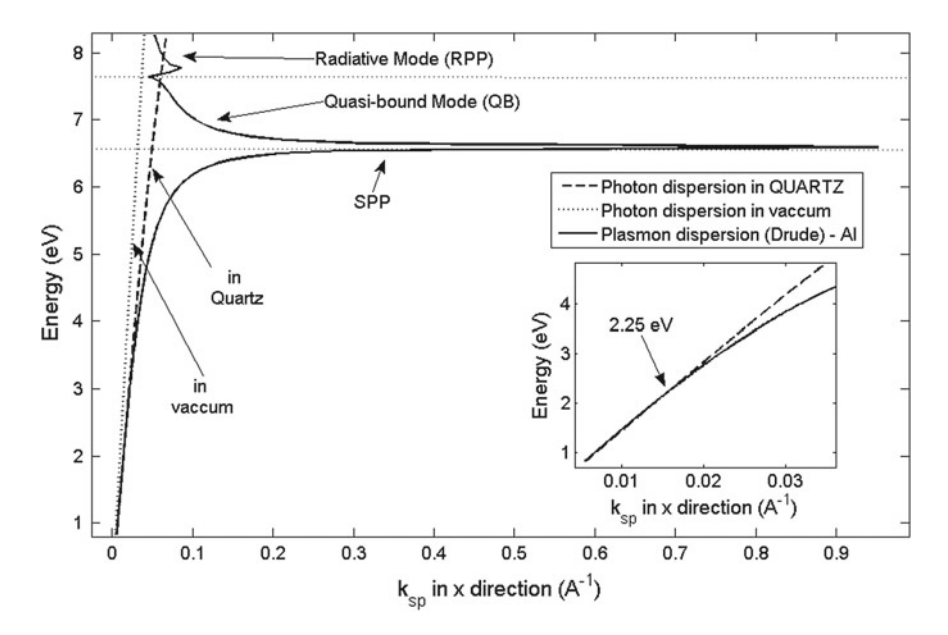


Fig. 2.1 Surface plasmon $E(k_{spp})$ and photon $E(k_{ph})$ dispersions for a free electron type metal on a quartz substrate, and described by the Drude equation, and deposited onto a quartz substrate. The metal surface is in contact with water. QB denotes the quasi bound, and RPP the radiative surface plasmon polariton branch. The cross-over is at 2.25 eV

Furthermore, as is shown later for certain metal films, both dispersion curves may quasi coincide at low k-values over an extended range, without existence of a sharp cross-over point. In this case, the slopes $dE(k_{spp})/dk \approx dE(k_{ph})/dk$ and results in a spectrally broadened resonance.

At moderate to high k_{SDD} -values, the energy of the SPP of Al within the Drude approximation remains constant at 6.6 eV. In accordance with the findings, reported in Ref. [1], a further split-off plasmon branch exists, known as the quasi-bound SPP. Its dispersion is placed within the so-called plasmonic gap, slightly above the dispersion curve of the bound SPP. It is imaginary, exhibits an oppositely directed group velocity and eventually evolves into the so-called a radiative plasmon mode or RPP at low k, where it coincides with the photon dispersion. The SPP intersects with the photon dispersion at around 2.25 eV, as is illustrated in the lower inset. It is important to recall that strong spectral modulations/wavelength dependence of the CDK may also result in weak variations of the SPP dispersion. For a few metals, this phenomenon leads to additional intersection points with the more or less linear photon dispersion, and it is independent of the actual eigen-modes of the SPP-wave function. Furthermore, under certain conditions, and not outlined here in more detail, a surface plasmon also may decay into an electron-hole pair (exciton), along with generation of a freely propagating electron, provided that wave vectors and particle energies match. This leads to enhanced internal photoemission, as is reported in Refs. [2, 3] for an electrochemically roughened Silver film in contact with water. Surface plasmon coupled UV-photon emission is a further plasmonic radiative decay process, and reported in Ref. [4].

References

- Kasarova, S.N., Sultanova, N.G., Inov, C.D., Nikolov, I.D.: Analysis of the dispersion of optical plastic materials. Opt. Mater. 29, 1481–1490 (2007)
- 2. Neff, H., Sass, J.K., Lewerenz, H.J.: A photoemission-into-electrolyte study of surface plasmon excitation on high index faces of silver. Surf. Sci. **143**, L356–L362 (1984)
- 3. Neff, H., Sass, J.K., Lewerenz, H.J., Ibach, H.: Photoemission studies of electron localization at very low excess energies. J. Phys. Chem. **84**, 1135 (1980)
- Gryczynski, I., Malicka, J., Gryczynski, Z., Nowaczyk, K., Lakowicz, J.R.: Ultraviolet surface plasmon-coupled emission using thin aluminum films. Anal. Chem. 76, 4076–4081 (2004)

Chapter 3 Physical Features of Surface Plasmon Resonance Sensors

SPR sensors are normally based on a Kretschmann configuration and may be operated in two different modes; the angular interrogation (AIM) and the wavelength interrogation mode (WIM). In principle, as said before, SPR sensors are optical refractometers, and provide a refractive index n_{an} -value. This quantity is available in dimensionless refractive index units (RIU), either for bulk liquid analyte solutions adjacent to, or of thin dielectric films adsorbed onto an SPR-active thin metal film, in contact with a liquid solution behind.

Schematics of the optical set-up are shown in Fig. 4.1a, b, each setup comprising a flat dove type prism chip. The design route allows the construction of compact instruments and avoids implementation of a bulky optical prism. The optical function of SPR chips is similar to a wave guide. In the AIM, incident radiation is spectrally narrow band, whilst the angle range is wide and the resonance angle is recorded. In the WIM, the incident radiation is spectrally broadband, the incident angle range is narrow, comprising a collimated light beam, and the resonance wavelength is tracked by a spectrometer. A third-less popular-hybrid sensor configuration is the Intensity Mode (IM), as shown in Fig. 4.1c, where a collimated beam at fixed (resonance) angle and wavelength is employed.

The intensity minimum, as illustrated in Fig. 5.2, indicates the resonance position. Intensity variations and displacements of the resonance are tracked by the electrical output signal of a simple single element optical receiver. A fourth operation mode, not considered here, relies on optical phase recordings. The experimentally demanding method utilizes an ellipsometric arrangement, where optical phase changes are detected by means of a rotating polarizer.

For extraction of the resonance minimum, two measurements are needed to locate its precise angle or wavelength, respectively, defined by the intensity ratio:

$$I_{res} = \frac{I_{wet}(\theta, \lambda)}{I_{dry}(\theta, \lambda)}$$
(3.1)

These quantities are taken either as function of angle θ in the AIM, or wavelength λ in the WIM. $I_{dry}(\theta, \lambda)$ is the reflectance signal, obtained from the dry cell, and $I_{wet}(\theta, \lambda)$ is recorded in presence of the liquid analyte. This normalization procedure eliminates spatial or spectral non-uniformities within the detected beam profile, caused by the characteristics of light source and/or optical receiver. As a result, the resonance feature is extracted, as illustrated in Fig. 5.2. Outside of the resonance, the ratio approaches unity, whilst virtually all radiation is absorbed at the resonance minimum. A change of the bulk refractive index of the analyte Δn_{an} , or presence of an adsorption layer with nanometer thickness d, comprising a refractive index different from the adjacent liquid dielectric, usually causes a shift of the minimum to a higher angle in the AIM, or to longer wavelength in the WIM.

Furthermore, dark current correction of the receiver output signal, as well as dynamic compensation of low frequency light source and/or receiver fluctuations (1/f-noise) should be taken into account, especially towards reduction of long term thermal drift effects. Mathematical signal averaging and smoothing routines are commonly implemented to further improve the signal-to-noise ratio. Short term fluctuations and noise magnitudes σ , respectively, of the refractive index $\langle \sigma n_{an} \rangle \approx 10^{-7}$ RIU, along with long time signal drift levels $\leq 10^{-4}$ RIU/h are achievable under optimum conditions. Both quantities determine the limit of detection (LOD), defined as the 3σ -value.

Short term noise originates primarily from fluctuations of the light source. It is determined and can be controlled by the quality of the power supply and electrical biasing settings for light emitting diodes or lasers. Noise contributions from state-ofthe art CMOS or CCD cameras usually are small and can be neglected. Long term instrumental drift is mostly caused by thermal effects. The total instrumental linear dynamic sensing range for a recorded refractive index variation $\Delta n_{an}^{\rm max}$ should reach 0.1 RIU. The optical sensing depth of SPR sensors, and associated electric fields, extends approximately $\lambda/3$ into the volume of the adjacent liquid analyte, albeit field penetration is much shorter within the metal film. If both signs of the electric fields are identical, then the associated SPP wave-function is symmetric, otherwise anti-symmetric. The refractive index change, resulting from the presence of a nonabsorptive ad-layer is obtained from the difference $\Delta n_{ads} = n_{eff} - n_{an}$, where n_{an} is the RIU value, as recorded for the plain analyte, and n_{eff} denotes the corresponding value in presence of an ad-layer. The former case is called an optical 3-layer set-up; the latter situation is assigned to an optical 4-layer system. Since both configurations are equivalent, it is sufficient to treat the 3-layer system in the Fresnel simulation.

Furthermore, for adsorbed dielectric films ≤ 100 nm thickness, a linear relation exists between the ad-layer induced refractive index change Δn_{ads} and its thickness or, alternatively, the particle surface concentration. Large molecules do not necessarily form a homogeneous film. With assumptions on size and orientation of adsorbed molecules, the effective surface coverage beneath a complete mono-layer can be estimated, as outlined in Ref. [1].

Reference 17

Reference

 Laborde, H.M., Lima, A.M.N., Loureiro, F.C.C.L., Thirstrup, C., Neff, H.: Adsorption, kinetics and biochemical interaction of biotin at the gold-water interface. Thin Solid Films 540, 221–226 (2013)

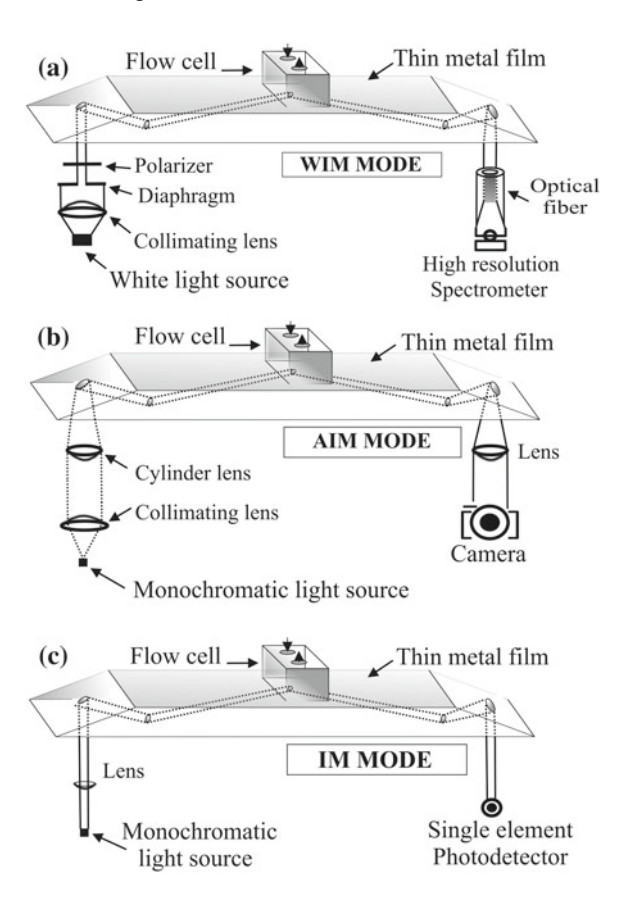
Chapter 4 Design Features of Surface Plasmon Resonance Sensors

4.1 Propagating Surface Plasmons

The two sensing modes under consideration exhibit advantages and disadvantages in terms of technical complexity, data processing and operation conditions. The temperature coefficient of the refractive index of water at ambient T, with -1.2×10^{-4} RIU/°C, is quite high and exceeds those of the optical components, typically used in the optics design. Hence, it should be recalled that SPR sensors are particularly sensitive to temperature fluctuations. They are also sensitive to mechanical vibrations or thermal distortions in the optical path, down to the micrometer or even sub-micrometer levels. A rigid mechanical design is therefore beneficial. Surface conditions, preparation and functionalization, as well as long term temporal stability and signal drift effects are further important issues, since recordings may last for several hours. Usually a flat exchangeable and/or disposable optical glass or polymer chip is used. The chip comprises a metal film on the top—in contact with the liquid analyte—and it is attached to a bulky glass prism on the bottom via an index matching oil or gel. Optical chips can also be designed as Dove type prisms or flat plates with integrated diffractive optical coupling elements. Compared to the classical bulk prism design, such optical chips are mechanically more easily integrated into an instrumental set-up, as outlined in Ref. [1]. Among other issues, this approach also avoids need for index matching optical elements, as gel or oil.

A retractable micro-fluidic cell is attached to the upper surface in the center of the Dove prism. An external peristaltic or syringe pump enables all solutions as well as the liquid analyte to be guided to the central sensing spot. To perform reliable and reproducible recordings, a proven protocol of surface cleaning, functionalization, surface rinse/wash and analyte admission steps is required, as well as use of high quality solvents and solutes. The possibility of chip fabrication from relatively low cost optical polymer materials and injection molding technology allows large volume production and disposable use. Schematics of the optical set-ups based on the Dove type prisms operating at the angular, wavelength and intensity interrogation modes are shown in Fig. 4.1.

Fig. 4.1 Principal design features, components and set-up for WIM, AIM and IM operation, using a Dove type glass prism chip with absence of a index matching gel or liquid



Until today, the majority of commercial SPR-instruments with real time operation capability utilize the AIM. It is evident that this mode offers considerably higher flexibility, since no moving parts or dispersive elements are required and the instrumental performance is largely determined by the quality of the data processing software. As is outlined later, the angular resonance position is much more pronounced than the corresponding spectral feature, especially for SP-active films, made from other than the noble metals.

An example of a compact SPR instrument, employing a disposable optical chip attached to a micro-fluidic cell, is shown in Fig. 4.2. Its outer dimensions are $12 \times 6 \times 6$ cm. The components of the device are made from Aluminum, and they are embedded in a thermally isolating PET housing. The unit is attached to an electrically controlled Peltier cooler device, to sustain a stable internal instrumental temperature. The data acquisition system utilizes a commercial FPGA (field programmable gate array) for processing the output data of a Hamamatsu CMOS image sensor. The instrument can be operated in all three modes (AIM, WIM and IM), depending on the selected light source, optical chip and radiation detector.

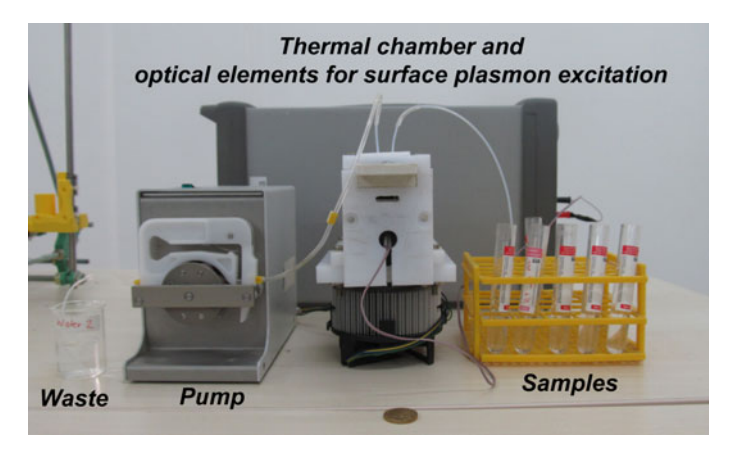


Fig. 4.2 Example of a compact, thermally stabilized SPR instrument that utilizes diffractive optical coupling chips in the AIM

Optical simulation results presented in this report address the relevant aspects of the SPR phenomenon, preferably for the metal-water interface and, in few cases, for the solid-hexane interface: optical reflectance for p-polarized radiation (with the E-field vector parallel to the incident plane) as function of wavelength, incident angle; selection of the metal film at its optimal thickness, and the most suitable substrate material. From these data, the achievable SPR-sensor responsivity, spectral and angular broadening at half maximum (FWHM) and achievable sensing range are extracted. An achievable LOD value is not provided, since this performance parameter largely depends on the quality and noise level of the opto-electronic components of the instrument. However, the LOD approximately scales with the spectral $(\Delta \lambda_{res})$ or angular $(\Delta \theta_{res})$ resonance width that defines the accuracy to which the actual resonance position can be determined. These quantities are the essential design parameters of interest for the construction of this sort of optical instruments.

In principle, each metal film will display a surface Plasmon resonance. However, its position may be placed at either a wavelength or an angle, which is technically difficult to use or to implement. The wavelength regime $\lambda < 1,000$ nm is easily accessible by means of silicon based light detectors. Especially CMOS detectors are available at moderate cost, while at larger wavelengths either germanium based, or expensive compound semiconductor receivers must be employed.

SP-resonance angles typically appear at incident angles $>55^{\circ}$ and extend up to 80° . For an optical construction, the upper angle limitation $\leq 75^{\circ}$. Furthermore, in the design and implementation of the radiation/image sensor, one needs to compromise on individual pixel size/area, and the distance between pixels (pitch). The larger the area, the higher the output signal is, while the angular resolution decreases. The achievable angular resolution 10^{-4} degree, but requires suitable data processing algorithms to achieve appropriate sub-pixel resolution. The spectral resolution of spectrometers for WIM operation should not be below 1 nm. Compact, high

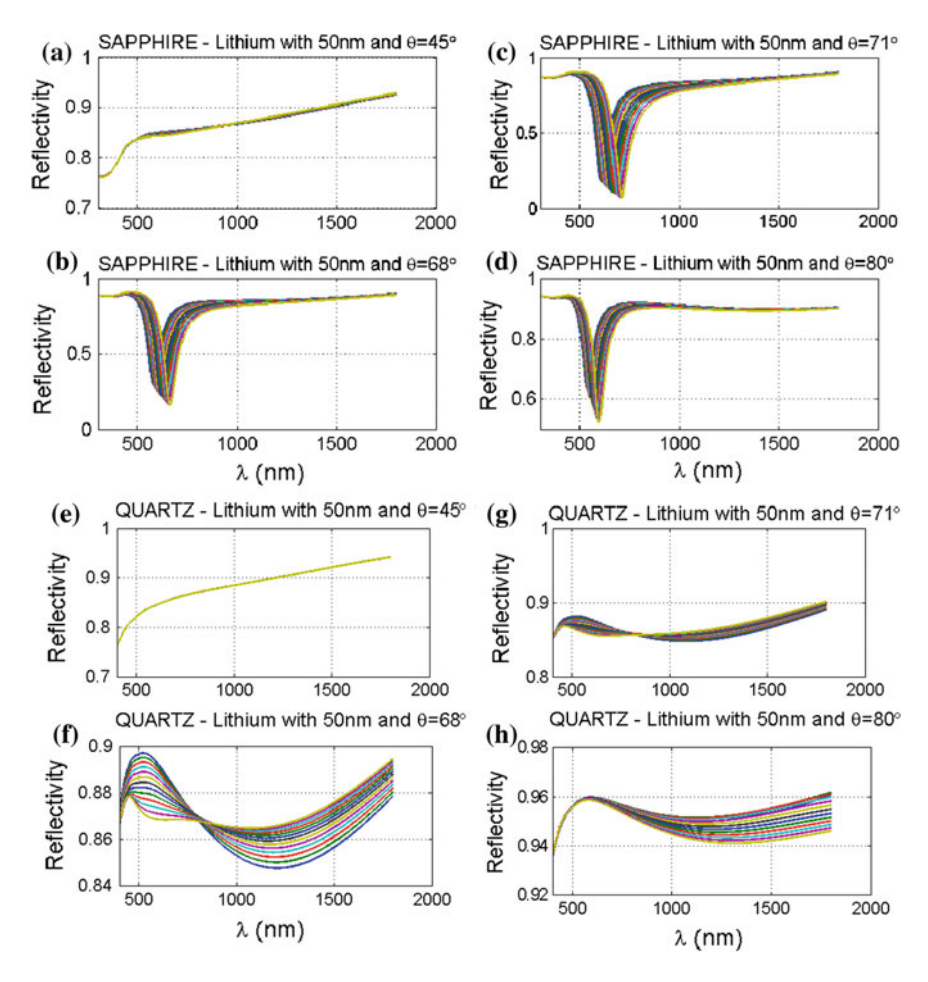


Fig. 4.3 Influence of the substrate material and angle on the shape and strength of the SPR signal in the WIM. Example of Lithium deposited on Sapphire (a-d) and Quartz (e-h)

resolution fiber optic spectrometers are now available at moderate cost. For AIM applications, diode lasers and LED's with excellent quality are available to wavelength $\leq 1.6\,\mu\text{m}$. However, it is quite difficult to find suitable spectrally broad band radiation emitters at wavelength $> 0.8\,\mu\text{m}$, which usually require so-called "globar" low resistive ceramics, along with high current power supply.

An example of a series of SPR plots, as will be presented in this report for the different metal films is shown below in Fig. 4.3.

The figures illustrate the optical reflectance of p-polarized radiation as function of wavelength for a 50 nm thin Lithium film, deposited onto a Sapphire (lower figures a–d), and on a quartz substrate (upper figure e–h). On the opposite side, the Li-metal film is in contact with a dielectric cyclo-hexane solution to prevent surface oxidation. The refractive index of this non-oxidizing organic liquid is displayed for

a series of increasing values, indicated by different colors. Four incident angles of 45° , 68° , 71° and 80° have been considered. Both dielectric substrate materials are frequently used for SPR sensors. It is evident, that the Sapphire substrate accounts for pronounced SPR dip near a wavelength of 600 nm for all angles, except 45° . In contrast, the quartz substrate in connection with Li-films is not suitable for SPR sensing (see Y-scale factor), since the associated SPR-dip appears only at very high incident angle $\approx 85^{\circ}$, which is unsuited for a reliable optical construction.

Also included and illustrated in this report are the materials specific photon and SP-dispersions and associated resonance conditions. As mentioned above, these investigations are made for a broad range of common substrate materials, as are organic polymers used in optics, glasses and inorganic crystals. Only such metals are considered, from which thin films can be readily made by established sputtering methods, and reliable optical materials parameters are available. The optimal film thickness that is required for SPR excitation is determined and it is typically within the 20–70 nm nanometer range. It depends considerably on the metal film materials, and it is also sensitive to and varies with the selected dielectric substrate. However, for certain SPR-active, highly doped semiconductors or semi-metals, the optimal film thickness is substantially higher. Resonance wavelengths vary broadly from the UV region to the near infrared part of the electromagnetic spectrum, and incident angles for SP excitation usually exceed 55°.

The present work also treats the SPR characteristic of a selected dielectric-metal multilayer system, beyond the immediate need for practical application. The optical properties of these artificial structures are yet not established and suitable experimental deposition methods thereof have not been exploited.

The primary feature of interest in the design of an SPR sensor is:

SPR responsivity in the AIM: ratio of the variation of the resonance angle $\Delta\theta_{res}$ with the refractive index variation Δn_{an} , defined as $R_{AIM} = \Delta\theta_{res}/\Delta n_{an}$.

SPR responsivity in the WIM: ratio of the variation of the resonance wavelength $\Delta \lambda_{res}$ with the refractive index variation Δn_{an} , defined as the differential $R_{WIM} = \Delta \lambda_{res}/\Delta n_{an}$.

If the imaginary part of the metal CDK is sufficiently small, an analytical expression can be derived for the optical responsivity R_{AIM} in the AIM from (2.4) by differentiation. For the noble metals Au, Ag and Cu, it writes with sufficient accuracy as:

$$R_{AIM} = \frac{\varepsilon_{mr}\sqrt{-\varepsilon_{mr}}}{\left(\varepsilon_{mr} + n_{an}^2\right)\sqrt{\varepsilon_{mr}\left(n_{an}^2 - n_{\text{MAT}}^2\right) - n_{an}^2 n_{\text{MAT}}^2}}$$
(4.1)

This expression requires that the associated spectral resonance wavelength λ_{res} is reliably known:

 ε_{mr} is the real part of the dielectric function of the metal film, $n_{\rm MAT}$ is the refractive index of the dielectric substrate and n_{an} is the effective refractive index of the liquid analyte under consideration. In general, R_{AIM} is a non-linear function of all variables. However, neglecting the imaginary part of the metallic CDK is inappropriate for most other metals, and the approximation given in 4.1 is not applicable.

At present, an analytical representation for $R_{WIM} = \Delta \lambda_{res}/\Delta n_{an}$ in the WIM is not available. Inclusion of all optical dispersion relations for the different materials involved leads to rather odd analytical expressions. Nevertheless, R_{WIM} is numerically accessible from a Fresnel analysis, as is outlined below for the individual materials combinations.

4.2 Localized SP's

There are a number of experimental configurations for measurements of the localized surface plasmon response, including direct optical transmission measurements [2–4] and reflectance measurements [2, 5] for measuring extinction spectra of an ensemble of nano-particles. An example of a Dove prism set-up, analog to those of Fig. 4.1a–c, is given below in Fig. 4.4

Since the extinction spectrum of a nano-particle (NP) sensitively depends on its size and shape, extinction spectra of an ensemble of particles are inhomogeneously broadened [6]. It is therefore often desirable to obtain extinction spectra from colloidal particles. Dark-field imaging using a high-numerical aperture dark-field condenser and a low numerical aperture microscope objective combined with a liquid crystal tunable filter and a cooled CCD camera have been used to record single NP scattering spectra [7]. An alternative configuration utilizes Dove prism coupled total-internal-reflection (TIR) spectrometry, where the extinction spectrum is obtained collecting the scattered light by a photo-spectrometer, or an image is recorded by a CCD camera [4, 8]. A micro-fluidic cell is attached to the upper prism surface. It supplies the analyte solution, through a micro-flow channel to the central sensing spot. Through the TIR effect at the upper prism surface, a considerable E-field component of the incoming radiation extends into the flow channel and

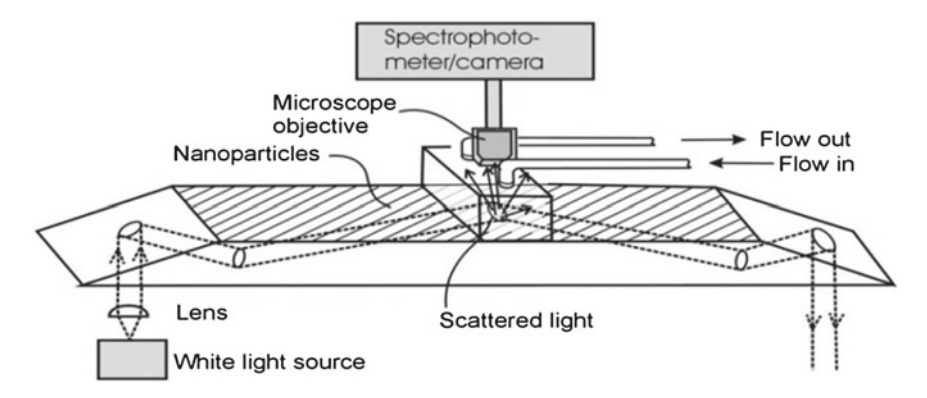


Fig. 4.4 Principal design features, components and set-up for LSPR spectroscopy, using a Dove type glass prism chip (NP's are detected in flow cell)

4.2 Localized SP's 25

interacts with the NP's. The latter configuration, as illustrated schematically in Fig. 4.4, is similar to the Kretschmann prism coupling configuration, as used in the design of a conventional surface plasmon resonance sensor, outlined before. However, this arrangement does not comprise a thin semi-transparent metal film on the prism's upper surface. A microscope objective collects the scattered light from the NP's, illumination is achieved by white light source and a photo-spectrometer measures the spectra or images are recorded by a camera, which may be combined with a tunable wavelength filter. An additional photo-spectrometer may also measure the light spectra at the output of the prism similar to the case of conventional wavelength interrogation SPR sensors (not shown in Fig. 4.4).

Compared to conventional propagation SPR sensors, the sensitivity of LSPR sensors is lower because of a smaller evanescent wave decay length, unless the sensing layer thickness is smaller than or similar to the evanescent wave decay length of the LSPR, i.e. of the order of 20 nm [9]. In this case, the LSPR sensor has the advantage of being less sensitive to temperature fluctuations [10]. The synthesis of metallic NP's is discussed in Ref. [11].

References

- Thirstrup, C., Zong, W., Borre, M., Neff, H., Pedersen, H.C., Holzhueter, G.: Diffractive optical coupling element for surface plasmon resonance sensors. Sens. Actuators B 100, 298–308 (2004)
- 2. Willets, K.A., Van Duyne, R.P.: Localized surface plasmon resonance spectroscopy and sensing. Annu. Rev. Phys. Chem. **58**, 267–297 (2007)
- 3. Liao, W.S., Chen, X., Yang, T., Castellana, E.T., Chen, J., Cremer, P.S.: Transmission localized surface plasmon resonance platforms: benchtop chemistry for the rapid prototyping of label-free biosensors. Biointerphases 4, 80–85 (2009)
- Estevez, M.-C., Otte, M.A., Sepulveda, B., Lechuga, L.M.: Trends and challenges of refractometric nanoplasmonic biosensors: a review. Anal. Chim. Acta 806, 55–73 (2014)
- Kim, D.K., Kerman, K., Saito, M., Sathuluri, R.R., Endo, T., Yamamura, S., Kwon, Y.S., Tamiya, E.: Label-free DNA biosensor based on localized surface plasmon resonance coupled with interferometry. Anal. Chem. 79, 1855–1864 (2007)
- Sherry, L.J., Jin, R.C., Mirkin, C.A., Mirkin, G.C., Scharz, G.C., Van Duyne, R.P.: Localized surface plasmon resonance spectroscopy of single silver triangular nanoprisms. Nano Lett. 6(9), 2060–2065 (2006)
- Henry, A.I., Bingham, J.M., Ringe, E., Marks, L.D., Schatz, G.C., Van Duyne, R.P.: Correlated structure and optical property studies of plasmonic nanoparticles. J. Phys. Chem. C 115, 9291– 9305 (2011)
- Hutter, E., Fendler, J.H.: Exploitation of localized surface plasmon resonance. Adv. Mater. 16, 1685–1706 (2004)
- Kerker, M.: The Scattering of Light and Other Electromagnetic Radiation. Academic Press, New York (1969)
- Zalyubovskiy, S.J., Bogdanova, M., Deinega, A., Lozovik, Y., Pris, A.D., Hyup An, K., Hall, W.P., Potyrailo, R.A.: Theoretical limit of localized surface plasmon resonance sensitivity to local refractive index change and its comparison to conventional surface plasmon resonance sensor. J. Opt. Soc. Am. A 29, 904–1001 (2012)
- Rao, C.N.R., Kulkarni, G.U., Thomasa, P.J., Edwards, P.P.: Metal nano-particles and their assemblies. Chem. Soc. Rev. 29, 27–35 (2000)

Chapter 5 Data Extraction Algorithms

5.1 Multilayer Fresnel Analysis for Extended Metal Films

The Fresnel equation system in its matrix representation is the appropriate tool to analyze the optical properties of multi-layer systems, treating all interference effects, except diffraction. It has been introduced about 50 years ago by F. Abelés. We refer to Ref. [1], and references cited therein. The outcome is a precise value for the reflection and transmission coefficients of an optical wave, incident onto an ensemble of several interfaces and media, with a given incident angle and different (complex) refractive indices.

Here, the equations are applied to a film arrangement that comprises 3 layers with different refractive indices, as is illustrated in Fig. 5.1a. For comparison the 4 layer configuration is included in Fig. 5.1b. The different media are described as follows:

Medium 1: The optically transmitting substrate material with a known high (real) refractive index n_{1re} and a thickness d_1 , considered as being infinite.

Medium 2: A thin metal film, with a known complex refractive index $n_2 = n_2 + i\kappa_2$. The thickness d_2 is much smaller than the wavelength of the incident light.

Medium 3: A liquid layer, which is usually aqueous solution, with a known (real) refractive index n_3 . The thickness is d_3 , considered to be infinite.

All optical quantities vary with wavelength.

Briefly, reflection, absorption and transmission of a p-polarized light beam, impinging onto a planar multilayer structure (see Fig. 6) are computed by means of the transfer matrix method. As the first step for creation of the transfer matrix both, the admittance q_i and layer phase shift β_i are defined

$$q_j = \frac{\sqrt{n_j^2(\lambda) - (n_{\text{MAT}}(\lambda)\sin(\theta_1))^2}}{n_k^2(\lambda)}$$
 (5.1)

$$\beta_j = \frac{2\pi}{\lambda} d_j \sqrt{n_j^2(\lambda) - (n_{\text{MAT}}(\lambda)\sin(\theta_1))^2}$$
 (5.2)

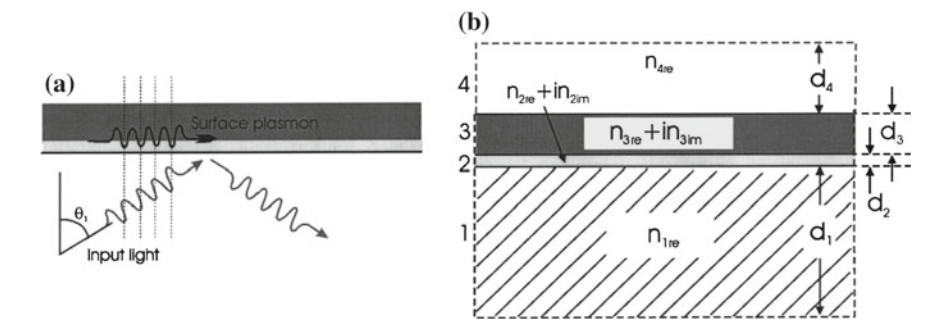


Fig. 5.1 Three-layer system and optical boundary conditions used for the Fresnel calculations in a, b illustrates the 4-layer configuration

for each layer. In (5.1) and (5.2) $n_j = n_{jr} + i n_{jl}$ ($i = \sqrt{-1}$), n_j is the refractive index of the medium j; θ_j is the incident angle of light into the medium j; d_j denotes the width of the layer and λ the wavelength of the incident radiation. The incident light beam experiences multiple reflections until it reaches the last layer, and all of them must be taken into account in the total reflection/transmission calculation. The transfer matrix that describes the transfer of a wave, propagating from medium j to medium j+1 is then defined as:

$$M_{j} = \begin{bmatrix} \cos(\beta_{j}) & (i\sin(\beta_{i}))/q_{j} \\ -iq_{j}\sin(\beta_{j}) & \cos(\beta_{j}) \end{bmatrix}$$
(5.3)

The total transfer matrix, M_{tot} , calculated as a function of the individual matrices M_i for each interface between the media, writes as:

$$M_{tot} = \prod_{j=2}^{m-1} \begin{bmatrix} m_{11} & m_{12} \\ m_{21} & m_{22} \end{bmatrix}$$
 (5.4)

The total reflection R and the transmission coefficients T, the so-called Fresnel coefficients, of a multilayer structure composed of m layers is obtained from (5.9) and given by

$$R = \frac{(m_{11} + m_{12}q_m) q_1 - (m_{21} + m_{22}) q_m}{(m_{11} + m_{12}q_m) q_1 + (m_{11} + m_{12}) q_m}$$
(5.5)

$$T = \frac{2q_m}{(m_{11} + m_{12}q_m)q_1 + (m_{11} + m_{12})q_m}$$
 (5.6)

It is illustrated in Fig. 5.2 that the minimum of the reflectivity (θ_{res} in the AIM and λ_{res} in the WIM) defines the resonance condition.

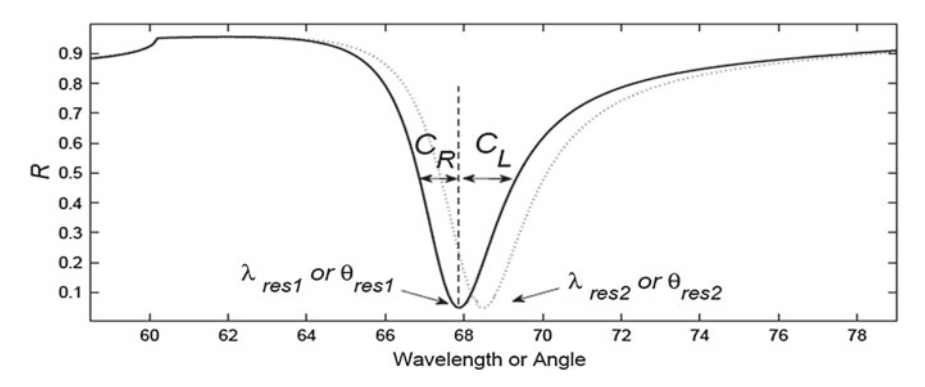


Fig. 5.2 Example of an asymmetric surface Plasmon resonance curve, as obtained from the Fresnel analysis. The displacement from λ_{res1} to λ_{res2} in the WIM, or from θ_{res1} to θ_{res2} in the AIM indicates a change of the refractive index of layer 3. The broadening parameter taken at FWHM is calculated as Cr+Cl, where Cr and CL are the distances in degrees (AIM) or nanometers (WIM) between resonance minimum and right and left edges of the curve, respectively

Modifications of the chemical composition of the analyte solution, or presence of a dielectric ad-layer on the metal surface cause a displacement of θ_{res} and/or resonance wavelength λ_{res} . On experimental data, numerous, fast tracking algorithms have been developed to extract the exact reflectance minimum of the SPR curve in real time.

5.2 Long Range Surface Plasmon Polaritons

Long range surface plasmon polaritons (LRSPP) are a special case and exist under selected layer conditions. Calculations for the LRSPP utilize the same Fresnel equations system as outlined before. However, a second thin dielectric layer is additionally placed onto a BK7 bulk substrate to form a dielectric bi-layer. Here, a Teflon film with varying thickness, ranging from 200–400 nm has been selected. This polymer exhibits a low refractive index, close to those of the aqueous analyte solution. It almost establishes the symmetric dielectric layer configuration that is needed for excitation of the LRSPP. With this condition, the SPP dispersion splits into a symmetric (same sign of the E-field of the SPP across the interface) and an anti-symmetric branch (with opposite sign). Both branches intersect with the photon dispersion. This results in two co-existing SP-resonances, which are detectable in both the WIM and AIM mode. For further details of this SP-sensing method, we refer to Ref. [2].

5.3 Localized Surface Plasmon Resonance in Small Particles

As mentioned earlier, SP's, linked to an extended conductive material-dielectric interface are propagating transverse magnetic (TM) surface waves. They exhibit the maximum field intensity at the interface that decays exponentially into both media. In an aqueous dielectric medium, the evanescent wave decay length is of the order of 200–400 nm and surface plasmon resonance sensors utilize the extreme sensitivity of the resonance position to refractive index changes within approximately the evanescent wave decay length into the adjacent dielectric medium. Employing a nano-particle (NP) smaller than the wavelength of light and composed by the same conductive material, the surface plasmon will be localized at the NP, and thus represent an eigenmode of the wave equation. The associated evanescent wave decay length is of the order of 5–30 nm. Within the NP, free conduction electrons will oscillate coherently with the frequency of light that illuminates the NP. There exist various chemical reactions and treatments for generation of colloidal metal particles with defined geometric properties.

The theoretical description of extinction and scattering of a particle by light can be described by the Mie theory [3–6]. There are extensive reviews about this electromagnetic model, and descriptions can be found in several monographs and text books [7–10]. The Mie theory applies to homogeneous and spherical particles.

Briefly, assuming that a conductive spherical particle is illuminated by a plane wave of light exciting a localized surface plasmon, the problem of scattering can be solved by expanding the incident, scattered, and internal fields in a series of vector spherical harmonics, where the coefficients of expansion are determined by requiring continuity of the tangential components of the electric and magnetic fields across the surface of the spherical particle. The coefficients of the infinite series for the extinction and scattering coefficients are [8]:

$$C_{ext} = \frac{2\pi}{k^2} \sum_{i=1}^{\infty} (2j+1) \operatorname{Re} \left\{ a_j + b_j \right\}$$
 (5.7)

$$C_{sca} = \frac{2\pi}{k^2} \sum (2j+1) \operatorname{Re} \left\{ \left| a_j \right|^2 + \left| b_j \right|^2 \right\}$$
 (5.8)

and the absorption coefficient is then obtained from

$$C_{abs} = C_{ext} - C_{sca} (5.9)$$

Assuming that the permeability (μ) of the particle and the dielectric surrounding it is the same, the scattering coefficients in Eqs. (5.7) and (5.8) can be written [8]:

$$a_{j} = \frac{\left[\frac{\psi'_{j}(mx)}{m\psi_{j}(mx)} + \frac{j}{x}\right]\psi_{j}(mx) - \psi_{j-1}(mx)}{\left[\frac{\psi'_{j}(mx)}{m\psi_{j}(mx)} + \frac{j}{x}\right]\xi_{j}(mx) - \xi_{j-1}(mx)}$$

$$b_{j} = \frac{\left[\frac{m\psi'_{j}(mx)}{\psi_{j}(mx)} + \frac{j}{x}\right]\psi_{j}(mx) - \psi_{j-1}(mx)}{\left[\frac{\psi'_{j}(mx)}{\psi_{j}(mx)} + \frac{j}{x}\right]\xi_{j}(mx) - \xi_{j-1}(mx)}$$

where x = ka is a size parameter, with a being the radius of the spherical particle and k being the wavenumber of the incident light; m is the ratio between the complex refractive index of the particle n_m , where $n_m^2 = \varepsilon'_{mr}(\lambda) + i\varepsilon''_{mr}(\lambda)$, and the refractive index of the surrounding dielectric (n_{an}) ; ψ_j and ξ_j are oscillating, but non-periodic Riccati-Bessel functions. A number of web sites provides programs for computations of light scattering from nanoparticles by solving Eqs. (5.7-5.9) [11].

5.4 Partial Differential Equation Formulation

The rigorous study of surface plasmon lies within the framework of the Maxwell's equations and eventually leads to the solution of the partial differential equation that represents a relatively complex physical phenomenon. Such approach permits a complete evaluation of the electro-optical characteristics of the surface plasmon, whilst exploiting optical reflections, interferences and scattering. The basic model is provided by the wave equation which is given by

$$(\nabla - i\mathbf{k}) \times \mu_r^{-1} ((\nabla - i\mathbf{k}) \times \mathbf{E}) - k_0^2 \left(\varepsilon_r - \frac{j\sigma}{\omega\varepsilon_0}\right) \mathbf{E} = 0$$
 (5.10)

which includes wave-vectors and relevant physical constants. Examples of a surface plasmon related reflectance curves for a thin Iron films in presence of a magnetic field that utilizes changes in the magnetic permeability (μ) are shown in Chap. 9.

The Finite Element Method (FEM) is widely used for solving partial differential equations. A important advantage of FEM is the flexible assessment of geometry effects in two or three dimensions and inclusion of magnetic phenomena, where the magnetic permeability μ exceeds 1. Hence, the FEM expands research work to a substantially higher level, and principally inclusion of all phenomena that affect the SPR signal: adsorption kinetics, thermal and hydrodynamic effects by flow injection, influence of mechanical, magnetic and optical phenomena.

References

- 1. Abelès, F.: Optical properties of very thin films. Thin Solid Films **34**, 291 (1976)
- 2. Berini, P.: Long-range surface plasmon polaritons. Adv. Opt. Photonics 1, 484–588 (2009)
- 3. Baffou, G.: Mie theory for metal nanoparticles. http://www.guillaume.baffou.com/courses.php
- 4. Bohren, C.F., Huffman, D.R.: Absorption and Scattering of Light by Small Particles. Wiley Interscience, New York (1983)
- 5. Mie, G.: Beiträge zur optik trüber medien, speziell kolloidaler metallösungen. Ann. Phys. **330**(3), 377 (1908)
- Hergert, W., Wriedt, T. (eds.): The Mie Theory, Springer Series in Optical Sciences, vol. 169.
 Springer, Berlin (2012) (Chapter 2, Mie Theory: A Review by T. Wriedt)
- 7. Masumura, A., Daimon, M.: Measurement of the refractive index of distilled water from the near-infrared region to the ultraviolet region. Appl. Opt. 46, 18 (2007)
- 8. Bass, M. (ed. in chief): Handbook of Optics, Fundamentals, Techniques and Design, 2nd edn., vol. I. McGraw-Hill Inc, New York (1995) (Chapter 6, Scattering by Particles by C. Bohren)
- Kerker, M.: The Scattering of Light and Other Electromagnetic Radiation. Academic Press, New York (1969)
- Mayer, K.M., Hafner, J.H.: Localized surface plasmon resonance sensors. Chem. Rev. 111, 3828–3857 (2011)
- 11. See e.g. http://www.scattport.org/, http://code.google.com/p/scatterlib/ or http://www.guillaume.baffou.com/courses.php

Chapter 6 SPR-Sensor Properties of Metal Films and Particles: Free Electron Type Metals

6.1 Thin Aluminum Films and Colloidal Particles

The complex optical constant $\varepsilon_{mr}(\lambda) = \varepsilon'_{mr}(\lambda) + j\varepsilon''_{mr}(\lambda)$ of the weakly paramagnetic metal has been taken from Ref. [1], as illustrated in the right inset of Fig. 6.1. The electron configuration of the single atom in the ground state is $[Ne]3s^23p^1$. The outer single 3p and 3s electron states account for the partially occupied and nearly parabolic conduction band in the solidified material. The band-structure of the metal is reported in Ref. [2] and exhibits a high electrical dc-conductivity of $35.5 \times 10^6 \, (\Omega \text{m})^{-1}$ at ambient T (20°C). Electrical materials parameters for Al and the following metals were taken from Ref. [3]. The CDK can be approximated by a modified form of the Drude model. $\varepsilon(\lambda)$ decreases steadily to high negative values within the spectral range of interest. However, both $\varepsilon'(\lambda)$ and $\varepsilon(\lambda)''$, reveal a prominent feature near 800 nm. It originates from an inter-band transition that is not considered in the simple DA. The SPP and photon dispersions are shown in Fig. 6.1; Polycrystalline or amorphous Aluminum films are most easily deposited by magnetron sputtering from a massive Al-target in low pressure Ar-atmosphere, by electron beam or thermal evaporation from electrically heated Tungsten or Ta foils or carbon boats in high vacuum to avoid bulk contamination of the films with oxygen. The boiling temperature of Al with 2,470 °C is rather high. Upon contact with air or water (pH 7), a dense, amorphous self-limiting native oxide layer of 0.2–0.4 nm thickness and chemical composition Al₂O₃ forms on the pure Al-film surface very fast. The SP-resonance is only weakly affected through its presence.

Towards high **k**-values, the surface Plasmon energy $E_{SPP}(k)$ at the Al-water interface approaches 7.6 eV. In case of a BK7 substrate, photon and SP-dispersion curves intersect at two points: near 4 eV at short and around 1.5 eV at much longer wavelength, as is illustrated in the magnified left lower inset. The spectral distribution of the reflectance $R(\lambda)$ in the WIM, as is resolved in Fig. 6.2 for most substrate materials, exhibits resonance splitting: an SP-dip at short (Sw) and longer wavelength (Lw). Both resonances belong to short range SP's, with symmetric E-field distributions into the adjacent dielectrics and the metal film. The resonance features seem most

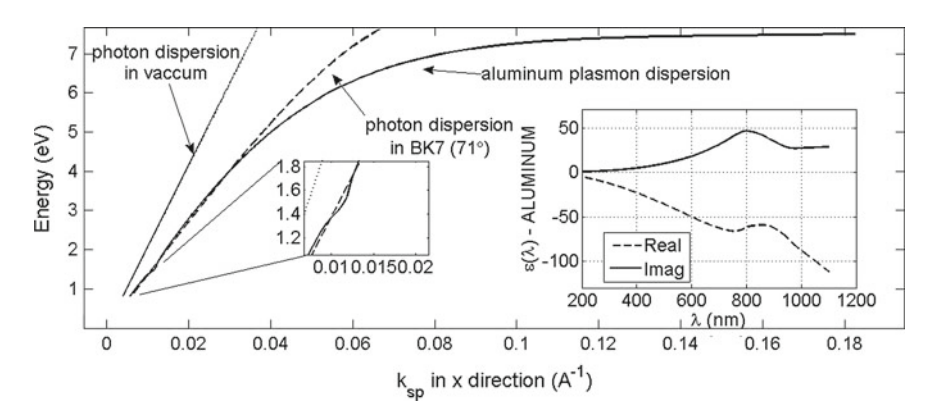


Fig. 6.1 Photon and symmetric SPP-dispersion at the Al-water interface (*solid-line*) for BK7 substrates (*dashed-line*). *Right inset* reveals the real and imaginary fractions of the CDK of the metal. The primary *upper intersection* point is located at 4 eV. *Left lower inset* illustrates a magnified section of two further cross-over points at low k-value and energy near 1.4 and 1.6 eV

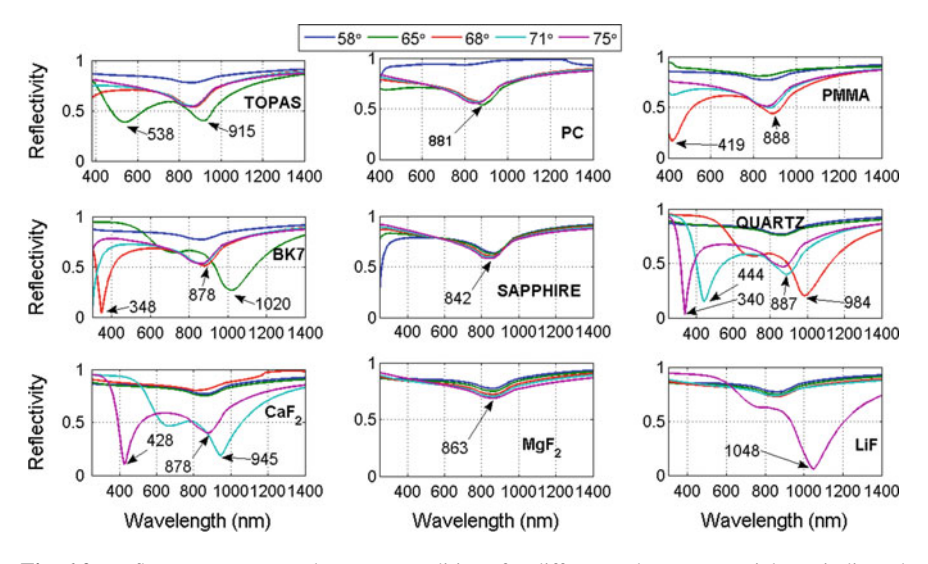


Fig. 6.2 Reflectance curves under WIM-conditions for different substrate materials, as indicated in the *plots*, and incident angles of 58°, 65°, 68°, 71° and 75° for the wavelength range 400 nm $< \lambda < 1,400$ nm. The Al-film thickness is 20 nm, being in contact with water as the liquid dielectric

pronounced for Quartz and BK7 glass substrates. PC, PMMA, Sapphire, MgF₂ and LiF apparently are poorly suited as substrates for SPR sensing. This is most clearly visible in the data set of Fig. 6.3, computed for AIM conditions.

For the Quartz substrate, the SP-energy (eV) varies with the incident angle within the range $65^{\circ} < \theta < 75^{\circ}$ approximately linearly as: $E_{SP}(\theta) = 0.357\theta - 23.02$.

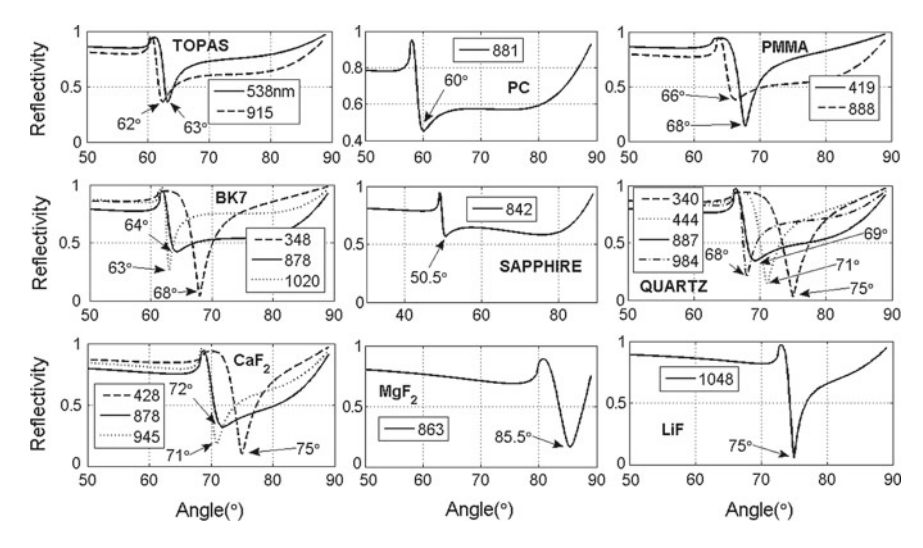


Fig. 6.3 Reflectance curves under AIM-conditions and best SP-depths for different substrate materials, as indicated in the *plots*, and different incident wavelengths for the angle range $50^{\circ} < \theta < 80^{\circ}$. Al-film thickness is 20 nm, in contact with water

The sensing characteristic of each metal are obtained from of the aqueous analyte with RIU-values 1.33 $< n_{an} < 1.39$ and increases of 5×10^{-3} RIU. The WIM sensing characteristic for Al-film is shown in Fig. 6.4 for BK7, comprising a resonance angle of 68°. Two resonances, i.e. a resonance splitting effect at short (Sw) and long (Lw)

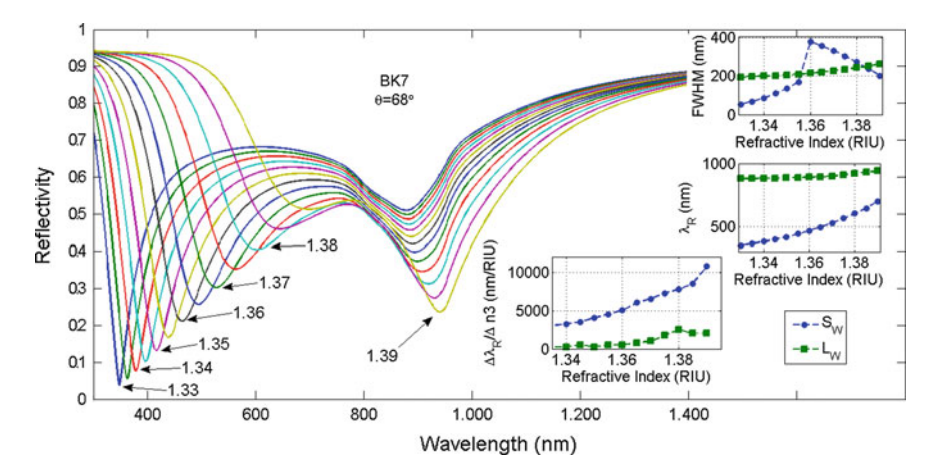


Fig. 6.4 WIM-sensor properties, spectral reflectance $R(\lambda)$ for different RIU-value of the aqueous analyte 1.33 < n_{an} < 1.39 with increases of 5 × 10⁻³ RIU, indicating resonance splitting. Substrate is BK7, incident angle is 68°. *Insets* show resonance displacements $\lambda_{res}(n_{an})$, responsivity $R_{WIM}(n_{an})$ and *line* broadening $\Delta\lambda_{res}(n_{an})$ for Sw and Lw excitations

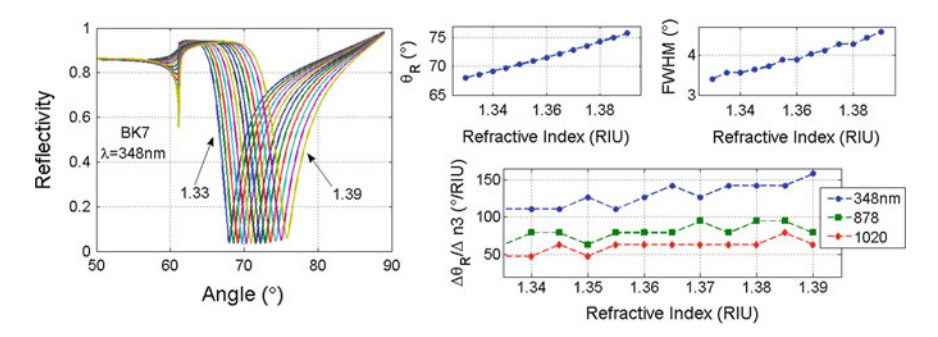


Fig. 6.5 AIM-sensor properties: angular reflectance $R(\theta)$ for different RIU-values of the aqueous analyte 1.33 < n_{an} < 1.39 with increases of 5×10^{-3} RIU. Substrate is BK7, incident wavelength 345 nm (Sw-excitation). Three figures at right show resonance displacements $\theta_{res}(n_{an})$, and line broadening $\Delta\theta_{res}(n_{an})$ for Sw at top, responsivity $R_{AIM}(n_{an})$ for three wavelength below

wavelength are resolved. The displacement of the resonance position in the Sw (start at 380 nm) and Lw (start at 840 nm) as function of the refractive index (RIU) of the liquid analyte are shown in the lower left inset. The depth/contrast of both resonances varies oppositely with increasing RIU-values of the analyte. The associated sensor responsivities are illustrated in the lower right inset. The Sw-resonance substantially exceeds the responsivity of the Lw-excitation. Both quantities increase weakly nonlinear with the RIU variation of the analyte. The SPR-line broadening effect (at Full Width at Half Maximum (FWHM)) of both resonances is presented in the upper right inset, and indicates smaller values with Sw excitation conditions.

The SPR-sensing characteristic in the AIM is shown in Fig. 6.5, comprising an initial resonance angle of 68° and wavelength of 348 nm (Sw-resonance). The depth of the SPR resonance is independent of the RIU of the analyte, in contrast to the WIM. A nearly linear increase of resonance angle, SPR sensor responsivity R_{AIM} and line broadening with the RIU of the analyte are resolved in the upper right and lower insets. The analysis reveals that the responsivity R_{AIM} at short wavelengths (Sw) with a value centered around 130°/RIU, is favorable.

Eventually, the influence of film thickness for the WIM and AIM is outlined in Figs. 6.6 and 6.7 comprising Sw and Lw-optical excitation conditions. This data set clearly indicates that the Al-film thickness for optimum SPR sensor operation is placed at 20 nm.

6.1.1 Long Range Surface Plasmon Polaritons (LRSPP-Mode)

The spectral SP-sensor properties in presence of an addition LRSPP mode in the WIM are depicted at the left side of Fig. 6.8, and reveal three prominent co-existing SP-excitations: two symmetric, short range modes (blue lines at right figures) at 400 and 800 nm, and the addition anti-symmetric, long range (LRSPP) mode (green lines) at 1,200 nm. All plotted for a set of different n_{an} -values The weaker SP-feature

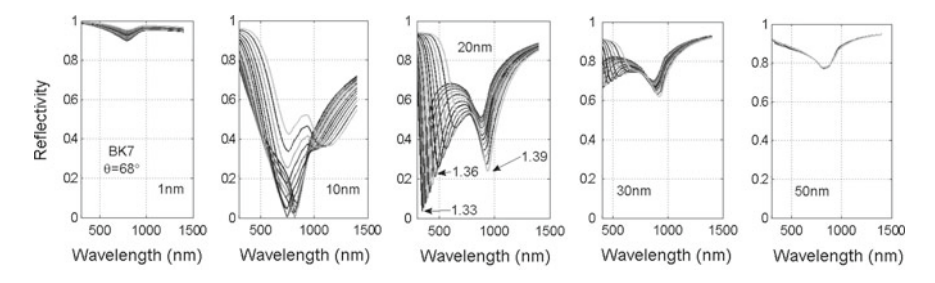


Fig. 6.6 WIM-reflectance at the SP-resonance for different Al-film thickness values of 1, 10, 20, 30 and 50 nm. RIU-value of the aqueous analyte: $1.33 < n_{an} < 1.39$ with increases of 5×10^{-3} RIU

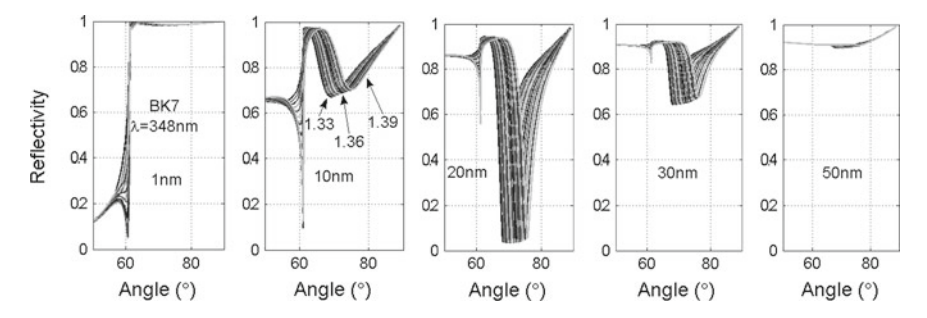


Fig. 6.7 AIM-reflectance at the SP-resonance for different Al-film thickness values of 1, 10, 20, 30 and 50 nm. RIU-value of the aqueous analyte: $1.33 < n_{an} < 1.39$ with increases of 5×10^{-3} RIU

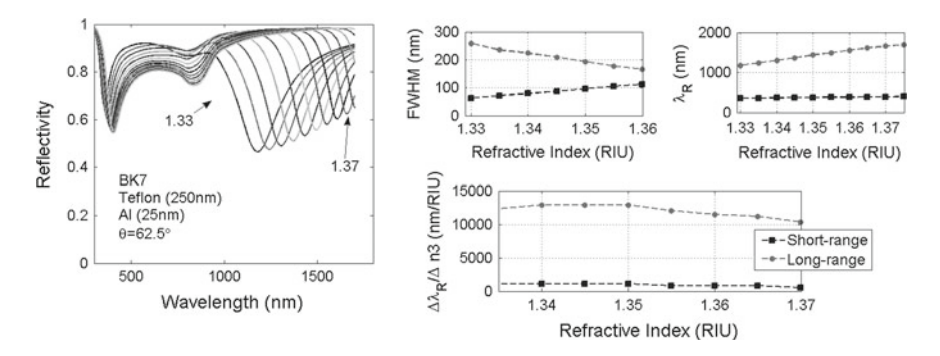


Fig. 6.8 WIM-sensor properties in presence of the LRSPP mode (line with circles): spectral reflectance $R(\lambda)$ (left figure) for different RIU-values of the aqueous analyte 1.33 < n_{an} < 1.39, indicating three SP-dips. Substrate is BK7, with a 250 nm Teflon film on top, incident angle is 62.5°. Three figures at right show line broadening $\Delta \lambda_{res}(n_{an})$ and resonance displacements $\lambda_{res}(n_{an})$ at top and responsivity $R_{WIM}(n_{an})$ below for short (line with squares) and long range SPP's (line with circles)

at 800 nm is also a short range symmetric mode, assigned before as Lw-mode. Comparison with Fig. 6.4 illustrates an increase by a factor 2 for the responsivity $R_{WIM}(\lambda)$ for the LRSPP-mode, up to high values of 13,000 nm/RIU. In contrast to

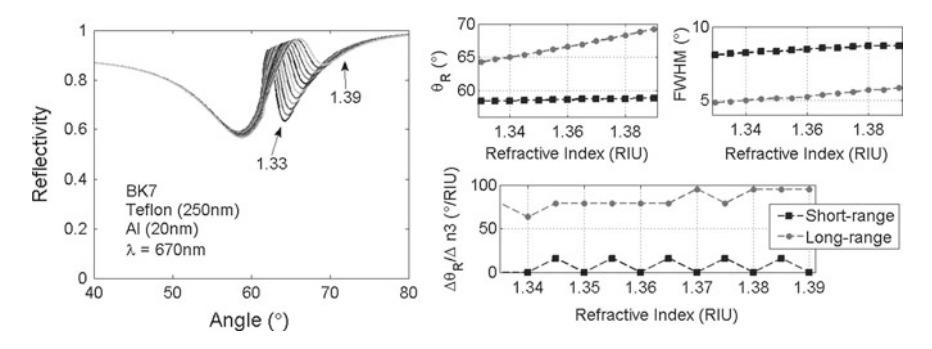


Fig. 6.9 AIM-sensor properties with the addition anti-symmetric LRSPP-mode: angular reflectance $R(\theta)$ (left) for different RIU-values of the aqueous analyte 1.33 $< n_{an} < 1.39$ indicating two SP-dips. Substrate is BK7 with a 250 nm Teflon film on top, and the metal film placed thereon. Incident wavelength is now 670 nm. Three figures at right show line broadening $\Delta\theta_{res}(n_{an})$ and angular resonance displacements $\theta_{res}(n_{an})$ at top, and responsivities $R_{AIM}(n_{an})$ for both modes below

the short range Surface Plasmon, shown before, this sensor quantity does not vary significantly with n_{an} .

SP-sensor properties of the LRSPP mode in the AIM are depicted in Fig. 6.9. In this mode, the highest achievable sensor responsivity $R_{AIM}(\theta)$ is not much different from the short range SPP, depicted in Fig. 6.5, except the wavelength shift to 670 nm.

6.1.2 Localized Plasmons in Colloidal Al-Particles (LSPR-Mode)

The optical absorption characteristic of colloidal Al-particles with 45 nm diameter, immersed into an aqueous solution with varying refractive index n_{an} as function of wavelength, is depicted in Fig. 6.10. Upper right insets reveal spectral reso-

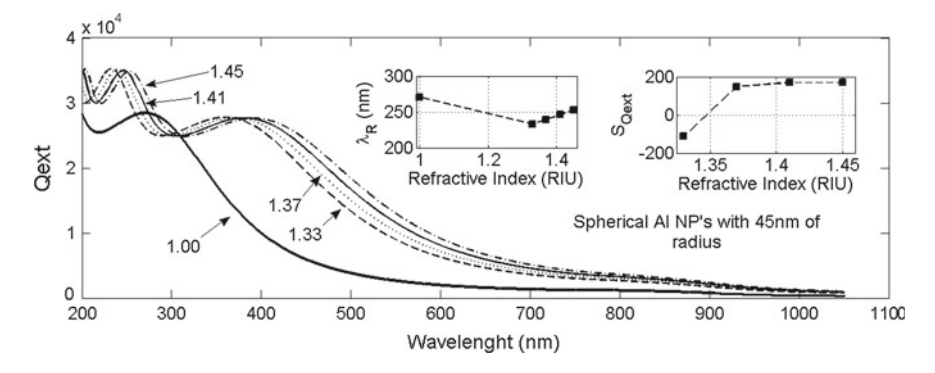


Fig. 6.10 Oscillating optical absorption for Al-particles of 45 nm diameter, calculated as function of wavelength for different refractive index (RIU) values of the surrounding solution. *Insets* show resonance position $\lambda_R(n_{an})$ and optical responsivity $S_{Q_{ext}}(n_{an})$, taken at the first spectral maximum

nance position $\lambda_{res}(n_{an})$, which is in agreement with the Ref. [4], and responsivity $S_{Qext}(n_{an}) = \Delta \lambda_R/\Delta n_{an}$. This quantity is considerably smaller than calculated before for both, short and long range SPP's.

A compilation of achievable SPR sensor performance is displayed in Table 6.1.

6.2 Thin Lithium (Li) Films

The complex optical constant $\varepsilon_{mr}(\lambda) = \varepsilon'_{mr}(\lambda) + j\varepsilon''_{mr}(\lambda)$ of the weakly paramagnetic metal has been taken from Ref. [5], as illustrated in the right inset of Fig. 6.11. The atomic ground state electron configuration is $[He]2s^1$. In the solidified material, the outer single 2s electron contributes to a partially occupied, nearly parabolic conduction band, according to Ref. [6]. The low electrical dc-conductivity of $10.77 \times$ $10^6 (\Omega \,\mathrm{m})^{-1}$ and CDK is in accord with the free electron or Drude model, which also applies to other Alkali metals like Na, K and Cs. $\varepsilon_{mr}^{"}$ is positive and relatively small at wavelengths <1,000 nm and increases slowly towards longer wavelength. The surface plasmon and photon dispersions are shown in Fig. 6.11; Lithium films can be made by magnetron sputtering from a massive target in inert Ar-atmosphere, by electron beam or thermal evaporation from an electrically heated Tungsten foil or carbon boat in high vacuum. The boiling temperature of Lithium is 1,330 °C. The metal is highly reactive and exhibits a strong exothermic oxidation reaction. Upon contact with air or water, the complete metal film ultimately transforms into an oxide or hydroxide. It does not form a stable, thin native oxide layer on the metal surface. Hence, a non-oxidizing cyclo-hexane solution has been selected in this case as the liquid analyte.

Towards high k-values, the energy of the surface Plasmon $E_{SPP}(k)$ at the Li-cyclo-hexane interface remains at approximately 3.5 eV. For the Sapphire substrate, the photon and SP-dispersion curves display a single cross-over point near 2 eV. The spectral features of the reflectance $R(\lambda)$ in the WIM are shown in Fig. 6.12 for the substrate materials under consideration. Apparently, few substrates are suited for SP-sensing applications. A clearly defined resonance exists only for TOPAS, PC and the Sapphire substrate, but is virtually absent for all other materials. The spectral resonance positions are favorable for Sapphire. This is most pronounced in the data set of Fig. 6.13 for AIM conditions, where SP-resonances are placed around 60° for a selected set of wavelengths.

For the Sapphire substrate, the SP-energy (eV) of thin Li-films varies non-linearly with the resonance angle within the range $50^{\circ} < \theta < 65^{\circ}$ approximately as: $E_{SP}(\theta) = 0.0097\theta^2 + 1.1992\theta - 35.048$.

Figure 6.14 illustrates the spectral characteristic of the resonance under WIM conditions for a set of RIU values of the dielectric analyte. Comprising a Sapphire substrate, the displacement of the resonance wavelength as function of the refractive index of the liquid dielectric within the range $1.33 < n_{an} < 1.39$ for WIM conditions

Table 6.1 SP-sens	or performance and figu	res of merit for thin Al-f	ilms and small particle at	netal-aqueous	Table 6.1 SP-sensor performance and figures of merit for thin Al-films and small particle at metal-aqueous solution interface for five different operation modes	ifferent operation modes
Operation mode	Suited/best substrate	Optical responsivity	Linear dynamic range	SPR width	Suited/best substrate Optical responsivity Linear dynamic range SPR width Optimum film thickness Remarks	Remarks
AIM	BK7/CaF ₂ /Quartz	90–140°/RIU	$>6 \times 10^{-2} \text{ RIU}$	$4 \pm 0.2^{\circ}$	20 nm	Resonance split effect
WIM	BK7/CaF ₂ /Quartz	400–6,000 nm/RIU None	None	200 nm	20 nm	Resonance split effect
AIMLRSPP	BK7/TFb	80°/RIU	$6 \times 10^{-2} \mathrm{RIU}$	$8\pm0.2^{\circ}$	20 nm	Split resonance
WIMLRSPP	BK7/TFb	13,000 nm/RIU	$3 \times 10^{-2} \mathrm{RIU}$	200 nm	20 nm	Split resonance
LSPR	Nano-particles	150 nm/RIU	$10 \times 10^{-2} \text{ RIU}$		10–50 nm diameter	Colloidal particles

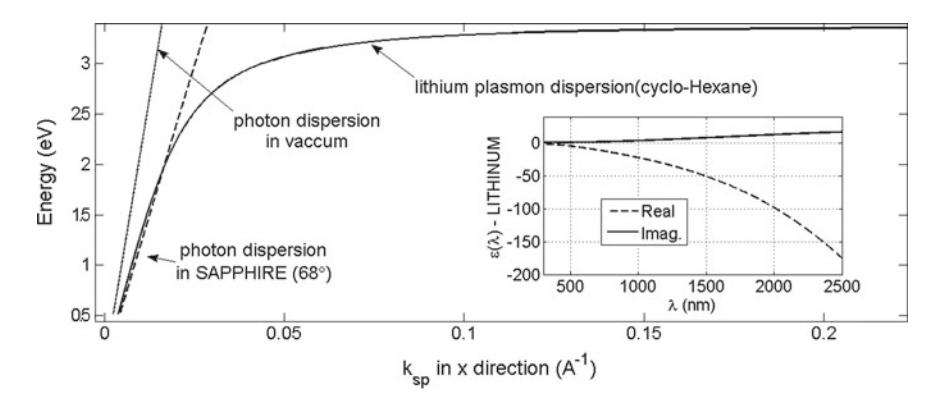


Fig. 6.11 Photon and SPP-dispersion curves of the symmetric mode at the Li-cyclo-hexane interface (*solid-line*), calculated for a Sapphire substrate (*dashed line*). *Right inset* reveals the real and imaginary fractions of the CDK of Lithium. The intersection point is near 2 eV

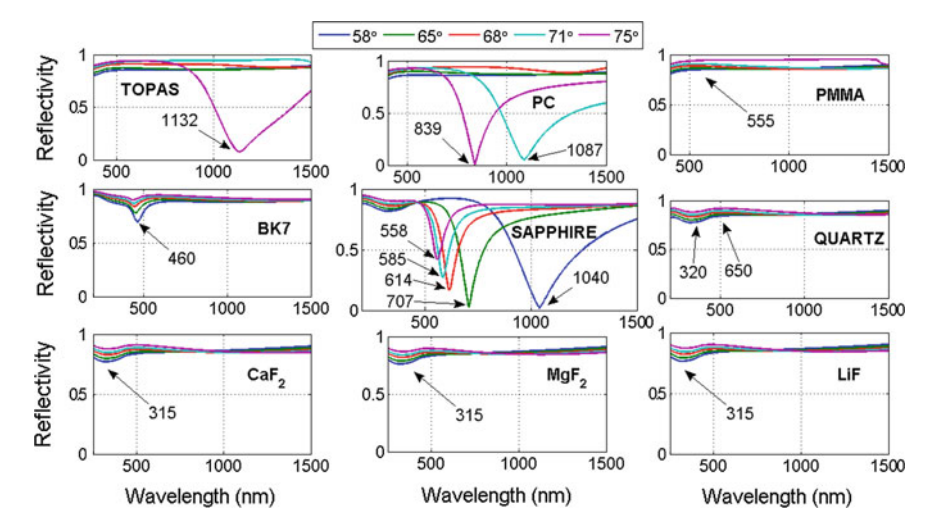


Fig. 6.12 Reflectance curves under WIM-conditions for different substrate materials, as indicated in the plots, and incident angles of 58° , 68° , 68° , 71° and 75° for the wavelength range $300 \text{ nm} < \lambda < 1,400 \text{ nm}$. The Li-film thickness is 50 nm, and is in contact with cyclo-hexane as the liquid dielectric

is shown in the upper left inset of the figure. The depth/contrast of the resonance remains approximately constant towards increasing n_{an} of the liquid dielectric. The width of the resonance (FWHM) is illustrated in the lower left inset and increases slightly non-linear towards higher RIU values of the analyte. The WIM-responsivity R_{WIM} is displayed in the right inset, comprising a magnitude of 2,000 \pm 500 nm/RIU, and increases roughly linear with n_{an} .

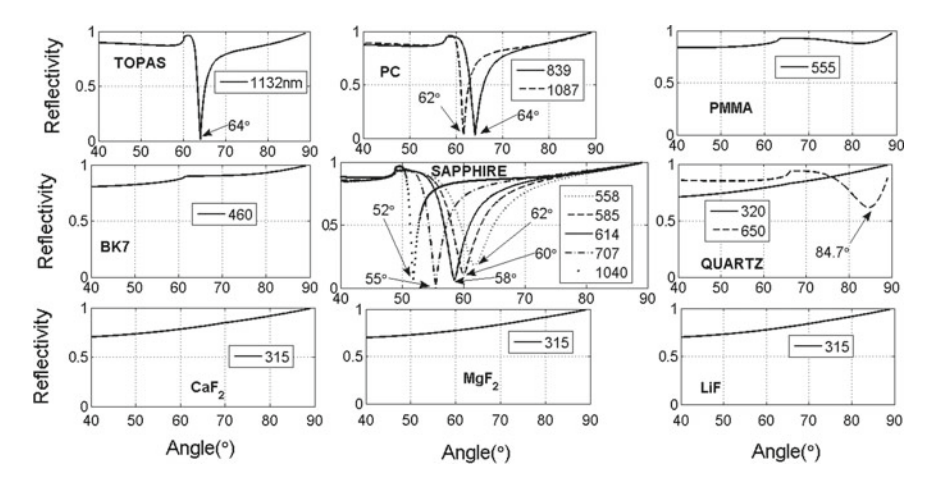


Fig. 6.13 Reflectance curves under AIM-conditions for different substrate materials, as indicated in the plots, and different incident wavelengths for the angle range $50^{\circ} < \theta < 80^{\circ}$. Li-film thickness is 50 nm, in contact with cyclo-hexane

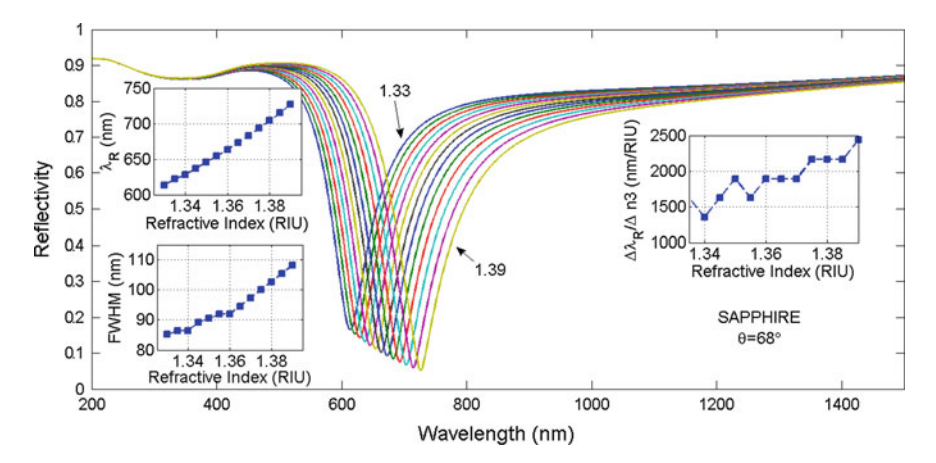


Fig. 6.14 WIM-sensing properties, spectral reflectance $R(\lambda)$ for different RIU-values of the organic analyte 1.33 < n_{an} < 1.39. Substrate is Sapphire, incident angle is 60°. *Left insets* show resonance displacements $\lambda_{res}(n_{an})$ and *line* broadening $\Delta\lambda(n_{an})$ and responsivity $R_{WIM}(n_{an})$ at *right*

Eventually, the influence of film thickness for the WIM and AIM is outlined in Figs. 6.15 and 6.16. This data set clearly indicates that the Li-film thickness for optimum SPR sensor operation is placed at 50 nm. Not shown here are the SP-properties of thin metallic Na-films and K-films. Both metals exhibit an electronic structure that well compares to Lithium, and thus almost identical SPP features.

A compilation of achievable SPR sensor performance is displayed in Table 6.2.

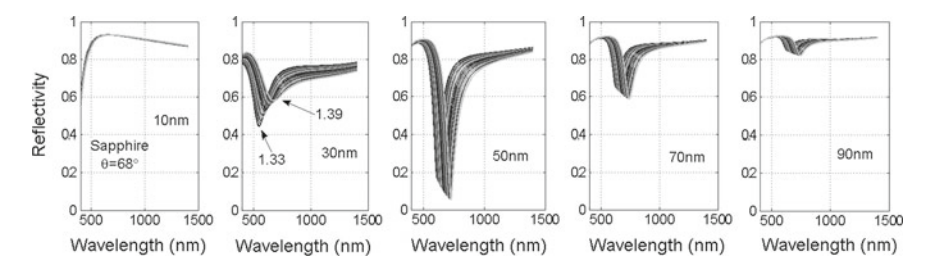


Fig. 6.15 WIM-reflectance at the SP-resonance for different Li-films thickness values of 10, 30, 50, 70 and 90 nm

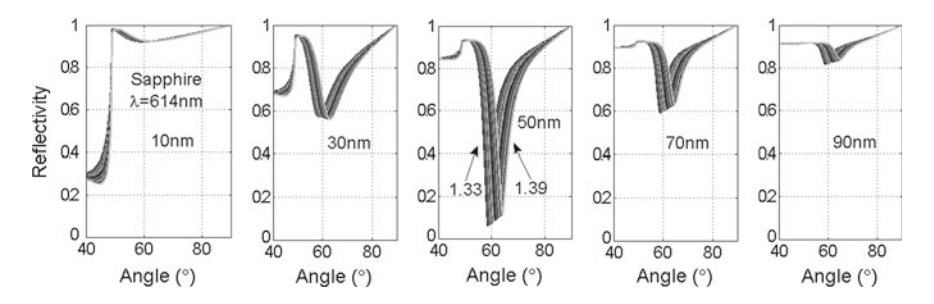


Fig. 6.16 AIM-reflectance at the SP-resonance for different Li-films thickness values of 10, 30, 50, 70 and 90 nm

Operation mode	Suited/best substrate	Optical responsivity	Linear dynamic range	SPR width	Optimum film thickness	Remarks
AIM	Sapphire	60–130°/RIU	$ > 5 \times 10^{-2} $ RIU	8°	20 nm	Very few substrate materials available
WIM	Sapphire	1,500–2,600 nm/RIU	None	85 nm	20 nm	

Table 6.2 SP-sensor performance and figures of merit for thin Li-films metal-cyclohexane interface

6.3 Thin Magnesium (Mg) Films

The complex optical constant $\varepsilon_{mr}(\lambda) = \varepsilon'_{mr}(\lambda) + j\varepsilon''_{mr}(\lambda)$ of the paramagnetic metal has been taken from Refs. [7, 8] and is illustrated in the inset to Fig. 6.17. The atomic electron configuration is $[Ne]3s^2$. In the solid material, the two outer 3s electrons form a partially filled, parabolic conduction band, according to Ref. [9]. The metal exhibits a high electrical dc-conductivity of $22.77 \times 10^6 (\Omega \, \text{m})^{-1}$ at ambient T. Since $\varepsilon''_{mr}(\lambda)$ increases quickly to very high positive values up to a wavelength of 700 nm due to a strong inter-band transition, the metal is inappropriately described

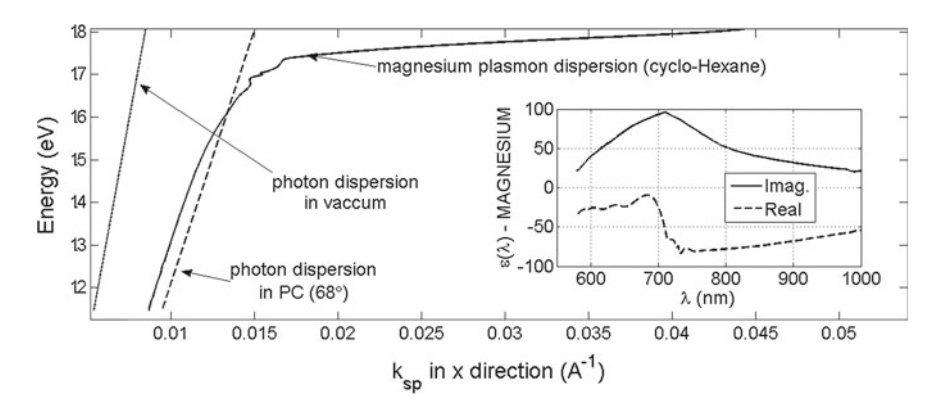


Fig. 6.17 Photon and SPP-dispersion curves of Magnesium at the metal-cyclohexane interface (*solid-line*), calculated for a poly-carbonate (PC) substrate (*dashed-line*). Right inset reveals the real and imaginary fractions of the CDK of Magnesium. The intersection point is near 1.6 eV

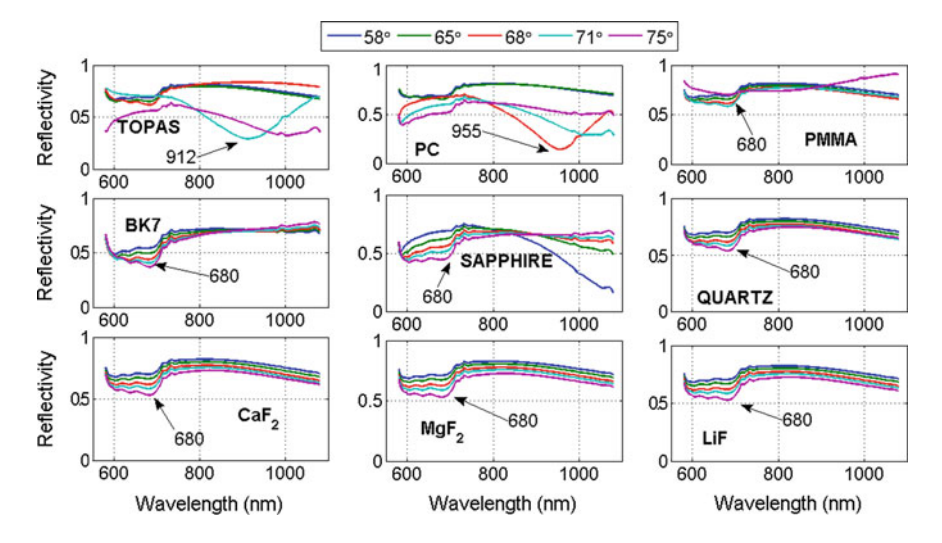


Fig. 6.18 Reflectance curves under WIM-conditions for different substrate materials, as indicated in the plots, and incident angles of 58°, 65°, 68°, 71° and 75° for the wavelength range 600 nm $< \lambda < 1{,}100$ nm. The Mg-film thickness is 20 nm, in contact with cyclo-hexane as the liquid dielectric

by the Drude model. Likewise, $\varepsilon'_{mr}(\lambda)$ quickly falls off to very large negative values within the same spectral range. The surface Plasmon dispersion of Fig. 6.17 exhibits distinct modulations near the sharp cross-over point at 1.6 eV. At high k-values the SP-energy approaches 1.8 eV at the metal-liquid interface. Thin polycrystalline or amorphous Magnesium films can be readily made by magnetron sputtering from a massive target in inert Ar-atmosphere, by electron beam or by evaporation from an electrically heated Tungsten foil or carbon boat in high vacuum. The Mg-boiling temperature is only 1,110 °C. Although the metal is less reactive than Lithium, films immediately transform exothermic into a hydroxidic layer upon contact with water.

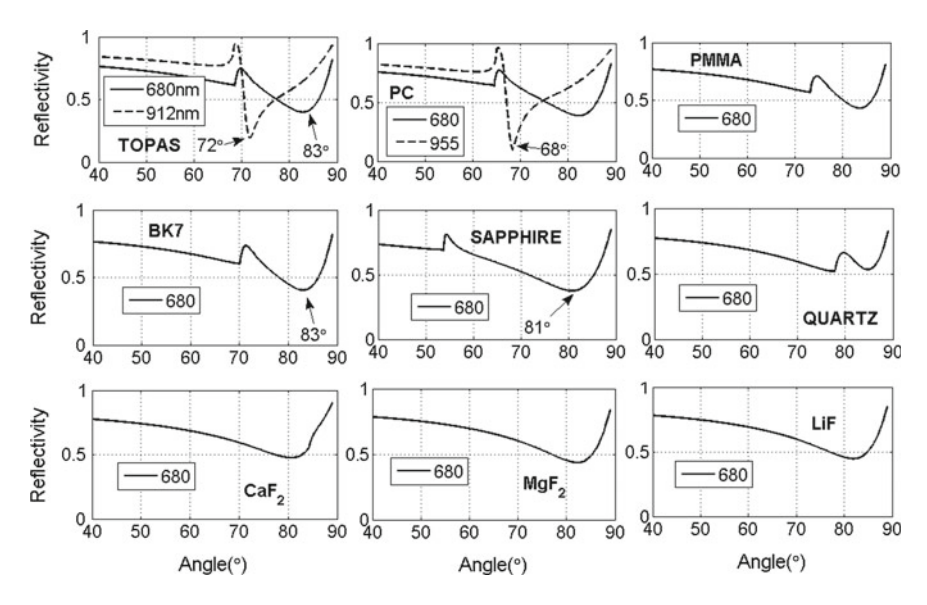


Fig. 6.19 Reflectance curves under AIM-conditions for different substrate materials, as indicated in the plots, and different incident wavelengths for the angle range $40^{\circ} < \theta < 90^{\circ}$. Mg-film thickness is 20 nm, in contact with cyclo-hexane

Oxide layers on the metal surface are porous. Hence, a non-oxidizing cyclo-hexane solution also has been chosen as the liquid analyte.

For the PC-substrate for an incident angle of 68° , photon and SP-dispersion curves exhibit a sharp cross-over and resonance near 1.6 eV. Related spectral features of the reflectance $R(\lambda)$ in the WIM are shown in Fig. 6.18 for the substrate materials under consideration. Again, few substrates are suited for SP-sensing applications. For TOPAS and PC, the resonance locates at rather long wavelength and high angle, and is virtually absent for other substrate materials. The reflectance under AIM conditions is shown in Fig. 6.19, indicating that solely PC and TOPAS are suited substrate materials.

A compilation of achievable SPR sensor performance is displayed in Table 6.3.

face						
Operation mode	Suited/best substrate	Optical responsivity	Linear dynamic range	SPR width	Optimum film thickness	Remarks
AIM	TOPAS/PC	90°/RIU	>5×10 ⁻² RIU	8°	20 nm	Single resonance
WIM	TOPAS/PC	-3,000±1,000 nm/RIU	None	200 nm	20 nm	Single resonance

 Table 6.3
 SP-sensor performance and figures of merit for thin Mg-films metal-cyclohexane interface

References

- 1. Palik, E.D.: Handbook of Optical Constants of Solids. Academic Press, Boston (1985)
- 2. Levinson, H.J., Greuter, F., Plummer, E.W.: Experimental band-structure of aluminum. Phys. Rev. B 27, 727–747 (1983)
- 3. Haynes, W.M.: Handbook of Chemistry and Physics; 1.Edition, CRC Press (1987)
- 4. Knight, M.W., King, N.S., Liu, L., Everitt, H.O., Nordlander, P., Halas, N.J.: Aluminium for Plasmonics. ACS Nano 8, 834–840 (2014)
- 5. Sopra, SA.: Optical Data. http://www.sspectra.com/sopra.html
- Doll, K., Harrison, N.M., Saunders, V.R.: A density functional study of lithium bulk and surfaces. J. Phys.: Condens. Matter 11, 5007–5019 (1999)
- Machorro, R., Siqueiros, J.M., Wang, S.: Optical properties of Mg, from UV to IR, using ellipsometry and reflectometry. Thin Solid Films 15, 1–5 (1995)
- 8. Jones, D., Lettington, A.H.: The optical properties and electronic structure of magnesium. Proc. Phys. Soc. **92**, 948–955 (1967)
- 9. Canney, S.A., Sashin, V.A., Ford, M.J., Kheifets, A.S.: Electronic band structure of magnesium and magnesium oxide: experiment and theory. J. Phys.: Condens. Matter 11, 7507–7522 (1999)

Chapter 7 Classical Noble Metals

7.1 Thin Copper (Cu) Films and Colloidal Particles

The complex optical constant $\varepsilon_{mr}(\lambda) = \varepsilon_{mr}'(\lambda) + j\varepsilon_{mr}''(\lambda)$ of the diamagnetic metal has been taken from Ref. [1], and is illustrated in the right inset of Fig. 7.1. The atomic electron configuration is $[Ar]3d^{10}4s^1$. In the solidified material the outer 4s state accounts for the partially occupied conduction band. The band-structure of Copper is reported in Ref. [2]. The high electrical dc-conductivity of 59.6 × $10^6 \, (\Omega \, \text{m})^{-1}$ and CDK can be described with a modified Drude model, but does not resemble the CDK. $\varepsilon'_{mr}(\lambda)$ decreases steadily to negative values at $\lambda > 550$ nm, whilst $\varepsilon''_{mr}(\lambda)$ is positive and remains relatively small within the spectral range of interest. Both, $\varepsilon'_{mr}(\lambda)$ and $\varepsilon''_{mr}(\lambda)$ reveal a distinct swing near 600 nm that originates from an inter-band transition. The SP-dispersion appears heavily distorted above the cross-over point around 1.9 eV. At high k, the energy E_{SP} of the surface Plasmon approaches 3.5 eV at the metal-water interface. Copper films are easily deposited by magnetron sputtering from a massive metal-target in inert atmosphere, or by evaporation from electrically heated Tungsten foils or carbon boats in high vaccum. The boiling temperature of Cu is 2,562 °C. Since Cu belongs to the group of noble metals, formation of thin native oxide films on the metal surface upon contact with air or plain water is rather slow Ref. [3]. Experimental studies suggests the presence of a duplex type structure of the Cu-oxide (passive) layer with an outer CuO part of ca. 1.3 nm thickness and an inner Cu₂O layer of about 2.0 nm. The SP-resonance is only weakly affected through its presence.

For the BK7-substrate at an incident angle of 71°, photon and SP-dispersion curves exhibit a sharp cross-over near 1.9 eV. Related spectral features of the reflectance $R(\lambda)$ in the WIM are shown in Fig. 7.2 for the substrate materials under consideration. Except Sapphire and MgF₂, all other substrates exhibit a distinct SP-resonance and are suited for SP-sensing applications. For LiF, the resonance is located at rather long wavelength and high angle.

The reflectance under AIM conditions is shown in Fig. 7.3, indicating that particularly the MgF₂ substrate is unsuited for SP sensing applications. For the remaining

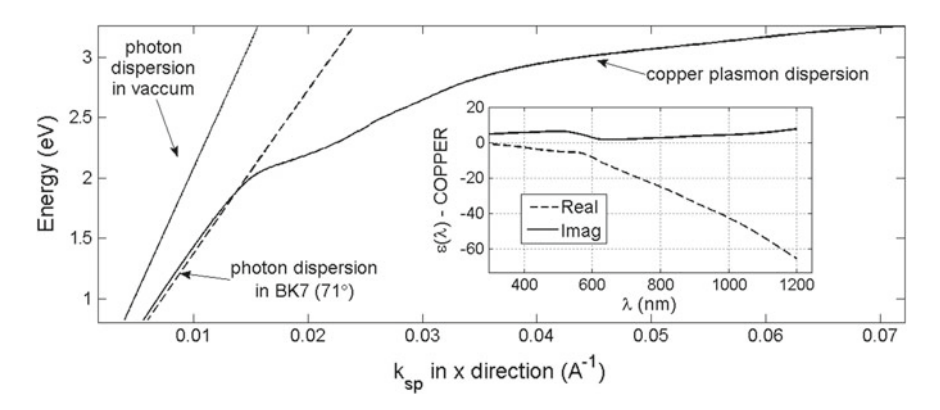


Fig. 7.1 Photon and SPP-dispersion curves for the symmetric mode at the Cu metal-water interface (*solid-line*), calculated for a BK7 substrate (*dashed-line*). The intersection point is near 1.9 eV. *Right inset* reveals the real and imaginary fractions of the CDK

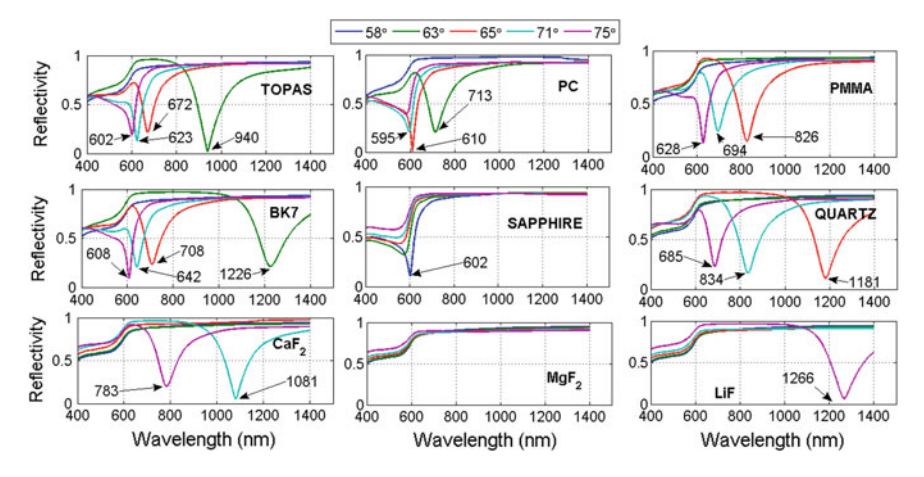


Fig. 7.2 Reflectance curves under WIM-conditions for different substrate materials, as indicated in the plots, and incident angles of 58° , 65° , 68° , 71° and 75° for the wavelength range $400\,\mathrm{nm} < \lambda < 1,400\,\mathrm{nm}$. The Cu-film thickness is $50\,\mathrm{nm}$, in contact with water as the liquid dielectric

SP-active substrates, the SP-line broadening parameters $\Delta \lambda_{res}$ and $\Delta \theta_{res}$ decreases substantially towards lower angle and longer wavelength respectively. BK7 and TOPAS exhibit the lowest SP-broadening parameter $\Delta \theta_{res}$ at convenient angle, but wavelength >1,200 nm.

For the BK7 substrate, the SP-energy (eV) of thin Cu-films varies non-linearly with the resonance angle within the range $60^{\circ} < \theta < 75^{\circ}$, approximately as: $E_{SP}(\theta) = 0.0082\theta^2 + 1.22\theta - 43.191$.

Figure 7.4 illustrates the spectral characteristic of the resonance under WIM conditions for a set of RIU values of the aqueous dielectric analyte. The depths/contrast of the resonance increases slightly towards higher n_{an} -values, whilst the resonance

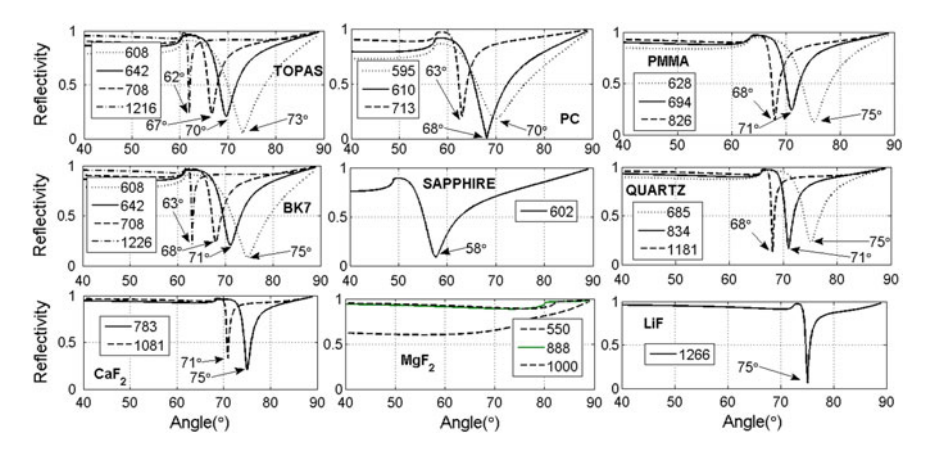


Fig. 7.3 Reflectance curves under AIM-conditions for different substrate materials, as indicated in the plots, and different incident wavelengths for the angle range $40^{\circ} < \theta < 90^{\circ}$. Cu-film thickness is 50 nm, in contact with water

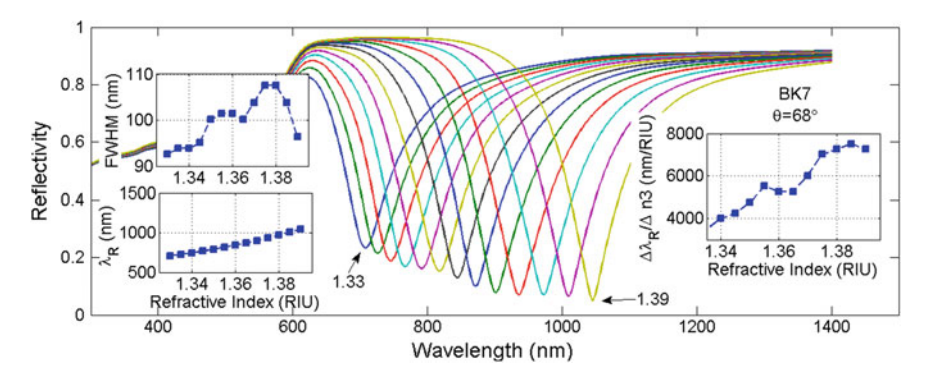


Fig. 7.4 WIM-sensing properties and spectral reflectance $R(\lambda)$ of Copper, calculated for a set of different RIU-values of the aqueous analyte 1.33 < n_{an} < 1.39. Substrate is BK7, incident angle is 68°. *Insets* show line broadening (*lower left*) $\Delta\lambda_{res}(n_{an})$, resonance displacements $\lambda_{res}(n_{an})$ and responsivity $R_{WIM}(n_{an})$ at *lower right*

minimum shifts towards longer wavelengths. For the BK7 substrate, the displacement of the resonance wavelength $\lambda_{res}(n_{an})$ as function of the refractive index (RIU) of the liquid dielectric within the range $1.33 < n_{an} < 1.39$ for WIM conditions is shown in the right upper inset. The broadening parameter of the resonance $\Delta\lambda_{res}(n_{an})$, taken at FWHM, is illustrated in the left inset at 85 ± 15 nm and slightly increases with n_{an} . The WIM-responsivity R_{WIM} is fairly high, as displayed in the right lower inset and comprises a magnitude of $4,500 \pm 2,000$ nm/RIU. Its values increase with n_{an} , as does the resonance position $\lambda_{res}(n_{an})$.

The SPR-sensing characteristic in the AIM is shown in Fig. 7.5, comprising initial resonance angle 68° and wavelength of 708 nm. The AIM-responsivity R_{AIM}

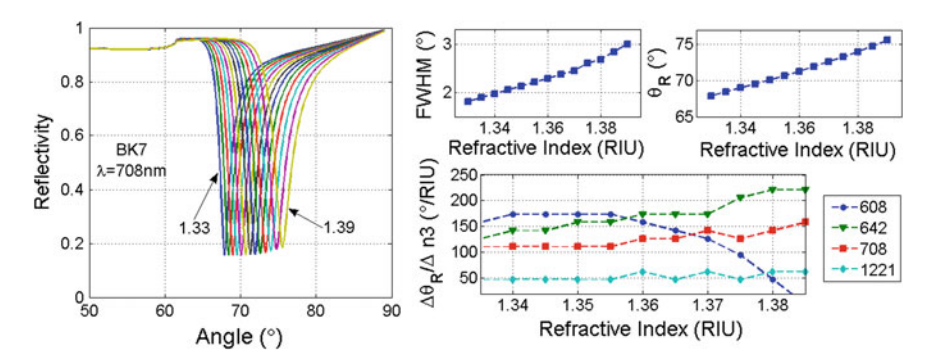


Fig. 7.5 AIM-sensing properties and angular reflectance $R(\lambda)$ in *left* and *right figures* for different RIU-values of the aqueous analyte 1.33 < n_{an} < 1.39. Substrate is BK7, incident wavelengths are 708 nm, *insets* show line broadening $\Delta\theta_{res}(n_{an})$. Resonance displacements $\theta_{res}(n_{an})$ and SP-responsivity $R_{AIM}(n_{an})$ for four wavelength, depicted in *three left figures*

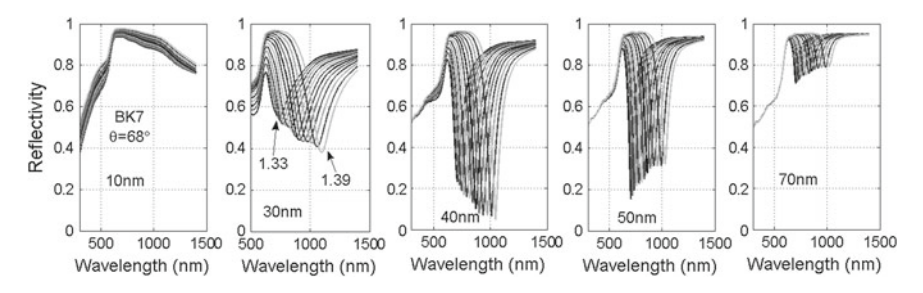


Fig. 7.6 WIM-reflectance at the SP-resonance for different Cu-film thickness values of 10, 30, 40, 70 and 90 nm

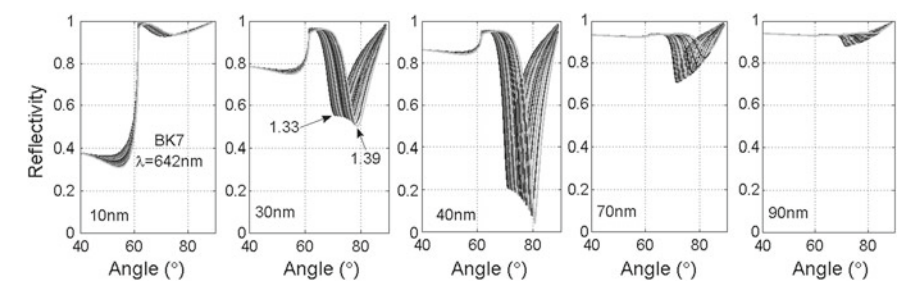


Fig. 7.7 AIM-reflectance at the SP-resonance for different Cu-film thickness values of 10, 30, 40, 70 and 90 nm

is high up to $150^{\circ}/RIU$, and increases with decreasing wavelength, whilst the line broadening parameter $\Delta\theta_{res}(n_{an})$ behaves opposite.

Eventually, the influence of film thickness for WIM and AIM conditions is outlined in Figs. 7.6 and 7.7. This data set clearly indicates that the Cu-film thickness for optimum SPR sensor operation is placed at around 40 nm.

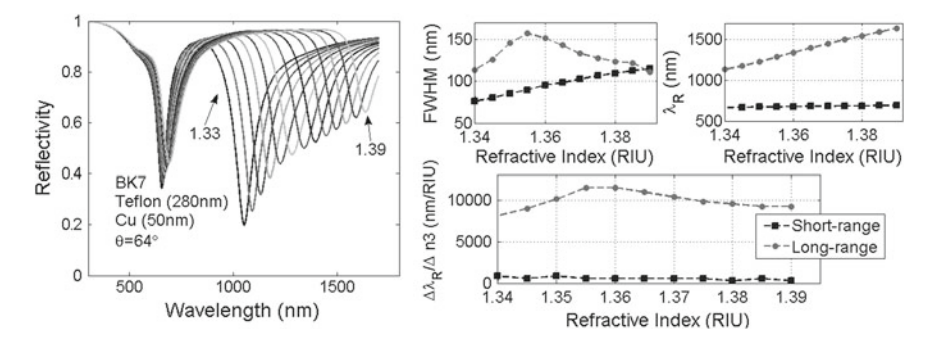


Fig. 7.8 WIM-sensor properties in presence of the LRSPP mode: spectral reflectance $R(\lambda)$ (left figure) for different RIU-values of the aqueous analyte 1.33 < n_{an} < 1.39, indicating two co-existing SP-dips. Substrate is BK7, with a 280 nm Teflon® film on top, incident angle is 64°. Three figures at right show line broadening $\Delta \lambda_{res}(n_{an})$ and resonance displacements $\lambda_{res}(n_{an})$ at top and responsivities $R_{WIM}(n_{an})$ below for short (lines with squares) and long range SPP's (lines with circles)

7.1.1 Long Range Surface Plasmon Polariton (LRSPP-mode)

SP-sensor properties in the LRSPP mode in the WIM are depicted in Fig. 7.8. The spectral characteristics (left figure) reveals two co-existing SP-dips with the symmetric (short range) mode at around 650 nm (lines with squares in right figures) and the anti-symmetric, long range (LRSPP) mode at 1,040 nm (line with circles). Comparison with Fig. 7.4 illustrates an increase by more than a factor 2 for the responsivity $R_{WIM}(n_{an})$ in the LRSPP-mode in the lower right figure, up to values of 11,000 nm/RIU that remains fairly constant.

SP-sensor properties in presence of the LRSPP mode in the AIM are depicted in Fig. 7.9. In the AIM mode, the sensor responsivity $R_{AIM}(\lambda)$ for the LRSPP is not much different from the short range SPP, depicted in Fig. 7.5, except for a wavelength shift to 670 nm.

7.1.2 Localized Plasmons in Colloidal Cu-Particles (LSPR-mode)

The optical absorption characteristic of colloidal Cu-particles with 45 nm diameter, immersed into an aqueous solution with varying refractive index n_{an} as function of wavelength, is depicted in Fig. 7.10. Upper right insets reveal spectral resonance position $\lambda_{res}(n_{an})$ at top and responsivity $S_{Q_{ext}}(n_{an})$ at bottom. This quantity is considerably smaller than calculated before for both, short and long range SPP's.

A compilation of achievable SPR sensor performance is displayed in Table 7.1.

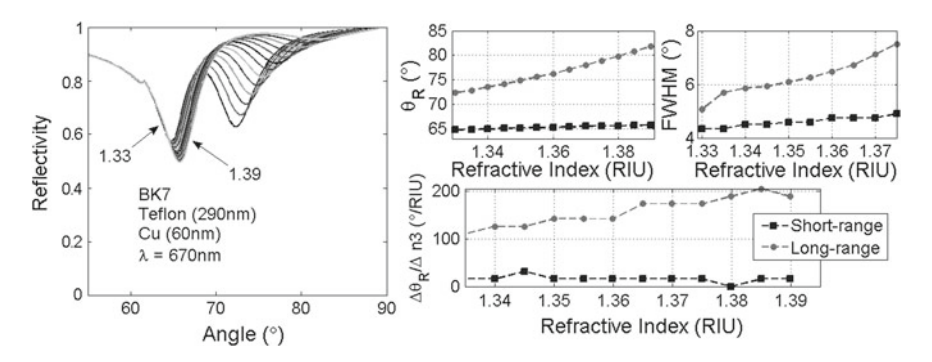


Fig. 7.9 AIM-sensor properties in presence of the anti-symmetric LRSPP-mode: angular reflectance $R(\lambda)$ at *left figure* for different RIU-values of the aqueous analyte 1.33 < n_{an} < 1.39, indicating two SP-dips. Substrate is BK7 with a 280 nm Teflon film on *top* and the metal film placed thereon. Incident wavelength is 670 nm. *Three figures* at right show line broadening $\Delta \lambda_{res}(n_{an})$ and angular resonance displacements $\lambda_{res}(n_{an})$ at *top*, and associated responsivities $R_{AIM}(n_{an})$ below for short (*line with squares*) and long range modes (*line with circles*)

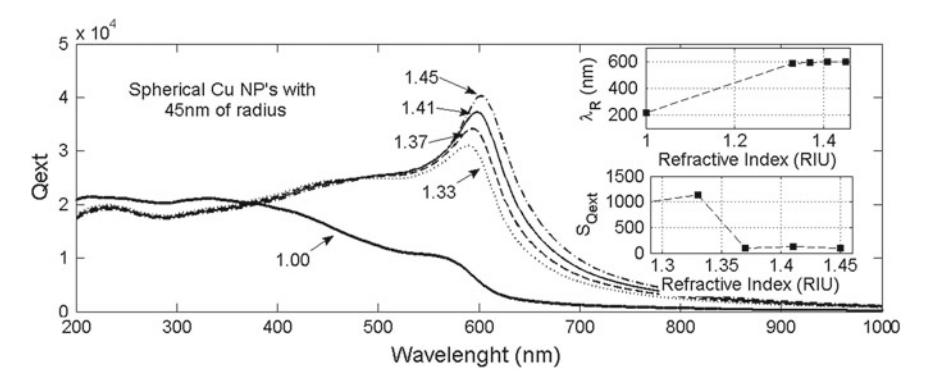


Fig. 7.10 Optical absorption for Cu-particles of 45 nm diameter, calculated as function of wavelength for different refractive index (RIU) values of the surrounding aqueous solution. Right two insets show resonance position $\lambda_R(n_{an})$ and optical responsivity $S_{Q_{ext}}(n_{an})$, taken at the spectral maximum near 600 nm

7.2 Thin Gold (Au) Films and Colloidal Particles

The complex optical constant $\varepsilon_{mr}(\lambda) = \varepsilon'_{mr}(\lambda) + j\varepsilon''_{mr}(\lambda)$ of the weakly paramagnetic metal has been taken from Ref. [1], and is illustrated in the right inset of Fig. 7.11. The electron configuration of the isolated atom is $[Xe]4f^145d^106s^1$. In the solidified material, the outer 6s state accounts for a partly filled conduction band that is hybridized with the lower 5d-states. The relativistic electronic band-structure is reported in Ref. [4]. The high electrical dc-conductivity of $45.16 \times 10^6 \, (\Omega \, \text{m})^{-1}$ and CDK are sufficiently described with a modified Drude model. $\varepsilon'_{mr}(\lambda)$ is initially very small and constant, but decreases at $\lambda > 500 \, \text{nm}$ steadily to large negative

Table 7.1 SP-sensc	Table 7.1 SP-sensor performance and figures of merit for thin Cu-films and nano-particle at metal-water interface	for thin Cu-films and nano-	particle at metal-wal	21 11110111400		
Operation mode	Operation mode Suited/best substrate	Optical responsivity	Linear dynamic range	SPR width	Optimum film thickness	Remarks
AIM	TOPAS/PC/PMMA/BK7/Quartz 150°/RIU	150°/RIU	$<4 \times 10^{-2} \mathrm{RIU}$ $>5^{\circ}$	>5°	50 nm	Single resonance
WIM	TOPAS/PC/PMMA/BK7/Quartz $4,500 \pm 2,000 \mathrm{nm/RIU}$ None	$4,500 \pm 2,000 \mathrm{nm/RIU}$	None	8 ± 15 nm	50 nm	Single resonance
AIMLRSPP	BK7/Teflon bi-layer	150°/RIU	None	>5°		Split resonance
WIMLRSPP	BK7/Teflon bi-layer	12,000 nm/RIU	$>4 \times 10^{-2} \text{ RIU}$ 140 ± 20 nm	$140 \pm 20 \text{nm}$		Split resonance
LSPR	Nano-particles	100 nm/RIU	$3 \times 10^{-2} \text{ RIU}$	25 nm	45 nm particles	45 nm particles Colloidal particles

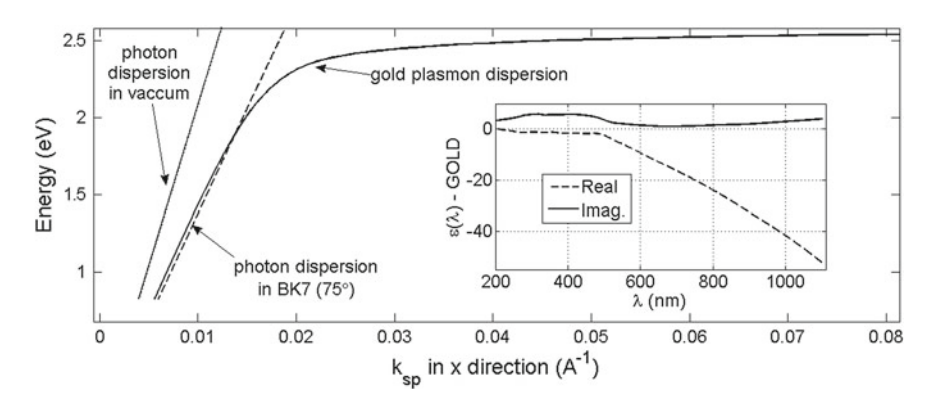


Fig. 7.11 Photon and SPP-dispersion curves of Gold for the symmetric mode at the metal-water interface (*solid-line*), calculated for a BK7 substrate (*dashed-line*) and incident angle of 75°. The related intersection point and resonance appears near 1.9 eV. *Right inset* reveals the real and imaginary fractions of the CDK

values. $\varepsilon_{mr}''(\lambda)$ is positive and remains relatively small within the spectral range of interest. Both, $\varepsilon_{mr}'(\lambda)$ and $\varepsilon_{mr}''(\lambda)$ reveal a distinct swing near 500 nm that originates from an inter-band transition. The SP-dispersion appears undistorted and exhibits a sharp cross-over around 1.9 eV. At high k-values, towards the asymptotic limit, the SP-energy saturates around 2.6 eV at the metal-water interface. Gold films are easily deposited by magnetron sputtering from a massive metal-target in inert atmosphere, by electron beam evaporation, or by thermal evaporation from electrically heated Tungsten foils or carbon boats in high vacuum. The evaporation/boiling temperature of Au with 2,970 °C is high. Native oxides do not form immediately on the metal surface upon contact with air or water at neutral pH. Dense, thin oxide layers can be grown in aqueous electrolytes at anodic potentials. Clean Au-metal surfaces, as well as the other noble metals, exhibit covalent chemical attraction to sulfur and many organic compounds that contain this element.

For the BK7-substrate, photon and SP-dispersion curves exhibit a sharp cross-over near 1.9 eV. Related spectral features of the reflectance $R(\lambda)$ in the WIM are shown in Fig. 7.12 for the substrate materials under consideration. Except Sapphire, and the crystalline fluorides, especially MgF₂ and LiF, all substrates are suited for SP-sensing applications. For LiF, the resonance is located at rather long wavelength and high angle. The reflectance under AIM conditions is shown in Fig. 7.13, indicating that particularly the MgF₂ substrate is unsuited for SP sensing applications. The SP-line broadening parameter $\Delta\theta_{res}$ decreases towards smaller angle and longer wavelength.

For the BK7 substrate, the SP-energy (eV) of thin Au-films varies non-linearly with the resonance angle within the range $60^{\circ} < \theta < 75^{\circ}$, approximately as: $E_{SP}(\theta) = 0.0074\theta^2 + 1.1105\theta - 39.077$.

Figure 7.14 illustrates the spectral characteristic of the resonance under WIM conditions for a set of RIU values of the aqueous dielectric analyte. The depths/contrast of the resonance remains approximately constant towards higher n_{an} -values, whilst

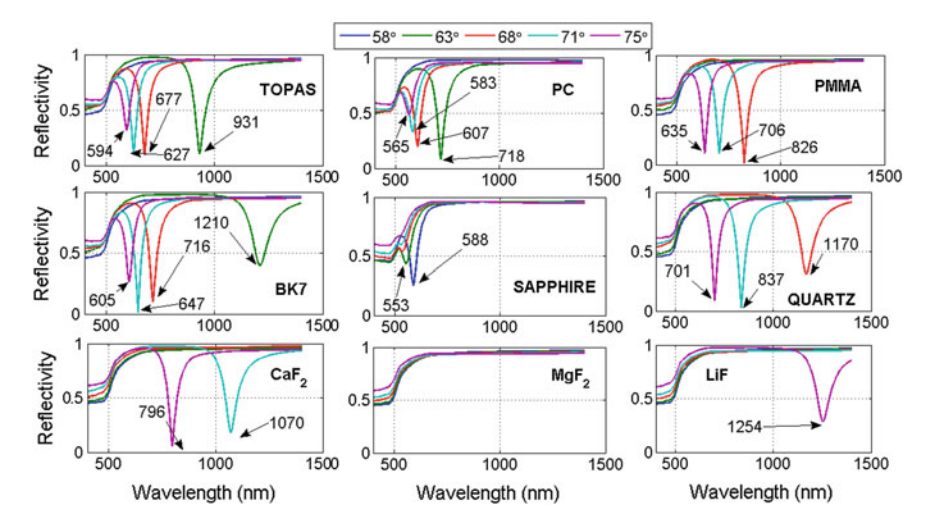


Fig. 7.12 Reflectance curves under WIM-conditions, calculated for different substrate materials, as indicated in the plots. Incident angles are: 58° , 63° , 68° , 71° and 75° for the wavelength range $400 \, \text{nm} < \lambda < 1,400 \, \text{nm}$. The Au-film thickness is $50 \, \text{nm}$, in contact with water as the liquid dielectric

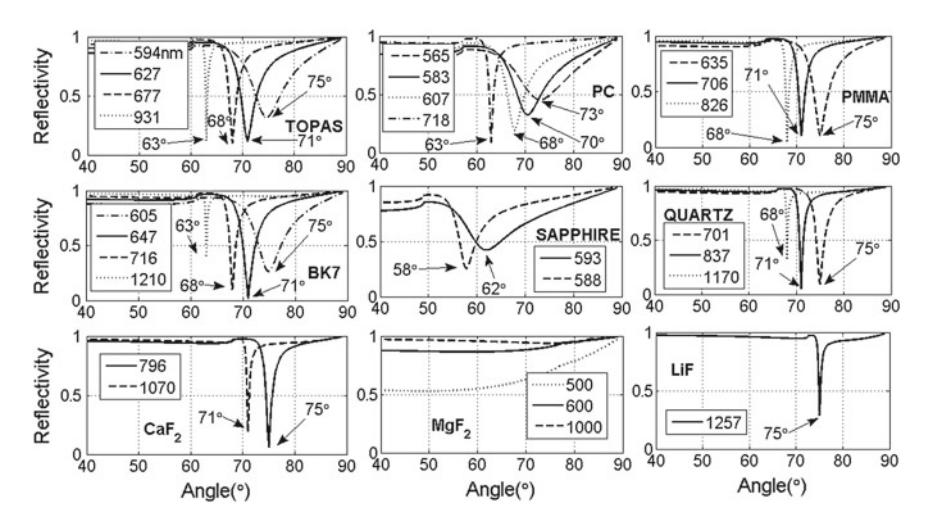


Fig. 7.13 Reflectance curves under AIM-conditions for different substrate materials, as indicated in the plots, and different incident wavelengths for the angle range $40^{\circ} < \theta < 90^{\circ}$. Au-film thickness is 50 nm, in contact with water

the resonance minimum shifts towards longer wavelengths. For the BK7 substrate, the slightly non-linear displacement of the resonance wavelength $\lambda_{res}(n_{an})$ as function of the refractive index of the liquid dielectric within the range $1.33 < n_{an} < 1.39$ is shown in the right upper insets. The broadening parameter of the resonance $\Delta \lambda_{res}(n_{an})$, taken at FWHM, is calculated to 40 ± 5 nm, and increases at large n_{an} . The

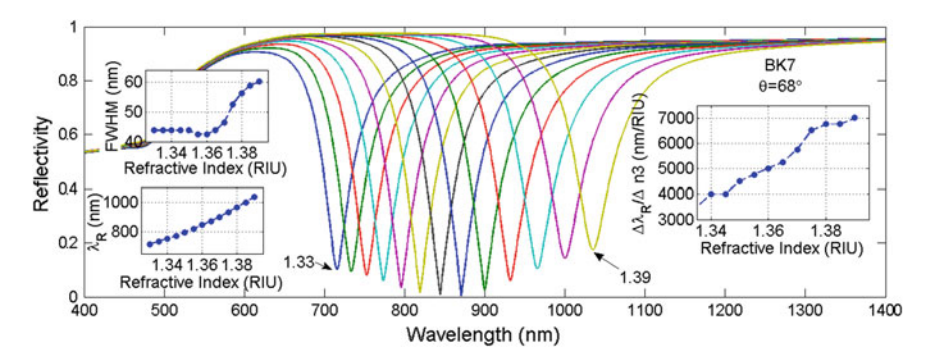


Fig. 7.14 WIM-sensing properties and spectral reflectance $R(\lambda)$ of Gold, calculated for a set of different RIU-values of the aqueous analyte 1.33 $< n_{an} < 1.39$. Substrate is BK7, incident angle is 68°. Right upper insets show line broadening $\Delta \lambda_{res}(n_{an})$, resonance displacements $\lambda_{res}(n_{an})$ and SP-responsivity $R_{WIM}(n_{an})$ at lower inset

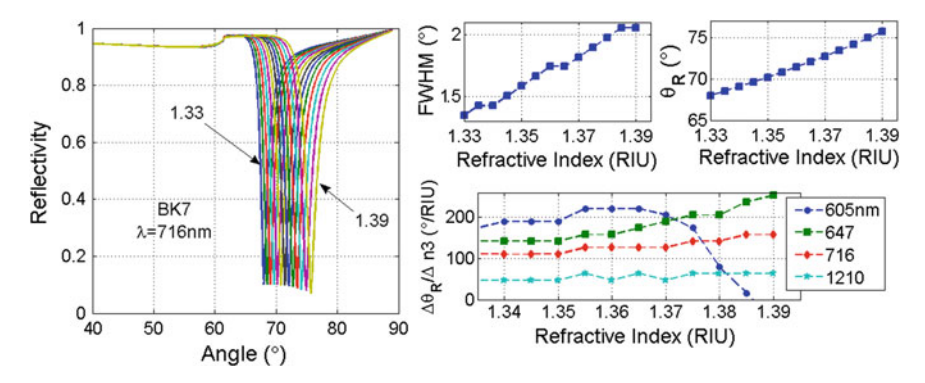


Fig. 7.15 AIM-sensing properties and angular reflectance $R(\theta)$, calculated for different RIU-values of the aqueous analyte 1.33 < n_{an} < 1.39. Substrate is BK7, incident wavelengths are 716 nm with line broadening $\Delta\theta_{res}(n_{an})$. *Central insets* depict resonance displacements $\theta_{res}(n_{an})$ and responsivities $R_{AIM}(n_{an})$ for four different wavelength

WIM-responsivity R_{WIM} is fairly high, displayed in the lower right inset, comprising a magnitude of $4,000 \pm 1,000$ nm/RIU and steady increase with n_{an} .

The SPR-sensing characteristic in the AIM is shown in Fig. 7.15 for wavelengths of 716 nm, comprising initial resonance angle 68°. The AIM-responsivity R_{AIM} is high, and increases with decreasing wavelength, whilst the line broadening parameter $\Delta\theta_{res}(n_{an})$ behaves oppositely.

The influence of film thickness for WIM and AIM conditions is outlined in Figs. 7.16 and 7.17. This data set clearly indicates that the Au-film thickness for optimum SPR sensor operation is placed at around 50 nm.

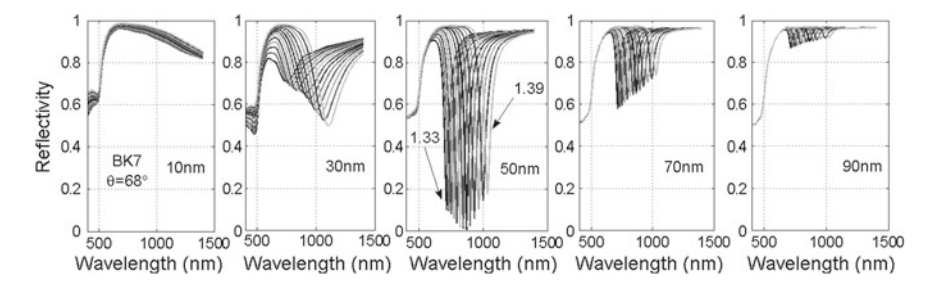


Fig. 7.16 WIM-reflectance at the SP-resonance for different Au-film thickness values of 10, 30, 50, 70 and 90 nm

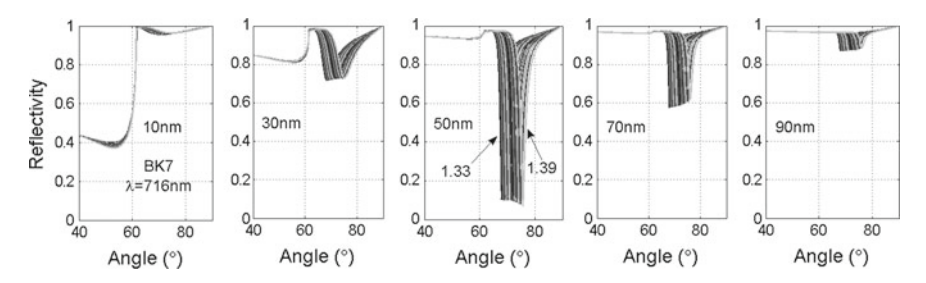


Fig. 7.17 AIM-reflectance at the SP-resonance for different Au-film thickness values of 10, 30, 50, 70 and 90 nm

7.2.1 Long Range Surface Plasmon Polariton (LRSPP-mode)

SP-sensor properties of the LRSPP mode in the WIM are depicted in Fig. 7.18. The spectral characteristics (left figure) reveals two co-existing SP-dips: the symmetric (short range mode) at 600 nm (blue line in right figures) and the addition anti-symmetric, long range (LRSPP) mode at 900 nm (green line). Comparison with Fig. 7.14 illustrates that the responsivity $R_{WIM}(n_{an})$ in the LRSPP-mode is marginally higher (Factor 1.5), and increases slightly with n_{an} .

SP-sensor properties in presence of the LRSPP mode in the AIM are depicted in Fig. 7.19. In the AIM mode, the magnitude of the sensor responsivity $R_{AIM}(\lambda)$ for the LRSPP does not differ significantly from the short range SPP, depicted from Fig. 7.15, except for a slightly shifted wavelength to 670 nm.

7.2.2 Localized Plasmons in Colloidal Au-Particles (LSPR-mode)

The optical absorption characteristic of colloidal Au-particles with 45 nm diameter, immersed into an aqueous solution with varying refractive index n_{an} as function

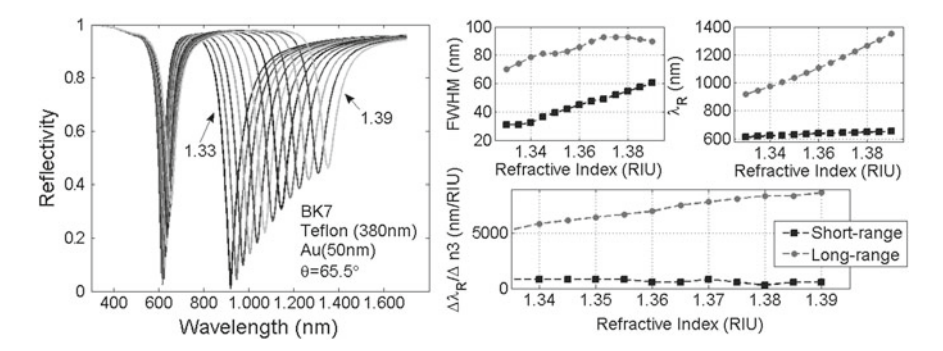


Fig. 7.18 WIM-sensor properties in presence of the LRSPP mode: spectral reflectance $R(\lambda)$ (left figure) for different RIU-values of the aqueous analyte $1.33 < n_{an} < 1.39$, indicating two coexisting SP-dips. Substrate is BK7, with a 380 nm Teflon film on top, incident angle is 65.5°. Three figures at right show line broadening $\Delta \lambda_{res}(n_{an})$ and resonance displacements $\lambda_{res}(n_{an})$ at top and responsivities $R_{WIM}(n_{an})$ bottom for short (lines with squares) and long range SPP's (lines with circles)

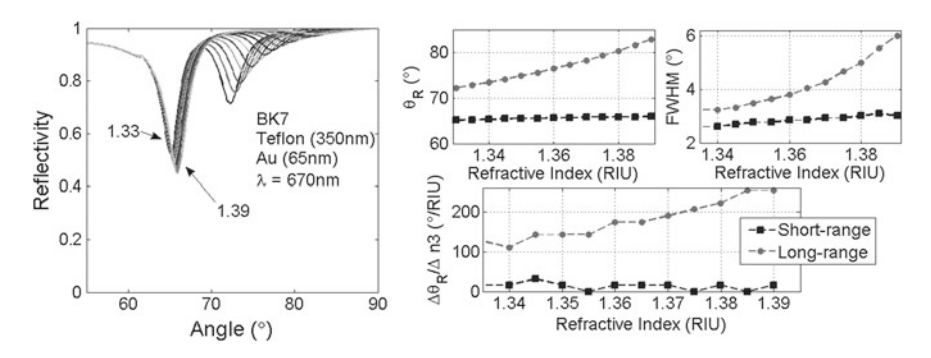


Fig. 7.19 AIM-sensor properties in presence of the anti-symmetric LRSPP-mode: angular reflectance $R(\lambda)$ at *left figure* for different RIU-values of the aqueous analyte 1.33 < n_{an} < 1.39, indicating two SP-dips. Substrate is BK7 with a 380 nm Teflon film on *top* and the metal film placed thereon. Incident wavelength is 670 nm. *Three figures* at *right* show line broadening $\Delta\theta_{res}(n_{an})$ and angular resonance displacements $\theta_{res}(n_{an})$ at *top*, and associated responsivities $R_{AIM}(n_{an})$ at *bottom* for short (*lines with squares*) and long range modes (*lines with circles*)

of wavelength, is depicted in Fig. 7.20. Upper right insets reveal spectral resonance position $\lambda_{res}(n_{an})$ and responsivity $S_{Q_{ext}}(n_{an})$. This quantity is considerably smaller than calculated before for both, short and long range SPP's.

The influence of particle size onto optical absorbance is illustrated in Fig. 7.21, for different diameter, which vary from 10 to 150 nm. The number of maxima increases with larger diameter, indicating a higher number of SP-eigenmodes.

A compilation of achievable SPR sensor performance is displayed in Table 7.2.

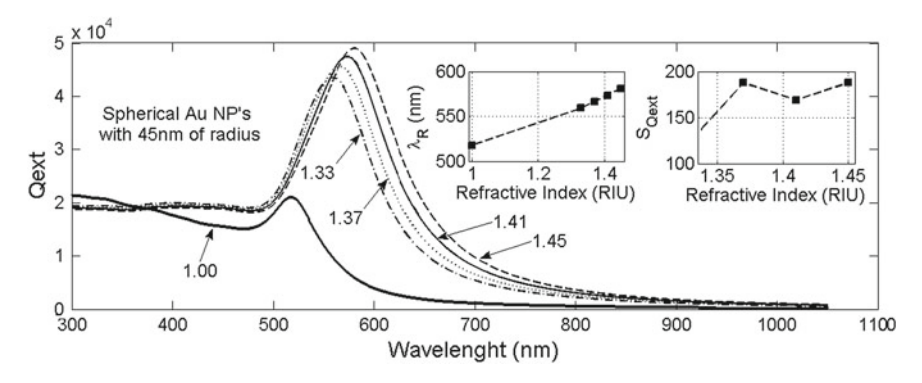


Fig. 7.20 Optical absorbance for Au-particles of 45 nm diameter, calculated as function of wavelength for different refractive index (RIU) values of the surrounding aqueous solution. Right two insets show resonance position $\lambda_R(n_{an})$ and optical responsivity $S_{Q_{ext}}(n_{an})$, taken at the spectral maximum near 500 nm

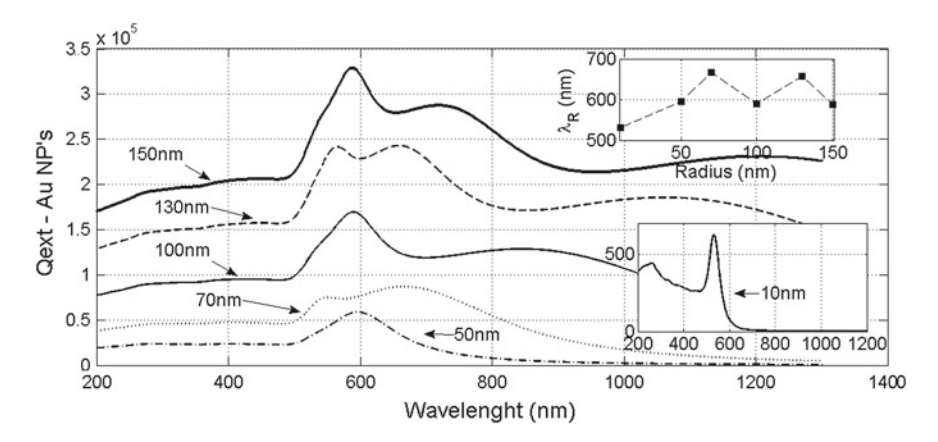


Fig. 7.21 Spectral variation of the optical absorbance of colloidal Au-particles for different particle diameters

7.3 Thin Silver (Ag) Films and Colloidal Particles

The complex optical constant $\varepsilon_{mr}(\lambda) = \varepsilon'_{mr}(\lambda) + j\varepsilon''_{mr}(\lambda)$ of the diamagnetic metal has been taken from Ref. [1] and is illustrated in the right inset of Fig. 7.22. The electron configuration of the isolated atom is $[Kr]4d^{10}5s^1$. In the solidified material, the outer 5s state largely accounts for the partially occupied conduction band, as revealed in the band-structure calculations of Ref. [5]. The high electrical dc-conductivity of $63 \times 10^6 (\Omega \, \text{m})^{-1}$ and CDK of the diamagnetic metal are sufficiently described by a modified Drude model. Within the wavelength range of interest, $\varepsilon'_{mr}(\lambda)$ decreases at $\lambda > 300 \, \text{nm}$ steadily to large negative values. $\varepsilon'_{mr}(\lambda)$ is positive and remains rather small. Both, $\varepsilon'_{mr}(\lambda)$ and $\varepsilon''_{mr}(\lambda)$ reveal a distinct feature near 300 nm (not

Table 7.2 SP-sensor performance and figures of merit for thin Au-films and nano-particle at metal-water interface

	the state of the s	to min the mining and many	Paracra ar morar un	2001		
Operation mode	Pperation mode Suited/best substrate	Optical responsivity	Linear dynamic SPR width		Optimum film Remarks	Remarks
			range		thickness	
AIM	TOPAS/PC/PMMA/BK7/Quartz 50-220°/RIU	50–220°/RIU	$<5 \times 10^{-2} \text{ RIU}$ 2–10°	2–10°	50 nm	Single resonance
WIM	TOPAS/PC/PMIMA/BK7/Quartz $4,000 \pm 1,000 \mathrm{nm/RIU}$ $<5 \times 10^{-2} \mathrm{RIU}$ $40 \pm 2 \mathrm{nm}$	$4,000 \pm 1,000 \mathrm{nm/RIU}$	$<5 \times 10^{-2} \text{ RIU}$		50 nm	Single resonance
AIMLRSPP	BK7/Teflon bi-layer	200°/RIU	None	2–5°		Split resonance
WIMLRSPP	BK7/Teflon bi-layer	8,000 nm/RIU	$>4 \times 10^{-2} \text{ RIU}$ $140 \pm 20 \text{ nm}$	$140 \pm 20 \mathrm{nm}$		Split resonance
LSPR	Nano-particles	180 nm/RIU	$> \times 10^{-2} \text{ RIU}$ 150 nm	150 nm	45 nm particles	45 nm particles Colloidal particles

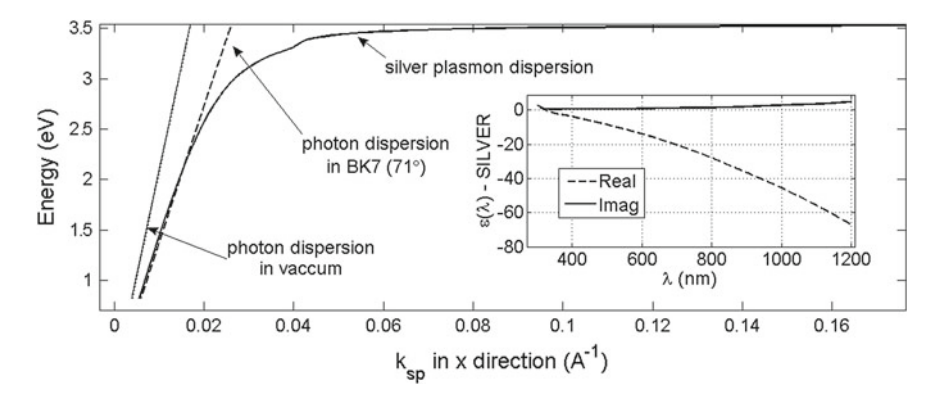


Fig. 7.22 Photon and SPP-dispersion curves of Silver for the symmetric mode at the metal-water interface (*solid-line*), calculated for a BK7 substrate (*dashed-line*) and incident angle of 71°. The related intersection point and resonance appears near 2.1 eV. *Right inset* depicts the real and imaginary fractions of the CDK

shown) that originates from an inter-band transition. For the BK7 substrate at 71°, the SP-dispersion is weakly distorted and exhibits a resonant cross-over at around 2.1 eV. In the asymptotic limit, at high k, the SP-energy remains at around 3.51 eV at the metal-water interface. Silver films are easily deposited by magnetron sputtering from a massive metal-target in inert atmosphere, by electron beam evaporation, or by thermal evaporation from electrically heated Tungsten foils or boatsin high vacuum. The evaporation/boiling temperature of Ag is 2,162 °C. Native oxides form slowly on the metal surface, upon exposure to air or water at neutral pH. Comparable to clean Au-and Cu-metal surfaces, Silver also favors covalent binding to sulfur and many compounds that contain this element. Plain Silver and nano-particles thereof exhibit some biological and anti-inflammatory activity.

For the BK7-substrate, photon and SP-dispersion curves exhibit a sharp crossover and resonance near 2.1 eV. Related spectral features of the reflectance $R(\lambda)$ in the WIM are shown in Fig. 7.23 for the substrate materials under consideration. Except MgF₂, all other substrates exhibit a clear SP-resonance, and potentially are suited for sensing applications. However, for CaF₂ and LiF, resonances are located at rather long wavelength and/or high angle. The reflectance under AIM conditions is shown in Fig. 7.23, again indicating that particularly the MgF₂ and LiF substrates are unsuited for SP sensing applications. The SP-line broadening parameter $\Delta\lambda_{res}$ decreases considerably for the remaining SP-active substrates towards lower angle and longer wavelength. The Quartz substrate exhibits the mostly narrow SP-resonance at 1,143 nm and 68°, as show in Fig. 7.24.

For the BK7 substrate, the SP-energy (eV) of thin Ag-films varies non-linearly with the resonance angle within the range $60^{\circ} < \theta < 75^{\circ}$ approximately as: $E_{SP}(\theta) = 0.0079\theta^2 + 1.198\theta - 43.084$.

Figure 7.25 illustrates the spectral characteristic of the resonance under WIM conditions for a set of RIU values of the aqueous dielectric analyte. The depths/contrast

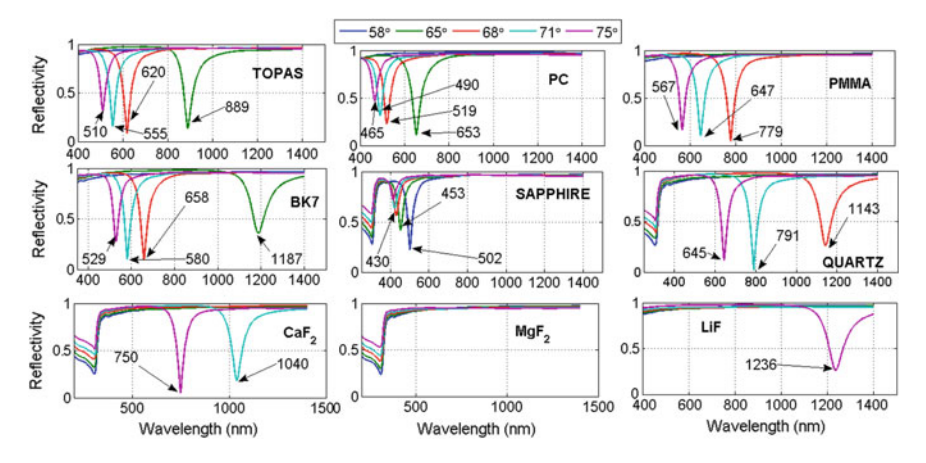


Fig. 7.23 Reflectance curves under WIM-conditions, calculated for different substrate materials, as indicated in the plots. Incident angles are: 58° , 63° , 68° , 71° and 75° for the wavelength range $400 \, \text{nm} < \lambda < 1,400 \, \text{nm}$. The Ag-film thickness is $50 \, \text{nm}$, in contact with water as the liquid dielectric

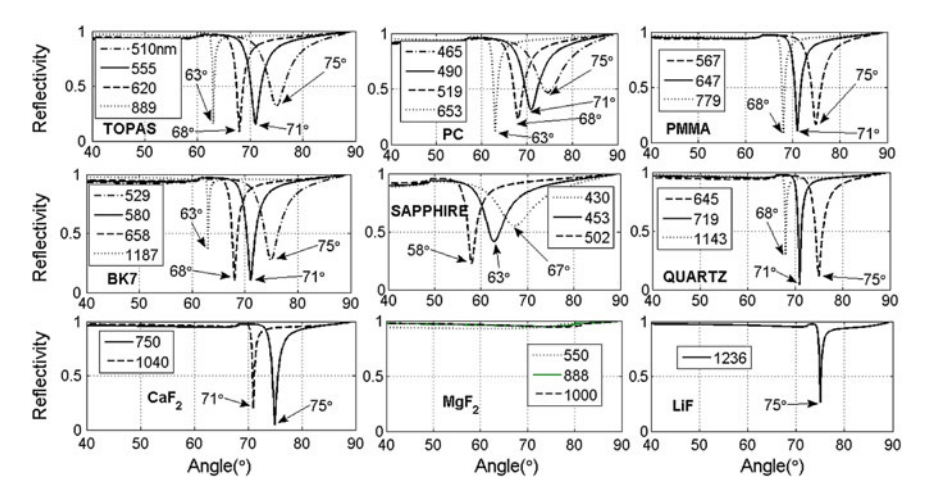


Fig. 7.24 Reflectance curves under AIM-conditions for different substrate materials, as indicated in the plots, and different incident wavelengths for the angle range $40^{\circ} < \theta < 90^{\circ}$. Ag-film thickness is 50 nm, in contact with water

of the resonance remains approximately constant towards higher n_{an} -values, whilst the resonance minimum shifts towards longer wavelengths. For the BK7 substrate, the slightly non-linear displacement of the resonance wavelength $\lambda_{res}(n_{an})$ as function of the refractive index of the liquid dielectric within the range $1.33 < n_{an} < 1.39$ is shown in the right upper sub figures. The broadening parameter of the resonance $\lambda_{res}(n_{an})$, as taken at FWHM, is calculated to 38 ± 4 nm, and reveals an oscillating variation with n_{an} . The WIM-responsivity R_{WIM} is fairly high, depicted in the lower

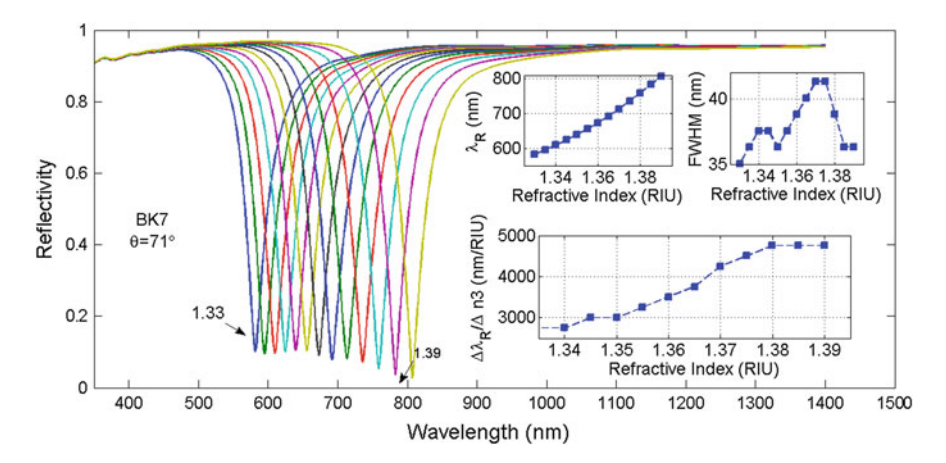


Fig. 7.25 WIM-sensing properties and spectral reflectance $R(\lambda)$ of Silver at 590 nm, calculated for a set of different RIU-values of the aqueous analyte: $1.33 < n_{an} < 1.39$. Substrate is BK7, incident angle is 71°. *Right upper insets* show line broadening $\Delta \lambda_{res}(n_{an})$, resonance displacements $\lambda_{res}(n_{an})$ and SP-responsivity $R_{WIM}(n_{an})$ at *lower inset*

right inset, comprises a magnitude of $4,000 \pm 1,000 \,\text{nm/RIU}$ and a steady increase with n_{an} .

The SPR-sensing characteristic in the AIM is shown in Fig. 7.26 for a wavelength of 658 nm, comprising initial resonance angle of 68°. The maximum achievable AIM-responsivity with $R_{AIM} = 300^{\circ}/RIU$ is high, and decreases with increasing wavelength. The line broadening parameter $\Delta\theta_{res}$ increases towards higher values of n_{an} .

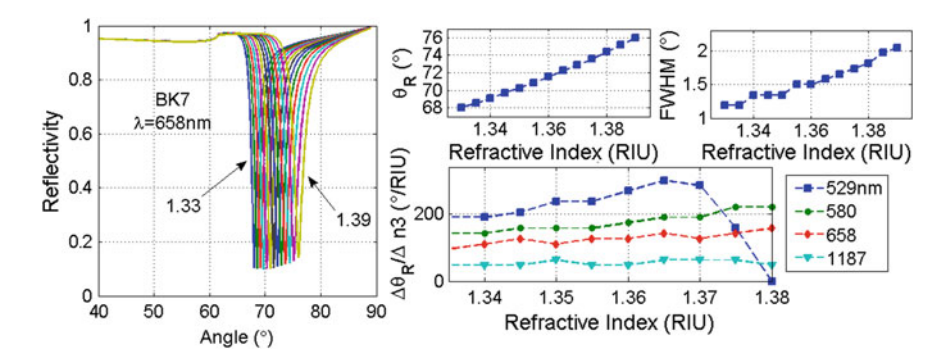


Fig. 7.26 AIM-sensing properties and angular reflectance $R(\theta)$, calculated for a set of different RIU-values of an aqueous analyte at range $1.33 < n_{an} < 1.39$. Substrate is BK7 and incident wavelength is 658 nm. *Right sub-figures* depict resonance displacements $\theta_{res}(n_{an})$, line broadening $\Delta\theta_{res}(n_{an})$ and SP-responsivity $R_{AIM}(n_{an})$ for four different wavelength

64 7 Classical Noble Metals

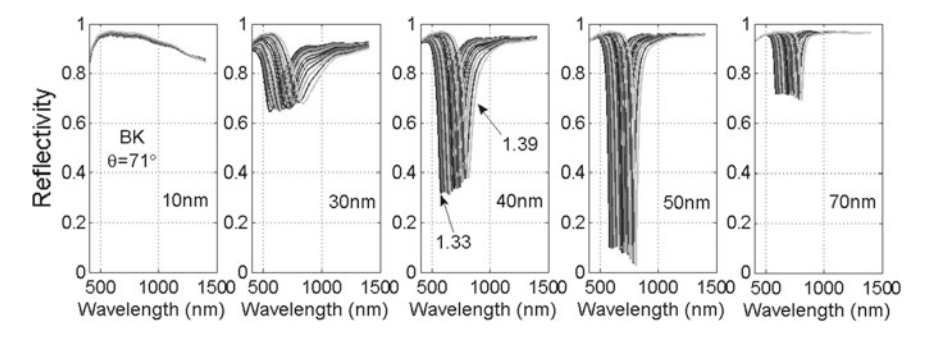


Fig. 7.27 WIM-reflectance at the SP-resonance for different Ag-film thickness values of 10, 30, 40, 50 and 70 nm

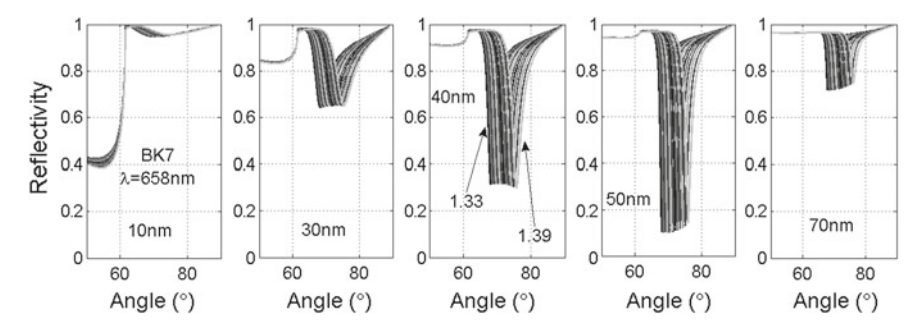


Fig. 7.28 AIM-reflectance at the SP-resonance for different Ag-film thickness values of 10, 30, 40, 50 and 70 nm

Eventually, the influence of film thickness for WIM and AIM conditions is outlined in Figs. 7.27 and 7.28. This data set clearly indicates that the Ag-film thickness for optimum SPR sensor operation is placed at around 50 nm, in accord with other noble metals.

7.3.1 Long Range Surface Plasmon Polaritons (LRSPP-mode)

SP-sensor properties of the LRSPP mode in the WIM are depicted in Fig. 7.29. The spectral characteristics (left figure) reveals two co-existing SP-dips: the symmetric (short range mode) near 500 nm (lines with squares in right figures) and the addition anti-symmetric, long range (LRSPP) mode at 850 nm (lines with circles). Comparison with Fig. 7.25 illustrates that the resonsivlity $R_{WIM}(n_{an})$ of the LRSPP is a factor 2 higher and also increases with n_{an} .

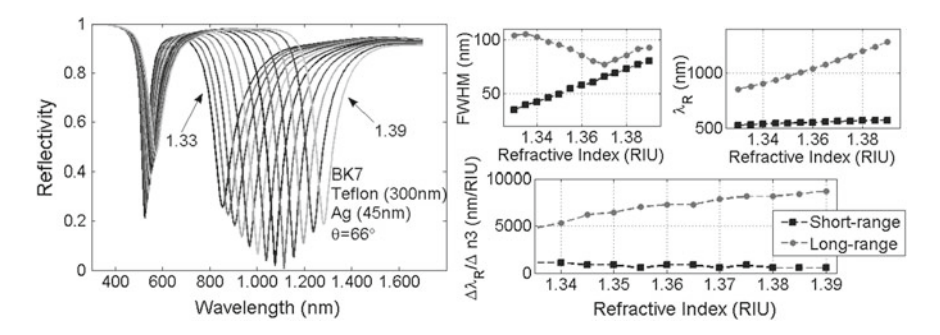


Fig. 7.29 WIM-sensor properties in presence of the LRSPP mode: spectral reflectance $R(\lambda)$ (left figure) for different RIU-values of the aqueous analyte 1.33 < n_{an} < 1.39, indicating two co-existing SP-dips. Substrate is BK7, with a 300 nm Teflon film on top, incident angle is 68°. Three figures at right show line broadening $\Delta\lambda_{res}(n_{an})$ and resonance displacements $\lambda_{res}(n_{an})$ at top and responsivities $R_{WIM}(n_{an})$ at bottom for short (lines with squares) and long range SPP's (lines with circles)

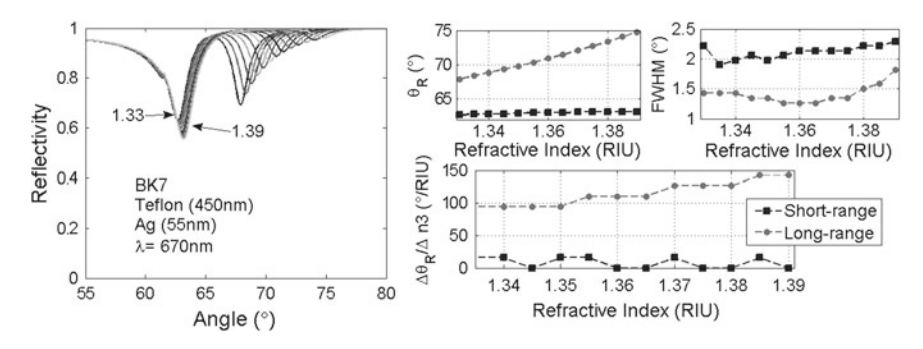


Fig. 7.30 AIM-sensor properties in presence of the anti-symmetric LRSPP-mode: angular reflectance $R(\lambda)$ at *left figure* for different RIU-values of the aqueous analyte 1.33 < n_{an} < 1.39, indicating two SP-dips. Substrate is BK7 with a 450 nm thin Teflon film on *top* and the metal film placed thereon. Incident wavelength is 670 nm. *Three figures* at *right* show line broadening $\Delta\theta res(n_{an})$ and angular resonance displacements $\theta_{res}(n_{an})$ at *top*, and associated responsivities $R_{AIM}(n_{an})$ at *bottom* for short (*lines with squares*) and long range modes (*lines with circles*)

SP-sensor properties in presence of the LRSPP mode in the AIM are depicted in Fig. 7.30. In the AIM mode, the magnitude of the sensor resonsivlity $R_{AIM}(\lambda)$ for the LRSPP does not differ significantly from the short range SPP from Fig. 7.26, except for a slightly shifted wavelength to 670 nm.

7.3.2 Localized Plasmons in Colloidal Ag-Particles (LSPR-mode)

The optical absorption characteristic of colloidal Ag-particles with 45 nm diameter, immersed into an aqueous solution with varying refractive index n_{an} as function

66 7 Classical Noble Metals

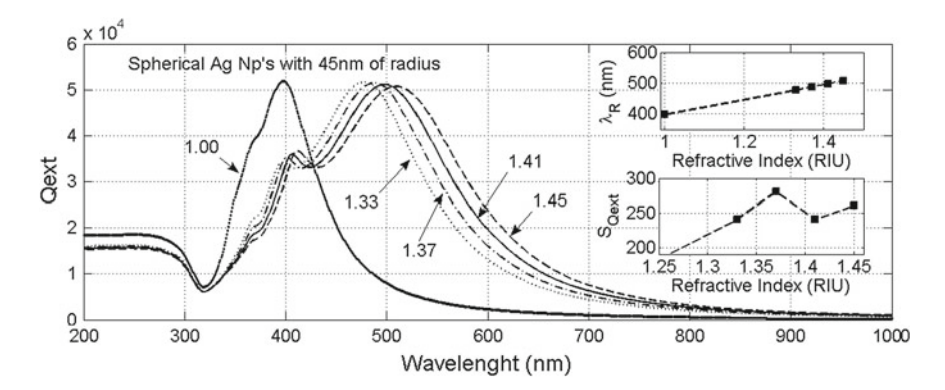


Fig. 7.31 Optical absorbance for Ag-particles with 45 nm diameter, calculated as function of wavelength for different refractive index (RIU) values of the surrounding aqueous solution. *Right two insets* show resonance position $\lambda_R(n_{an})$ and optical responsivity $S_{Q_{ext}}(n_{an})$, taken at the spectral maximum near 400 nm

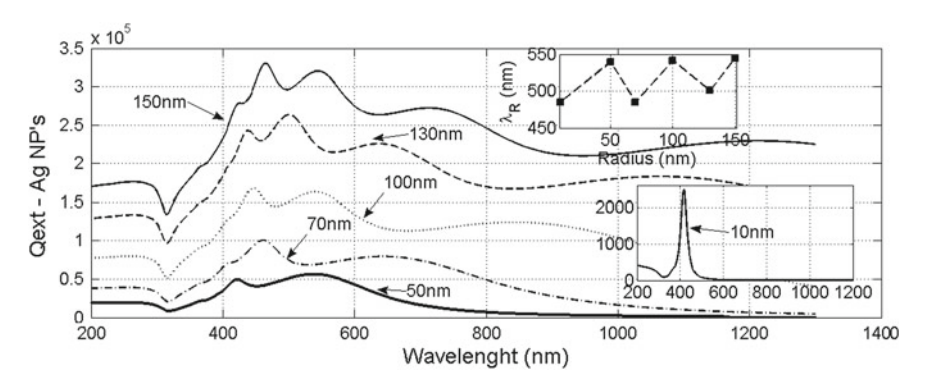


Fig. 7.32 Spectral variation of the optical absorbance of colloidal Ag-particles in aqueous solution, plotted for different particle diameter

of wavelength, is depicted in Fig. 7.31. Upper right insets reveal spectral resonance position $\lambda_{res}(n_{an})$ at top and responsivity $S_{Q_{ext}}(n_{an})$ at bottom. This quantity is considerably smaller than calculated before for both, short and long range SPP's.

The influence of size onto optical absorbance is illustrated in Fig. 7.32, as calculated for different diameter of the spherical particles that varies from 10 to 150 nm. The number of maxima of the oscillating function increases with larger diameter, indicating a higher number of SP-eigenmodes. A compilation of achievable SPR sensor performance is displayed in Table 7.3.

Table 7.3 SP-sensor		performance and figures of merit for thin Ag-films and colloidal particles at metal-water interface; BK7 substrate	ms and colloidal particles	at metal-wate	r interface; BK7 substrate	
Operation mode Su	Suited/best substrate	uited/best substrate Optical responsivity Linear dynamic range SPR width Optimum film thickness Remarks	Linear dynamic range	SPR width	Optimum film thickness	Remarks
AIM	All except fluorides 50–300°/RIU	50-300°/RIU	$< 5 \times 10^{-2} \mathrm{RIU}$	$1.8 \pm 0.2^{\circ}$ $50 \pm 3 \mathrm{nm}$	$50 \pm 3 \mathrm{nm}$	Single resonance
WIM	All except fluorides	Il except fluorides $ 4,000 \pm 1,000 \text{ nm/RIU} < 1 \times 10^{-2} \text{ RIU}$	$<1 \times 10^{-2} \mathrm{RIU}$	$38 \pm 2 \mathrm{nm}$ $50 \pm 3 \mathrm{nm}$	$50 \pm 3 \mathrm{nm}$	Single resonance
AIMLRSPP	BK7/Teflon bi-layer 150°/RIU	150°/RIU	None	$1.5 - 2^{\circ}$		Split resonance
WIMLRSPP	BK7/Teflon bi-layer 7,000 nm/RIU	7,000 nm/RIU	$>4 \times 10^{-2} \mathrm{RIU}$	$80 \pm 20 \mathrm{nm}$		Split resonance
LSPR	Nano-particles	250 nm/RIU	$> \times 10^{-2} \text{ RIU}$	200 nm	45 nm particles	Colloidal particle

68 7 Classical Noble Metals

References

- 1. Palik, E.D.: Handbook of Optical Constants of Solids. Academic Press, Boston (1985)
- 2. Burdick, G.A.: Energy band structure of copper. Phys. Rev. 129, 138–150 (1963)
- 3. Keil, P., Lützenkirchen-Hecht, D., Frahm, R.: Investigation of room temperature oxidation of Cu in air by Yoneda-XAFS. AIP Conf. Proc. 882, 492 (2007)
- Christensen, N.E., Seraphin, B.O.: Relativistic Band calculation and optical properties of gold. Phys. Rev. B 4, 3321–3344 (1971)
- 5. Christensen, N.E.: Bandstructure of silver. Phys. Status Solidi B 54, 551 (1972)

Chapter 8 Noble Transition Metals of the Platinum Group

8.1 Thin Iridium (Ir) Films and Colloidal Particles

The complex optical constant $\varepsilon_{mr}(\lambda) = \varepsilon'_{mr}(\lambda) + j\varepsilon''_{mr}(\lambda)$ of the paramagnetic metal has been taken from Ref. [1] and is illustrated in the right inset of Fig. 8.1. The electron configuration of the single atom is $[Xe]4f^{14}5d^{7}6s^{2}$. In the solid material, the two outer 6s electrons and the incomplete 5d shell hybridize and account for the partly occupied conduction band, as shown in the band-structure calculation of Ref. [2]. The moderately high electrical dc-conductivity of $21.2 \times 10^6 (\Omega \text{ m})^{-1}$ and CDK are insufficiently described by the DA, or free electron model. Within the wavelength range of interest, $\varepsilon'_{mr}(\lambda)$ decreases at $\lambda > 300$ nm steadily to large negative values. $\varepsilon''_{mr}(\lambda)$ is positive and increases steadily to high value, most likely related to intra-band or phonon assisted transitions. For the BK7 substrate at 68°, the SP-dispersion is strongly distorted and exhibits a resonant cross-over at around 0.8 eV. In the asymptotic limit at high k, the SP-energy approaches approximately 6 eV at the metal-water interface. Iridium films are readily produced by magnetron sputtering from a massive metal-target in inert atmosphere, possibly also by electron beam evaporation. Due to the high boiling/evaporation temperature of 4,130 °C, films cannot be made by thermal evaporation from electrically heated Tungsten foils or carbon boats, due to their lower melting temperatures. Iridium belongs to the group of transition noble metals. Native oxides do not form on the metal surface upon exposure to air or aqueous solution at any pH. However, stable thin oxide layers can be made electrochemically at moderate anodic potentials in acidic solution, and reveal a strong electro-chromic effect. The metal is highly corrosion resistant.

For the BK7-substrate at 68°, photon and SP-dispersion curves exhibit a clear cross-over and resonance near 0.8 eV. Related spectral features of the reflectance $R(\lambda)$ in the WIM are shown in Fig. 8.2 for the substrate materials under consideration. In comparison with the metals, depicted before, Iridium exhibits severely distorted SP-resonances that are shifted far into the Infrared region of the electromagnetic spectrum. Except MgF₂, all other substrates exhibit a resonance. Ir-films are thus of limited value for SP-sensing applications.

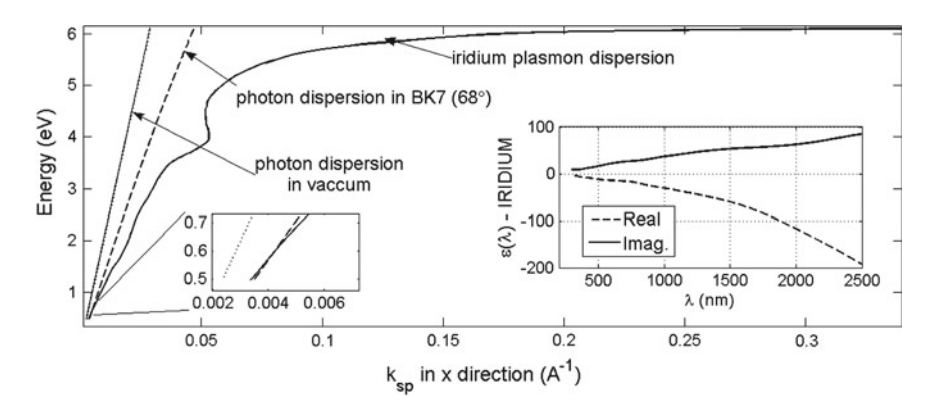


Fig. 8.1 Photon and SPP-dispersion curves of Iridium at the metal-water interface (*solid-line*) for the symmetric mode, calculated for a BK7 substrate (*dashed-line*) and incident angle of 68°. The related intersection point and resonance appears near 0.8 eV at very low k-values. *Right inset* reveals the real and imaginary fractions of the CDK; as function of wavelength

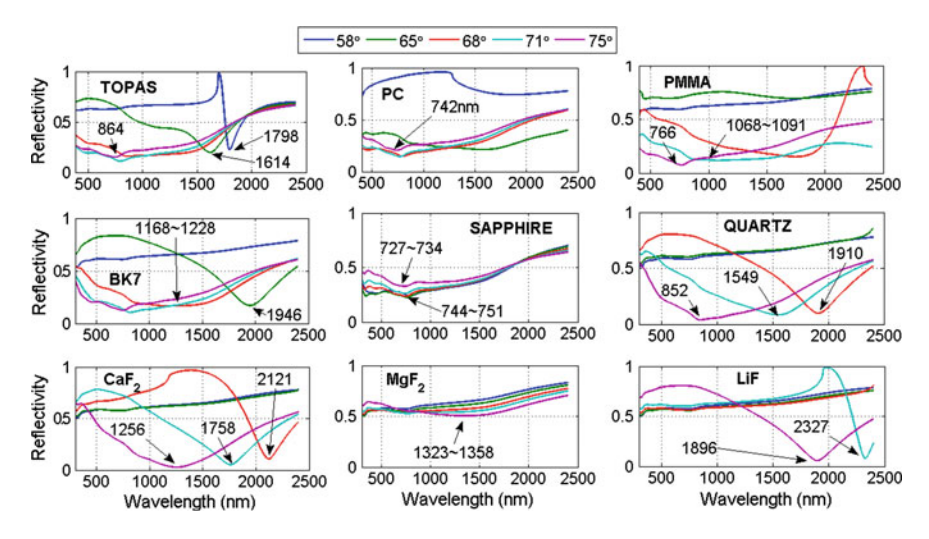


Fig. 8.2 Reflectance curves under WIM-conditions, calculated for different substrate materials, as indicated in the *plots*. Incident angles are: 58° , 65° , 68° , 71° and 75° for the wavelength range $400 \text{ nm} < \lambda < 2.500 \text{ nm}$. The Ir-film thickness is 20 nm, in contact with water as the liquid dielectric

The reflectance under AIM conditions is shown in Fig. 8.3, again indicating that particularly the MgF₂ substrate does not exhibit a clear SP-resonance. The SP-line broadening parameter θ_{res} decreases considerably for the remaining SP-active substrates towards lower angle and longer wavelength. The LiF-substrate exhibits the mostly narrow SP-resonance.

For the Quartz substrate, the SP-energy (eV) of thin Ir-films at the metal water interface varies non-linearly with the resonance angle within the range $65^{\circ} < \theta < 75^{\circ}$ approximately as: $E_{SP}(\theta) = 0.0162\theta^2 - 2.1973\theta - 75.294$.

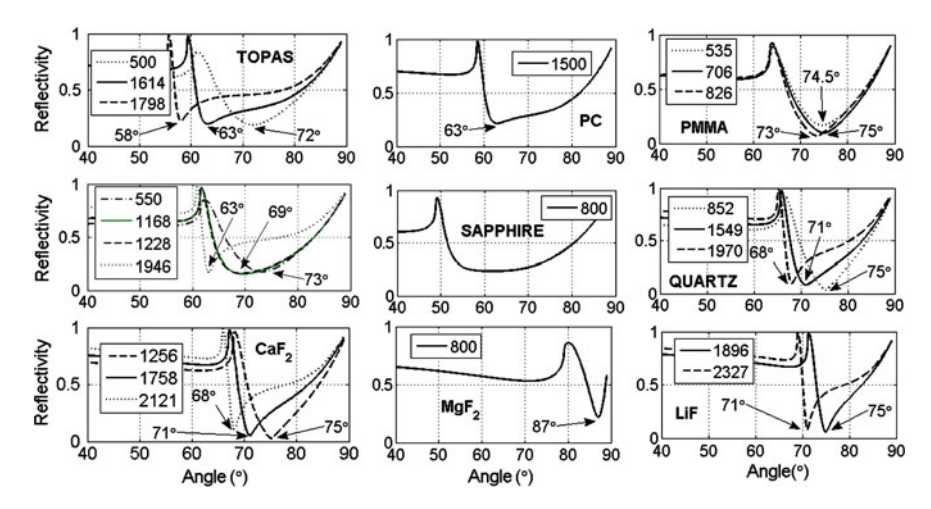


Fig. 8.3 Reflectance curves under AIM-conditions for different substrate materials, as indicated in the plots, and different incident wavelengths for the angle range $50^{\circ} < \theta < 90^{\circ}$. Ir-film thickness is 20 nm, in contact with water

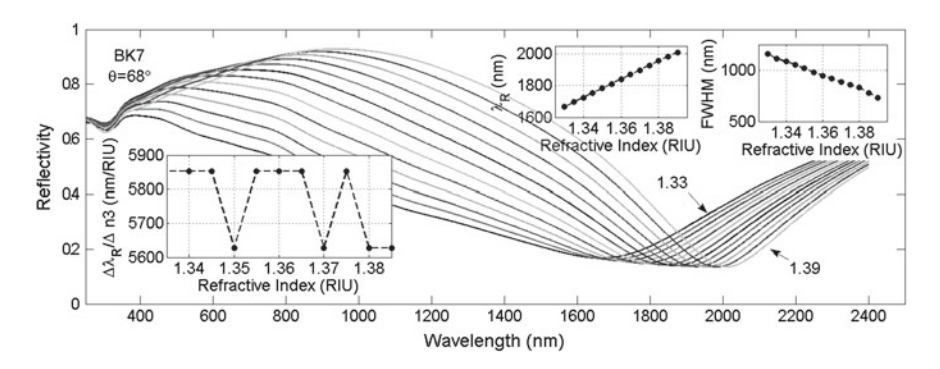


Fig. 8.4 WIM-sensing properties and spectral reflectance $R(\lambda)$ of Iridium, initial wavelength is near 1,500 nm, calculated for a set of different RIU-values of the aqueous analyte: $1.33 < n_{an} < 1.39$. Substrate is BK7, incident angle is 68° . *Upper right upper insets* show line broadening $\Delta \lambda_{res}(n_{an})$, resonance displacements $\lambda_{res}(n_{an})$ and SP-responsivity $R_{WIM}(n_{an})$ at *lower left inset*

Figure 8.4 illustrates the spectral characteristic of the resonance under WIM conditions, calculated for a set of RIU values of the aqueous dielectric analyte. The depths/contrast of the resonance increases considerably towards higher n_{an} -values, whilst the resonance minimum shifts towards longer wavelengths. For the BK7 substrate, a fairly linear displacement of the resonance wavelength $\lambda_{res}(n_{an})$ as function of the refractive index (RIU) of the liquid dielectric within the range $1.33 < n_{an} < 1.39$ is shown in the right inset. The broadening parameter of the resonance $\Delta \lambda_{res}(n_{an})$, taken at FWHM, is very high and calculated to 900 ± 300 nm within the given range of n_{an} . The WIM-responsivity $R_{WIM}(n_{an})$ is considerable and

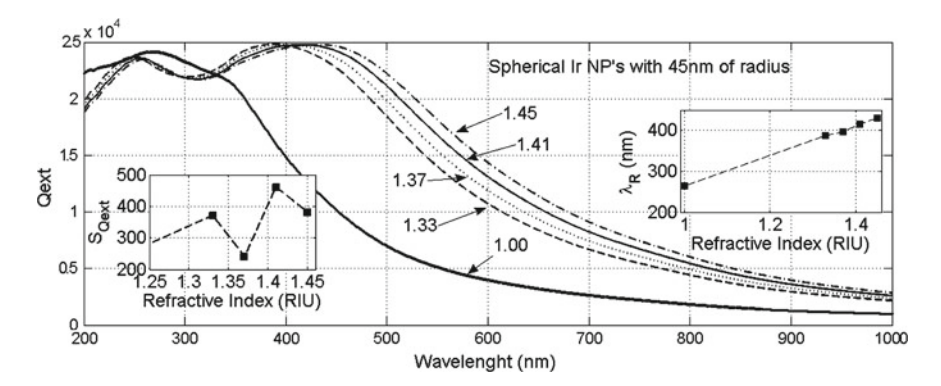


Fig. 8.5 Optical absorbance for Ir-particles with 45 nm diameter, calculated as function of wavelength for different refractive index (RIU) values of the surrounding aqueous solution. *Right* and *left lower insets* shows resonance position $\lambda_R(n_{an})$ and related optical responsivity $S_{Q_{ext}}(n_{an})$, respectively, with reference to the first spectral maximum near 300 nm

depicted in the lower left inset, comprising a magnitude of $5,800 \pm 100$ nm/RIU that does not vary with n_{an} .

8.1.1 Localized Plasmon in Colloidal Ir-Particles (LSPR-Mode)

The optical absorption characteristic of colloidal Ir-particles with 45 nm diameter, immersed into an aqueous solution with varying refractive index n_{an} as function of wavelength, is depicted in Fig. 8.5. Upper right insets reveal spectral resonance position $\lambda_{res}(n_{an})$ and responsivity $S_{Q_{ext}}(n_{an})$ at lower left. This quantity is considerably smaller than calculated before for short SPP's of Fig. 8.4.

A compilation of achievable SPR sensor performance is displayed in Table 8.1.

8.2 Thin Osmium (Os) Films and Colloidal Particles

The complex optical constant $\varepsilon_{mr}(\lambda) = \varepsilon'_{mr}(\lambda) + j\varepsilon''_{mr}(\lambda)$ of the diamagnetic metal has been taken from Ref. [3], and is illustrated in the right inset of Fig. 8.6. The electron configuration of the isolated Os-atom is $[Xe]4f^{14}5d^66s^2$. In the solid material, the two outer 6s electrons and the only partly filled 5d shell hybridize, and account for a partially occupied conduction band, as reported in the band-structure calculations of Ref. [4]. The rather low electrical dc-conductivity of $12.3 \times 10^6 \ (\Omega \ m)^{-1}$ and CDK are insufficiently described by the DA. Within the wavelength range of interest, $\varepsilon'_{mr}(\lambda)$ decreases at $\lambda > 850$ nm rapidly to large negative values. $\varepsilon''_{mr}(\lambda)$ is positive and shows, unlike $\varepsilon''_{mr}(\lambda)$, a pronounced feature around 400 nm. For the BK7 substrate at 75°,

Table 8.1 SP-sensor perfor	sor performance and figu	mance and figures of merit for thin Ir-films and colloidal particle at metal-water interface	is and colloidal particle a	metal-water inte	rface	
Operation mode	Suited/best substrate	Operation mode Suited/best substrate Optical responsivity	Linear dynamic range SPR width 0	SPR width	Optimum film thickness Remarks	Remarks
AIM	All except MgF2	50-80°/RIU	$< 5 \times 10^{-2} \mathrm{RIU}$	$18 \pm 2^{\circ}$	20 nm	Single resonance
WIM	All except MgF2	$ 5,800\pm1,000 \text{ nm/RIU} < 5 \times 10^{-2} \text{ RIU}$	$< 5 \times 10^{-2} \mathrm{RIU}$	900±300 nm 20 nm	20 nm	Single resonance
LSPR	45 nm particle	350 ± 100 nm/RIU	$> \times 10^{-1} \mathrm{RIU}$	100 nm	10-100 nm diam.	

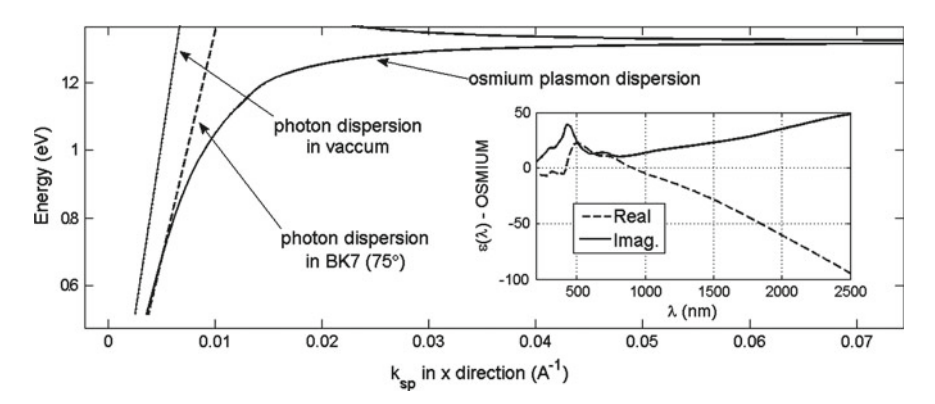


Fig. 8.6 Photon and SPP-dispersion curves of Osmium at the metal-water interface (*solid-line*), calculated for a BK7 substrate (*dashed-line*) and incident angle of 75°. The related intersection point and resonance appears near 0.7 eV at low k-values. *Right inset* reveals the real and imaginary fractions of the CDK as function of wavelength

the SP-dispersion appears virtually undistorted and exhibits a resonant cross-over at around 0.7 eV. In the asymptotic limit at high k, the SP-energy approaches only 1.32 eV at the metal-water interface. Osmium films are best produced by magnetron sputtering from a massive metal-target in inert atmosphere, possibly by electrodeposition in aqueous solution. Due to the very high boiling/evaporation temperature of 5,012 °C, Os-films cannot be prepared by thermal evaporation from electrically heated Tungsten foils or carbon boats, or by electron beam evaporation in high vacuum. There is not much known about native oxide formation on the metal surface upon exposure to air or aqueous solution. Most likely the metal behaves similar to Iridium and Platinum. Certain bulk oxides, especially OsO₄ are highly toxic. Stable thin oxide layers also can be made electrochemically at anodic potentials. The metal appears more reactive than Iridium.

For the BK7-substrate at 75°, photon and SP-dispersion curves exhibit a cross-over and resonance near 0.7 eV. Related spectral features of the reflectance $R(\lambda)$ in the WIM are shown in Fig. 8.7 for the substrate materials under consideration. Similar to Iridium, the metal exhibits severely distorted SP-resonances that are shifted far into the Infrared region of the electromagnetic spectrum. All substrates exhibit a resonance, but poor SP properties are resolved for MgF₂.

Os-films are suited for SP-sensing applications. The reflectance under AIM conditions is shown in Fig. 8.8, again indicating that particularly the MgF₂, LiF, PMMA and Sapphire substrates are not a good choice. The SP-line broadening parameter λ_{res} does not change significantly with either angle or wavelength.

For a BK substrate, the SP-energy (eV) of thin Os-films varies approximately non-linear with the resonance angle within the range $62^{\circ} < \theta < 75^{\circ}$ as: $E_{SP}(\theta) = 0.0487\theta^2 - 2.476\theta$.

Figure 8.9 illustrates the spectral characteristic of the resonance under WIM conditions for a set of RIU values of the aqueous dielectric analyte. The depths/contrast of the resonance remains approximately constant towards higher n_{an} -values, whilst

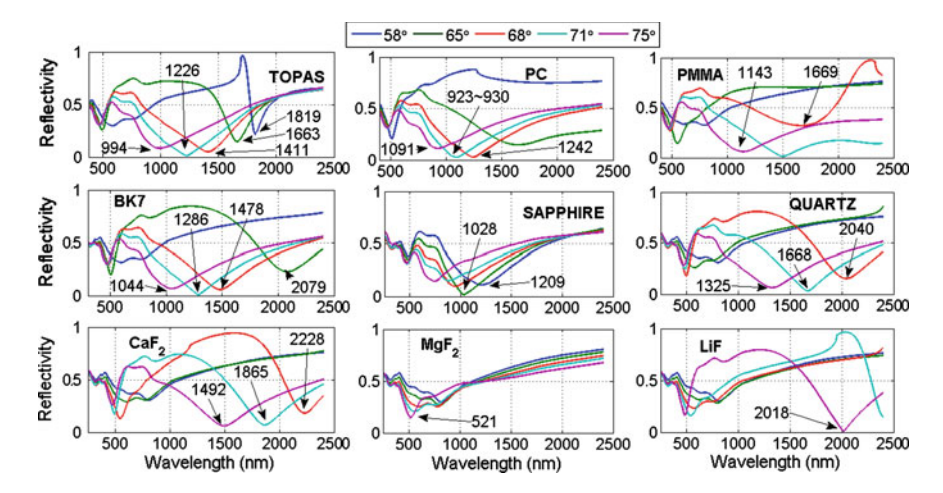


Fig. 8.7 Reflectance curves under WIM-conditions, calculated for different substrate materials, as indicated in the plots. Incident angles are: 58° , 65° , 68° , 71° and 75° for the wavelength range $500 \text{ nm} < \lambda < 2,500 \text{ nm}$. The Os-film thickness is 35 nm, in contact with water as the liquid dielectric

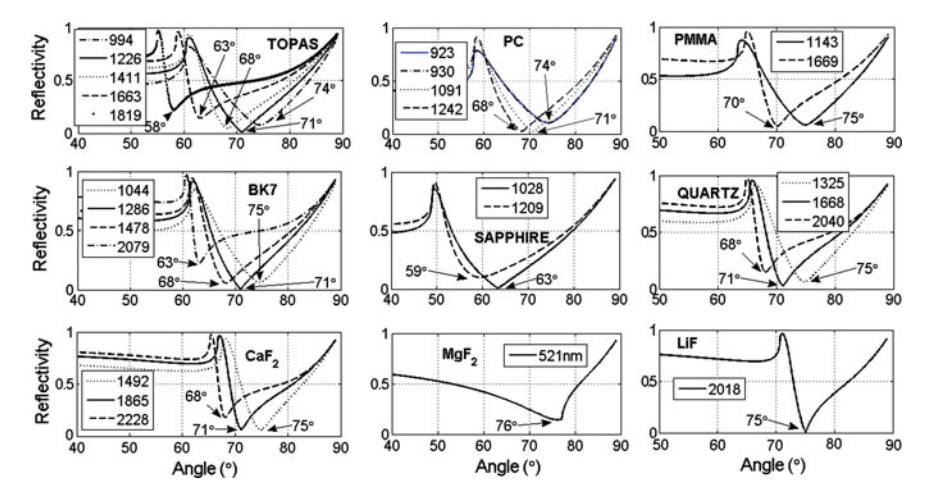


Fig. 8.8 Reflectance curves under AIM-conditions, calculated for different substrate materials, as indicated in the plots, and different incident wavelengths for the angle range $40^{\circ} < \theta < 90^{\circ}$. Os-films thickness is 35 nm, in contact with water

the resonance minimum shifts towards longer wavelengths. For the BK7 substrate, a nearly linear displacement of the resonance wavelength $\theta_{res}(n_{an})$ as function of the refractive index of the liquid dielectric within the range $1.33 < n_{an} < 1.39$ is revealed in the upper left inset. The broadening parameter of the resonance $\Delta\theta_{res}(n_{an})$, as taken at FWHM, is calculated to 900 ± 100 nm, and increases with n_{an} . The WIM-responsivity $R_{WIM}(n_{an})$ appears fairly high, depicted in the upper right inset, comprises a magnitude of $4,000 \pm 1,000$ nm/RIU and a slight increase with n_{an} .

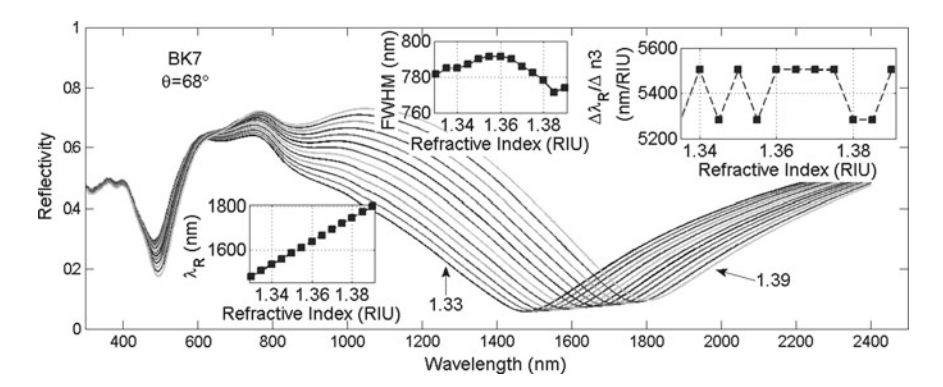


Fig. 8.9 WIM-sensing properties and spectral reflectance $R(\lambda)$ of thin Osmium films: the initial minimum is near 1,040 nm, calculated for a set of different RIU-values of the aqueous analyte: 1.33 < n_{an} < 1.39. Substrate is BK7, incident angle is 75°. *Upper right* and *left insets* shows the SP-responsivity $R_{WIM}(n_{an})$ and resonance displacements $\lambda_{res}(n_{an})$, respectively. *Lower right inset* depicts line broadening $\Delta\theta_{res}(n_{an})$

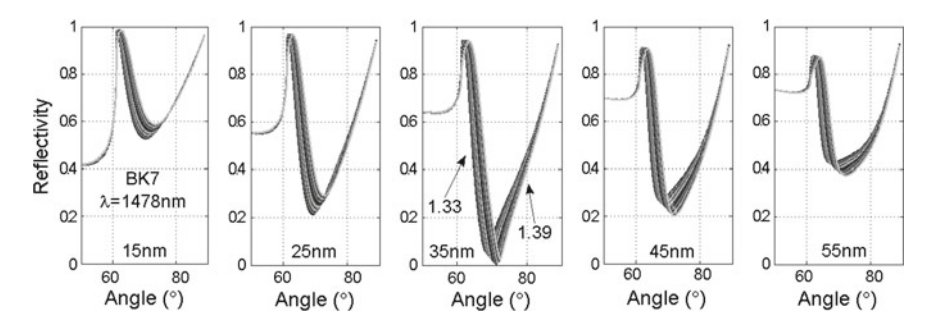


Fig. 8.10 AIM-reflectance at the SP-resonance for different Os-film thickness values of 15, 25, 35, 45 and 55 nm

Eventually, the influence of film thickness for AIM conditions is outlined in Fig. 8.10. This data set clearly indicates that the Os-film thickness for optimum SPR sensor operation is placed at around 35 nm.

8.2.1 Long Range Surface Plasmon Polaritons (LRSPP-Mode)

SP-sensor properties of the LRSPP in the WIM are depicted in Fig. 8.11. The spectral characteristics (left figure) reveals two co-existing relatively broad SP-dips: the symmetric (short range mode) near 700 nm (line with squares) and the addition antisymmetric, long range (LRSPP) mode at 2,200 nm (line with circles). Comparison with Fig. 8.9 illustrates that the responsibility $R_{WIM}(n_{an})$ of the LRSPP is of similar magnitude, but decreases slightly with n_{an} .

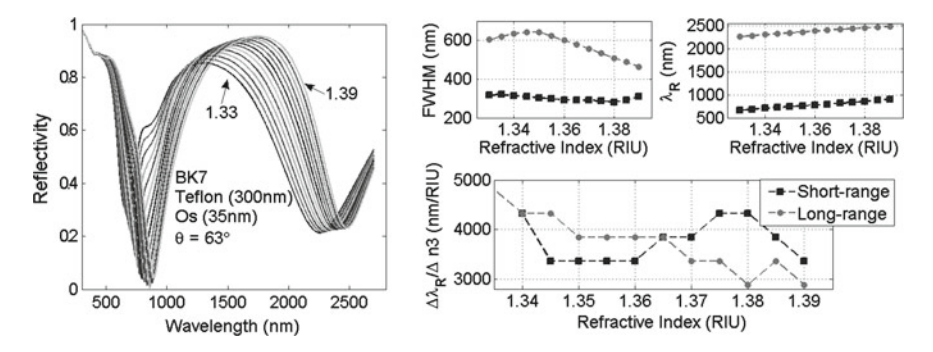


Fig. 8.11 WIM-sensor properties in presence of the LRSPP mode: spectral reflectance $R(\lambda)$ (*left figure*) for different RIU-values of the aqueous analyte 1.33 < n_{an} < 1.39, indicating two coexisting SP-dips. Substrate is BK7, with a 300 nm Teflon film on top, incident angle is 63°. Three figures at *right show line* broadening $\Delta\lambda(n_{an})$ and resonance displacements $\lambda_{res}(n_{an})$ at top and responsivities $R_{WIM}(n_{an})$ at *bottom* for short (*line with squares*) and long range SPP's (*line with circles*)

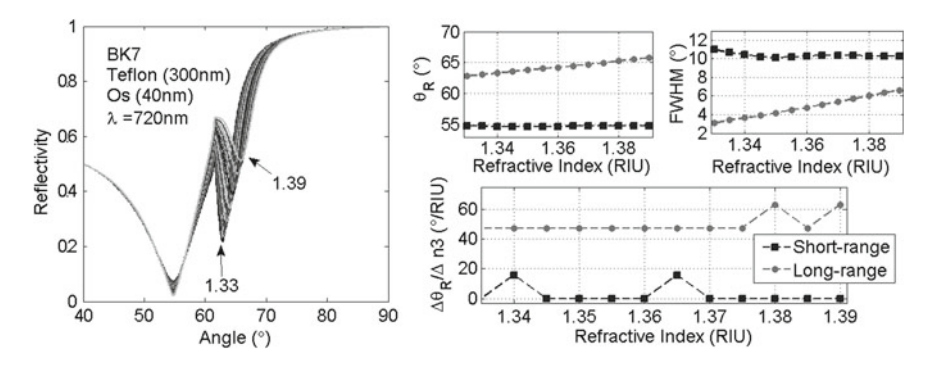


Fig. 8.12 AIM-sensor properties in presence of the anti-symmetric LRSPP-mode: angular reflectance $R(\lambda)$ at *left figure* for different RIU-values of the aqueous analyte 1.33 < n_{an} < 1.39, indicating two SP-dips. Substrate is BK7 with a 300 nm thin Teflon[®] film on *top* and the metal film placed thereon. Incident wavelength is 720 nm. Three figures at *right show line* broadening $\Delta \lambda_{res}(n_{an})$ and angular resonance displacements $\theta_{res}(n_{an})$ at *top*, and associated responsivities $R_{AIM}(n_{an})$ at *bottom* for short (*line with squares*) and long range modes (*line with circles*)

SP-sensor properties in presence of the LRSPP mode in the AIM are depicted in Fig. 8.12. In the AIM mode, the magnitude of the sensor responsibility $R_{AIM}(\lambda)$ for the LRSPP does not differ significantly from the short range SPP from Fig. 8.10, except for a wavelength shift to 720 nm.

8.2.2 Properties of Localized Plasmons in Os-Colloidal Particles

The optical absorption characteristic of colloidal Os-particles with 45 nm diameter, immersed into an aqueous solution with varying refractive index n_{an} as function

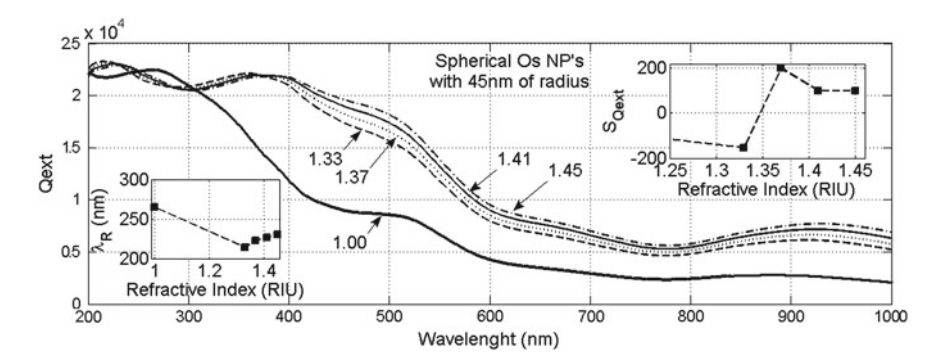


Fig. 8.13 Optical absorbance for Os-particles with 45 nm diameter, calculated as function of wavelength for different refractive index (RIU) values of the surrounding aqueous solution. *Right upper insets* shows resonance position $\lambda_R(n_{an})$ and optical responsivity $S_{Q_{ext}}(n_{an})$, respectively, taken at the first spectral maximum near 260 nm. The initial spectral shift is negative towards shorter wavelength

of wavelength, is depicted in Fig. 8.13. Upper right insets reveal spectral resonance position $\lambda_{res}(n_{an})$ and responsivity $S_{Q_{ext}}(n_{an})$. This quantity is considerably smaller than calculated before for long range SPP's.

A compilation of achievable SPR sensor performance is displayed in Table 8.2.

8.3 Thin Palladium (Pd) Films

The complex optical constant $\varepsilon_{mr}(\lambda) = \varepsilon'_{mr}(\lambda) + j\varepsilon''_{mr}(\lambda)$ of the paramagnetic metal has been taken from Ref. [1] and is illustrated in the right inset of Fig. 8.14. The electron configuration of the isolated Pd-atom is [Kr] $4d^{10}$. Unlike the other noble metals, the outer s-electron state is absent, which could supply a freely moving particle. Nevertheless, the solid material still behaves metallic at ambient T, caused by extending d-states, according to Ref. [5]. The low electrical conductivity of $9.52 \times 10^6 \, (\Omega \text{ m})^{-1}$ at $20 \,^{\circ}\text{C}$ and CDK are insufficiently described by the free electron model. Within the wavelength range of interest, $\varepsilon'_{mr}(\lambda)$ decreases at $\lambda > 250$ nm steadily to large negative numbers. $\varepsilon''_{mr}(\lambda)$ exhibits high positive and increasing values and a swing at 2,000 nm. For the CaF₂ substrate at 75°, the SP- dispersion appears virtually undistorted, with a resonant cross-over at around 1.4 eV. In the asymptotic limit at high k, the SP-energy approaches a high value of nearly 6 eV at the metalwater interface. Palladium films are most easily produced by magnetron sputtering from a massive metal-target in inert Ar-atmosphere at low pressure, electro-less plating and also atomic layer deposition, by electron beam or thermal evaporation from electrically heated Tungsten foils or carbon boats in high vacuum. The boiling/evaporation temperature is 2,963 °C. There is no native oxide formation known on the metal surface upon exposure to air or aqueous solution. Most likely, the metal

strate Optical responsivity Linear dynamic SPR width AMA/BK7/Quartz 40-80°/RIU <5 × 10 ⁻² RIU 15±2° \$7/Quartz/CaF2 4,000±1,000 nm/RIU <5 × 10 ⁻² RIU 900±100 nm layer 150°/RIU None >5° layer 12,000 nm/RIU >4 × 10 ⁻² RIU 140±20 nm layer 100 nm/RIU 3 × 10 ⁻² RIU 25 nm		0	,	1	,		
AIM TOPAS/PC /PMMA/BK7/Quartz 40–80°/RIU <5 × 10 ⁻² RIU 15±2° WIM TOPAS/PC /BK7/Quartz/CaF2 4,000±1,000 nm/RIU <5 × 10 ⁻² RIU 900±100 nm AIM_LRSPP BK7/Teflon bi-layer 150°/RIU None >5° WIM_LRSPP BK7/Teflon bi-layer 12,000 nm/RIU >4 × 10 ⁻² RIU 140±20 nm LSPR Nano-particles 100 nm/RIU 3 × 10 ⁻² RIU 25 nm	Operation mode	Suited/best substrate	Optical responsivity	Linear dynamic range		Optimum film thickness	Remarks
WIM TOPAS/PC /BK7/Quartz/CaF2 $4,000 \pm 1,000 \text{ nm/RIU}$ $<5 \times 10^{-2} \text{ RIU}$ $900 \pm 100 \text{ nm}$ AIM_LRSPP BK7/Teffon bi-layer 150° /RIU None $>5^{\circ}$ WIM_LRSPP BK7/Teffon bi-layer $12,000 \text{ nm/RIU}$ $>4 \times 10^{-2} \text{ RIU}$ $140 \pm 20 \text{ nm}$ LSPR Nano-particles 100 nm/RIU $3 \times 10^{-2} \text{ RIU}$ 25 nm	AIM	TOPAS/PC /PMMA/BK7/Quartz	40–80°/RIU	$<5 \times 10^{-2} \text{ RIU}$	15±2°	35 nm	Single resonance
i-layer 150°/RIU None i-layer 12,000 nm/RIU $>4 \times 10^{-2}$ RIU s 100 nm/RIU 3×10^{-2} RIU	WIM	TOPAS/PC /BK7/Quartz/CaF2	4,000 ± 1,000 nm/RIU	$<5 \times 10^{-2} \mathrm{RIU}$	900±100 nm	35 nm	Single resonance
i-layer 12,000 nm/RIU $>4 \times 10^{-2}$ RIU s 100 nm/RIU 3×10^{-2} RIU	AIMLRSPP	BK7/Teflon bi-layer	150°/RIU	None	>5°		Split resonance
s 100 nm/RIU $3 \times 10^{-2} \text{ RIU}$	WIMLRSPP	BK7/Teflon bi-layer	12,000 nm/RIU		$140 \pm 20 \text{ nm}$		Split resonance
	LSPR	Nano-particles	100 nm/RIU	$3 \times 10^{-2} \text{ RIU}$	25 nm	45 nm particles	45 nm particles Colloidal particles

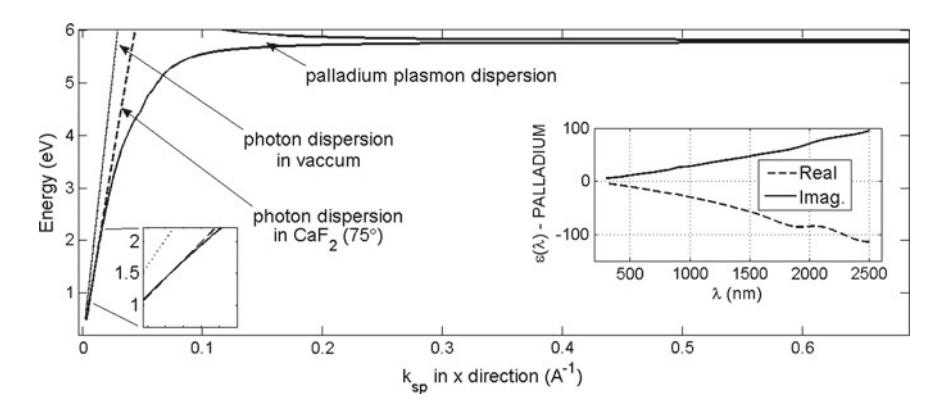


Fig. 8.14 Photon and SPP-dispersion curves of Palladium at the metal-water interface (*solid-line*), calculated for a CaF₂ substrate (*dashed-line*) and incident angle of 75°. The related intersection point and resonance appears near 1.5 eV at low k-values. *Right inset* reveals the real and imaginary fractions of the CDK as function of wavelength

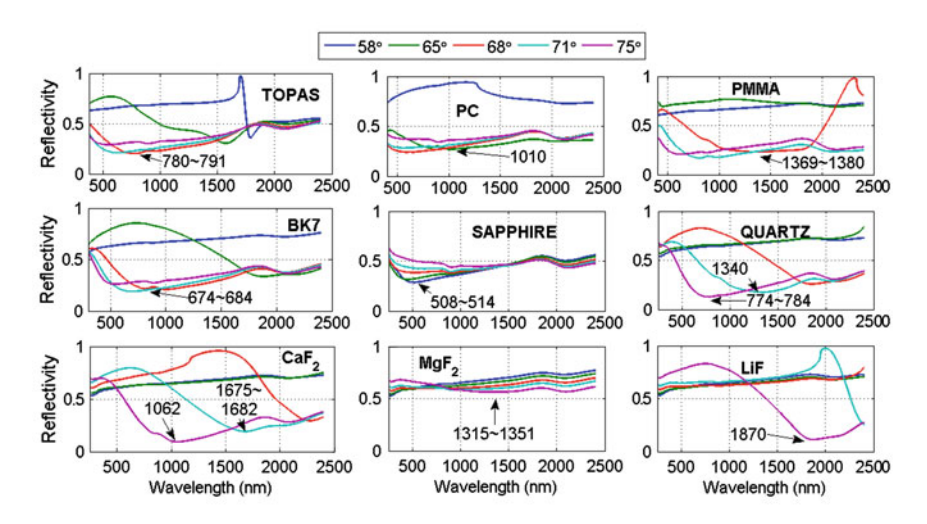


Fig. 8.15 Reflectance curves under WIM-conditions, calculated for different substrate materials, as indicated in the plots. Incident angles are: 58° , 65° , 68° , 71° and 75° for the wavelength range $500 \text{ nm} < \lambda < 2,500 \text{ nm}$. The Pd-film thickness is 25 nm, in contact with water as the liquid dielectric

behaves electrochemically similar to Iridium and Platinum. Pd-films exhibit unusually high diffusion-and bulk absorption coefficients for hydrogen. There are reports on anti-microbial activity of Pd-complexes.

Related spectral features of the reflectance $R(\lambda)$ in the WIM are shown in Fig. 8.15 for the substrate materials under consideration. Similar to Iridium and Osmium, the metal exhibits severely distorted SP-resonances that are mostly shifted into the

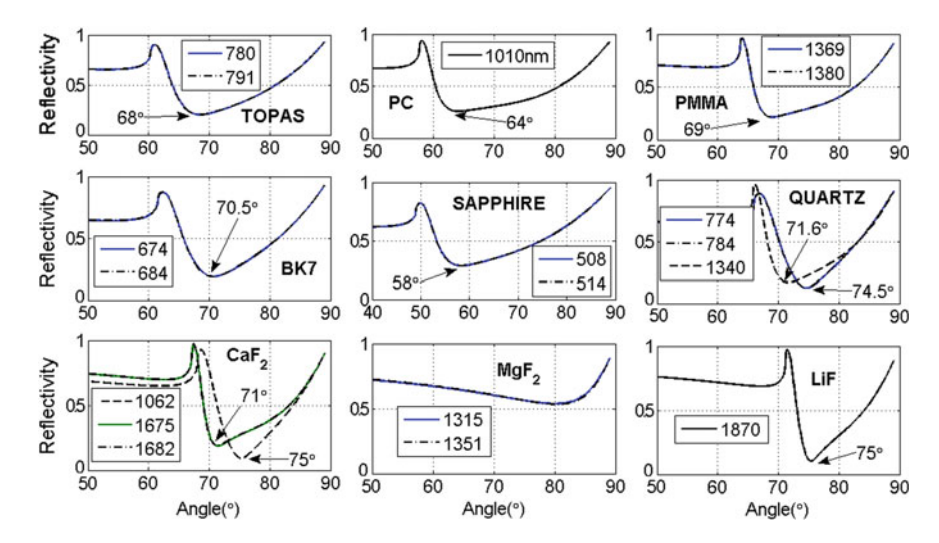


Fig. 8.16 Reflectance curves under AIM-conditions for different substrate materials, as indicated in the plots, and different incident wavelengths for the angle range $40^{\circ} < \theta < 90^{\circ}$. Pd-film thickness is 25 nm, in contact with water

infrared region of the electromagnetic spectrum. In general, Pd-films are poorly suited for SP-sensing applications in the WIM.

The reflectance under AIM conditions is shown in Fig. 8.16, indicating that solely the CaF₂-substrate exhibits some useful SP-sensing properties. The SP-line broadening parameter $\Delta\theta_{res}$ is consistently very high.

A compilation of achievable SPR sensor performance is displayed in Table 8.3.

8.4 Thin Platinum (Pt) Films

The complex optical constant $\varepsilon_{mr}(\lambda) = \varepsilon'_{mr}(\lambda) + j\varepsilon''_{mr}(\lambda)$ of the paramagnetic metal has been taken from Ref. [3] and is illustrated in the right inset of Fig. 8.17. Its atomic electron configuration is [Xe] $4f^{14}5d^96s^{11}$. In the solid material, the outer 6s electron and the incompletely filled 5d-state hybridize, and account for the partially occupied conduction band, as shown in the band structure calculations of Ref. [6]. The relatively low electrical conductivity of $9.5 \times 10^6 \ (\Omega \ m)^{-1}$ and CDK are inconsistent with the free electron model. Within the wavelength range of interest, $\varepsilon'_{mr}(\lambda)$ decreases at $\lambda > 250$ nm steadily to moderate negative values, but exhibits a strong feature around 1,800 nm, which is also resolved in ε''_{mr} . $\varepsilon''_{mr}(\lambda)$ is positive and increases with a maximum at 1,800 nm to rather high values. For the PMMA substrate at 71°, the SP-dispersion is undistorted and exhibits a resonant cross-over at near 1.5 eV. In the asymptotic limit at high k, the SP-energy approaches 4.55 eV at the metal-water interface. Platinum films are best produced by magnetron sputtering from a massive

Table 8.3 SP-sensor performance and figures of merit for thin Pd-films at metal-water interface, CaF3-substrate

	The Later was a read to			ammana 7 ma ia		
Operation mode	Suited/best substrate	Optical responsivity	Linear dynamic range SPR width	SPR width	Optimum film thickness	Remarks
AIM	CaF ₂	80°/RIU	$<5 \times 10^{-2} \mathrm{RIU}$	10 ± 4°	25 nm	Single resonance
WIM	CaF ₂	9, 000 nm/RIU	$< 4 \times 10^{-2} \mathrm{RIU}$	1, $600 \pm 100 \text{RIU}$ 25 nm	25 nm	Single resonance

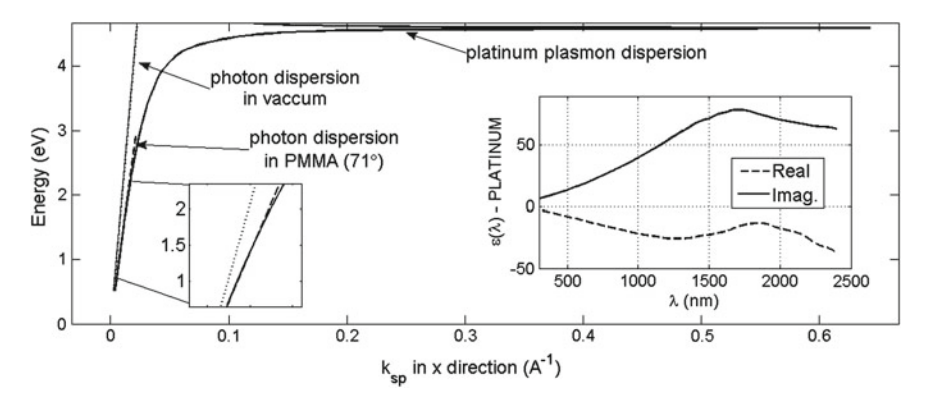


Fig. 8.17 Photon and SPP-dispersion curves of Platinum at the metal-water interface (*solid-line*), calculated for a PMMA substrate (*dashed-line*) and incident angle of 71°. The related intersection point and resonance appears near 1.5 eV at low k-values. *Right inset* reveals the real and imaginary fractions of the CDK as function of wavelength. The quasi-bound SPP-state is visible a $k < 0.3 \, A^{-1}$

metal-target in inert atmosphere, possibly also by electron beam evaporation and electrolytic deposition. Due to the high boiling/evaporation temperature of 3,825 °C, films cannot be made by thermal evaporation from electrically heated Tungsten foils or carbon boats, due to their lower melting temperatures. Native oxides do not form on the metal surface upon exposure to air or aqueous solution. However, stable thin Pt-oxide layers can be made electrochemically at moderate anodic potentials and by reactive magnetron sputtering in oxygen atmosphere. The metal is highly corrosion resistant.

Related spectral features of the reflectance $R(\lambda)$ in the WIM are shown in Fig. 8.18 for the substrate materials under consideration. Similar to the other noble metals, Platinum exhibits severely distorted SP-resonances that are mostly shifted into the infrared region of the electromagnetic spectrum and high angle. A weak SP-splitting effect is resolved for the TOPAS substrate. In general, Pt-films are poorly suited for SP-sensing applications in the WIM.

The reflectance under AIM conditions is shown in Fig. 8.19, indicating that particularly the crystalline substrates as Quartz, CaF₂, MgF₂ and LiF-substrate exhibit high resonance angles, which are difficult to realize technically. The SP-line broadening parameters $\Delta\lambda_{res}$ and $\Delta\theta_{res}$ is consistently very high for all substrate materials.

For the TOPAS substrate, the SP-energy (eV) of thin Pt-films varies non-linearly with the resonance angle within the range $55^{\circ} < \theta < 75^{\circ}$ approximately as: $E_{SP}(\theta) = 0.0053\theta^2 + 0.6508\theta - 20.36$.

Figure 8.20 illustrates the spectral characteristic of the resonance under WIM conditions, calculated for a set of RIU values of the aqueous dielectric analyte. The depths/contrast of the resonance is low, but remains constant towards higher n_{an} -values, whilst the resonance minimum shifts towards longer wavelengths. For the PMMA substrate, an unsteady displacement of the resonance wavelength $\lambda_{res}(n_{an})$ with the refractive index of the liquid dielectric within the range $1.33 < n_{an} < 1.39$

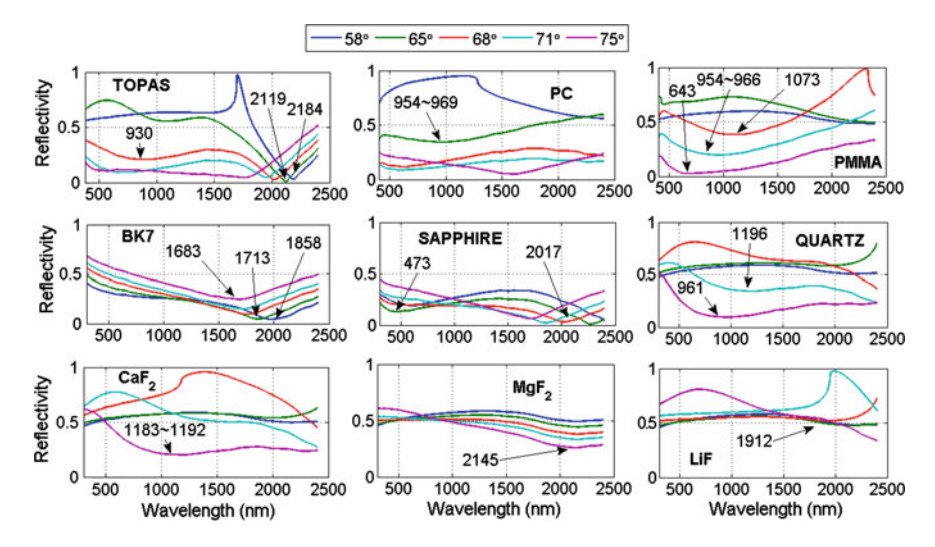


Fig. 8.18 Reflectance curves under WIM-conditions, calculated for different substrate materials, as indicated in the plots. Incident angles are: 58° , 65° , 68° , 71° and 75° for the wavelength range $500 \text{ nm} < \lambda < 2,500 \text{ nm}$. The Pt-film thickness is 20 nm, in contact with water as the liquid dielectric

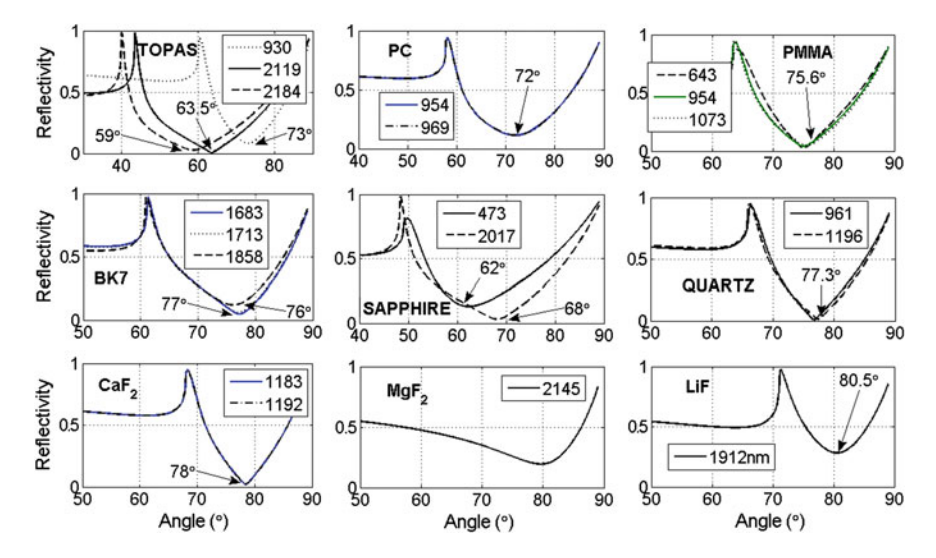


Fig. 8.19 Reflectance curves under AIM-conditions for different substrate materials, as indicated in the plots, and different incident wavelengths for the angle range $50^{\circ} < \lambda < 90^{\circ}$. Pt-film thickness is 20 nm. in contact with water

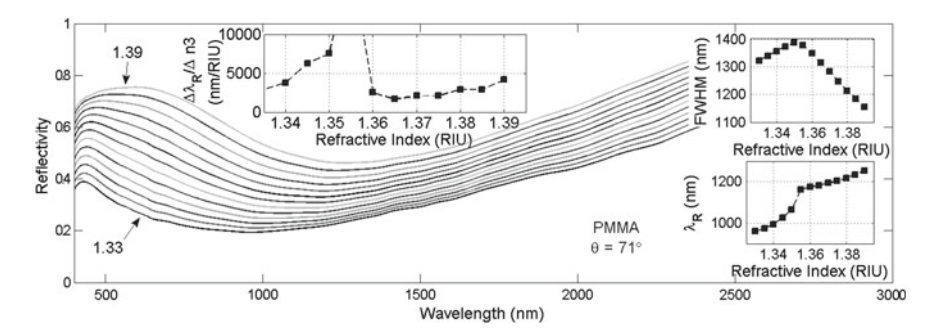


Fig. 8.20 WIM-sensing properties and spectral reflectance $R(\lambda)$ of Pt, initial wavelength λ_{res} near 900 nm, calculated for a set of different RIU-values: $1.33 < n_{an} < 1.39$. Substrate is PMMA, incident angle is 71°. Upper left and right insets show the SP-responsivity $R_{WIM}(n_{an})$ and line broadening $\Delta\lambda_{res}(n_{an})$. Lower right inset depicts resonance displacements $\lambda_{res}(n_{an})$

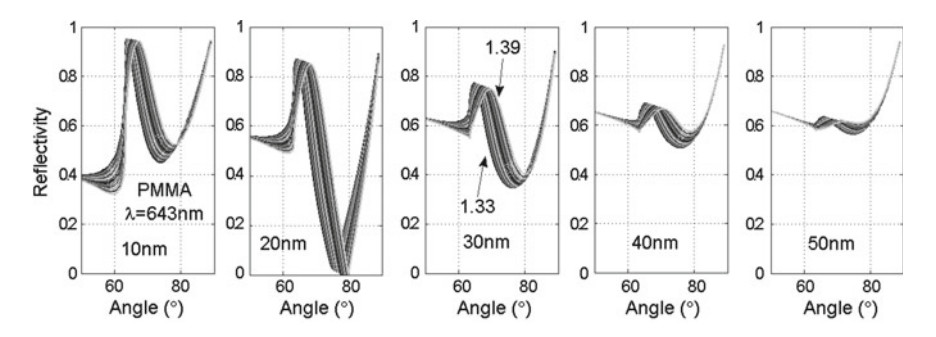


Fig. 8.21 AIM-reflectance at the SP-resonance for different Pt-film thickness values of 10, 30, 20, 40 and 50 nm

is revealed in the lower right inset. The WIM-responsivity $R_{WIM}(n_{an})$ appears fairly high, as depicted in the upper left inset, comprising a peak with magnitude >9,000 nm/RIU, but exhibits a distinct discontinuity at low values of n_{an} . The broadening parameter $\Delta \lambda_{res}(n_{an})$, as taken at FWHM, is also very high, with 1,400 nm at $n_{an} = 1.35$ and decreases with n_{an} .

The influence of film thickness for AIM conditions is outlined in Figs. 8.21. This data set clearly indicates that the Pt-film thickness for optimum SPR sensor operation is placed at around 20 nm.

8.4.1 Properties of Localized Plasmons in Pt-Colloidal Particles

The optical absorption characteristic of colloidal Pt-particles with 45 nm diameter, immersed into an aqueous solution with varying refractive index n_{an} as function of

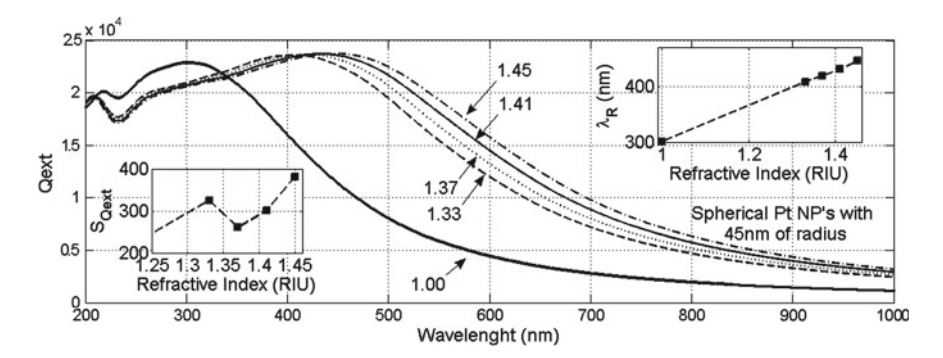


Fig. 8.22 Optical absorbance for Pt-particles with 45 nm diameter, calculated as function of wavelength for different refractive index (RIU) values of the surrounding aqueous solution. *Right upper inset* shows resonance position $\lambda_R(n_{an})$ and optical responsivity $S_{Q_{ext}}(n_{an})$ at *lower left*, taken at the first spectral maximum near 300 nm

wavelength, is depicted in Fig. 8.22. Upper right and left insets, respectively, reveal spectral resonance position $\lambda_{res}(n_{an})$ and responsivity $S_{Qext}(n_{an})$. This quantity is considerably smaller than calculated before for both, short and long range SPP's.

A compilation of achievable SPR sensor performance is displayed in Table 8.4.

8.5 Thin Rhodium (Rh) Films

The complex optical constant $\varepsilon_{mr}(\lambda) = \varepsilon'_{mr}(\lambda) + j\varepsilon''_{mr}(\lambda)$ of paramagnetic metal has been taken from Ref. [3] and is illustrated in the right inset of Fig. 8.23. The electron configuration of the isolated atom is $[Kr]4d^85s^1$. In the solid state, the outer 5s electron state hybridizes with the 4d-shell and forms the partially occupied conduction band (Ref. [7]). The metal exhibits moderate high electrical conductivity $23.1 \times 10^6 \, (\Omega \text{ m})^{-1}$, the CDK is not appropriately described by the free electron model. Within the wavelength range of interest, $\varepsilon'_{mr}(\lambda)$ decreases at $\lambda > 200$ nm steadily to large negative values. $\varepsilon''_{mr}(\lambda)$ is positive and increases steadily to high numbers. For the CaF2 substrate at 71°, the SP-dispersion is weakly distorted and exhibits a resonant cross-over at around 0.8 eV. In the asymptotic limit at high k, the SP-energy approaches 6.3 eV at the metal-water interface. Rhodium films are best produced by magnetron sputtering from a massive metal-target in inert atmosphere, electro-plating or by electron beam evaporation in high vacuum. Due to the high boiling/evaporation temperature of 3,685 °C, Rhodium-films cannot be made by thermal evaporation from electrically heated Tungsten foils or carbon boats. Native oxides do not form on the metal surface upon exposure to air or aqueous solution at neutral pH. However, stable thin oxide layers can be made electrochemically at moderate anodic potentials in acidic solution. The metal is highly corrosion resistant. There is no biological activity or impact reported for the pure metal.

Table 8.4 SI	2-sensor performance and figures of merit for thin Pt-films and nano-particles at the metal-water interface, PMMA substrate	thin Pt-films and nano-par	ticles at the metal-v	water interface	, PMMA substrate	
Operation Suited/b mode	Suited/best substrate	Optical responsivity Linear dynamic SPR width Optimum film Remarks range thickness (nm)	Linear dynamic range	SPR width	Optimum film thickness (nm)	Remarks
AIM	TOPA S/PC/PMMA/sapphire	50-80°/RIU	$<5 \times 10^{-2} \text{ RIU} 13 \pm 2^{\circ}$	13±2°	25 nm	Single resonance
WIM	TOPAS/PC/PMMA/BK7/Quartz/sapphire $4,000\pm1,000\mathrm{nm/RIU}$ $<1\times10^{-2}\mathrm{RIU}$ $38\pm2\mathrm{nm}$ $25\pm3\mathrm{nm}$	$4,000 \pm 1,000 \text{ nm/RIU}$	$<1 \times 10^{-2} \text{ RIU}$	38±2 nm	25 ± 3 nm	Single resonance
LSPR	Nano-particles	300 nm/RIU	$5 \times 10^{-2} \text{RIU}$ 100 nm	100 nm		Colloidal
						particis

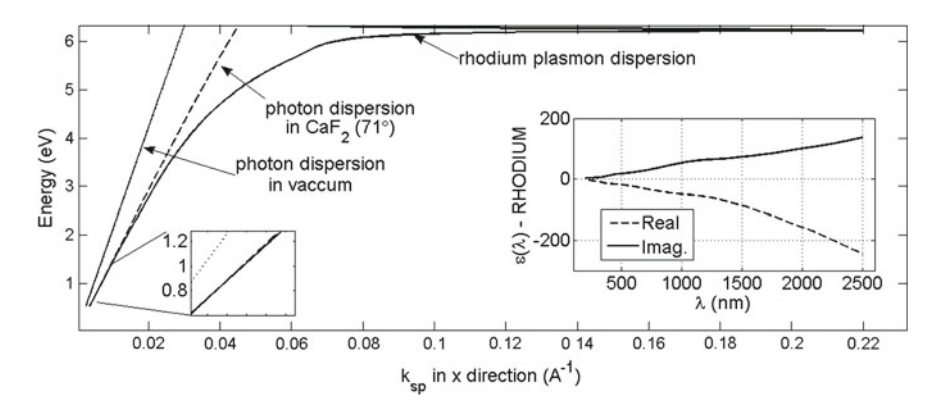


Fig. 8.23 Photon and SPP-dispersion curves of Rhodium at the metal-water interface (*solid-line*), calculated for a CaF₂ substrate (*dashed-line*) and incident angle of 71°. The related intersection point and resonance appears near 0.8 eV at low k-values. *Right inset* reveals the real and imaginary fractions of the CDK as function of wavelength

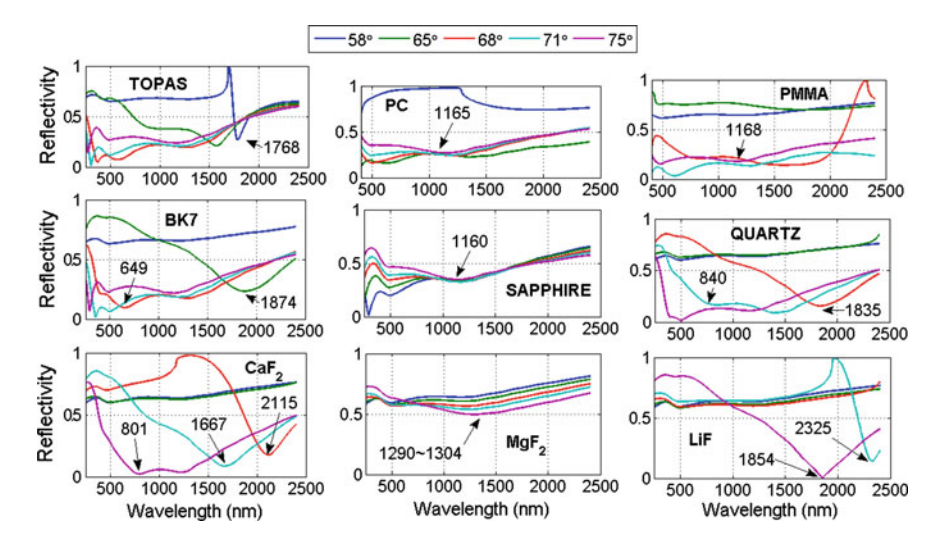


Fig. 8.24 Reflectance curves under WIM-conditions, calculated for different substrate materials, as indicated in the plots. Incident angles are: 58° , 65° , 68° , 71° and 75° for the wavelength range $500 \text{ nm} < \lambda < 2,500 \text{ nm}$. The Rh-film thickness is 15 nm, in contact with water as the liquid dielectric

Related spectral features of the reflectance $R(\lambda)$ in the WIM are shown in Fig. 8.24 for the substrate materials under consideration. Similar to the other noble metals, the metal exhibits severely distorted SP-resonances that are mostly shifted into the infrared region of the electromagnetic spectrum. An SP-splitting effect is resolved for BK7 and TOPAS substrates. Due to the broad S-resonance, Rh-films appear poorly suited for SP-sensing applications in the WIM.

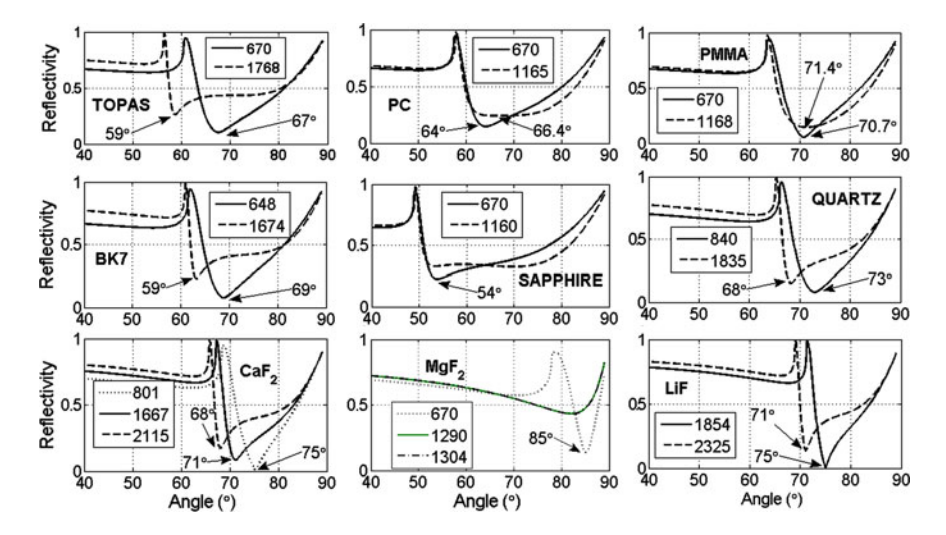


Fig. 8.25 Reflectance curves under AIM-conditions for different substrate materials, as indicated in the plots, and different incident wavelengths for the angle range $40^{\circ} < \theta < 90^{\circ}$. Rh-film thickness is 15 nm, in contact with water

The reflectance under AIM conditions is shown in Fig. 8.25, indicating that all substrates, except MgF₂ exhibit suited resonance angles. The SP-line broadening parameters $\Delta \lambda_{res}$ and $\Delta \theta_{res}$ is high for all substrate materials.

For the CaF₂-substrate, the SP-energy (eV) of thin Rh-films varies non-linearly with the resonance angle within the range $65^{\circ} < \theta < 75^{\circ}$ approximately as: $E_{SP}(\theta) = 0.0204\theta^2 - 2.772\theta - 94.909$.

The SPR-sensing characteristic in the AIM is shown in Fig. 8.26 at a wavelength of 1667 nm, comprising initial resonance angle of 70°. The resonance angle θ_{res} increases linearly with n_{an} . The maximum achievable responsivity R_{AIM} is approximately $100^{\circ}/RIU$ and decreases for longer wavelength. The line broadening parameter $\Delta\theta_{res}(n_{an})$ decreases towards higher values of n_{an} .

Eventually, the influence of film thickness for WIM and AIM conditions is outlined in Figs. 8.27 and 8.28. This data set clearly indicates that the Rh-film thickness for optimum SPR sensor operation is placed at around 15 nm.

A compilation of achievable SPR sensor performance is displayed in Table 8.5.

8.6 Thin Ruthenium (Ru) Films

The complex optical constant $\varepsilon_{mr}(\lambda) = \varepsilon'_{mr}(\lambda) + j\varepsilon''_{mr}(\lambda)$ of the metal has been taken from Ref. [8] and is illustrated in the right inset of Fig. 8.29. The atomic electron configuration is $[Kr]4d^75s^1$. In the solid state, the outer 5s electron hybridizes with the only partly filled 4d-shell, and forms the energetically broadened, partially

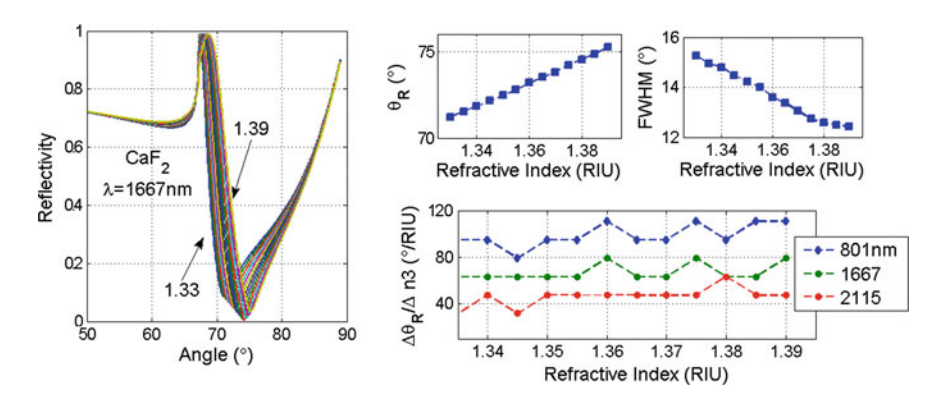


Fig. 8.26 AIM-sensing properties and angular reflectance $R(\theta)$, calculated for a set of different RIU-values, at range 1.33 < n_{an} < 1.39. Substrate is CaF₂ and the incident wavelength 1667 nm. Left and right upper sub-figures depict resonance displacements $\theta_{res}(n_{an})$ and line broadening $\Delta\theta_{res}(n_{an})$. SP-responsivity $R_{AIM}(n_{an})$ shown below for three different wavelength

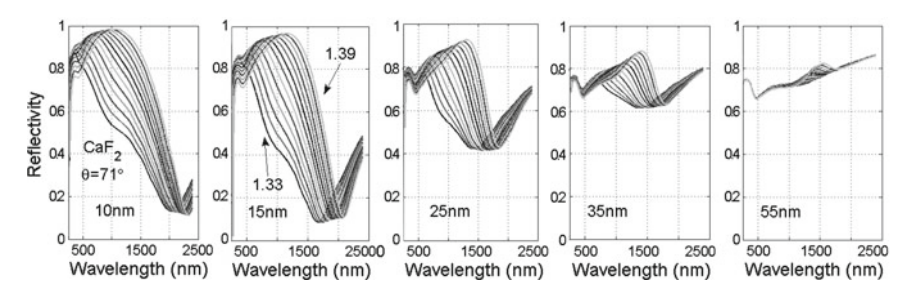


Fig. 8.27 WIM-reflectance at the SP-resonance for different Rh-film thickness values of 10, 15, 25, 35 and 55 nm

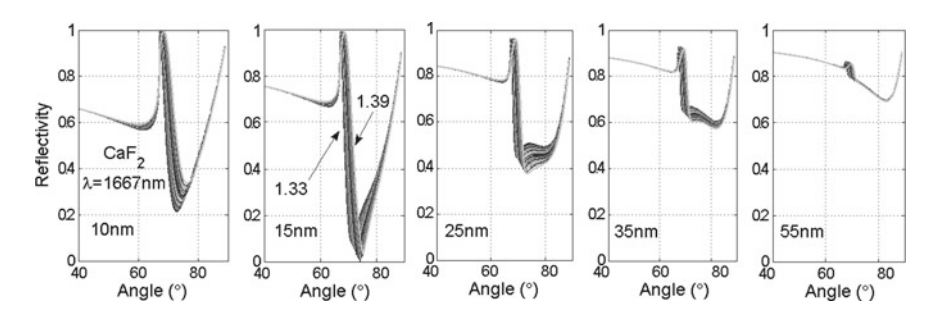


Fig. 8.28 AIM-reflectance at the SP-resonance for different Rh-film thickness values of 10, 15, 25, 35 and 55 nm

 Table 8.5
 SP-sensor performance and figures of merit for thin Rh-films at metal-water interface; CaF2-substrate

Table On Street	THEORY OF SCHOOL POLICITIES WITH THE WITH THE WITH WHICH WENT THEORY WENT THEORY OF Z SHOOTHING	tes of metricion dimitali	mins at metal water	meriace, car 2 3	acstrace	
Operation mode	Suited/best substrate	Optical responsivity Linear dynamic range		SPR width	Optimum film thickness	Remarks
AIM	CaF ₂	100°/RIU	$<5 \times 10^{-2} \text{ RIU}$ $14 \pm 2^{\circ}$		15 nm	
WIM	CaF ₂	8,000 nm/RIU	$<5 \times 10^{-2} \text{ RIU}$ $900 \pm 200 \text{ nm}$ 15 nm	$900 \pm 200 \text{ nm}$	15 nm	Weak SP-split for BK7, TOPAS

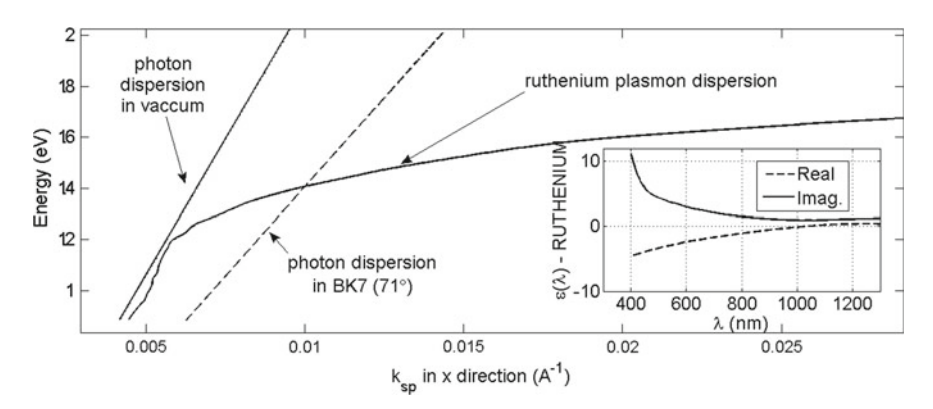


Fig. 8.29 Photon and SPP-dispersion curves of Ruthenium at the metal-water interface (*solid-line*), calculated for a BK7 substrate (*dashed-line*) and incident angle of 71°. The related intersection point and resonance appears near 1.4 eV at low k-values. *Right inset* reveals the real and imaginary fractions of the CDK as function of wavelength

occupied conduction band, as calculated in Ref. [9]. The weakly paramagnetic metal exhibits low electrical conductivity of $14 \times 10^6~(\Omega~\text{m})^{-1}$. The spectral characteristic of the CDK is unusual and not in agreement with the DA. Within the wavelength range of interest, and unlike the other metals depicted before, $\varepsilon'_{mr}(\lambda)$ increases at $\lambda > 400$ nm steadily to smaller negative values. $\varepsilon''_{mr}(\lambda)$ is positive and decreases steadily to smaller values. For the BK7 substrate at 71°, the SP-dispersion is heavily distorted and exhibits a resonant cross-over at around 1.4 eV. In the asymptotic limit at high k, the SP-energy approaches 1.7 eV at the metal-water interface. Ruthenium films are best produced by magnetron sputtering from a massive metal-target in inert atmosphere, and by electro-plating. Due to the high boiling/evaporation temperature of 4150.6°C, films cannot be made by thermal evaporation from electrically heated Tungsten foils or carbon boats, due to their lower melting temperatures or by electron beam evaporation. Native oxides do not form on the metal surface upon exposure to air or aqueous solution. Stable, electrically conducting thin oxide layers can be made electrochemically at moderate anodic potentials.

Related spectral features of the reflectance $R(\lambda)$ in the WIM are shown in Fig. 8.30 for the substrate materials under consideration. In contrast to other noble metals of the Platinum group, Ru-films exhibit fairly undistorted SP-resonances that are placed at or slightly below 1,000 nm in the near infrared region of the electromagnetic spectrum, where CMOS image sensors can be used. An SP-splitting effect is resolved for Sapphire and PC substrates at moderate angle. Ru-films apparently are suited for SP-sensing applications in the WIM.

The reflectance under AIM conditions is shown in Fig. 8.31, indicating that all substrates, except MgF₂ and LiF exhibit suited resonance angles. The SP-line broadening parameter $\Delta \lambda_{res}$ is moderate for all SP-active substrate materials. For a BK

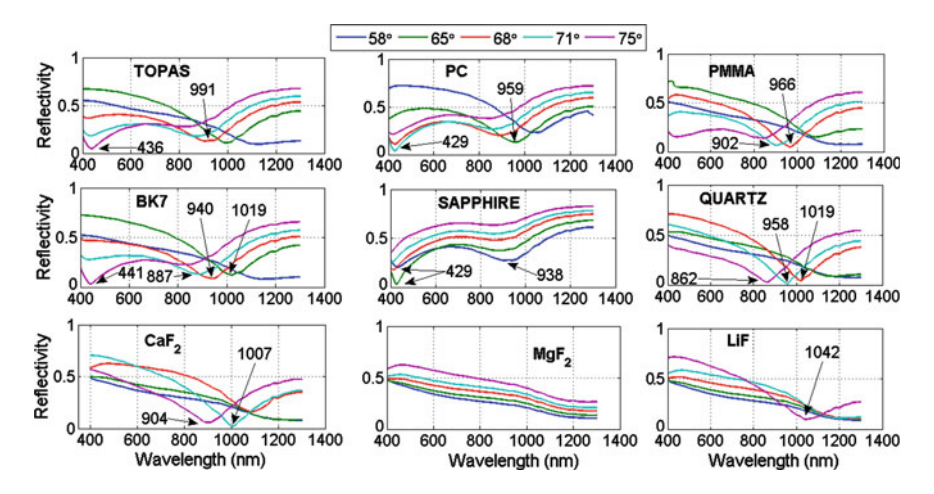


Fig. 8.30 Reflectance curves under WIM-conditions, calculated for different substrate materials, as indicated in the plots. Incident angles are: 58° , 65° , 68° , 71° and 75° for the wavelength range $400 \text{ nm} < \lambda < 1,400 \text{ nm}$. The Ru-film thickness is 20 nm, in contact with water as the liquid dielectric

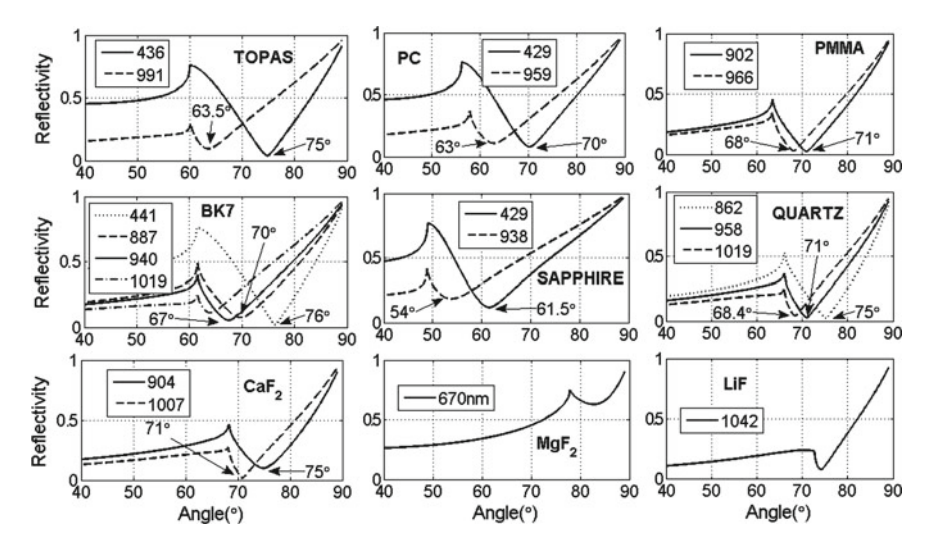


Fig. 8.31 Reflectance curves under AIM-conditions for different substrate materials, as indicated in the plots, and different incident wavelengths for the angle range $40^{\circ} < \theta < 90^{\circ}$. Ru-film thickness is 20 nm, in contact with water

7-substrate, the SP-energy (eV) of thin Ru-films varies weakly non-linear with the resonance angle within the range $62^{\circ} < \theta < 70^{\circ}$ approximately as: $E_{SP}(\theta) = 0.0016\theta^2 - 0.187\theta + 6.5088$.

A compilation of achievable SPR sensor performance is displayed in Table 8.6.

Table 8.6 SP-sensor performance and figures of merit for thin Ru-films at metal-water interface; BK7-substrate

ode	Suited/best Substrate	Optical Responsivity	Linear dynamic range	SPR width	Optimum film thickness	Remarks
TOPAS	OPAS/BK //Quartz	80°/RIU	$< 5 \times 10^{-2}$ KIU	$14 \pm 2^{\circ}$	70 nm	
TOPAS	'OPAS/BK7/Quartz	1,500 nm/RIU	None	320±30 nm	20 nm	SP-split for Sapphire

References 95

References

- 1. SOPRA SA Optical Data. http://www.sspectra.com/sopra.html
- 2. Noffke, J., Fritsche, L.: Band structure calculation and photoemission analysis of iridium. J. Phys. F: Met. Phys. 12, 921–933 (1982)
- 3. Palik, E.D.: Handbook of Optical Constants of Solids. Academic Press, Boston (1985)
- 4. Ramchandani, M.G.: Electronic energy band structure of osmium metal. Phys. Status Solidi (b) 100, 155–158 (1980)
- 5. Mueller, F.M., Freeman, A.J., Dimmock, J.O., Furdyna, A.M.: Electronic structure of palladium. Phys. Rev. B 1, 4617–4635 (1970)
- 6. Fradin, F.Y., Koelling, D.D., Freeman, A.J., Watson-Yang, T.J.: Calculation of the electronic structure and related physical properties of platinum. Phys. Rev. B 12, 5570–5574 (1975)
- 7. Borstel, G., Braun, W., Neumann, M., Seitz, G.: Band structure of rhodium and photoemission from its low index surfaces. Phys. Status Solidi B **95**, 453–460 (1979)
- 8. Kress, K.A., Lapevre, G.J.: Optical properties of molybdenum and ruthenium. J. Opti. Soc. Am **60**(12), 1681–1684 (1970)
- Pelzer, T., Ceballos, G., Zbikowski, F., Willerding, B., Wandelt, K., Thomann, U., Reuß, Ch., Fauster, Th, Braun, J.: Electronic structure of the ru (0001) surface. J. Phys.: Condens. Matter 12, 2193–2207 (2000)

Chapter 9 Common Transition Metals

9.1 Thin Chromium (Cr) Films

The complex optical constant $\varepsilon_{mr}(\lambda) = \varepsilon'_{mr}(\lambda) + j\varepsilon''_{mr}(\lambda)$ of the metal has been taken from Ref. [1] and is illustrated in the right inset of Fig. 9.1. The atomic electron configuration is $[Ar]3d^54s^1$. In the solid state, the outer 4s electron state hybridizes with the partly filled 3d-shell, and forms the partially occupied conduction band. Related band structure calculations for the paramagnetic state are reported in Ref. [2]. The metal is anti-ferromagnetic at T < 312 K, exhibits a rather low electrical dc-conductivity of $8 \times 10^6 (\Omega \text{ m})^{-1}$ at ambient T and is not appropriately described by the DA. Within the wavelength range of interest, and unlike most of other metals depicted before, $\varepsilon'_{mr}(\lambda)$ becomes negative >200 nm, remains at quite small negative values over a broad range of wavelength, exhibits a swing near 600 nm and turns back positive at $\lambda > 1,100$ nm. $\varepsilon''_{mr}(\lambda)$ is positive, with a maximum at 600 nm, and increases further towards longer wavelength. For the BK7 substrate at 67°, the SP-dispersion appears undistorted and exhibits a resonant cross-over around 3.3 eV. Otherwise, photon-and SPP dispersions appear to coincide over a rather broad range of k-values. In the asymptotic limit at high k, the SP-energy approaches a high value of 7.7 eV at the metal-water interface. Due to the low boiling point of 2,670 °C, Chromium films can be readily produced by magnetron sputtering from a massive metal target in inert atmosphere, by electron beam and thermal evaporation, by electro-plating and chemical vapor deposition methods. A stable, few nm thin native oxide layer forms on the metal surface, immediately upon exposure to air or aqueous solution. Dense, oxide layers also can be made electrochemically at moderate anodic potentials.

Related spectral features of the reflectance $R(\lambda)$ in the WIM are shown in Fig. 9.2 for the substrate materials under consideration. Cr-films exhibit poorly resolved, broadened SP-resonances at around 800 nm that are placed at high angle and thus are not well suited for SP-sensing applications in the WIM. SP-resonances do not appear for MgF₂ and LiF-substrates.

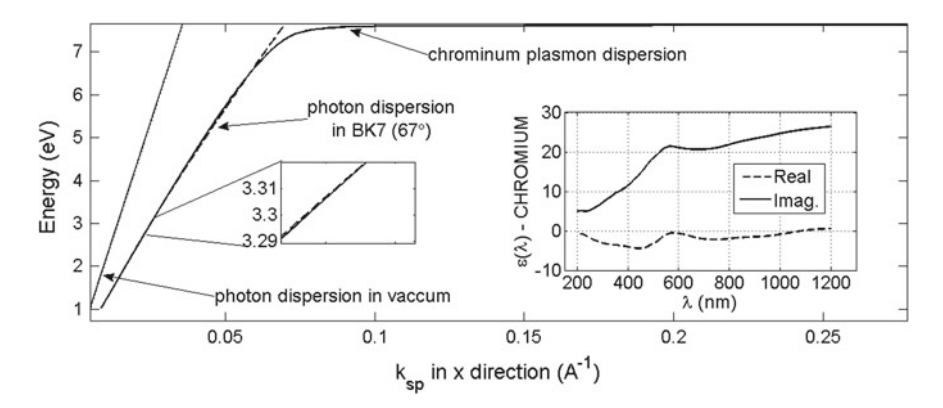


Fig. 9.1 Photon and SPP-dispersion curves of Chromium at the metal-water interface (*solid-line*), calculated for a BK7 substrate (*dashed-line*) and incident angle of 67°. The related intersection point and resonance appears in the UV-region near 6.7 eV at moderate k-values. *Right* inset reveals the real and imaginary fractions of the CDK as function of wavelength

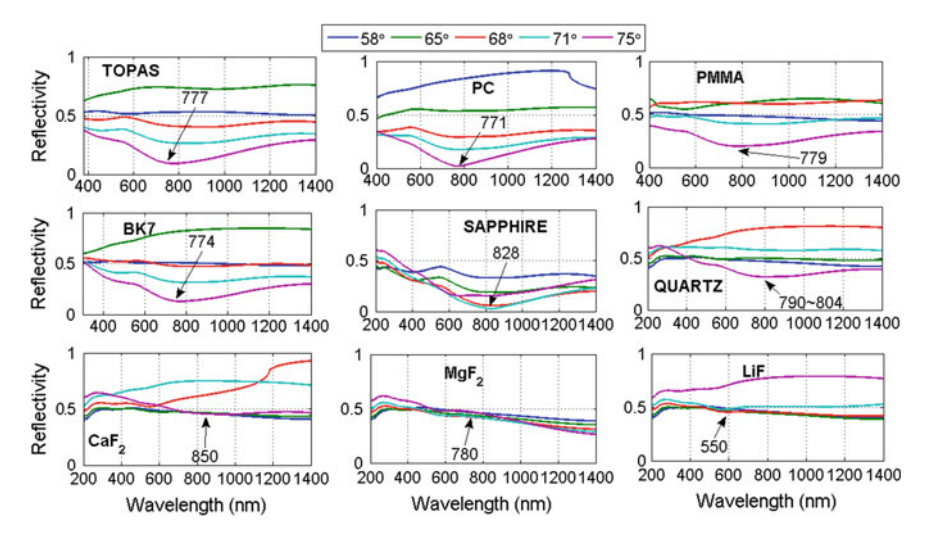


Fig. 9.2 Reflectance curves under WIM-conditions, calculated for different substrate materials, as indicated in the *plots*. Incident angles are: 58° , 65° , 68° , 71° and 75° for the wavelength range $400 \text{ nm} < \lambda < 1,400 \text{ nm}$. The Cr-film thickness is 25 nm, in contact with water as the liquid dielectric

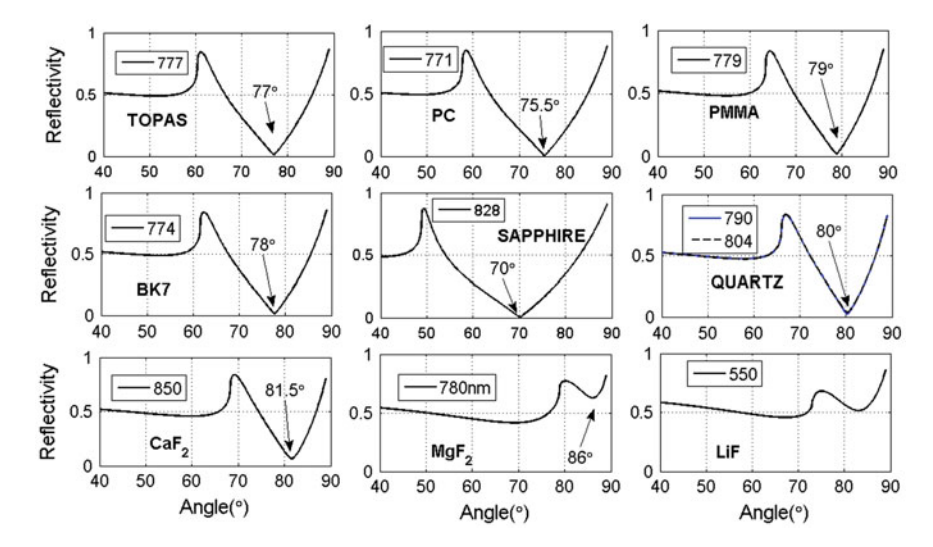


Fig. 9.3 Reflectance curves under AIM-conditions for different substrate materials, as indicated in the *plots*, and different incident wavelengths for the angle range $40^{\circ} < \theta < 90^{\circ}$. Cr-film thickness is 25 nm, in contact with water

Reflectance under AIM conditions is shown in Fig. 9.3, and confirms the consistently high resonance angles.

A compilation of achievable SPR sensor performance is displayed in Table 9.1.

9.2 Thin Cobalt (Co) Films

The complex optical constant $\varepsilon_{mr}(\lambda) = \varepsilon'_{mr}(\lambda) + j\varepsilon''_{mr}(\lambda)$ of the metal metal has been taken from Ref. [3] and is illustrated in the right inset of Fig. 9.4. The atomic electron configuration is $[Ar]3d^74s^2$. In the solid state, the two 4s electrons hybridize with the incompletely filled 3d-shell, and form a partially occupied, energetically broadened conduction band, as reported in Ref. [4]. The metal is ferromagnetic, exhibits moderate electrical dc-conductivity of $16 \times 10^6 (\Omega \, \text{m})^{-1}$ at ambient T, and is not appropriately described by the free electron model. Within the wavelength range of interest similar to Chromium, $\varepsilon'_{mr}(\lambda)$ increases initially to negative values, exhibits a shallow minimum, but little further variation. $\varepsilon''_{mr}(\lambda)$ is positive and increases steadily to high values towards longer wavelength. For the Quartz substrate at 67°, the SP-dispersion appears undistorted and exhibits also a resonant cross-over in the UV region at around 6.5 eV. There are no clear intersections resolved, since photonand SPP dispersions coincide over a very broad range of k-values. In the asymptotic limit at high k, the SP-energy approaches 7.8 eV at the metal-water interface. Due to the boiling temperature of 2,927 °C, thin Cobalt-films can be produced by magnetron

Table 9.1 SP-sensor performance and figures of merit for thin Cr-films at metal-water interface: BK7-substrate

Table 7.1 St. School	sor perrormance and nge	ites of intention time en-	annance and ingares of mention and extension are metal-water interface, Dry-substance	acc, Dix/-suosuat)	
Operation mode	Suited/best substrate	Optical responsivity	Linear dynamic range S	SPR width	Optimum film thickness	Remarks
AIM	Sapphire	50°/RIU	$< 5 \times 10^{-2} \text{ RIU}$	$14 \pm 2^{\circ}$	25 nm	Poor SP-sensing
WIM	Sapphire	500 nm/RIU	$<3 \times 10^{-2} \text{ RIU}$	900 ± 100 nm 25 nm	25 nm	Not suited

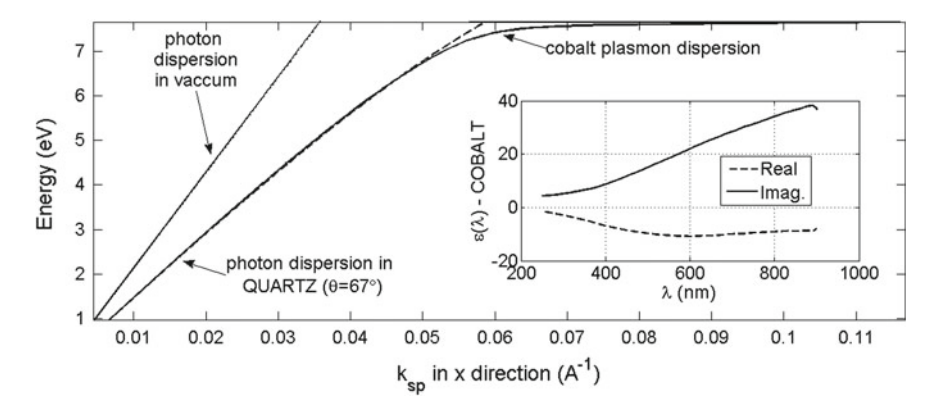


Fig. 9.4 Photon and SPP-dispersion curves of Cobalt at the metal-water interface (*solid-line*), calculated for a Quartz substrate (*dashed-line*) and incident angle of 67°. Photon-and SPP dispersions match of broad range of wave-vectors. *Right inset* reveals the real and imaginary fractions of the CDK as function of wavelength

sputtering from a massive metal target in inert Ar-atmosphere, by electron beam and thermal evaporation at high vacuum, as well as electro-plating. A thin dense oxide layer forms on the metal surface, immediately upon exposure to air. Most likely the hydroxidic form persists in aqueous solution. Passivating surface layers also can be produced electrochemically at moderate anodic potentials.

Related spectral features of the reflectance $R(\lambda)$ in the WIM are shown in Fig. 9.5 for the substrate materials under consideration. Co-films exhibit poorly resolved,

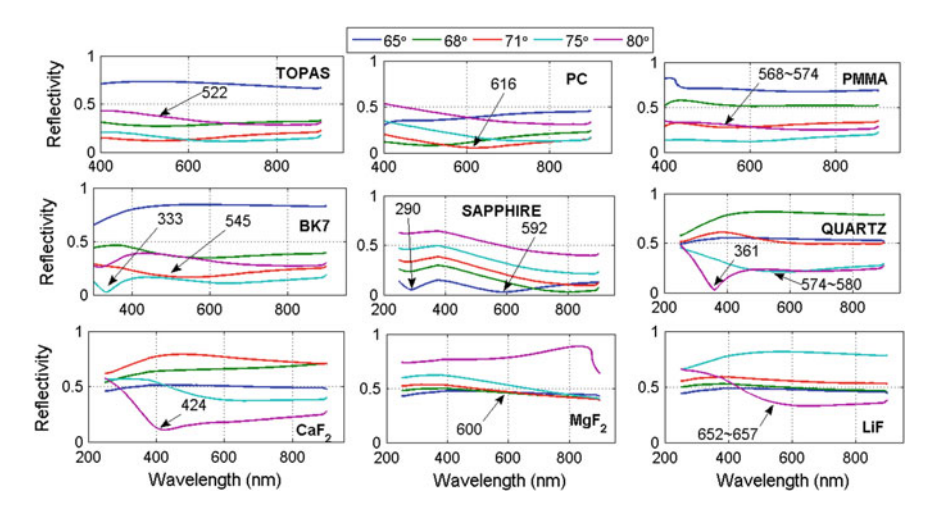


Fig. 9.5 Reflectance curves under WIM-conditions, calculated for different substrate materials, as indicated in the *plots*. Incident angles are: 58° , 65° , 68° , 71° and 75° for the wavelength range $200 \text{ nm} < \lambda < 1,000 \text{ nm}$. The Co-film thickness is 15 nm, in contact with water as the liquid dielectric

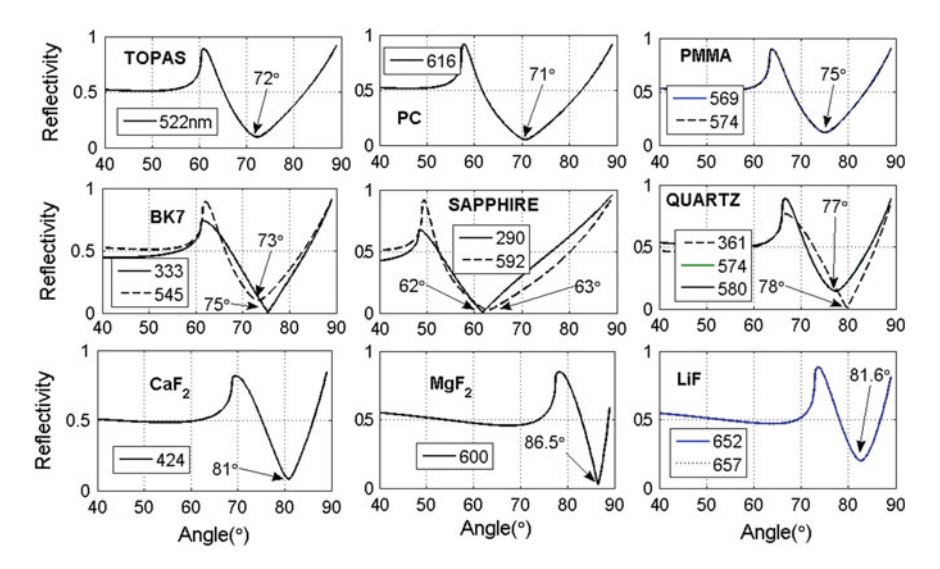


Fig. 9.6 Reflectance curves under AIM-conditions for different substrate materials, as indicated in the *plots*, and different incident wavelengths for the angle range $40^{\circ} < \theta < 90^{\circ}$. Co-film thickness is 15 nm. in contact with water

broadened SP-resonances at around 600 nm, mostly placed at high angle. Co-films thus are not well suited for SP-sensing applications in the WIM. SP-resonances do not appear for CaF₂, MgF₂ and LiF-substrates at useful angles. Resonance splitting is resolved for Sapphire.

Reflectance under AIM conditions is shown in Fig. 9.6, and confirms the high resonance angles, except for Sapphire substrates.

A compilation of achievable SPR sensor performance is displayed in Table 9.2.

9.3 Thin Iron (Fe) Films

The complex optical constant $\varepsilon_{mr}(\lambda) = \varepsilon'_{mr}(\lambda) + j\varepsilon''_{mr}(\lambda)$ of the metal has been taken from Ref. [10] and is illustrated in the right inset of Fig. 9.7. The atomic electron configuration of Fe is $[Ar]3d^64s^2$. In the solid state, two 4s electrons hybridize with the incompletely filled 3d-shell, and form the partially occupied, energetically broadened conduction band. A band-structure calculation of ferromagnetic Iron is revealed in Ref. [6]. Iron is also ferromagnetic and exhibits a low electrical dc-conductivity of $10.4 \times 10^6 (\Omega \text{ m})^{-1}$ at ambient T. The high value of the magnetic permeability μ suggests a pronounced magneto-optical effect in presence of a magnetic field. Within the wavelength range of interest at $\lambda > 350$ nm, $\varepsilon'_{mr}(\lambda)$ decreases steadily to moderate negative values. $\varepsilon''_{mr}(\lambda)$ is positive and remains constant at $\lambda < 700$ nm, comprising relatively small values. This suggests that the metal follows a modified

Table 9.2 SP-sensor performance and figures of merit for thin Co-films at metal-water interface; Quartz substrate

Operation mode	Suited/best substrate	Optical responsivity	Linear dynamic range SPR width	SPR width	Optimum film thickness R	Remarks
AIM	Sapphire/BK7/Quartz	/Quartz 10 ± 10°/RIU	$< 4 \times 10^{-2} \text{ RIU}$	$25 \pm 2^{\circ}$	15 nm	Single resonance
WIM	Sapphire BK7/Quartz	7/Quartz 3,900 \pm 1,000 nm/RIU $<4 \times 10^{-2}$ RIU		$1,000 \pm 300 \mathrm{nm}$ 15 nm	15 nm	Single resonance

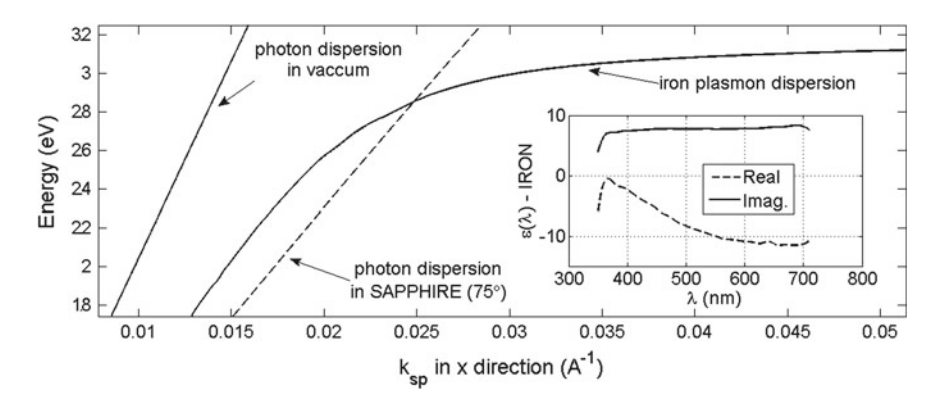


Fig. 9.7 Photon and SPP-dispersion curves of Iron at the metal-water interface (*solid-line*), calculated for a Sapphire substrate (*dashed-line*) and incident angle of 75°. Photon-and SPP dispersions and group velocities match for a broad range of wave-vectors. *Right inset* reveals the real and imaginary fractions of the CDK as function of wavelength

DA. For the Sapphire substrate at 75°, the SP-dispersion appears undistorted, and reveals a non-diffuse cross-over at around 2.8 eV. In the asymptotic limit at high k, the SP-energy approaches 3.21 eV at the metal-water interface. Iron films can be produced by magnetron sputtering from a massive metal target in inert atmosphere, by electron beam and thermal evaporation in high vacuum. Upon contact with aqueous solution, a porous hydroxide layer forms on the metal surface. Iron exhibits poor corrosion resistance, due to absence of a passivating surface oxide layer.

Related spectral features of the reflectance $R(\lambda)$ in the WIM are shown in Fig. 9.8 for the substrate materials under consideration. Like most other transition metals, Fefilms exhibit poorly resolved, broadened SP-resonances, centered at around 600 nm at moderate angle. TOPAS and BK7 appear suited for SP-sensing applications in the WIM. SP-resonances are not resolved for CaF₂, MgF₂ and LiF-substrates.

Reflectance under AIM conditions is depicted in Fig. 9.9, and confirms the moderate resonance angles, except for Quartz substrates.

Figure 9.10 illustrates the spectral characteristic of the resonance under WIM conditions, calculated for a set of RIU values of the aqueous dielectric analyte. The depths/contrast of the resonance is low, and decreases further towards higher n_{an} -values, whilst the resonance minimum shifts towards longer wavelengths. For the TOPAS substrate, a steady displacement of the resonance wavelength $\lambda_{res}(n_{an})$ with the refractive index of the liquid dielectric within the range $1.33 < n_{an} < 1.39$ is revealed in the upper central inset. The maximum achievable WIM-responsivity $R_{WIM}(n_{an})$ as depicted in the left upper inset comprises a magnitude of up to 4,000 nm/RIU at $n_{an} = 1.36$. The broadening parameter $\Delta \lambda_{res}(n_{an})$ changes non-steady. It is around 300 ± 50 nm at $n_{an} = 1.36$ and remains largely constant.

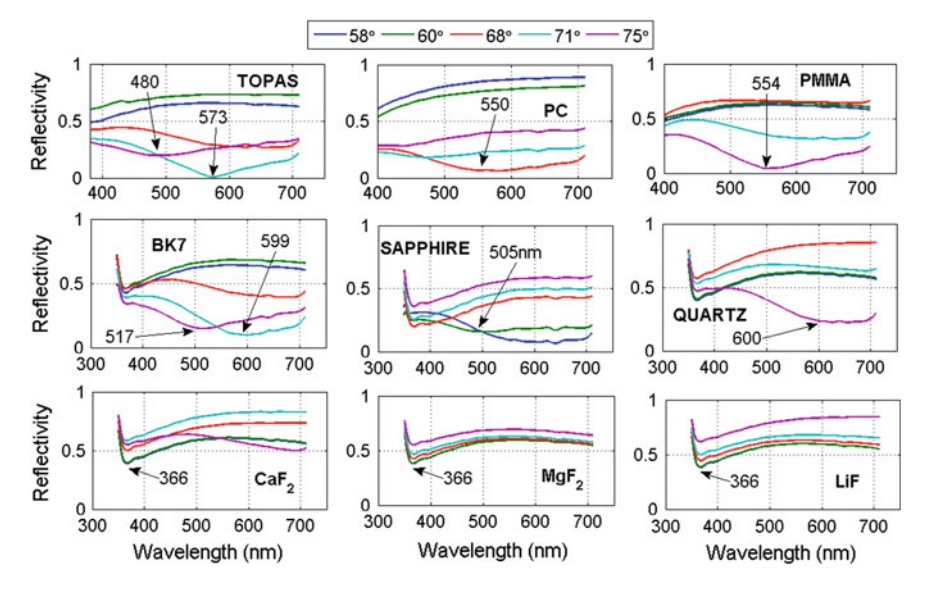


Fig. 9.8 Reflectance curves under WIM-conditions, calculated for different substrate materials, as indicated in the *plots*. Incident angles are: 58° , 60° , 68° , 71° and 75° for the wavelength range $300 \, \text{nm} < \lambda < 700 \, \text{nm}$. The Fe-film thickness is $25 \, \text{nm}$, in contact with water as the liquid dielectric

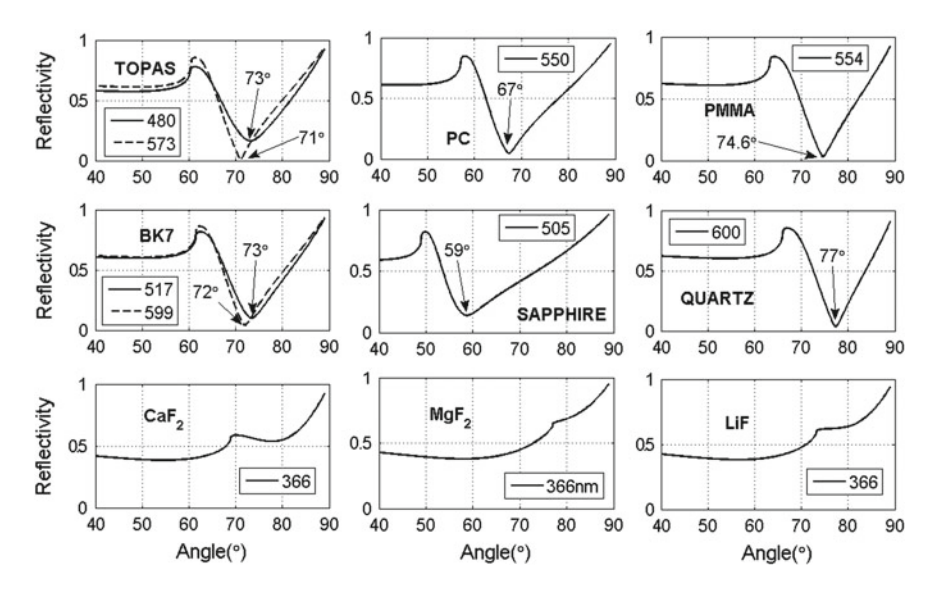


Fig. 9.9 Reflectance curves under for different substrate materials, as indicated in the *plots*, and different incident wavelengths for the angle range $40^{\circ} < \theta < 90^{\circ}$. Fe-film thickness is 25 nm, in contact with water

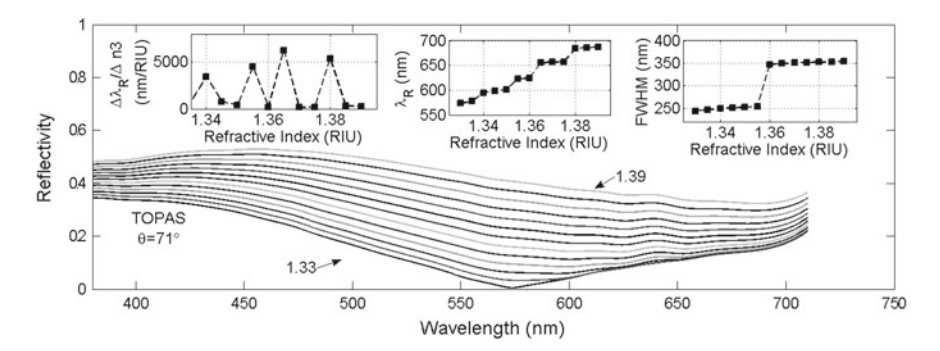


Fig. 9.10 WIM-sensing properties and spectral reflectance $R(\lambda)$ of Fe, initial wavelength λ_{res} near 550 nm, calculated for a set of different RIU-values: $1.33 < n_{an} < .39$. Substrate is TOPAS, incident angle is 71°. Upper three insets show SP-responsivity $R_{WIM}(n_{an})$, resonance displacement $\lambda_{res}(n_{an})$ and line broadening $\Delta\lambda_{res}(n_{an})$ at FWHM

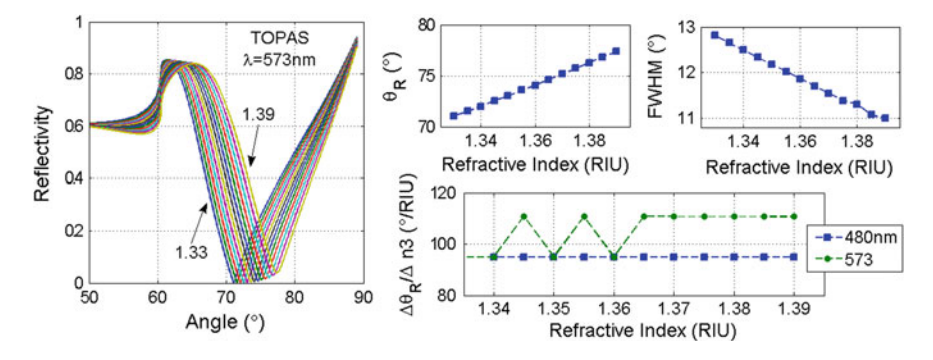


Fig. 9.11 AIM-sensing properties and angular reflectance $R(\theta)$ of Fe, calculated for a set of different RIU-values, at range 1.33 < n_{an} < 1.39. Substrate is TOPAS, incident wavelength is 573 nm. *Left* and *right upper* sub-figures depict resonance displacements $\theta_{res}(n_{an})$ and line broadening $\Delta\theta_{res}(n_{an})$. SP-responsivity $R_{AIM}(n_{an})$ shown below for wavelengths of 408 and 573 nm

The SPR-sensing characteristic in the AIM is shown in Fig. 9.11 for TOPAS at a wavelength of 573 nm, and comprises an initial resonance angle of 71° that increases linearly with n_{an} . The maximum achievable responsivity R_{AIM} is approximately $110^{\circ}/RIU$, and remains constant. The line broadening parameter $\Delta\theta_{res}(n_{an})$ decreases towards higher values of n_{an} .

The influence of film thickness for AIM conditions is outlined in Fig. 9.12. The data indicate that the Fe-film thickness for optimum sensor operation is around 25 nm.

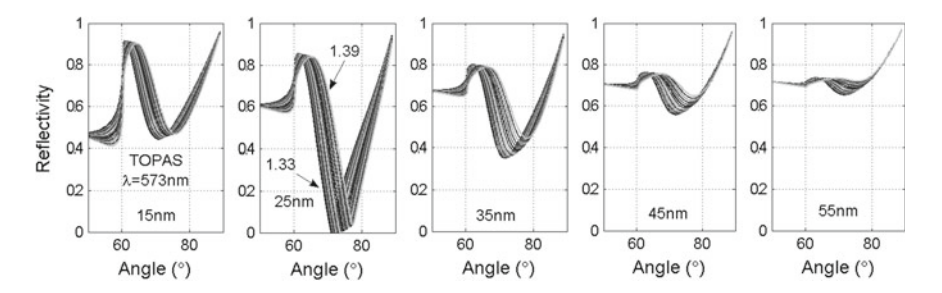


Fig. 9.12 AIM-reflectance at the SP-resonance for different Fe-film thickness values of 15, 25, 35, 45 and 55 nm

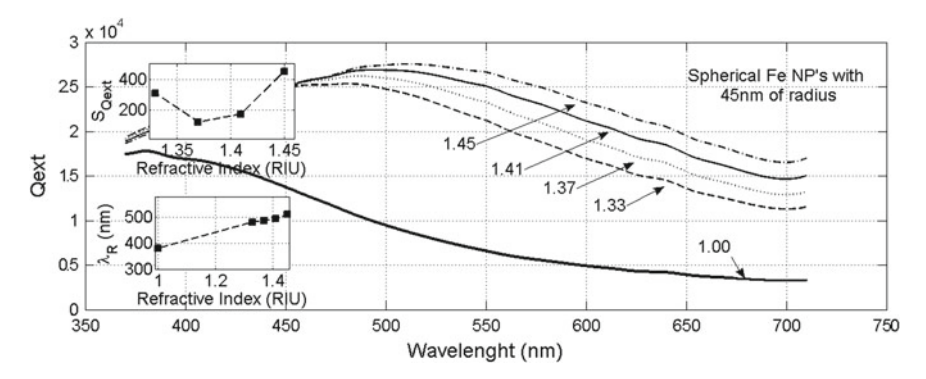


Fig. 9.13 Optical absorbance for Fe-particles with 45 nm diameter, calculated as function of wavelength for different refractive index (RIU) values of the surrounding aqueous solution. *Left lower inset* shows resonance position $\lambda_R(n_{an})$ and optical responsivity $S_{Qext}(n_{an})$ at *upper left*, taken at the first spectral maximum near 380 nm

9.3.1 Properties of Localized Plasmons in Colloidal Fe-Particles

The optical absorption characteristic of colloidal Fe-particles with 45 nm diameter, immersed into an aqueous solution with varying refractive index n_{an} as function of wavelength, is depicted in Fig. 9.13. Left lower and upper insets reveal spectral resonance position $\lambda_{res}(n_{an})$ and responsivity $S_{Q_{ext}}(n_{an})$, respectively. This quantity is more than one order of magnitude smaller than calculated before in Fig. 9.10 for the propagating SPP.

A compilation of achievable SPR sensor performance is displayed in Table 9.3.

Table 9.3 SP-sensor performance and figures of merit for thin Fe-films at metal-water interface: TOPAS-substrate

rame ver period period		ares of intention time i c	mance and negative of morning than 10 mins at mean water 101110 substant	iace, ioning same	in an	
Operation mode	Suited/best substrate	Optical responsivity	hest substrate Optical responsivity Linear dynamic range SPR width	SPR width	Optimum film thickness Remarks	Remarks
AIM	TOPAS/PC BK7	110°/RIU	$<4 \times 10^{-2} \text{ RIU}$	$12 \pm 2^{\circ}$	25 nm	Single resonance
WIM	TOPAS/PC BK7	4,000 nm/RIU	None	$300 \pm 50 \mathrm{nm}$ 25 nm	25 nm	Single resonance
LSPR	Nano-particles	200 nm/RII	None	75 nm		

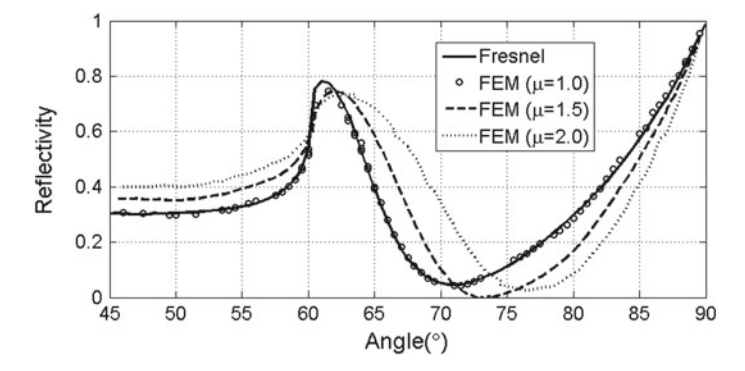


Fig. 9.14 Finite element computations. The parameters SPR sensor are the ones used in Fig. 9.9 for $\lambda = 750$ nm. Without magnetic field induces $\mu = 1.0$ the results obtained by the finite element method are similar to the ones obtained from the Fresnel model. In a presence of small magnetic field which induces $\mu = 1.5$ and at moderate magnetic field which induces $\mu = 2.0$

9.3.2 Magneto-Optical Effects

An example of SPR-sensing characteristic for thin Iron films in the presence of a magnetic field is shown in figures below. In the Fig. 9.14 when no magnetic field are applied, then the value of μ is equal 1 and the results are similar to those, shown in Fig. 9.9 for BK7 substrate. As the magnetic field increases the value of μ becomes higher and the resonance coupling conditions change as indicated by the shift in the θ_{res} position. To determine the performance of the SPR sensor in a presence of a quasi-static magnetic field that modifies the resonance condition one must employ the Maxwell equations since the Fresnel model does not include any magneto-optical effect. Figure 9.14 shows the results obtained by using the finite element method to solve the Maxwell equations when the metallic layer is affected by a external magnetic field.

9.4 Thin Molybdenum (Mo) Films

The complex optical constant $\varepsilon_{mr}(\lambda) = \varepsilon'_{mr}(\lambda) + j\varepsilon''_{mr}(\lambda)$ of the metal from Ref. [7] is illustrated in the right inset of Fig. 9.15. The electron configuration of the atomic ground state is $[Ar]4d^55s^1$. For the pure, solidified material, the outer 5s electron hybridizes with the incompletely filled 4d-shell and forms the broad, partially occupied conduction band, as shown in Ref. [8]. The weakly paramagnetic metal exhibits moderate electrical dc-conductivity of $18.7 \times 10^6 (\Omega \, \text{m})^{-1}$ at ambient T and suggests description by a modified form of the DA. At $\lambda > 750 \, \text{nm}$, $\varepsilon'_{mr}(\lambda)$ turns swiftly to negative values that decrease steadily. $\varepsilon''_{mr}(\lambda)$ is positive, with some distinct features around 700 nm, and remains fairly constant at moderate values within the

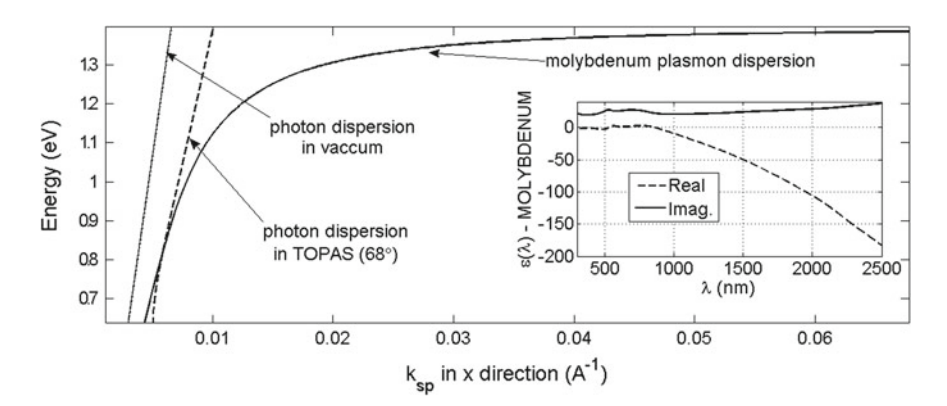


Fig. 9.15 Photon and SPP-dispersion curves of Molybdenum at the metal-water interface (*solid-line*), calculated for a TOPAS substrate (*dashed-line*) and incident angle of 68°. *Right inset* reveals the real and imaginary fractions of the CDK as function of wavelength

wavelength range of interest. For the TOPAS substrate at 68°, the SP-dispersion appears undistorted and exhibits a distinct resonant cross-over in the NIR region at around 0.8 eV. Intersections probably also exist at lower energy and low k-values. In the asymptotic limit at high k, the SP-energy approaches 1.4 eV at the metal-water interface. Due to a high boiling point of 4,639°C, Molybdenum films cannot be evaporated thermally from Tungsten foils or carbon boats, but are produced readily by magnetron sputtering from a massive metal target in inert atmosphere, or by laser ablation. A dense and very thin native self-limiting oxide layer with composition MoO₃ forms on the metal surface, immediately upon exposure to air or aqueous solution. Passivating surface oxide layers also can be made electrochemically at moderate anodic potentials. The metal is corrosion resistant up to high temperature.

Related spectral features of the reflectance $R(\lambda)$ in the WIM are shown in Fig. 9.16 for the substrate materials under consideration. Unlike most other transition metals, Mo-films exhibit clear SP-resonances centered, however, at long wavelength >1,000 nm, whilst comprising moderate incident angles. TOPAS and BK7 appear best suited for SP-sensing applications in the WIM. SP-resonances do not appear for the MgF₂-substrate.

Reflectance under AIM conditions is depicted in Fig. 9.17, and confirms the moderate resonance angles, except for MgF_2 substrates. The *plots* indicate a distinct decrease of the line broadening parameter $\Delta\theta_{res}$ with increasing wavelength, established towards smaller resonance angles.

For the BK7 substrate, the SP-energy (eV) varies with the incident angle within the range $65^{\circ} < \theta < 75^{\circ}$ non-linearly as: $E_{SP}(\theta) = -0.0015\theta^2 + 0.254\theta - 9.366$.

The sensing characteristic in the WIM is shown in Fig. 9.18 for BK7, comprising an initial wavelength of 1,250 nm. The displacement of the resonance position as function of the refractive index of the liquid analyte, is shown in the upper inset. The depth/contrast of both resonances increases with increasing RIU-values of the analyte. The associated sensor responsivity R_{WIM} is illustrated in the lower left inset

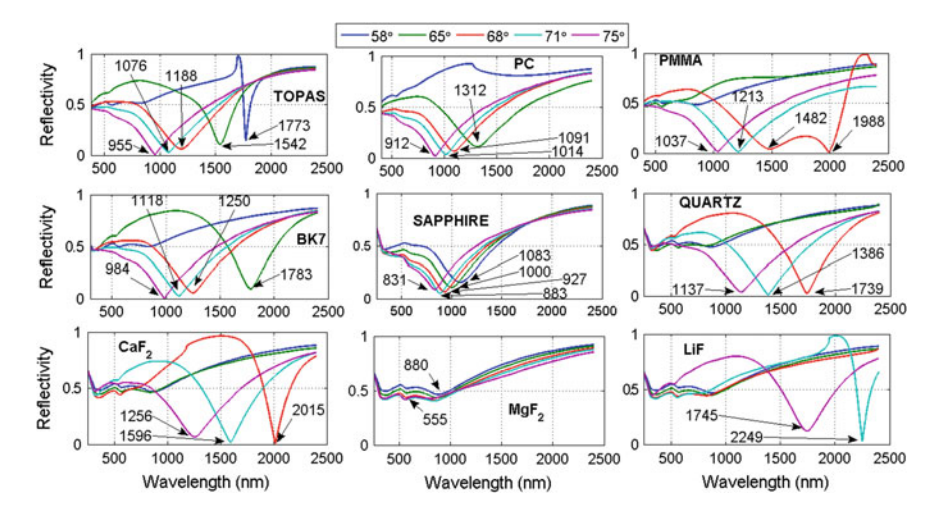


Fig. 9.16 Reflectance curves under WIM-conditions for different substrate materials, as indicated in the *plots*, and incident angles of 58°, 65°, 68°, 71° and 75° for the wavelength range 500 nm $< \lambda < 2,500$ nm. The film thickness is 30 nm, being in contact with water as the liquid dielectric

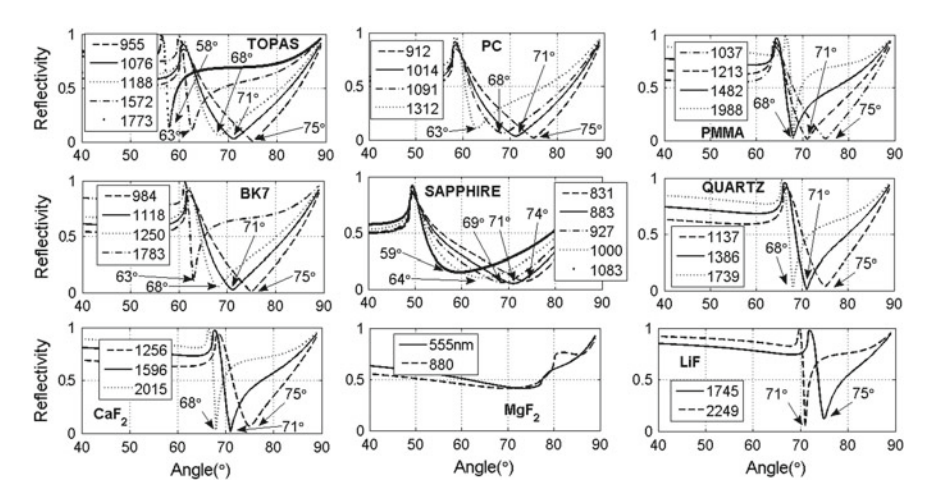


Fig. 9.17 Reflectance curves under AIM-conditions for different substrate materials, as indicated in the *plots*, and different incident wavelengths for the angle range $40^{\circ} < \theta < 90^{\circ}$. Mo-film thickness is 30 nm, in contact with water

and increases linearly with the RIU variation of the analyte. The SPR-line broadening effect (at FWHM) is depicted in the lower right inset and decreases with n_{an} .

Eventually, the influence of film thickness for the WIM is outlined in Fig. 9.19. This data set clearly indicates that the Mo-film thickness for optimum SPR sensor operation would be placed at 30 nm.

A compilation of achievable SPR sensor performance is displayed in Table 9.4.

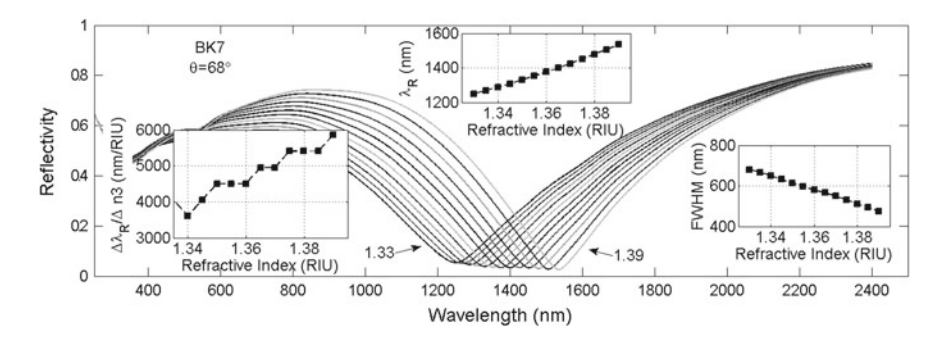


Fig. 9.18 WIM-sensor properties and spectral reflectance $R(\lambda)$ for different RIU-values of the aqueous analyte 1.33 < n_{an} < 1.39. Substrate is BK7, incident angle is 68°. Upper inset shows resonance displacements $\theta_{res}(n_{an})$, below depicted (left) responsivity $R_{WIM}(n_{an})$ and line broadening $\Delta\theta_{res}(n_{an})$

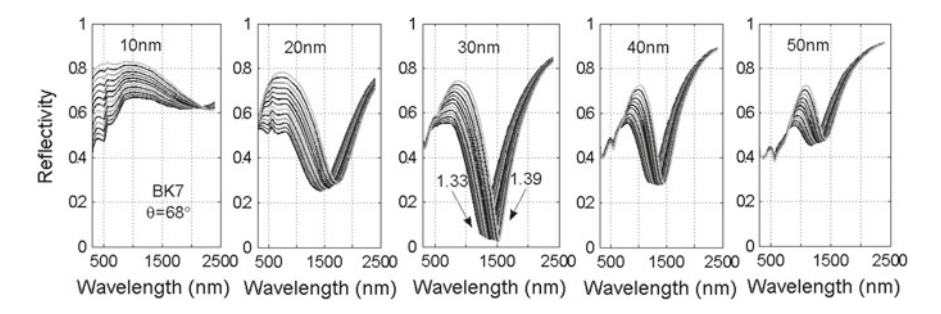


Fig. 9.19 WIM-reflectance at the SP-resonance for different Mo-film thickness values of 10, 20, 30, 40 and 50 nm

9.5 Thin Nickel (Ni) Films

The complex optical constant $\varepsilon_{mr}(\lambda) = \varepsilon'_{mr}(\lambda) + j\varepsilon''_{mr}(\lambda)$ of the metal has been taken from Ref. [7] and is illustrated in the right inset of Fig. 9.20. The atomic electron configuration of the ground state is most likely $[Ar]3d^94s^1$. In the solidified material, the outer 4s electron hybridizes with the only partly filled 3d-shell, and forms the partially occupied conduction band. The ferromagnetic metal exhibits moderate electrical dc-conductivity of $14.4 \times 10^6 (\Omega \text{ m})^{-1}$ at ambient T. It is inappropriately described by the DA, as outlined in the band-structure calculation of Ref. [9]. At wavelengths >250 nm, $\varepsilon'_{mr}(\lambda)$ drops steadily to negative values, while $\varepsilon''_{mr}(\lambda)$ is positive and increases linearly towards longer wavelengths. For the Quartz substrate at 71°, the SP-dispersion appears undistorted, but does not exhibit a clear resonant cross-over, since photon and SPP-group velocities coincide over a large range of k-values. In the asymptotic limit at high k, the SP-energy approaches 3.5 eV at the metal-water interface, similar to Silver. Due to a relatively low boiling point of 2,730°C, Nickel films can be produced by magnetron sputtering from a massive

Table 9.4 SP-senso	or perfor	res of merit for thin Mo-	mance and figures of merit for thin Mo-films at metal-water interface	face		
Operation mode	Suited/best substrate		Optical responsivity Linear dynamic range SPR width	SPR width	Optimum film thickness Remarks	Remarks
AIM	BK7/TOPAS/sapphire $ 40-80^{\circ}/RIU$	40–80°/RIU	$>7 \times 10^{-2} \text{ RIU}$	$15 \pm 1^{\circ}$	30 nm	Single resonance
WIM	BK7/TOPAS/sapphire	OPAS/sapphire 3,500–6,000 nm/RIU None	None	$550 \pm 200 \mathrm{nm}$ 30 nm	30 nm	Single resonance

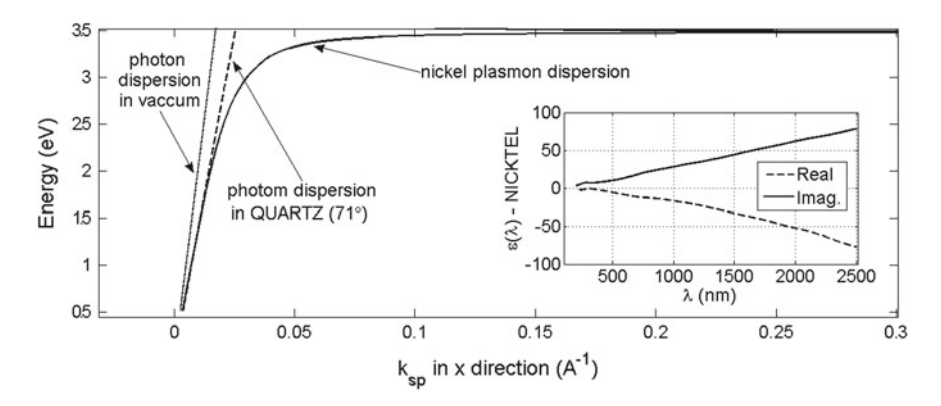


Fig. 9.20 Photon and SPP-dispersion curves of Nickel at the metal-water interface (*solid-line*), calculated for a Quartz substrate (*dashed-line*) and incident angle of 71°. There is no clear intersection point and resonance resolved. *Right inset* reveals the real and imaginary fractions of the CDK as function of wavelength

metal target in inert low pressure Ar-atmosphere, by electron beam and thermal evaporation from a Tungsten foil or Carbon boat in high vacuum, and by electro-plating. A stable, dense and thin native oxide layer forms on the metal surface, immediately upon exposure to air or aqueous solution. Dense, passivating oxide layers also can be made electrochemically at moderate anodic potentials.

Related spectral features of the reflectance $R(\lambda)$ in the WIM are shown in Fig. 9.21 for the substrate materials under consideration. Evidently, Ni-films on most substrates

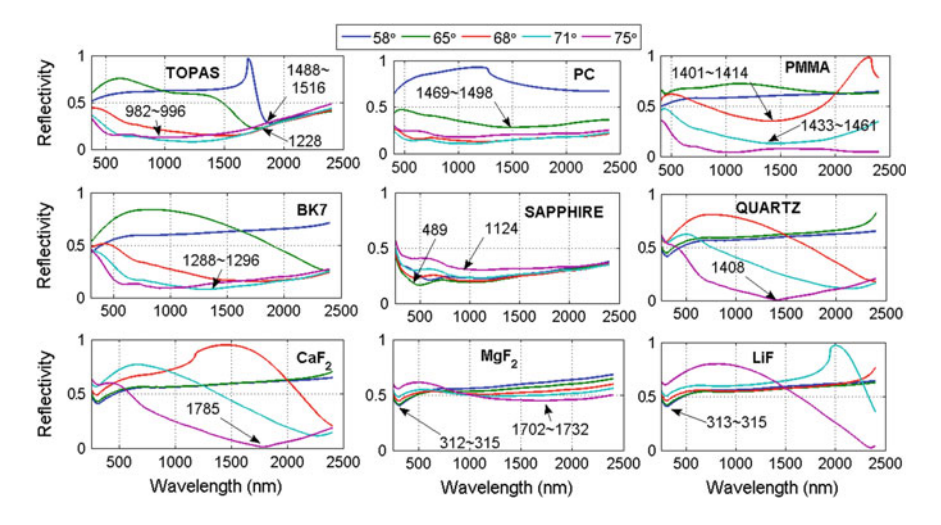


Fig. 9.21 Reflectance curves under WIM-conditions for different substrate materials, as indicated in the *plots*, and incident angles of 58°, 65°, 68°, 71° and 75° for the wavelength range 500 nm $< \lambda < 2,500$ nm. The Ni-film thickness is 25 nm, in contact with water as the liquid dielectric

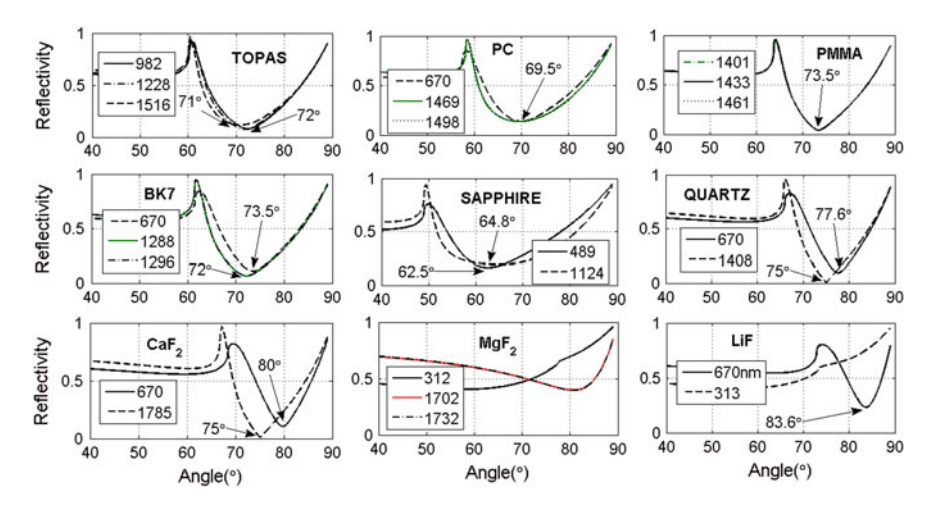


Fig. 9.22 Reflectance curves under AIM-conditions for different substrate materials, as indicated in the *plots*, and different incident wavelengths for the angle range $40^{\circ} < \theta < 90^{\circ}$. Ni-film thickness is 25 nm. in contact with water

do not exhibit clear SP-resonances and thus are poorly suited for SP-sensing applications in the WIM, especially Sapphire, MgF₂ and LiF.

Reflectance under AIM conditions is shown in Fig. 9.22, and confirms a manifold of resonance wavelength at nearly same angles for TOPAS, BK7, PC and PMMA.

A compilation of achievable SPR sensor performance is displayed in Table 9.5.

9.6 Thin Niobium (Nb) Films

The complex optical constant $\varepsilon_{mr}(\lambda) = \varepsilon'_{mr}(\lambda) + j\varepsilon''_{mr}(\lambda)$ of the metal has been taken from Ref. [10] and is illustrated in the right inset of Fig. 9.23. The atomic ground state electron configuration is $[Kr]4d^45s^1$. In the solidified material, the outer 5s electron hybridizes with the incompletely filled 4d-shell, and forms the partially occupied conduction band, according to the bandstructure calculations of Ref. [11]. The weakly paramagnetic metal exhibits low electrical dc-conductivity of $6.57 \times 10^6 (\Omega \text{ m})^{-1}$, and in part agrees with the DA, according to the band-structure calculation provided in Ref. [11]. At wavelengths $\lambda > 600$ nm, $\varepsilon'_{mr}(\lambda)$ drops steadily to high negative values. $\varepsilon''_{mr}(\lambda)$ is positive and increases slowly at $\lambda > 400$ nm. For the BK7 substrate at 71°, the SP-dispersion appears heavily distorted, but exhibits a clear resonant cross-over at approximately 1 eV. There is no clear SP-energy resolved at high k for the metal-water interface, but an apparent smooth transition at low k-values from the bound SPP to the quasi-bound (Qb) state, as defined before in Chap. 2. This unusual feature is not in agreement with the DA. Niobium films can be readily produced by magnetron sputtering from a massive metal target in low pressure Ar-atmosphere.

Table 9.5 SP-sensor performance and figures of merit for thin Ni-films at metal-water interface

$1,500 \text{ nm/RIU}$ None $1,500 \pm 500 \text{ nm}$ 25 nm	ture / 10 select performance and rightes of metrory times at meeting were meetings	Remarks Not suited for	Optimum film thickness 25 nm	SPR width $14 \pm 2^{\circ}$ 1,500 \pm 500 nm	Linear dynamic range $>6 \times 10^{-2} \mathrm{RIU}$ None	Optical responsivity 55°/RIU 7,000–15,000 nm/RIU	Suited/best substrate TOPAS BK7/PC/PMIMA TOPAS/BK7/Quartz	ation
	substrateOptical responsivityLinear dynamic rangeSPR widthOptimum film thickness7/PC/PMMA 55° /RIU $>6 \times 10^{-2}$ RIU $14 \pm 2^{\circ}$ 25 nm7/Quartz7,000-15,000 nm/RIUNone $1,500 \pm 500$ nm 25 nm	sensing application						
	Optical responsivity Linear dynamic range SPR width		25 nm	$14 \pm 2^{\circ}$		55°/RIU	TOPAS BK7/PC/PMMA	AIM
TOPAS BK7/PC/PMMA 55° /RIU $>6 \times 10^{-2}$ RIU $14 \pm 2^{\circ}$		Remarks	Optimum film thickness	SPR width	Linear dynamic range	Optical responsivity	Suited/best substrate	ation

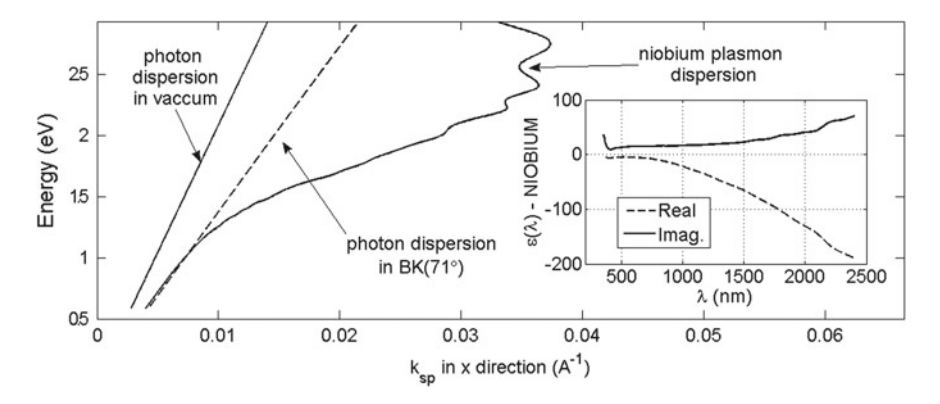


Fig. 9.23 Photon and SPP-dispersion curves of Niobium at the metal-water interface (*solid-line*), calculated for BK7 substrate (*dashed-line*) and incident angle of 71°. A resonant intersection point is resolved near 1 eV. *Right inset* reveals the real and imaginary fractions of the CDK as function of wavelength

However, the very high boiling temperature of $4,744\,^{\circ}\mathrm{C}$ prevents thermal evaporation from electrically heated Tungsten foils or Carbon boats possibly, or electron beam evaporation. The metal is corrosion resistant and does not oxidize below $400\,^{\circ}\mathrm{C}$. Properties or existence of thin native oxide layers on the pure metal surface upon exposure to air or aqueous solution are not known.

Related spectral features of the reflectance $R(\lambda)$ in the WIM are shown in Fig. 9.24 for the substrate materials under consideration. In contrast to numerous other transition metals, Nb-films on most substrates exhibit clear, although relatively broad

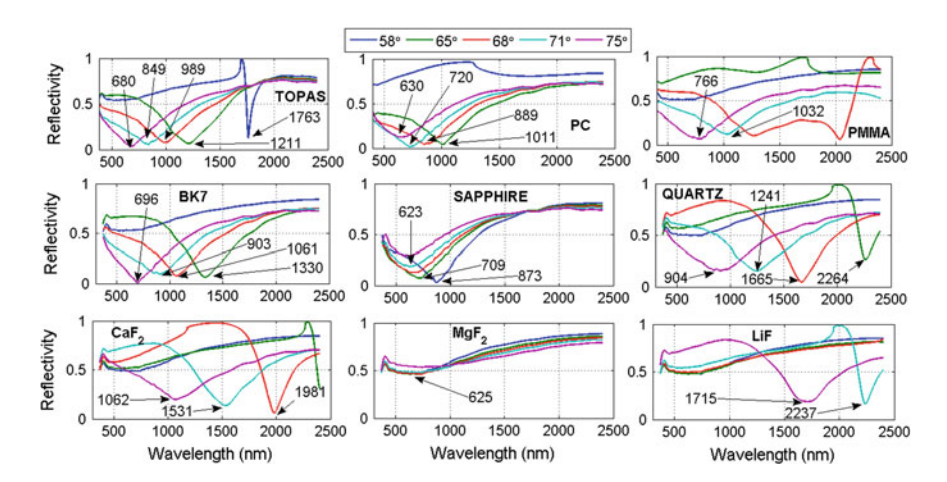


Fig. 9.24 Reflectance curves under WIM-conditions for different substrate materials, as indicated in the *plots*, and incident angles of 58°, 65°, 68°, 71° and 75° for the wavelength range 500 nm $< \lambda < 2,500$ nm. The Nb-film thickness is 25 nm, being in contact with water as the liquid dielectric

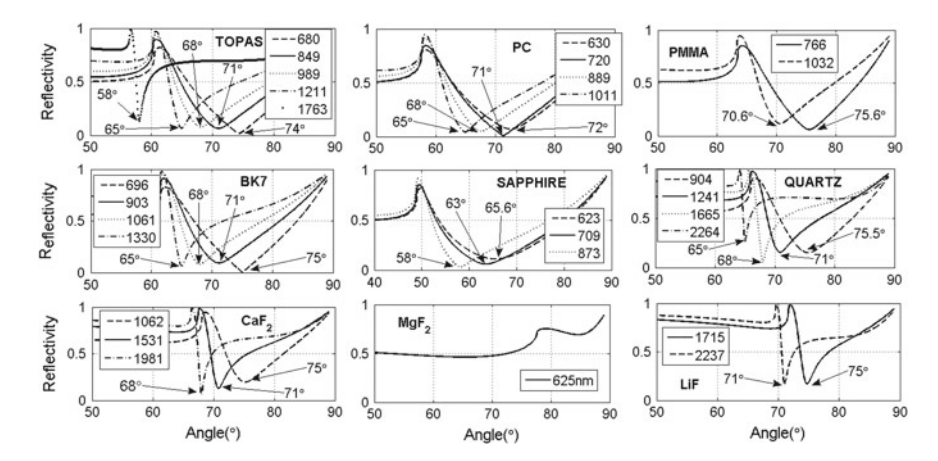


Fig. 9.25 Reflectance curves under AIM-conditions for different substrate materials, as indicated in the *plots*, and different incident wavelengths for the angle range $40^{\circ} < \theta < 90^{\circ}$. Nb-film thickness is 25 nm, in contact with water

SP-resonances, and thus are well suited for SP-sensing applications in the WIM, except MgF₂. An SP-splitting effect is resolved for PMMA.

Reflectance under AIM conditions is shown in Fig. 9.25, indicating a decrease of the resonance width with increasing wavelength for Quartz, BK7 and TOPAS substrates, whilst moving to smaller angle. For the BK7 substrate, the SP-energy (eV) varies with the incident angle within the range $65^{\circ} < \theta < 75^{\circ}$ weakly nonlinear as: $E_{SP}(\theta) = 0.0021\theta^2 - 0.2076\theta + 5.642$.

The SPR-sensing characteristic in the AIM is shown in Fig. 9.26, comprising an initial resonance angle of 71° and wavelength of 903 nm. The depth of the

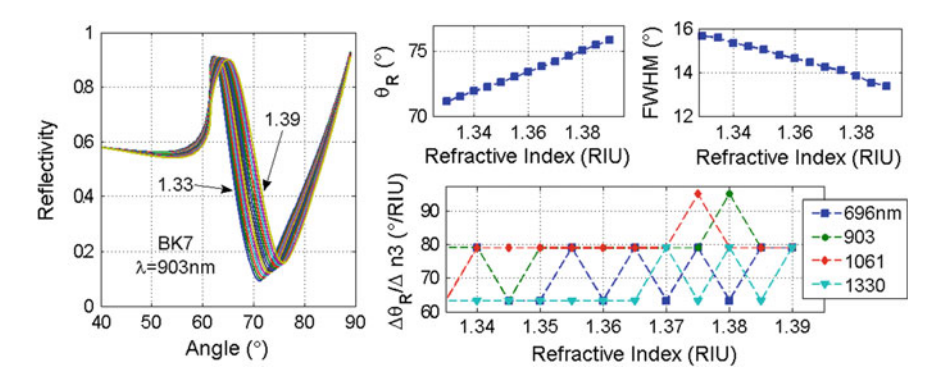


Fig. 9.26 AIM-sensor properties: angular reflectance $R(\theta)$ for different RIU-values of the aqueous analyte 1.33 $< n_{an} < 1.39$. Substrate is BK7, incident wavelength 903 nm. *Upper right* two sub-figures show resonance displacements $\theta_{res}(n_{an})$, SP-line broadening $\Delta\theta_{res}$ at FWHM and responsivity R_{AIM} below

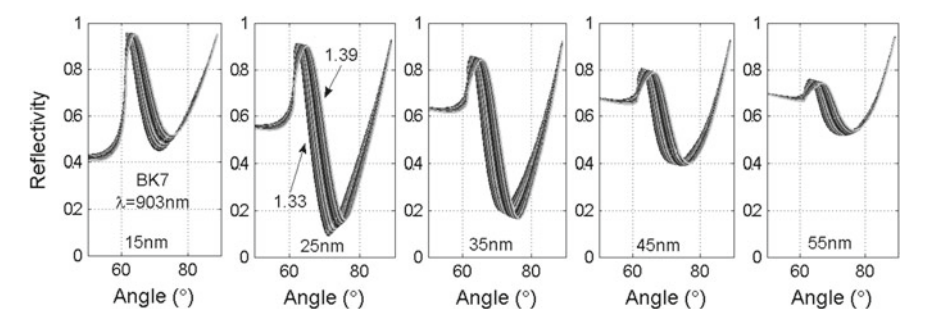


Fig. 9.27 AIM-reflectance at the SP-resonance for different Nb-film thickness values of 15, 25, 35, 45 and 55 nm

SP-resonance does not vary significantly with the RIU of the analyte. A linear increase of resonance angle $\theta_{res}(n_{an})$, but decrease of the line broadening parameter $\Delta\theta_{res}(n_{an})$ with the RIU of the analyte are resolved in the right two upper two sub-figures. SPR sensor responsivity R_{AIM} is shown for four different wavelengths below; their values are moderate and remain largely constant.

Eventually, the influence of film thickness for the AIM is outlined in Fig. 9.27. This data set clearly indicates that the Nb-film thickness for optimum SPR sensor operation would be placed at 25 nm.

A compilation of achievable SPR sensor performance is displayed in Table 9.6.

9.7 Thin Tantalum (Ta) Films

The material exists in two phases with different crystallographic structure: the α phase is bcc (body centered cubic), the β -phase is tetragonal and meta-stable. A phase transition occurs at elevated T. The complex optical constant $\varepsilon_{mr}(\lambda) =$ $\varepsilon'_{mr}(\lambda) + j\varepsilon''_{mr}(\lambda)$ of the former phase has been taken from Ref. [1] and is illustrated in the right inset of Fig. 9.28. The atomic ground state electron configuration is $[Xe]4f^{14}5d^36s^2$. In the solidified material, the outer 6s electrons hybridize with the partly filled 5d- and f shells, and form the partially occupied nearly parabolic conduction band. The weakly paramagnetic metal exhibits a slightly higher electrical dc-conductivity of $7.63 \times 10^6 (\Omega \text{ m})^{-1}$ in the α -phase. The CDK fairly well resembles the DA at low energy, in accord with the band-structure calculation provided in Ref. [12]. At wavelengths $\lambda > 500$ nm, $\varepsilon'_{mr}(\lambda)$ drops steadily to negative values. $\varepsilon''_{mr}(\lambda)$ is positive and increases slowly at $\lambda > 1,400$ nm. For the BK7 substrate at 68°, the SP-dispersion is undistorted, and exhibits a distinct resonant cross-over at approximately 1.2 eV. The SP-energy at high k for the metal-water interface is 1.87 eV. Tantalum-films can be readily produced by magnetron sputtering from a massive metal target in low pressure Ar-atmosphere, possibly by laser ablation. The very high boiling temperature of 5,458 °C prevents thermal evaporation

Table 9.6 SP-sensor performance and figures of merit for thin Nb-films at metal-water interface

	a como beneniane	designation of the control of the co	III TAG IIIIIII AL IIICAI HACA	The state of the s		
Operation mode	Suited/best substrate	Operation Suited/best substrate Optical responsivity Linear dynamic range SPR width mode	Linear dynamic range	SPR width	Optimum film thickness Remarks	Remarks
AIM	TOPAS/BK7/Quartz $70 \pm 10^{\circ}$ /RIU	$70 \pm 10^{\circ}$ /RIU	$>6 \times 10^{-2} \text{ RIU}$	$15 \pm 1^{\circ}$	25 nm	Multiple resonances at similar angles
WIM	TOPAS/BK7/Quartz	TOPAS/BK7/Quartz $3,000 \pm 100 \text{ nm/RIU}$ None	None	$550 \pm 200 \mathrm{nm}$ 25 nm	25 nm	Broadened resonances

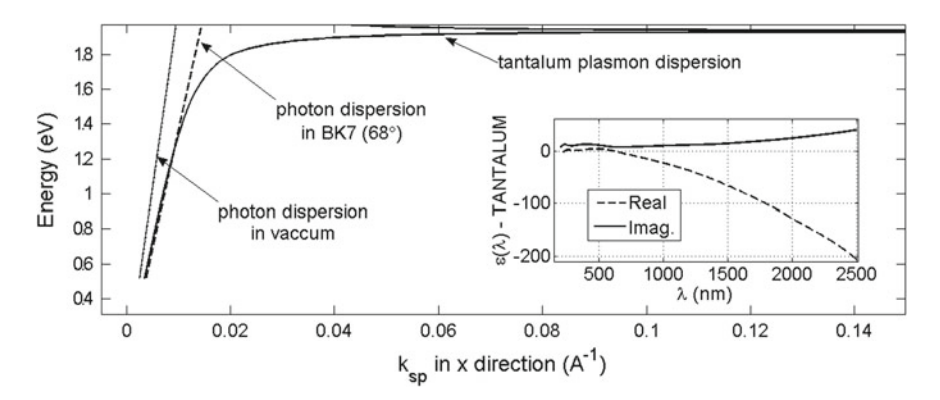


Fig. 9.28 Photon and SPP-dispersion curves of α -Ta at the metal-water interface (*solid-line*), calculated for BK7 substrate (*dashed-line*) and incident angle of 68°. A resonant intersection point is resolved near 1.2 eV. *Right inset* reveals the real and imaginary fractions of the CDK as function of wavelength

from electrically heated Tungsten foils or carbon boats at high vacuum, or electron beam evaporation. The metal is highly corrosion resistant. A few monolayer thin native oxide film forms on the pure metal surface immediately upon exposure to air or aqueous solution. Structural properties of thin Ta-films are reported in Ref. [13].

Related spectral features of the reflectance $R(\lambda)$ in the WIM are shown in Fig. 9.29 for the substrate materials under consideration. Quite similar to the optical properties of Nb-films depicted before, most substrates exhibit clear, moderately broadened SP-resonances. Tantalum is thus well suited for SP-sensing applications in the WIM, except MgF₂, as well as LiF. A distinct SP-splitting effect is also resolved for PMMA.

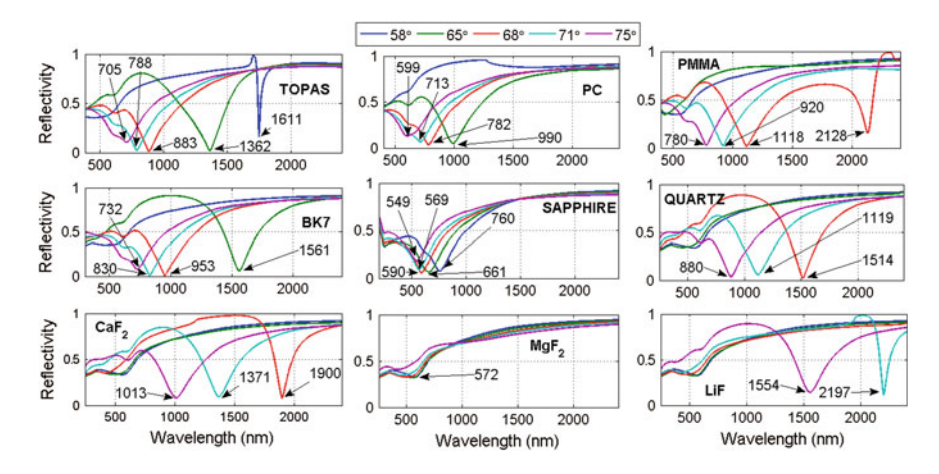


Fig. 9.29 Reflectance curves under WIM-conditions for different substrate materials, as indicated in the *plots*, and incident angles of 58°, 65°, 68°, 71° and 75° for the wavelength range 500 nm $< \lambda < 2,500$ nm. The Ta-film thickness is 35 nm, being in contact with water as the liquid dielectric

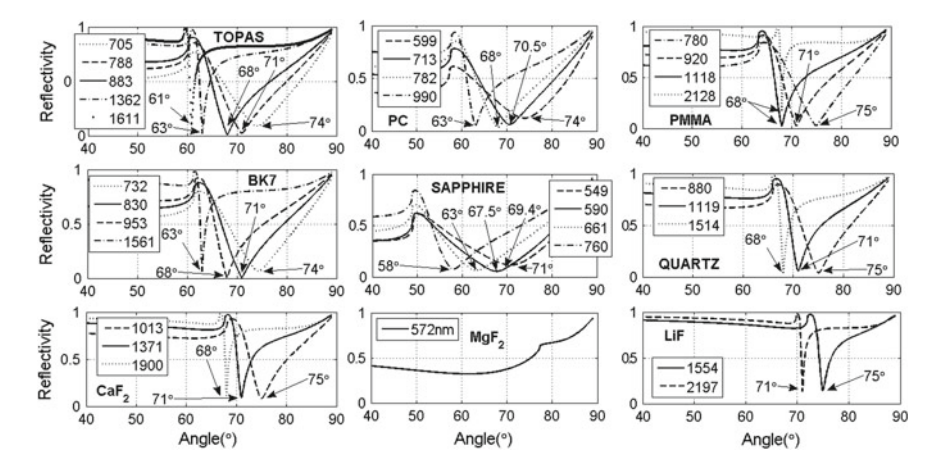


Fig. 9.30 Reflectance curves under AIM-conditions for different substrate materials, as indicated in the *plots*, and different incident wavelengths for the angle range $40^{\circ} < \theta < 90^{\circ}$. Ta-film thickness is 35 nm. in contact with water

Reflectance under AIM conditions is shown in Fig. 9.30, indicating a distinct decrease of the resonance width with increasing wavelength and towards smaller angle for Quartz, BK7, PMMA and TOPAS. For the BK7 substrate, the SP-energy (eV) varies with the incident angle within the range $65^{\circ} < \theta < 75^{\circ}$ weakly non-linear as: $E_{SP}(\theta) = -0.0028\theta^2 + 0.468\theta - 17.487$.

The sensing characteristic in the WIM is shown in Fig. 9.31 for BK7, comprising an initial wavelength 950 nm. The displacement of the resonance angle as function of the refractive index of the liquid analyte, is show in the lower left inset. The depth/contrast increase with increasing RIU-values of the analyte. The associated sensor WIM-responsivity R_{WIM} is illustrated in the lower right inset: its magnitude

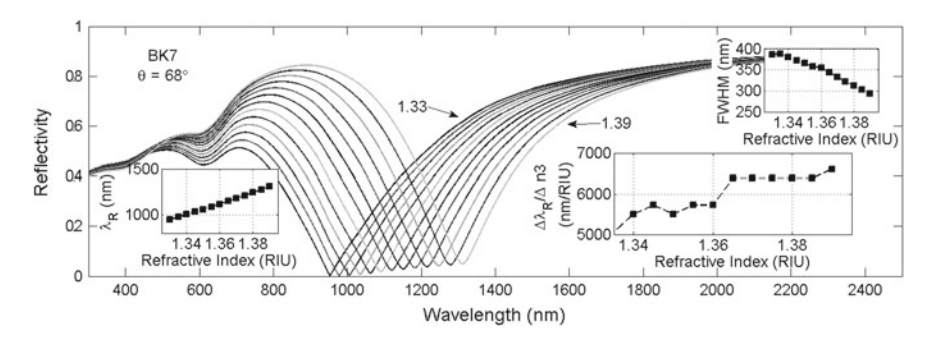


Fig. 9.31 WIM-sensor properties and spectral reflectance $R(\lambda)$ for different RIU-values of the aqueous analyte 1.33 < n_{an} < 1.39. Substrate is BK7, incident angle is 68°. Left inset shows resonance displacement $\theta_{res}(n_{an})$; responsivity $R_{WIM}(n_{an})$ at lower and line broadening $\Delta\theta_{res}(n_{an})$ at upper right

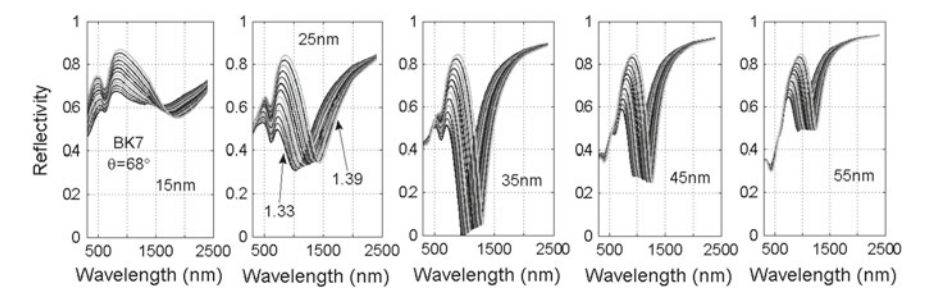


Fig. 9.32 WIM-reflectance at the SP-resonance for different Ta-film thickness values of 15, 25, 35, 45 and 55 nm

is rather high and increases towards higher n_{an} . The moderate SPR-line broadening parameter (at FWHM) is depicted in the upper right inset and decreases with n_{an} .

Eventually, the influence of film thickness for the WIM is outlined in Fig. 9.32. This data set clearly indicates that the Ta-film thickness for optimum SPR sensor operation would be placed at 35 nm.

A compilation of achievable SPR sensor performance is displayed in Table 9.7.

9.8 Thin Titanium (Ti) Films

The complex optical constant $\varepsilon_{mr}(\lambda) = \varepsilon'_{mr}(\lambda) + j\varepsilon''_{mr}(\lambda)$ of the hcp phase has been taken from Ref. [1] and is illustrated in the right inset of Fig. 9.33. The atomic electron configuration is $[Ar]3d^24s^2$. In the solidified material, the outer 4s electrons hybridize with the partly filled 3d-shell, and form the partially occupied conduction band. The paramagnetic metal exhibits a relatively low electrical dc-conductivity of $2.38 \times 10^6 (\Omega \text{ m})^{-1}$. The CDK is inappropriately described by the DA. A bandstructure calculation for the material is reported in Ref. [14]. $\varepsilon'_{mr}(\lambda)$ exhibits solely within the wavelengths range 300 nm $<\lambda<900$ nm rather small negative values. $\varepsilon_{mr}^{"}(\lambda)$ is positive, with small modulations and increases steadily at $\lambda > 300$ nm. For the BK7 substrate at 68°, the SP-dispersion appears heavily distorted, whilst a clear resonant cross-over is resolved only in the VUV-region at the photon energy of 7.5 eV. Intersections probably also exist at lower energy and low k-values. The SPenergy at high k for the metal-water interface is 7.7 eV. Titanium films can be readily produced by magnetron sputtering from a massive metal target in a low pressure Aratmosphere. The boiling temperature of 3,287 °C prevents thermal evaporation from electrically heated Tungsten foils or carbon boats. The metal is corrosion resistant. A stable thin native oxide layer forms on the pure metal surface, immediately upon exposure to air or aqueous solution. The oxide growth kinetics on a polycrystalline Ti-surface is reported in Ref. [15].

Related spectral features of the reflectance $R(\lambda)$ in the WIM are shown in Fig. 9.34 for the substrate materials under consideration. Unlike the optical properties of Ta

Table 9.7 SP-sensor performance and figures of merit for thin Ta-films at metal-water interface

	•)				
Operation mode	Suited/best substrate	Optical responsivity	Linear dynamic range SPR width	SPR width	Optimum film thickness Remarks	Remarks
AIM	All except MgF2	100°/RIU	$6 \times 10^{-2} \mathrm{RIU}$	$9.5 \pm 0.5^{\circ}$ 35 nm	35 nm	
WIM	All except MgF ₂	$6,000 \pm 500 \mathrm{nm/RIU}$ None	None	$320 \pm 30 \mathrm{nm}$ 20 nm	20 nm	SP-split for PMMA

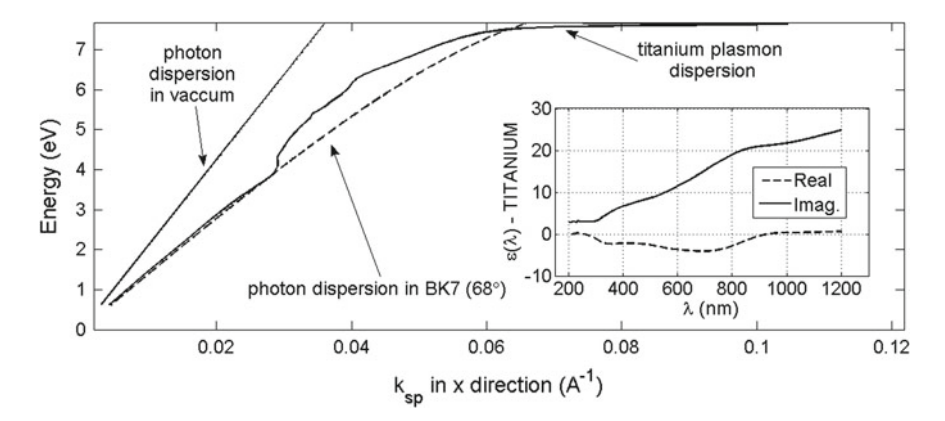


Fig. 9.33 Photon and SPP-dispersion curves of Titanium at the metal-water interface (*solid-line*), calculated for BK7 substrate (*dashed-line*) and incident angle of 68°. There is no clear resonant intersection point resolved at low energy. *Right inset* reveals the real and imaginary fractions of the CDK as function of wavelength

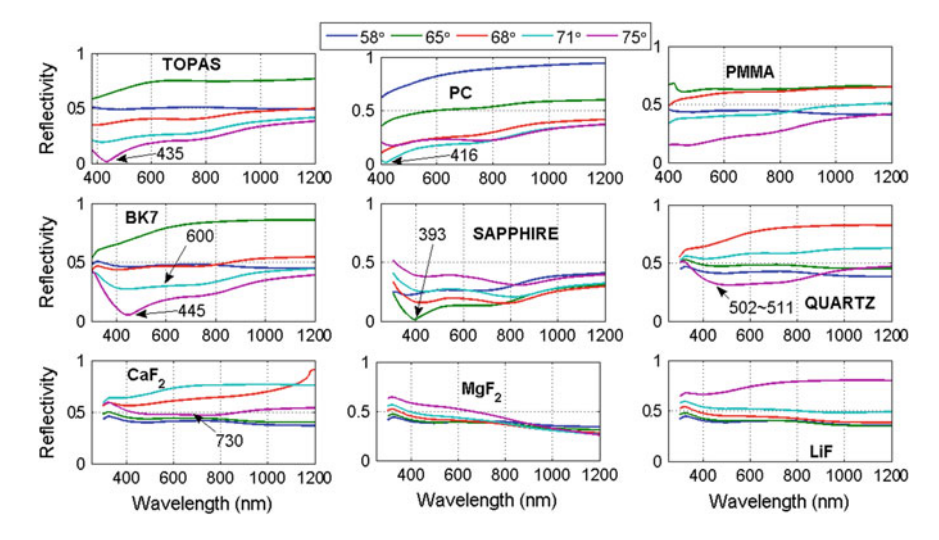


Fig. 9.34 Reflectance curves under WIM-conditions for different substrate materials, as indicated in the *plots*, and incident angles of 58°, 65°, 68°, 71° and 75° for the wavelength range 400 nm $< \lambda < 1,300$ nm. The Ti-film thickness is 20 nm, in contact with water as the liquid dielectric

and Nb-films depicted before, virtually all dielectric substrates lack presence of a clear SP-resonance at moderate angle and photon energy, except Sapphire. Titanium films are thus poorly suited for SP-sensing applications in the WIM.

Reflectance under AIM conditions is shown in Fig. 9.35, indicating again rather broad resonances and suited angles <75° only for PC and Sapphire substrates.

A compilation of achievable SPR sensor performance is displayed in Table 9.8.

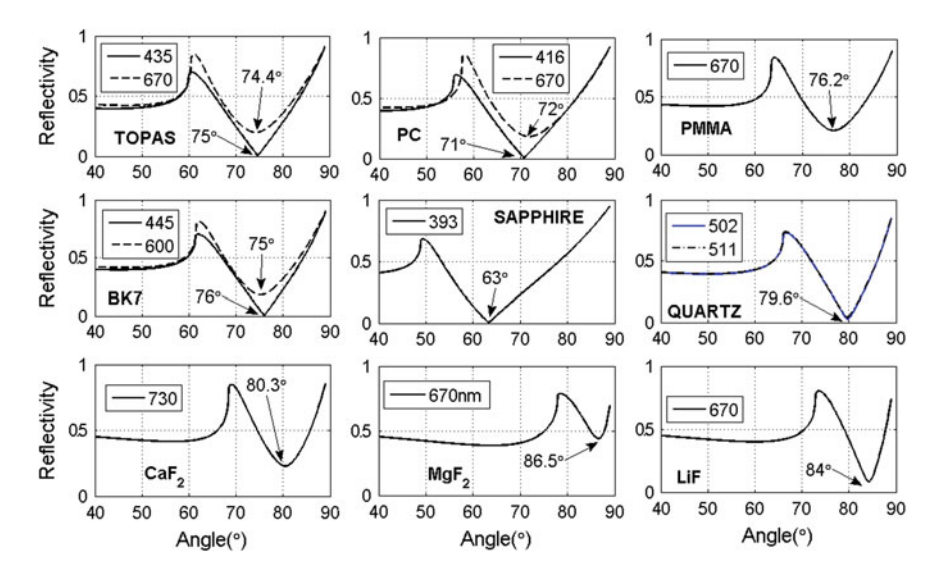


Fig. 9.35 Reflectance curves under AIM-conditions for different substrate materials, as indicated in the *plots*, and different incident wavelengths for the angle range $40^{\circ} < \theta < 90^{\circ}$. Ti-film thickness is 20 nm. in contact with water

9.9 Thin Tungsten (W) Films

The crystal structure of W is bcc (body centered cubic). The complex optical constant $\varepsilon_{mr}(\lambda) = \varepsilon'_{mr}(\lambda) + j\varepsilon''_{mr}(\lambda)$ has been taken from Ref. [7] and is illustrated in the right inset of Fig. 9.36. The atomic electron configuration is $[Xe]4f^{14}5d^46s^2$. In the solidified material, the two outer 6s electrons hybridize with the partly filled 5d-and 4f shells, and form the partially occupied conduction band. The weakly paramagnetic metal exhibits a moderate electrical dc-conductivity of $18.9 \times 10^6 (\Omega \text{ m})^{-1}$. Apart from modulations, the CDK seems to agree with the DA. Band-structure calculations are provided in Ref. [16]. At wavelengths $\lambda > 1,000$ nm, $\varepsilon'_{mr}(\lambda)$ drops steadily from small positive to negative values. $\varepsilon_{mr}^{"}(\lambda)$ is positive and reveals distinct oscillations within the spectral range of interest. For the BK7 substrate at 68°, the SP-dispersion is considerably distorted, but exhibits a distinct resonant cross-over at approximately 0.7 eV. The SP-energy at high k for the metal-water interface approaches 1.23 eV. Tungsten films can be readily produced by magnetron sputtering from a massive metal target in low pressure Ar-atmosphere. The very high boiling temperature of 5,930 °C prevents thermal evaporation or electron beam evaporation in low pressure vacuum. The metal is highly corrosion resistant. A thin native oxide layer forms immediately on the pure metal surface upon exposure to air or aqueous solution. The anodic oxidation of Tungsten electrodes is reported in Ref. [17].

Related spectral features of the reflectance $R(\lambda)$ in the WIM are shown in Fig. 9.37 for the substrate materials under consideration. Similar to the optical properties of Ta and Nb-films, depicted before, virtually all dielectric substrates, except LiF and

Table 9.8 SP-sensor performance and figures of merit for thin Ti-films at metal-water interface

Table 9.8 SP-sense	or pertormance and ngure	ormance and ngures of merit for thin 11-nims at metal-water interface	at metal-water interrace			
Operation mode	Suited/best substrate	Optical responsivity	Linear dynamic range	SPR width	Optimum film thickness	Remarks
AIM	BK7/Sapphire	$70 \pm 5^{\circ}$ /RIU	$6 \times 10^{-2} \text{ RIU}$	45 ± 3°	20 nm	
WIM	BK7/Sapphire	$1,600 \pm 500 \mathrm{nm/RIU}$ None	None	$450 \pm 10 \text{ nm}$	20 nm	Not suited

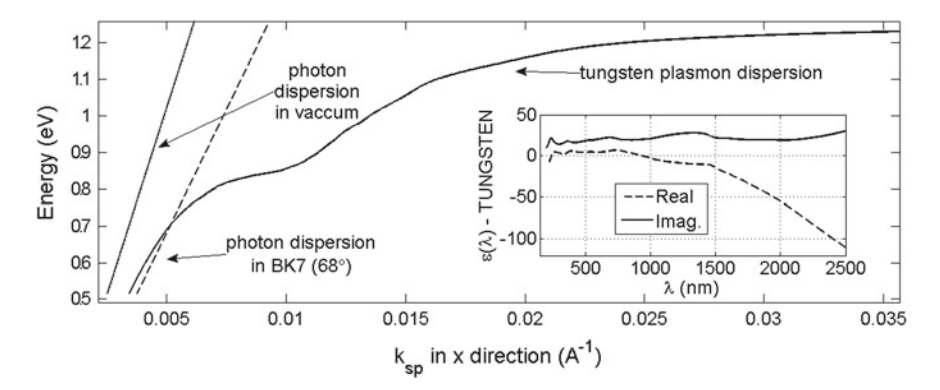


Fig. 9.36 Photon and SPP-dispersion curves of Tungsten at the metal-water interface (*solid-line*), calculated for BK7 substrate (*dashed-line*) and incident angle of 68°. There is a clear resonant intersection point resolved for photon energy of 0.7 eV. *Right inset* reveals the real and imaginary fractions of the CDK as function of wavelength

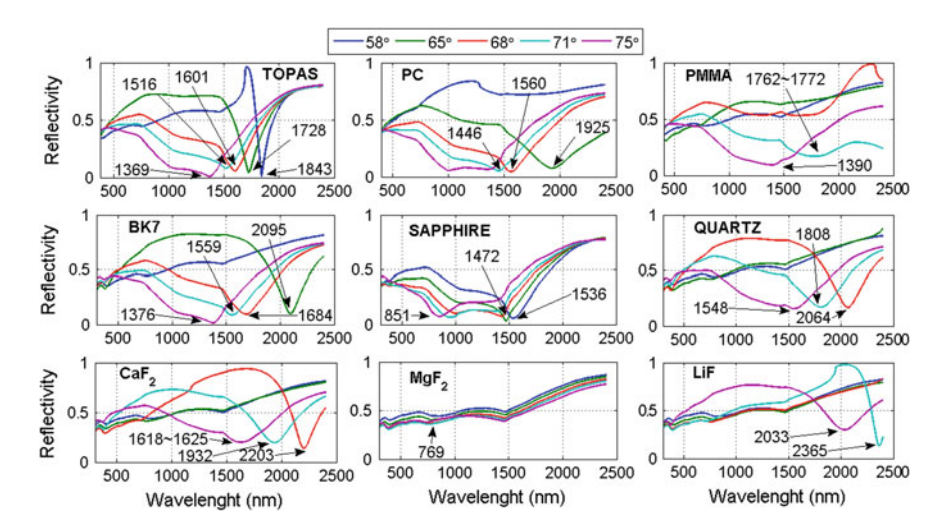


Fig. 9.37 Reflectance curves under WIM-conditions for different substrate materials, as indicated in the *plots*, and incident angles of 58°, 65°, 68°, 71° and 75° for the wavelength range 500 nm $< \lambda < 2,500$ nm. The W-film thickness is 45 nm, in contact with water as the liquid dielectric

MgF₂, exhibit clear, but fairly broad SP-resonances. W-films are thus suited for SP-sensing applications in the WIM.

Reflectance under AIM conditions is shown in Fig. 9.38, again indicating angularly broadened resonances and suited angles <75°, except the MgF₂ substrate. For the BK7 substrate, the SP-energy (eV) varies with the incident angle within the range $60^{\circ} < \theta < 75^{\circ}$ strictly linear as: $E_{SP}(\theta) = 0.0255\theta - 1.009$.

A compilation of achievable SPR sensor performance is displayed in Table 9.9.

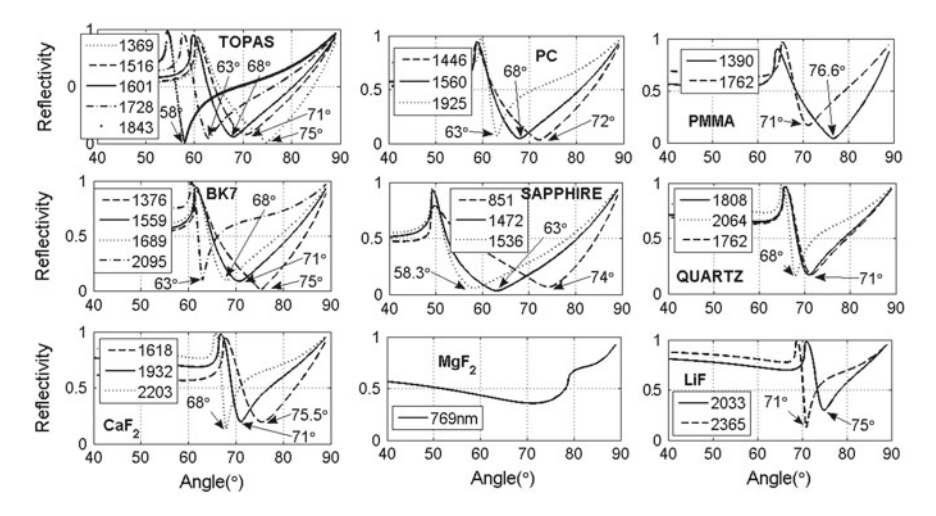


Fig. 9.38 Reflectance curves under AIM-conditions for different substrate materials, as indicated in the *plots*, and different incident wavelengths for the angle range $40^{\circ} < \theta < 90^{\circ}$. W-film thickness is 45 nm, in contact with water

9.10 Thin Vanadium (V) Films

The material crystallizes in the bcc structure. The complex optical constant $\varepsilon_{mr}(\lambda) =$ $\varepsilon'_{mr}(\lambda) + j\varepsilon''_{mr}(\lambda)$ in the former phase has been taken from Ref. [1] and is illustrated in the right inset of Fig. 9.39. The atomic electron configuration is $[Ar]3d^34s^2$. In the solidified material, the outer two 4s electrons hybridize with the partly filled 3d-shell, and form the partially occupied conduction band. The weakly paramagnetic metal exhibits a moderate electrical dc-conductivity of $5.07 \times 10^6 (\Omega \text{ m})^{-1}$. The CDK roughly agrees with the DA, except modulations, in accord with the band-structure calculation provided in Ref. [18]. At wavelengths $\lambda > 1,000$ nm, $\varepsilon'_{mr}(\lambda)$ drops steadily to negative values. $\varepsilon''_{mr}(\lambda)$ is positive and sharply increases at $\lambda > 250$ nm to high values. For the BK7 substrate at 71°, the SP-dispersion appears undistorted, and exhibits a distinct resonant cross-over at approximately 0.98 eV. The SP-energy at high k for the metal-water interface is 1.21 eV. Vanadium films can be readily produced by magnetron sputtering from a massive metal target in low pressure Aratmosphere, possibly by laser ablation. The high boiling temperature of 3,407 °C prevents thermal evaporation from electrically heated Tungsten foils or carbon boats. The metal is corrosion resistant. A thin, native oxide layer immediately forms on the pure metal surface upon exposure to air or an aqueous solution. Structural properties of native oxide films on Vanadium and V-CrTa alloys are reported in Ref. [19].

Related spectral features of the reflectance $R(\lambda)$ in the WIM are shown in Fig. 9.40 for the substrate materials under consideration. Similar to the optical properties of Ta and Nb-films, depicted before, virtually all dielectric substrates, except MgF₂,

Table 9.9 SP-sensor performance and figures of merit for thin W-films at metal-water interface

Table 7.7 31 -School pen	5	nance and ngaics of menting and williams at metal-water internace	metal-water internace			
Operation mode	Suited/best substrate	Optical responsivity	Linear dynamic range	SPR width	Optimum film thickness	Remarks
AIM	All except MgF2 and LiF \mid 50 \pm 20°/RIU	$50 \pm 20^{\circ}$ /RIU	$6 \times 10^{-2} \mathrm{RIU}$	$16 \pm 2^{\circ}$	$40 \pm 5 \mathrm{nm}$	
WIM	All except MgF2 and LiF	ccept MgF ₂ and LiF $3,800 \pm 400 \text{ nm/RIU}$ None	None	$600 \pm 200 \mathrm{nm} \mid 40 \pm 5 \mathrm{nm}$	40 ± 5 nm	

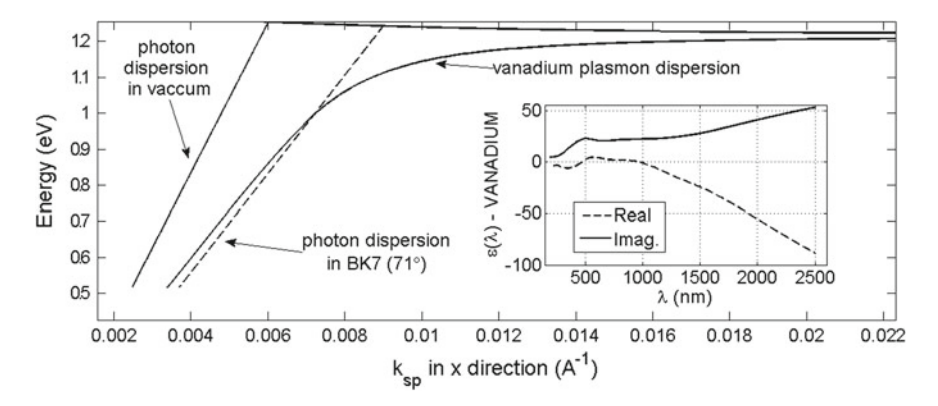


Fig. 9.39 Photon and SPP-dispersion curves of V at the metal-water interface (*solid-line*), calculated for BK7 substrate (*dashed-line*) and incident angle of 71°. There is a clear resonant intersection point resolved for photon energy of 0.98 eV. *Right inset* reveals the real and imaginary fractions of the CDK as function of wavelength

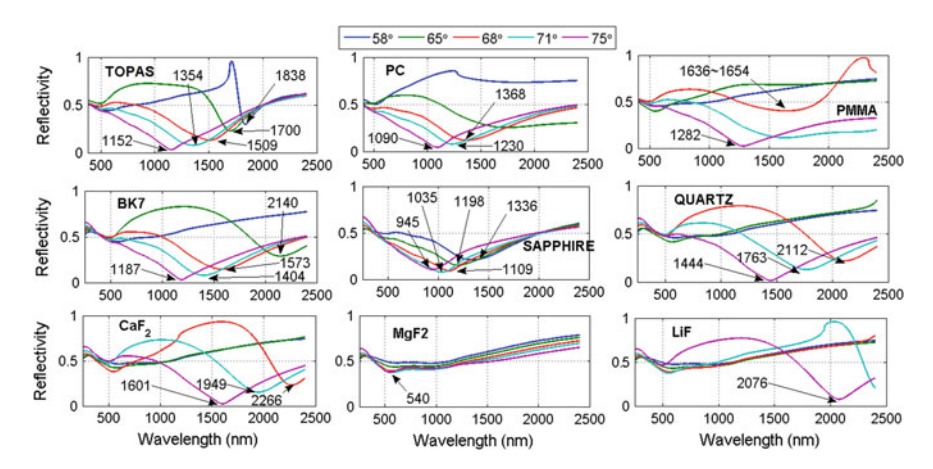


Fig. 9.40 Reflectance curves under WIM-conditions for different substrate materials, as indicated in the *plots*, and incident angles of 58° , 68° , 68° , 71° and 75° for the wavelength range 500 nm $< \lambda < 2,500$ nm. The V-film thickness is 35 nm, in contact with water as the liquid dielectric

exhibit clear, but fairly broad SP-resonances. V-films are thus suited for SP-sensing applications in the WIM.

Reflectance under AIM conditions is shown in Fig. 9.41, again indicating angularly broadened resonances and suited angles <75°, except the MgF₂ substrate. For the BK7 substrate, the SP-energy (eV) varies with the incident angle within the range $60^{\circ} < \theta < 75^{\circ}$ strictly linear as: $E_{SP}(\theta) = 0.0255\theta - 1.009$.

The SPR-sensing characteristic in the AIM is shown in Fig. 9.42, comprising an initial resonance angle of 71° at wavelength of 1,404 nm. The depth of the SP-resonance does not change with the RIU of the analyte. A linear increase

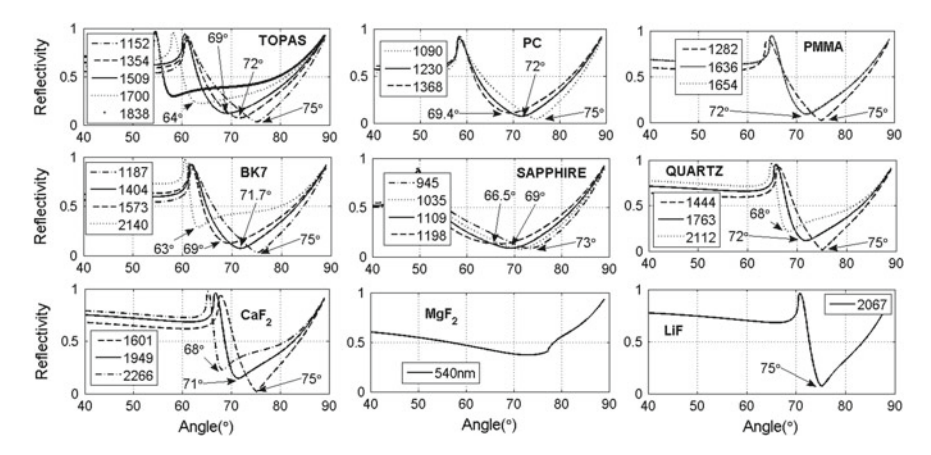


Fig. 9.41 Reflectance curves under AIM-conditions for different substrate materials, as indicated in the *plots*, and different incident wavelengths for the angle range $40^{\circ} < \theta < 90^{\circ}$. W-film thickness is 35 nm. in contact with water

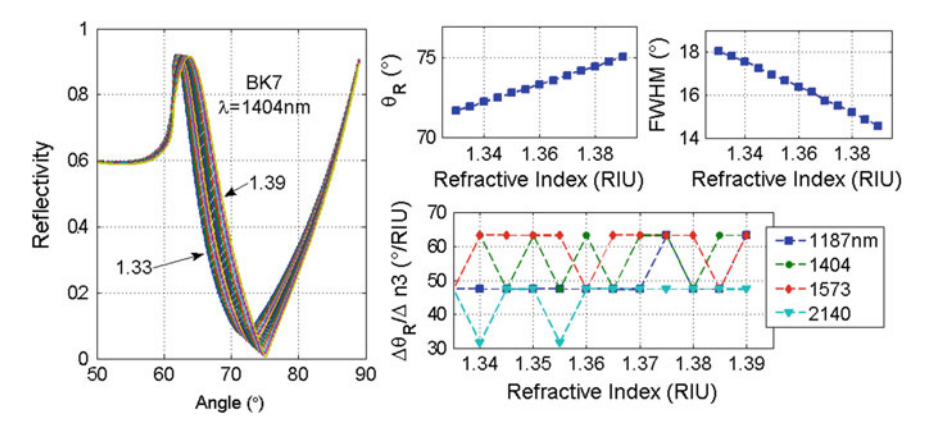


Fig. 9.42 AIM -sensor properties: angular reflectance $R(\theta)$ for different RIU-values of the aqueous analyte 1.33 < n_{an} < 1.39. Substrate is BK7, incident wavelength 1,404 nm. *Upper right* two subfigures show resonance displacements $\theta_{res}(n_{an})$, SP-line broadening $\Delta\theta_{res}(n_{an})$ at FWHM, and responsivity $R_{AIM}(n_{an})$ for four different wavelength below

of resonance angle $\theta_{res}(n_{an})$ and decrease of the line broadening parameter $\Delta\theta_{res}$ (n_{an}) with the RIU of the analyte are resolved in the right upper two sub-figures. SPR sensor responsivity R_{AIM} is shown for four different wavelengths below; their values are moderate and do not vary with the RIU of the analyte.

Eventually, the influence of film thickness for the WIM and AIM is outlined in Figs. 9.43 and 9.44. These data indicate that the V-film thickness for optimum SPR sensor operation would be placed at 35 nm.

A compilation of achievable SPR sensor performance is displayed in Table 9.10.

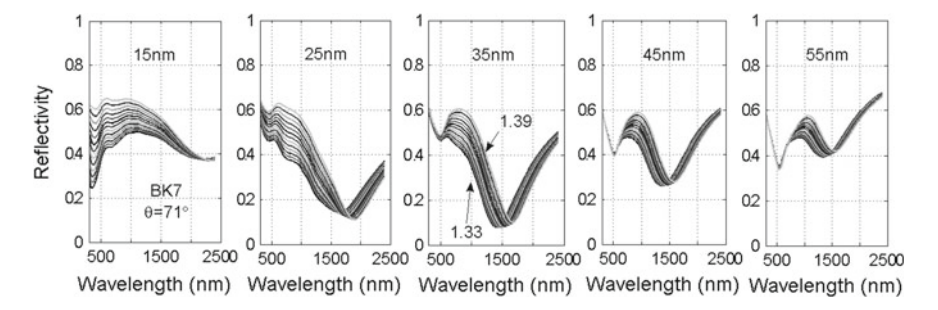


Fig. 9.43 WIM-reflectance at the SP-resonance for different V-film thickness values of 15, 25, 35, 45 and 55 nm

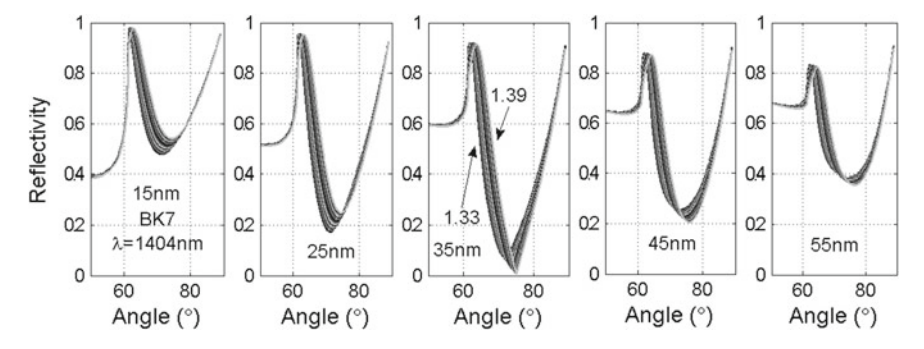


Fig. 9.44 AIM-reflectance at the SP-resonance for different V-film thickness values of 15, 25, 35, 45 and 55 nm

9.11 Thin Zirconium (Zr) Films

The metal crystallizes in the hcp structure. The complex optical constant $\varepsilon_{mr}(\lambda) =$ $\varepsilon'_{mr}(\lambda) + j\varepsilon''_{mr}(\lambda)$ has been taken for Ref. [20] and is illustrated in the right inset of Fig. 9.45. The atomic electron configuration is $[Kr]4d^25s^2$. In the solidified material, the outer two 5s electrons hybridize with the partly filled 4d-shell, and form the partially occupied conduction band. The weakly paramagnetic metal exhibits a low electrical dc-conductivity of $2.37 \times 10^6 (\Omega \text{ m})^{-1}$. The CDK is inappropriately described by the DA. Band-structure calculations of Zirconium are provided in Ref. [21]. At wavelengths $\lambda > 300$ nm, $\varepsilon'_{mr}(\lambda)$ drops steadily to negative values. $\varepsilon_{mr}^{"}(\lambda)$ is positive and steadily increases to moderate values within the spectral range of interest. For the BK7 substrate at 75°, the SP-dispersion appears undistorted, and exhibits a diffuse resonant cross-over at approximately 2 eV. The SP-energy at high k for the metal-water interface is 3.08 eV. Zirconium films can be readily produced by magnetron sputtering from a massive metal target in low pressure Ar-atmosphere. The high boiling temperature of 4,377 °C prevents thermal evaporation from electrically heated Tungsten foils or carbon boats. The metal is corrosion resistant. A thin native oxide layer immediately forms on the pure metal surface upon exposure to air

Table 9.10 SP-sen

Table 7.10 SF-Scills	or per	TOT III alice and iightes of file it for thin v-ninns at inclar-water interface	t ilictal-water iliterrace			
Operation mode	Suited/best substrate	Optical responsivity	Linear dynamic range	SPR width	Optimum film thickness Re	Remarks
AIM	All except MgF ₂ and LiF $ 50 \pm 10^{\circ}$ /RIU	$50 \pm 10^{\circ}$ /RIU	$6 \times 10^{-2} \text{ RIU}$	16 ± 3°	35 nm	
WIM	All except MgF2 and LiF	except MgF ₂ and LiF $ 4,500 \pm 300 \text{ nm/RIU} $ None	None	$1,000 \pm 50 \text{ nm}$ 35 nm	35 nm	

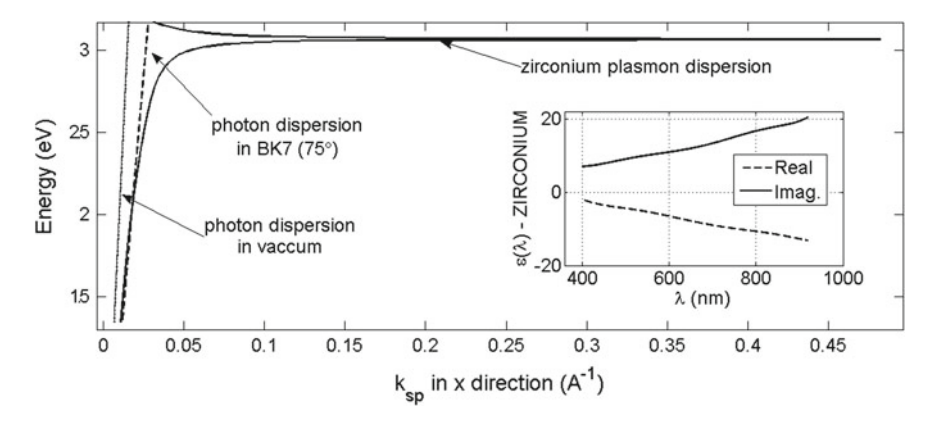


Fig. 9.45 Photon and SPP-dispersion curves of Zr at the metal-water interface (*solid-line*), calculated for BK7 substrate (*dashed-line*) and incident angle of 75°. A diffuse resonant intersection point is resolved for the photon energy of 2 eV. *Right inset* reveals the real and imaginary fractions of the CDK as function of wavelength

or an aqueous solution. Mechanisms and growth kinetics of Zirconium Oxide films is reported in Ref. [22].

Related spectral features of the reflectance $R(\lambda)$ in the WIM are shown in Fig. 9.46 for the substrate materials under consideration. Unlike the optical properties of V and Ta-films depicted before, virtually all dielectric substrates lack presence of a cleary defined SP-resonance at moderate angle and photon energy, except TOPAS and BK7 at high angle. Zirconium films are thus poorly suited for SP-sensing applications in the WIM.

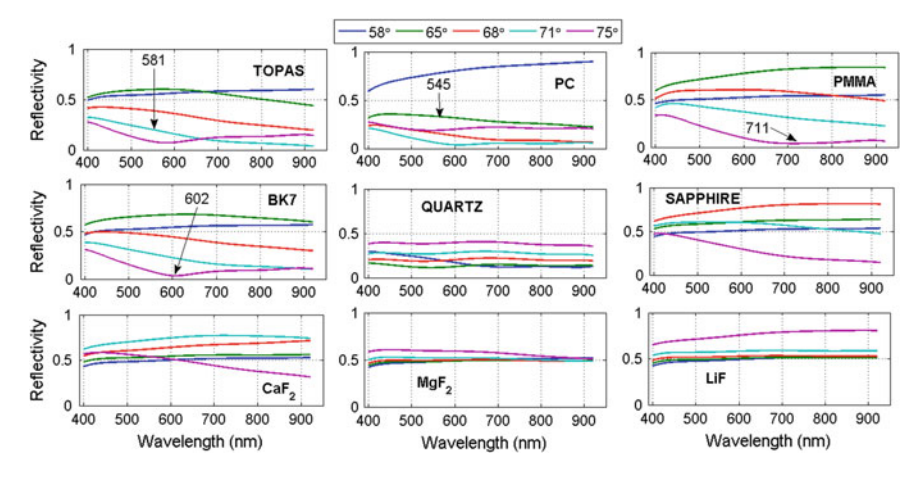


Fig. 9.46 Reflectance curves under WIM-conditions for different substrate materials, as indicated in the *plots*, and incident angles of 58° , 65° , 68° , 71° and 75° for the wavelength range 400 nm $< \lambda < 1,000$ nm. The Zr-film thickness is 25 nm, in contact with water as the liquid dielectric

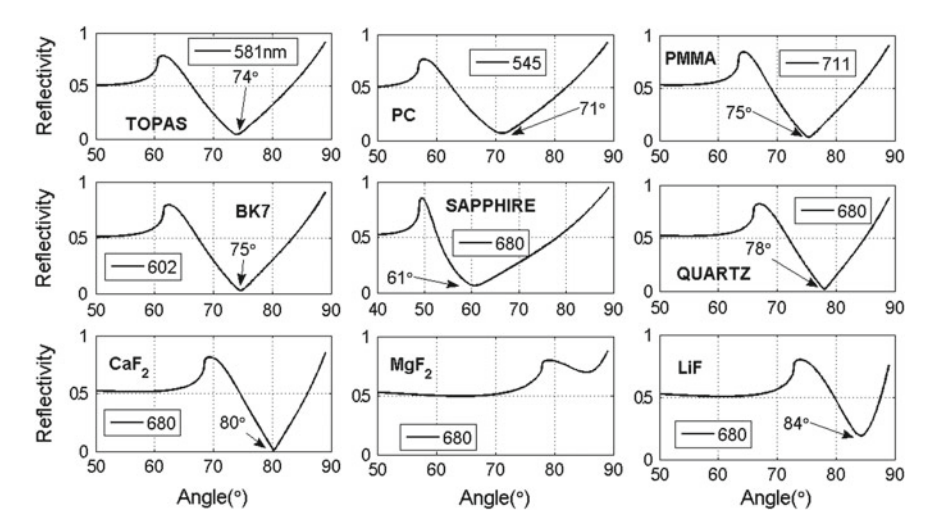


Fig. 9.47 Reflectance curves under AIM-conditions for different substrate materials, as indicated in the *plots*, and different incident wavelengths for the angle range $50^{\circ} < \theta < 90^{\circ}$. Zr-film thickness is 45 nm, in contact with water

Reflectance under AIM conditions is shown in Fig. 9.47, again indicating rather broad SP-resonances and suited angles <75° only for PC and Sapphire substrates.

The SPR-sensing characteristic in the AIM is shown in Fig. 9.48, comprising an initial resonance angle of 75° at wavelength of 602 nm. The depth of the SP-resonance does not change with the RIU of the analyte. A linear increase of resonance angle $\theta_{res}(n_{an})$ and decrease of the line broadening parameter $\Delta\theta_{res}(n_{an})$ with n_{an} are resolved in the right upper two sub-figures. SPR sensor responsivity R_{AIM} is shown for a single wavelength below; the value is moderate and does not vary with n_{an} .

A compilation of achievable SPR sensor performance is displayed in Table 9.11.

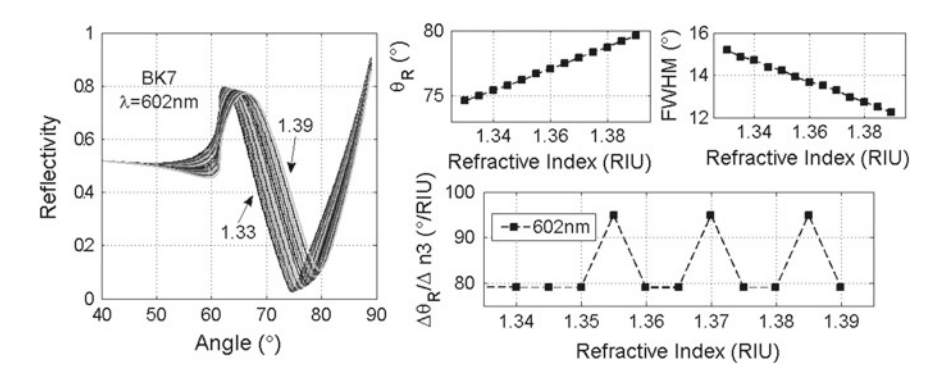


Fig. 9.48 AIM-sensor properties: angular reflectance $R(\lambda)$ for different RIU-values of the aqueous analyte 1.33 < n_{an} < 1.39. Substrate is BK7, incident wavelength 602 nm. *Upper right* two subfigures show resonance displacements $\theta_{res}(n_{an})$, SP-line broadening $\Delta\theta_{res}(n_{an})$ at FWHM, and responsivity $R_{AIM}(n_{an})$ for single wavelength of 602 nm below

Table 9.11 SP-sensor	r per	formance and figures of merit for thin Zr-films at metal-water interface	at metal-water interface			
Operation Mode	Suited/best Substrate	/best Substrate Optical Responsivity	Linear dynamic range SPR width	SPR width	Optimum film thickness Remarks	Remarks
AIM	TOPAS PC	$90 \pm 10^{\circ}$ /RIU	$6 \times 10^{-2} \text{ RIU}$	$14 \pm 2^{\circ}$	25 nm	
WIM	Sapphire BK7/TOPAS	ire BK7/TOPAS $ 4,000 \pm 2,000 \text{ nm/RIU} $ None		$500 \pm 50 \mathrm{nm}$ 25 nm	25 nm	Not suited

References

- 1. Sopra, S.A.: Optical Data. http://www.sspectra.com/sopra.html
- Persson, P.E.S., Johansson, L.I.: Bulk band structure of chromium. Phys. Rev. B 34, 2284–2292 (1986)
- 3. Ordal, M.A., Long, L.L., Bell, R.J., Bell, S.E., Bell, R.R., Alexander Jr, R.W., Ward, C.A.: Optical properties of the metals Al Co, Cu, Au, Fe, Pb, Ni, Pd, Pt, Ag, Ti, and W in the infrared and far infrared. Appl. Opt. 22(7), 1099–1120 (1963)
- 4. Batallan, F., Rosenman, I., Sommers, C.B.: Band structure and Fermi surface of hcp ferromagnetic cobalt. Phys. Rev. B 11, 545–557 (1975)
- Windt, D.L., Cash Jr, W.C., Scott, M., Arendt, P., Newnam, B., Fisher, R.F., Swartzlander, A.B.: Optical constants for thin films of Ti, Zr, Nb, Mo, Ru, Rh, Pd, Ag, Hf, Ta, W, Re, Ir, Os, Pt, and Au from 24Å to 1216Å. Appl. Opt. 27(2), 246–278 (1968)
- Nautiyal, T., Auluck, S.: Electronic structure of ferromagnetic iron: band structure and optical properties. Phys. Rev. B 34, 2299–2305 (1986)
- 7. Palik, E.D.: Handbook of Optical Constants of Solids. Academic Press, Boston (1985)
- 8. Jani, A.R., Tripathi, G.S., Brener, N.E., Callaway, J.: Band structure and related properties of molybdenum. Phys. Rev. B 40, 1593–1602 (1989)
- 9. Wang, C.S., Callaway, J.: Band structure of nickel: spin-orbit coupling, the Fermi surface, and the optical conductivity. Phys. Rev. B **9**, 4897–4907 (1974)
- Yolken, H.T., Kruger, J.: Optical constants of iron in the visible region. J. Opt. Soc. Am. 55(7), 842–844 (1965)
- 11. Jani, A.R., Brener, N.E., Callaway, J.: Band structure and related properties of bcc niobium. Phys. Rev. B **38**, 9425–9433 (1988)
- 12. Mattheiss, L.F.: Electronic structure of niobium and tantalum. Phys. Rev. B, 1, 373 (1970)
- 13. Myers, S., Lin, J., Souza, R.M., Sproul, W.D., Moore, J.J.: The β to α phase transition of tantalum coatings deposited by modulated pulsed power magnetron sputtering. Surf. Coat. Technol. **214**, 38–45 (2013)
- Jepson, O.: Electronic structure and magnetic breakdown in titanium. Phys. Rev. B 12, 2988– 2997 (1975)
- 15. Lu, G., Bernasek, S.L., Schwartz, J.: Oxidation of a polycrystalline titanium surface by oxygen and water. Surf. Sci. **458**, 80–90 (2000)
- Jansen, H.J.F., Freeman, A.J.: Total energy full potential linearized augmented plane wave method for bulk solids: electronic and structural properties of Tungsten. Phys. Rev. B 30, 56–568 (1984)
- Kelsey, G.S.: The anodic oxidation of tungsten in aqueous base. J. Electrochem. Soc. 124, 814–819 (1977)
- 18. Chassaing, G., Gravier, P., Sigrist, M.: Electronic band structure and optical properties of vanadium, niobium and molybdenum thin films. Thin Solid Films **35**, L25–L31 (1976)
- Teraoka, Y., Yoshigoe, A., Harries, J.: Synchrotron radiation photoemission spectroscopy for native oxide layer on Vanadium and VCrTa. J. Surf. Anal. 15, 303–306 (2009)
- Krishman, S., Anderson, D., Nordine, P.C.: Optical properties of liquid and solid zirconium. Phys. Rev. B 49(5), 3161–3166 (1994)
- Jepsen, O., Andersen, O.K., Mackintosh, A.R.: Electronic structure of hcp transition metals. Phys. Rev. B 12, 3084–3114 (1975)
- 22. Bakradze, G.: Ph.D-thesis, Initial oxidation of Zirconium: oxide film growth kinetics and mechanisms. University Stuttgart (2011)

Chapter 10 Other Common Metals

10.1 Thin Indium (In) Films

The solid metal crystallizes in the tetragonal structure. The complex optical constant $\varepsilon_{mr}(\lambda) = \varepsilon'_{mr}(\lambda) + j\varepsilon''_{mr}(\lambda)$ has been taken from Ref. [1] and is illustrated in right inset of Fig. 10.1. The atomic electron configuration is $[Kr]4d^{10}5s^25p^1$. The outer 5s and p electrons form the partially occupied conduction band. The weakly diamagnetic metal exhibits a moderate electrical dc-conductivity of $11.94 \times 10^6 (\Omega \, \text{m})^{-1}$. The CDK is in agreement with the free electron model, supported to band-structure calculation provided in Ref. [2]. At wavelengths $\lambda > 500 \, \text{nm}$, $\varepsilon'_{mr}(\lambda)$ declines steadily to large negative values. In the spectral range of interest, $\varepsilon''_{mr}(\lambda)$ is high positive, and steadily rises at $\lambda > 500$ nm. For the CaF₂ substrate at 75°, the SP-dispersion appears smooth and exhibits two diffuse resonant cross-over points near 1.4 and 5 eV. For the metal-water interface, the SP-energy at large k increases to unusually high values > 19 eV, unlike any other metal reported here. Thin Indium films can be readily produced by magnetron sputtering from a massive metal target in low pressure Ar-atmosphere, also by electron beam and thermal evaporation from electrically heated Tungsten and Tantalum foils or carbon boats. Despite of a very low melting point of 156.6 °C, the material exhibits a rather high evaporation/boiling temperature of 2,072 °C. The metal is corrosion resistant at low T in air or water. Properties of self-limiting native oxide films on the pure metal surface upon exposure to air or aqueous solution are reported in Ref. [3].

Related spectral features of the reflectance $R(\lambda)$ in the WIM are shown in Fig. 10.2 for the substrate materials under consideration. Clear resonances of In-films at accessible angles are resolved for TOPAS, BK7, PMMA, Quartz, CaF₂ and LiF, along with a distinct SP-splitting effect for PMMA. There is a large spectral resonance spreading resolved, ranging from 612 to 2,363 nm for CaF₂ substrates.

The reflectance under AIM conditions is shown in Fig. 10.3. Best suited are CaF_2 and Ouartz substrates.

The sensing characteristic in the AIM is shown in Fig. 10.4, comprising an initial resonance angle of 75° and wavelength of 612 nm. The depth of the SP-resonance decreases towards higher RIU of the analyte. A linear increase of resonance angle

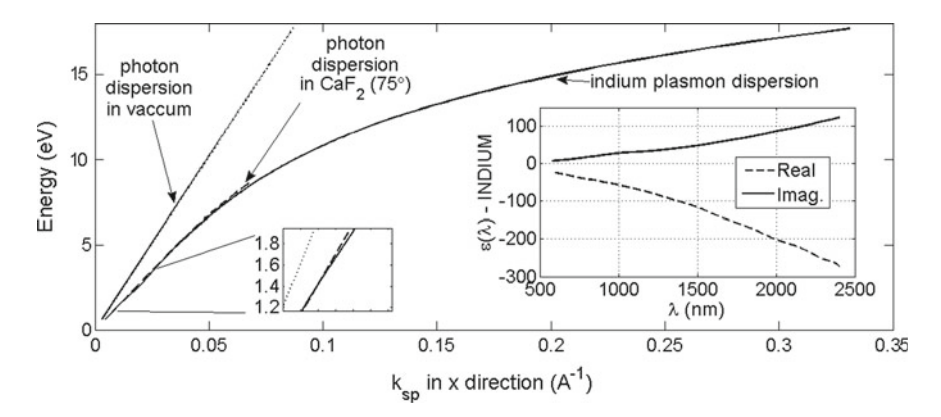


Fig. 10.1 Photon and SPP-dispersion curves of in at the metal-water interface (*solid-line*), calculated for CaF₂ substrate (*dashed-line*) and incident angle of 75°. Diffuse resonant intersection points are resolved near 1.4 eV and near 5 eV. *Right inset* reveals the real and imaginary fractions of the CDK as function of wavelength

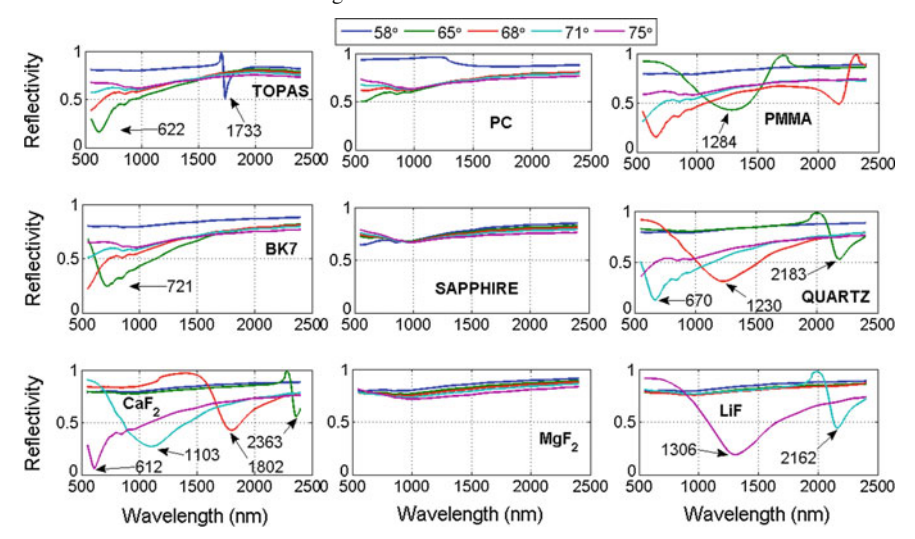


Fig. 10.2 Reflectance curves under WIM-conditions for different substrate materials, as indicated in the *plots*, and incident angles of 58° , 65° , 68° , 71° and 75° for the wavelength range $600\,\mathrm{nm} < \lambda < 2,500\,\mathrm{nm}$. The In-film thickness is $25\,\mathrm{nm}$, in contact with water as the liquid dielectric

 $\theta_{res}(n_{an})$ and weak decrease of the line broadening parameter $\Delta\theta_{res}(n_{an})$ with n_{an} are resolved in the right two upper two sub-figures. SPR sensor responsivity R_{AIM} is shown for a single wavelengths below; their values are high and increase with the RIU of the analyte.

Eventually, the influence of film thickness for the AIM is outlined in Fig. 10.5. This data set clearly indicates that the In-film thickness for optimum SPR sensor operation would be placed at 20 ± 5 nm.

A compilation of achievable SPR sensor performance is displayed in Table 10.1.

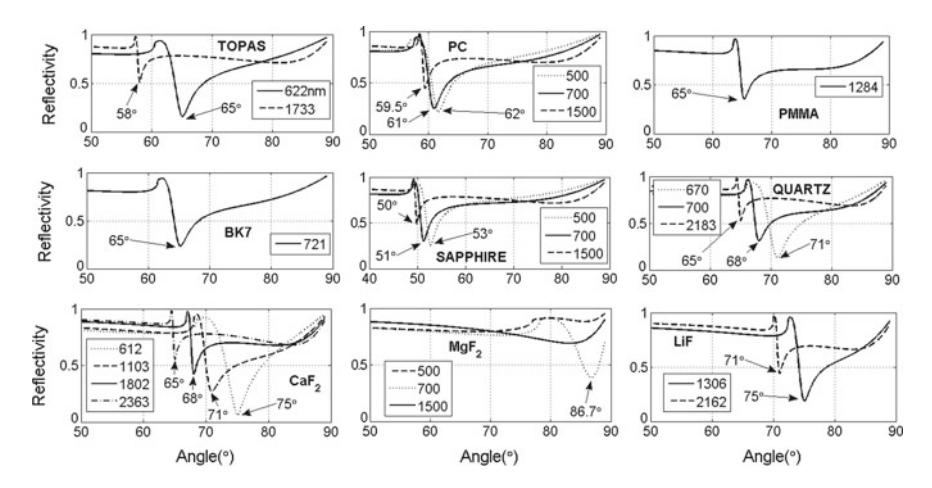


Fig. 10.3 Reflectance curves under AIM-conditions for different substrate materials, as indicated in the *plots*, and different incident wavelengths for the angle range $30^{\circ} < \theta < 90^{\circ}$. In-film thickness is 25 nm, in contact with water

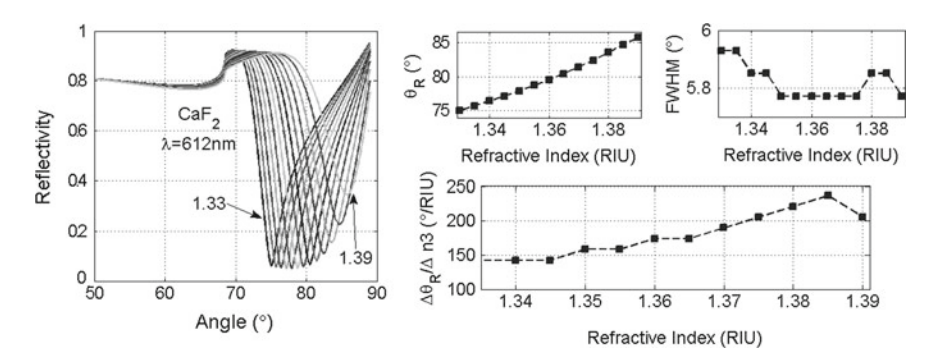


Fig. 10.4 AIM-sensor properties angular reflectance $R(\lambda)$ for different RIU-values of the aqueous analyte 1.33 < n_{an} < 1.39. Substrate is CaF₂, incident wavelength is 612 nm. *Upper right* two sub-figures show resonance displacements $\theta_{res}(n_{an})$ and angular SP-line broadening $\Delta\theta_{res}(n_{an})$ at FWHM and responsivity $R_{AIM}(n_{an})$ below for a single wavelength

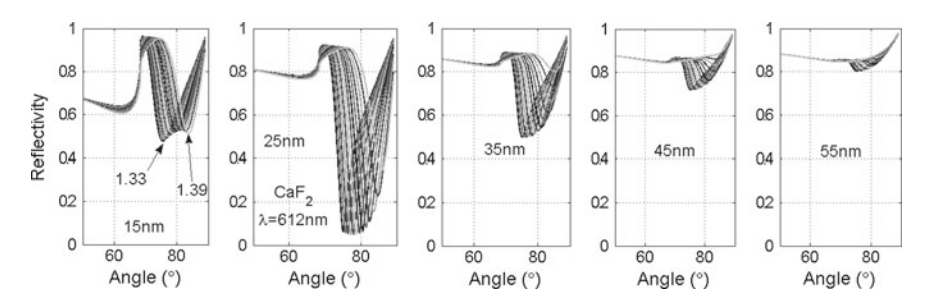


Fig. 10.5 AIM-reflectance at the SP-resonance for different In-film thickness values of 15, 25, 35, 45 and 55 nm

Table 10.1 SP-sensor performance and figures of merit for thin In-films at metal-water interface

Table 10.1 31 -sen	isor periormance and rigu	e and rigures of including unit in-initis at inclar-water interface	at ilictal-water illicitace			
Operation mode	Suited/best substrate	Optical responsivity	Linear dynamic range	SPR width	Optimum film thickness	Remarks
AIM	Quartz CaF ₂	$150 \pm 100^{\circ}$ /RIU	$<3 \times 10^{-2} \text{RIU}$	5.8°	25 nm	
WIM	Quartz CaF ₂	$6,000 \pm 2,000 \mathrm{nm/RIU}$	None	$400 \pm 100 \mathrm{nm}$ $20 \pm 5 \mathrm{nm}$	$20 \pm 5 \mathrm{nm}$	

10.2 Thin Tin (Sn) Films

The material exists in two different phases: as zero gap, semi-conducting α -Sn with covalent inter-atomic binding or as metallic β -Sn, depending on temperature, pressure and/or amount and type of impurities. The complex optical constant $\varepsilon_{mr}(\lambda) = \varepsilon'_{mr}(\lambda) + j\varepsilon''_{mr}(\lambda)$ of the metal has been taken from Ref. [4] and is illustrated in the right inset of Fig. 10.6. The atomic electron configuration is $[Kr]4d^{10}5s^25p^2$. In the β -phase, apparently the outer 5s and p electrons form the partially occupied conduction band. The weakly paramagnetic metal exhibits low electrical deconductivity of $8.69 \times 10^6 (\Omega \text{ m})^{-1}$. The CDK partially agrees with the DA, according to band-structure calculation provided in Ref. [5]. At wavelengths $\lambda > 100$ nm, $\varepsilon'_{mr}(\lambda)$ declines steadily to large negative values. In the spectral range of interest, $\varepsilon_{mr}^{"'}(\lambda)$ is positive and relatively small and slowly rises at $\lambda > 500$ nm. For the BK7 substrate at 71°, the SP-dispersion appears smooth and exhibits a diffuse resonant cross-over at approximately 2.5 eV. For the metal-water interface, the SP-energy at high k approaches 6.8 eV. β -Tin-films can be produced by magnetron sputtering from a massive metal target in low pressure Ar-atmosphere, also by electron beam and thermal evaporation from electrically heated Tungsten and Tantalum foils or carbon boats. Despite of a very low melting point of 232 °C, the material exhibits a very high evaporation/boiling temperature of 2,602 °C. The metal is highly corrosion resistant at low T in air or water. Properties and existence of thin native oxide layers on the pure metal surface upon exposure to air or aqueous solution are reported in Ref. [6].

Related spectral features of the reflectance $R(\lambda)$ in the WIM are shown in Fig. 10.7 for the substrate materials under consideration. Clear resonances of Sn-films at accessible angles are resolved for TOPAS and BK7, including a weak SP-splitting effect at high angle. Reflectance under AIM conditions is shown in Fig. 10.8.

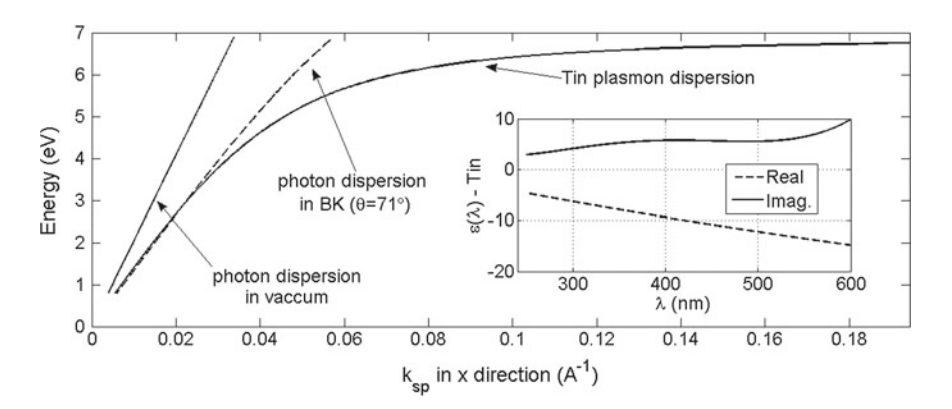


Fig. 10.6 Photon and SPP-dispersion curves of β -Sn at the metal-water interface (*solid-line*), calculated for BK7 substrate (*dashed-line*) and incident angle of 71°. A diffuse resonant intersection point is resolved near 3 eV. *Right inset* reveals the real and imaginary fractions of the CDK as function of wavelength

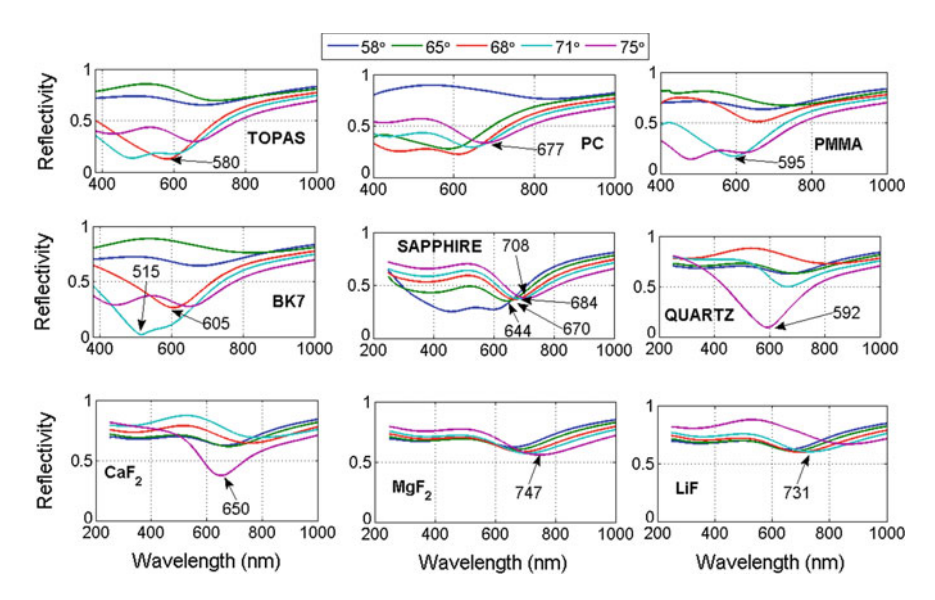


Fig. 10.7 Reflectance curves under WIM-conditions for different substrate materials, as indicated in the *plots*, and incident angles of 58° , 65° , 68° , 71° and 75° for the wavelength range $300\,\mathrm{nm} < \lambda < 1,000\,\mathrm{nm}$. The Sn-film thickness is $25\,\mathrm{nm}$, in contact with water as the liquid dielectric

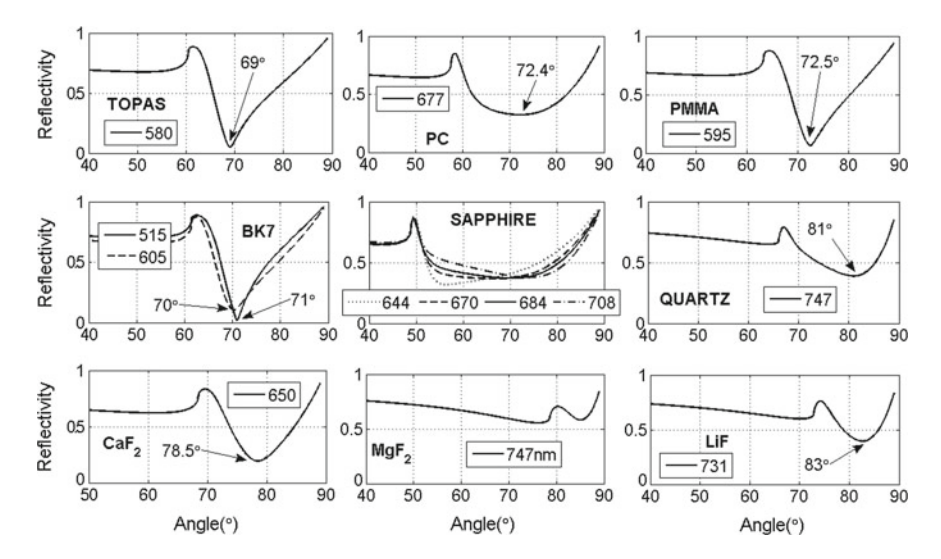


Fig. 10.8 Reflectance curves under AIM-conditions for different substrate materials, as indicated in the plots, and different incident wavelengths for the angle range $40^{\circ} < \theta < 90^{\circ}$. β-Sn-film thickness is 25 nm, in contact with water

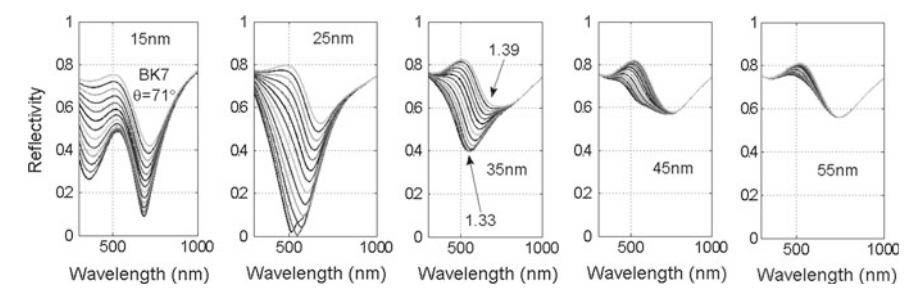


Fig. 10.9 WIM-reflectance at the SP-resonance for different β -Sn-film thickness values of 15, 25, 35, 45 and 55 nm

Operation Suited/best Optical SPR width Optimum Remarks Linear mode substrate responsivity dynamic range film thickness (RIU) $>5 \times 10^{-2}$ $9.5 \pm 1^{\circ}$ AIM TOPAS/BK7 $| 120 \pm 10^{\circ}$ /RIU 25 nm 4×10^{-2} TOPAS/BK7 2,000 nm/RIU $200 \pm 40 \,\mathrm{nm} | 25 \,\mathrm{nm}$ WIM Poorly suited method

Table 10.2 SP-sensor performance and figures of merit for thin Ru-films at metal-water interface

The influence of film thickness for the WIM is outlined in Fig. 10.9. This data set clearly indicates that the β -Sn-film thickness for optimum SPR sensor operation would be placed at 25 nm.

A compilation of achievable SPR sensor performance is displayed in Table 10.2.

10.3 Thin Zinc (Zn) Films

Zn-metal crystallizes in the hcp structure. The complex optical constant $\varepsilon_{mr}(\lambda) =$ $\varepsilon'_{mr}(\lambda) + j\varepsilon''_{mr}(\lambda)$ has been taken from Ref. [7] and is illustrated in the right inset of Fig. 10.10. The atomic electron configuration is $[Ar]3d^{10}4s^2$. In the solidified material, the outer two 4s electrons hybridize with the partly filled 4d-shell, and form the partially occupied conduction band. The metal is diamagnetic and exhibits moderate electrical dc-conductivity of $16.9 \times 10^6 \, (\Omega \, \text{m})^{-1}$. The CDK is inappropriately described by the DA. Band-structure calculations are provided in Ref. [8]. At wavelengths $\lambda > 1$, 060 nm, $\varepsilon'_{mr}(\lambda)$ drops steadily to negative values. $\varepsilon''_{mr}(\lambda)$ -values are high positive and exhibit distinct modulations within the spectral range of interest. For the BK7 substrate at 68°, the SP-dispersion appears undistorted, with presence of a diffuse resonant cross-over point at around 0.8 eV. The SP-energy at high k for the metal-water interface is 1.06 eV. Zinc films can be produced by magnetron sputtering from a massive metal target in low pressure Ar-atmosphere, or by electrochemical deposition. The high vapor pressure and very low boiling temperature of 907 °C prevents thermal evaporation from electrically heated Tungsten foils or carbon boats in high vacuum systems. This would result in a severe contamination of the vacuum

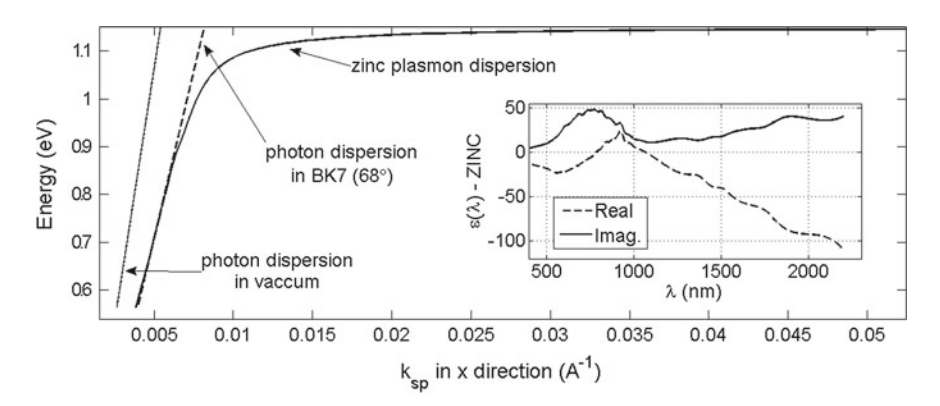


Fig. 10.10 Photon and SPP-dispersion curves of Zn at the metal-water interface (*solid-line*), calculated for BK7 substrate (*dashed-line*) and incident angle of. *Right inset* reveals the real and imaginary fractions of the CDK as function of wavelength

chamber by internal metal deposits. The metal is corrosion resistant. A thin native self-limiting oxide layer immediately forms on the pure metal surface immediately upon exposure to air or an aqueous solution. Related structural and kinetic properties are reported in Ref. [9].

Related spectral features of the reflectance $R(\lambda)$ in the WIM are shown in Fig. 10.11 for the substrate materials under consideration. Similar to the optical properties of Ta and W-films, depicted before, virtually all dielectric substrates, except LiF and MgF₂, exhibit moderately broadened SP-resonances. Zn-films are thus suited for SP-sensing applications in the WIM.

Reflectance under AIM conditions is shown in Fig. 10.12, again indicating angularly broadened resonances and suited angles $<75^{\circ}$, except the MgF₂ substrate.

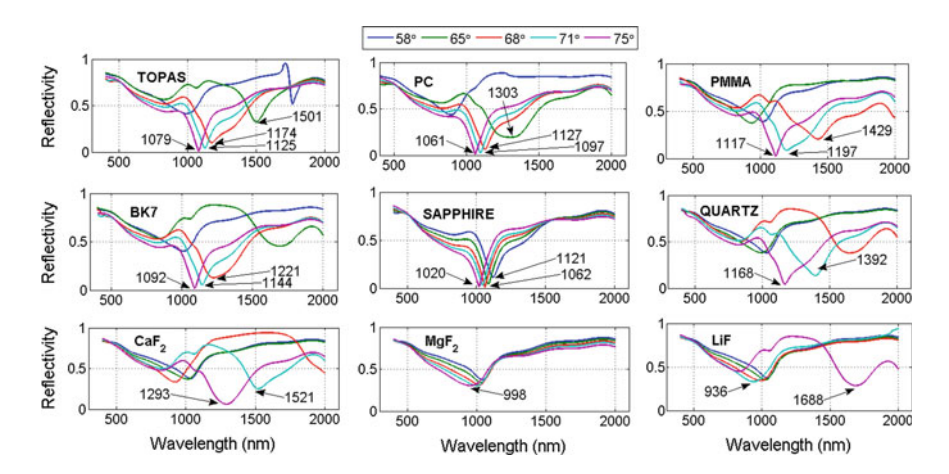


Fig. 10.11 Reflectance curves under WIM-conditions for different substrate materials, as indicated in the *plots*, and incident angles of 58° , 68° , 68° , 71° and 75° for the wavelength range $400 \, \mathrm{nm} < \lambda < 2,000 \, \mathrm{nm}$. The Zn-film thickness is $45 \, \mathrm{nm}$, in contact with water as the liquid dielectric

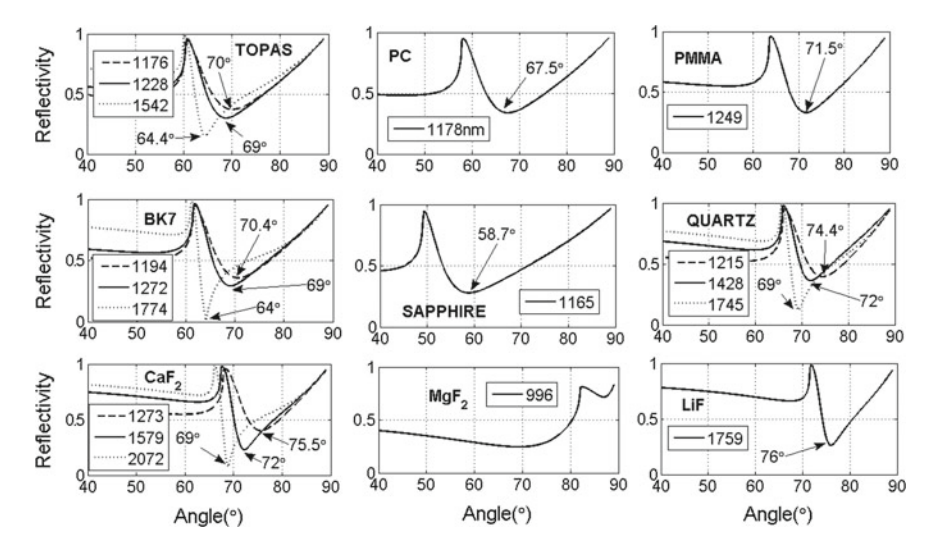


Fig. 10.12 Reflectance curves under AIM-conditions for different substrate materials, as indicated in the *plots*, and different incident wavelengths for the angle range $40^{\circ} < \theta < 90^{\circ}$. Zn-film thickness is 45 nm, in contact with water

For the BK7 substrate, the SP-energy (eV) varies with the incident angle within the range $65^{\circ} < \theta < 75^{\circ}$ non-linearly as: $E_{SP}(\theta) = -0.001\theta^2 + 0.027\theta - 9.323$.

A compilation of achievable SPR sensor performance is displayed in Table 10.3.

10.4 Thin Lead (Pb) Films

The Pb-metal crystal structure is fcc (face centered cubic). The complex optical constant $\varepsilon_{mr}(\lambda) = \varepsilon'_{mr}(\lambda) + j\varepsilon''_{mr}(\lambda)$ has been taken from Ref. [10] and is illustrated in the right inset of Fig. 10.13. The atomic electron configuration is $[Xe]4f^{14}5d^{10}6s^26p^2$. In the solidified material, the outer 6s, p electrons hybridize with the partly filled 5d-and f shells, and form the partially occupied conduction band. The metal is diamagnetic and exhibits a poor electrical dc-conductivity of $4.21 \times 10^6 \, (\Omega \, \text{m})^{-1}$. The CDK is in accord with the free electron model and the band-structure calculations are provided in Ref. [11]. At wavelengths $\lambda > 1$, 000 nm, $\varepsilon'_{mr}(\lambda)$ drops steadily to negative values. $\varepsilon''_{mr}(\lambda)$ -values are positive and increases further towards $\lambda > 1$, 500 nm. For the BK7 substrate at 63°, the SP-dispersion appears heavily distorted, but exhibits a resonant cross-over point around 1.37 eV. The SP-energy is not clearly resolved at moderate k for the metal-water interface, but an apparent smooth transition at low k-values from the bound SPP to the quasi-bound (Qb) state, as defined before in Chap. 2. This unusual feature is not in agreement with the DA. Lead films can be produced by magnetron sputtering from a massive metal target in low pressure Ar-atmosphere, in inert atmosphere, by electron beam and thermal evaporation in high vacuum. Lead has a relative low melting temperature at 327 °C and boiling points 1,749 °C. The figures for electrode potential show that Lead is slightly easier

Table 10.3 SP-sensor performance and figures of merit for thin Zn-films at metal-water interface

Operation mode	Suited/best substrate	Optical responsivity	Linear dynamic range	SPR width	Linear dynamic range SPR width Optimum film thickness Remarks	Remarks
AIM	All except MgF2 and LiF	MgF $_2$ and LiF $ 80 \pm 10^\circ/\mathrm{RIU} $	$>6 \times 10^{-2} \mathrm{RIU}$	$9.5 \pm 1^{\circ}$	45 nm	
WIM	All except MoF, and LiF	JoE and LiF 4, 000 + 2, 000 nm/RIII None	None	$200 + 40 \mathrm{nm}$ 45 nm	45 nm	SP-split for Sapphire

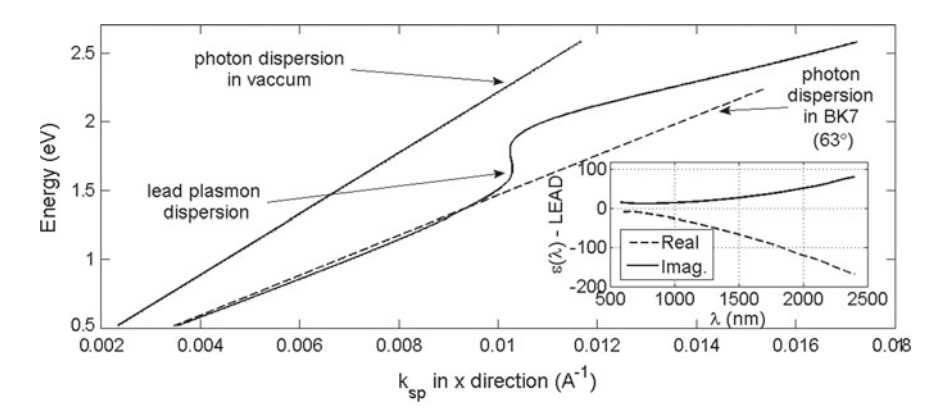


Fig. 10.13 Photon and SPP-dispersion curves of Lead metal-water interface (*solid-line*), calculated for a BK7 substrate (*dashed-line*). The intersection point is near 1.37 eV. *Right inset* reveals the real and imaginary fractions of the CDK

to oxidize; with a high corrosion resistance and ability to react with organic chemicals. Related structural and kinetic properties are reported in Ref. [12].

Related spectral features of the reflectance $R(\lambda)$ in the WIM are shown in Fig. 10.14 for the substrate materials under consideration. Similar to the optical properties of Mo, virtually all dielectric substrates, except MgF₂, exhibit moderately exhibit clear SP-resonances centered, however, at long wavelength or at moderate incident angles. Pb-films are thus suited for SP-sensing applications in the WIM.

Reflectance under AIM conditions is depicted in Fig. 10.15, and confirms the moderate resonance angles, except for MgF_2 substrates. The plots indicate a distinct

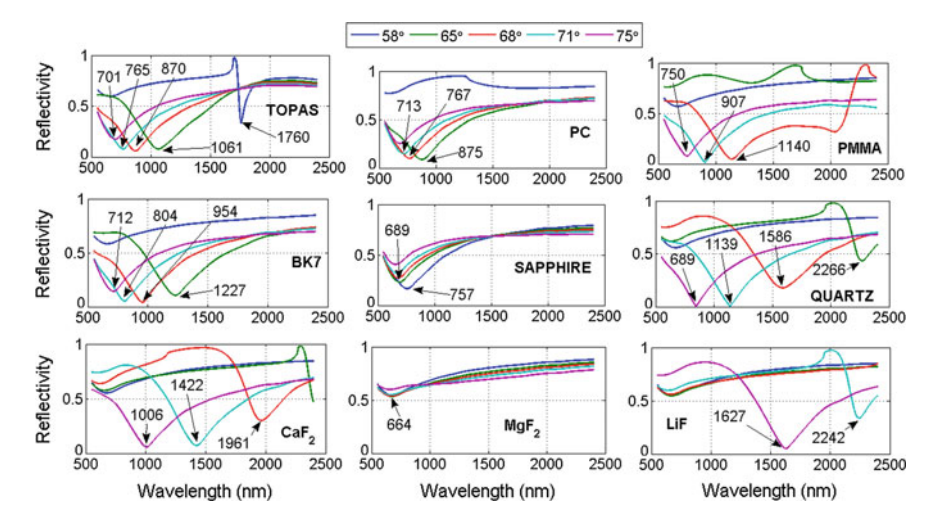


Fig. 10.14 Reflectance curves under WIM-conditions for different substrate materials, as indicated in the *plots*, and incident angles of 58°, 65°, 68°, 71° and 75° for the wavelength range 500 nm $< \lambda < 2,500$ nm. The film thickness is 30 nm, being in contact with water as the liquid dielectric

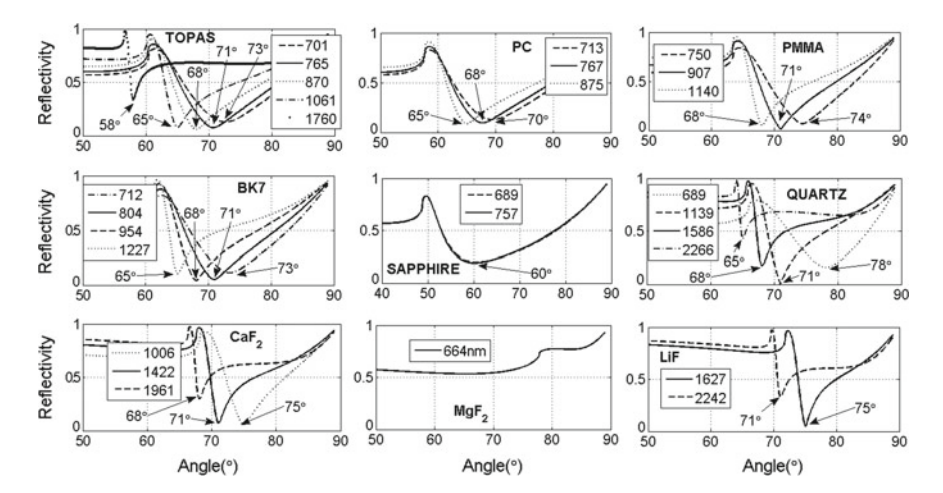


Fig. 10.15 Reflectance curves under AIM-conditions for different substrate materials, as indicated in the *plots*, and different incident wavelengths for the angle range $40^{\circ} < \theta < 90^{\circ}$. Pb-film thickness is 30 nm, in contact with water

decrease of the line broadening parameter $\Delta\theta_{res}$ with increasing wavelength, established towards smaller resonance angles.

For the BK7 substrate, the SP-energy (eV) varies with the incident angle within the range $65^{\circ} < \theta < 75^{\circ}$ non-linearly as: $E_{SP}(\theta) = -0.0055\theta - 2.407$.

The SPR-sensing characteristic in the AIM is shown in Fig. 10.16, comprising an initial resonance angle of 68° and wavelength of 954 nm. The depth of the SPR resonance appears independent of the RIU of the analyte. A nearly linear increase of resonance angle $\theta_{res}(n_{an})$, but decrease of line broadening parameter with the RIU of the analyte are resolved in the upper two sub-figures at right. SPR sensor responsivities R_{AIM} are shown for four different wavelengths below, and decrease towards larger values.

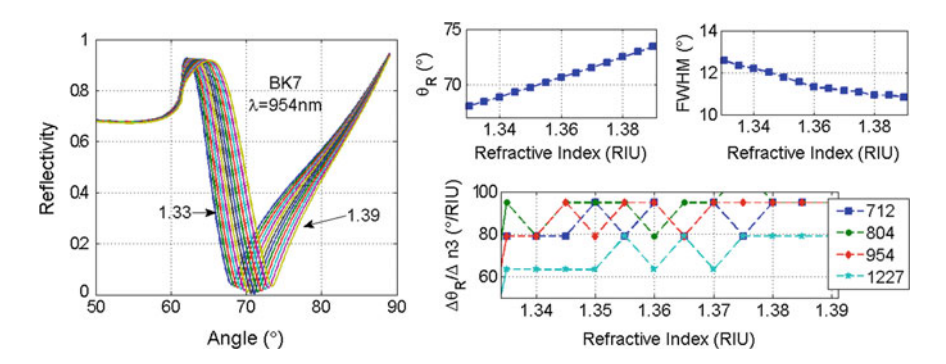


Fig. 10.16 AIM-sensor properties: angular reflectance $R(\lambda)$ for different RIU-values of the aqueous analyte 1.33 < n_{an} < 1.39. Substrate is BK7, incident wavelength 954 nm. *Right* three sub-figures show resonance displacements $\theta_{res}(n_{an})$, SP-line broadening $\Delta\theta_{res}$ at FWHM and responsivity R_{AIM}

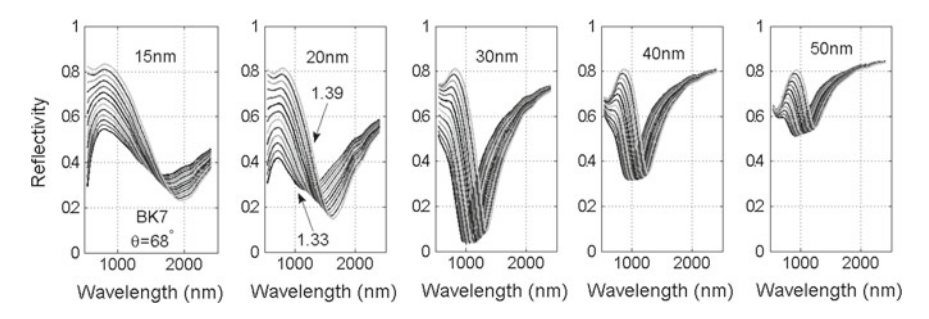


Fig. 10.17 WIM-reflectance at the SP-resonance for different Pb-film thickness values of 10, 20, 30, 40 and 50 nm

Eventually, the influence of film thickness for the WIM is outlined in Fig. 10.17. This data set clearly indicates that the Pb-film thickness for optimum SPR sensor operation would be placed at 30 nm.

10.4.1 Long Range Surface Plasmon Polariton (LRSPP-mode)

SP-sensor properties in the LRSPP mode in the WIM are depicted in Fig. 10.18. The spectral characteristics (left figure) reveals two co-existing SP-dips with the symmetric (short range) mode at around 600 nm (blue line in right figures) and the anti-symmetric, long range (LRSPP) mode at 1,550 nm (green line). Comparison with Fig. 10.17 illustrates an increase by more than a factor 1.5 for the responsivity $R_{WIM}(n_{an})$ in the LRSPP-mode in the lower right figure, but decreases with n_{an} .

SP-sensor properties in presence of the LRSPP mode in the AIM are depicted in Fig. 10.19. In the AIM mode, the magnitude of the sensor resonsivity $R_{AIM}(\lambda)$ for the LRSPP does not differ significantly from the short range SPP from Fig. 10.16, for the shifted wavelength to 950 nm.

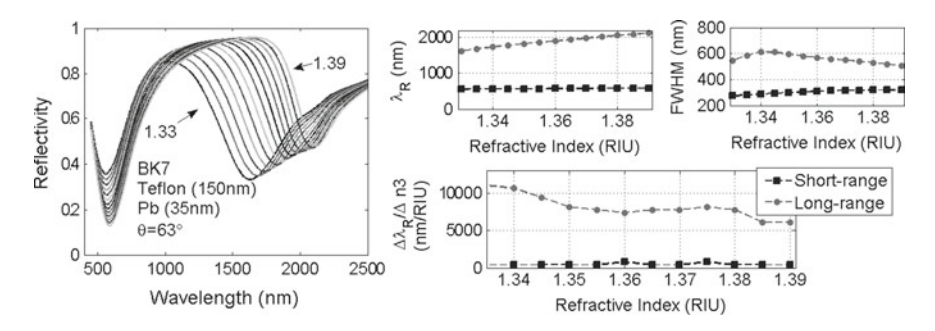


Fig. 10.18 WIM-sensor properties in presence of the LRSPP mode: spectral reflectance $R(\lambda)$ (left figure) for different RIU-values of the aqueous analyte $1.33 < n_{an} < 1.39$, indicating two coexisting SP-dips. Substrate is BK7, with a 150 nm Teflon film on top, incident angle is 63°. Three figures at right show line broadening $\Delta \lambda_{res}(n_{an})$ and resonance displacements $\lambda_{res}(n_{an})$ at top and responsivities $R_{WIM}(n_{an})$ below for short (lines with squares) and long range SPP's (lines with circles)

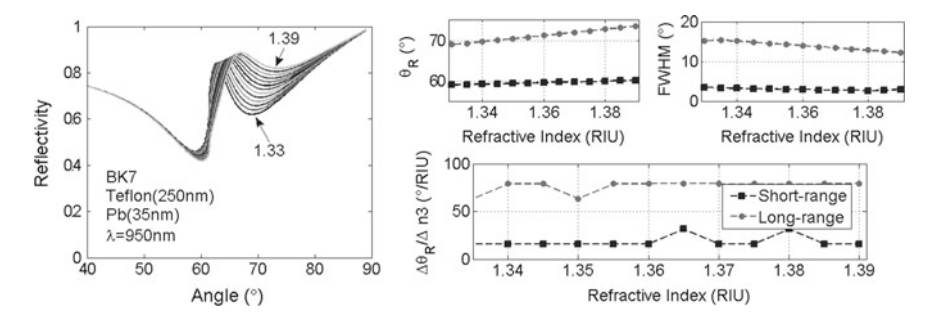


Fig. 10.19 AIM-sensor properties in presence of the anti-symmetric LRSPP-mode: angular reflectance $R(\lambda)$ at left figure for different RIU-values of the aqueous analyte 1.33 < n_{an} < 1.39, indicating two SP-dips. Substrate is BK7 with a 450 nm thin Teflon film on top and the metal film placed thereon. Incident wavelength is 670 nm. Three figures at right show line broadening $\Delta\theta res(n_{an})$ and angular resonance displacements $\theta_{res}(n_{an})$ at top, and associated responsivities $R_{AIM}(n_{an})$ at bottom for short (lines with squares) and long range modes (lines with circles)

10.4.2 Localized Plasmons in Colloidal Pb-Particles (LSPR-mode)

The optical absorption characteristic of colloidal Pb-particles with 45 nm diameter, immersed into an aqueous solution with varying refractive index n_{an} as function of wavelength, is depicted in Fig. 10.20. Upper right insets reveal spectral resonance position $\lambda_{res}(n_{an})$ at top and responsivity $S_{Q_{ext}}(n_{an})$ at bottom. This quantity is considerably smaller than calculated before for both, short and long range SPP's.

A compilation of achievable SPR sensor performance is displayed in Table 10.4.

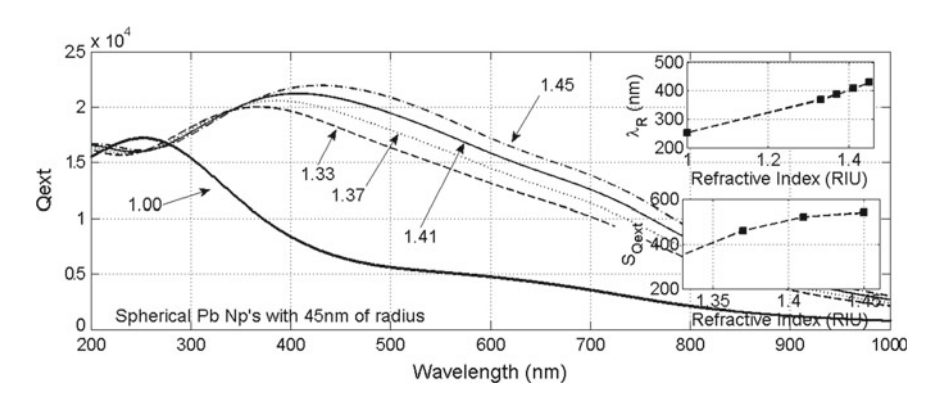


Fig. 10.20 Optical absorption for Pb-particles of 45 nm diameter, calculated as function of wavelength for different refractive index (RIU) values of the surrounding aqueous solution. *Right* two *insets* show resonance position $\lambda_R(n_{an})$ and optical responsivity $S_{Q_{ext}}(n_{an})$, taken at the spectral maximum near 450 nm

Table 10.4 St School	or periorinance and it	tame 10:4 of escribed performance and rightes of meeti for thin 10-mins at meetal-water miterace	או-שמניו וווניוומככ			
Operation mode	Suited/best	Optical responsivity	Linear dynamic range SPR width		Optimum film Remarks	Remarks
	substrate				thickness	
AIM	All except MgF ₂ $ 65-95^{\circ}/RIU $	65–95°/RIU	$<5 \times 10^{-2} \mathrm{RIU}$	$12 \pm 2^{\circ}$	30 nm	Single resonance
WIM	All except MgF2	All except MgF ₂ 5,500–7,500 nm/RIU	none	$500 \pm 50 \mathrm{nm}$ 30 nm	30 nm	Single resonance
AIMLRSPP	BK7/Teflon	80°/RIU	$< 5 \times 10^{-2} \text{ RIU}$	$14 - 10^{\circ}$		Split resonance
	bi-layer					
WIMLRSPP nm/RIU BK7/Teflon	BK7/Teflon	7,000–10,000 nm/RIU 550 \pm 20 nm		$550 \pm 20 \text{nm}$		Split resonance
	bi-layer $<4 \times 10^{-2}$					
LSPR	Nano-particles	540 nm/RIU	$> \times 10^{-2} \text{ RIU}$	200 nm	45 nm particles	45 nm particles Colloidal particles

10.5 Thin Bismuth (Bi) Films

The Bismuth complex optical constant $\varepsilon_{mr}(\lambda) = \varepsilon'_{mr}(\lambda) + j\varepsilon''_{mr}(\lambda)$ has been taken from Ref. [13] and is illustrated in the right inset of Fig. 10.21. The electron configuration of the single atom is $[Xe]4f^{14}5d^{10}6s^26p^3$. In the solid state, the two outer 6s, p electrons hybridize with the incomplete 5d-shell, and form the partially occupied conduction band, as the band-structure calculation show in Refs. [14, 15]. The metal is most naturally diamagnetic metal and exhibits low electrical de-conductivity of $8.67 \times 10^6 \, (\Omega \, \text{m})^{-1}$. The CDK is insufficiently described by the DA, or free electron model. Within the wavelength range of interest, $300 \, \mathrm{nm} < \lambda < 1{,}200 \, \mathrm{nm}, \, \varepsilon'_{mr}(\lambda)$ exhibits rather small negatives values. $\varepsilon_{mr}^{"}(\lambda)$ is positive and increases steadily to high numbers. For the Sapphire substrate at 85°, the SP-dispersion is weakly distorted and exhibits a resonant cross-over at around 0.55 eV. In the asymptotic limit at high k, the SP-energy approaches 1.05 eV at the metal-water interface. Bismuth films are best produced by thermal evaporation technique, magnetron sputtering from a massive metal-target in inert atmosphere or electro-plating. The metal has a relative low boiling/evaporation temperature of 1,564 °C and melting point of 271 °C. Native iridescent oxides appears on the metal surface and variations in the thickness of the oxide layer causes different wavelengths of light that interfere upon reflection. The electrical resistivity of Bismuth increases in presence of a magnetic field and shows the highest Hall coefficient among metals.

Related spectral features of the reflectance $R(\lambda)$ in the WIM are shown in Fig. 10.22 for the substrate materials under consideration. The metal exhibits severely distorted SP-resonances that are mostly shifted into the infrared region of the electromagnetic spectrum similar to Platinum. Due to the broad resonance, Bi-films appear poorly suited for SP-sensing applications in the WIM.

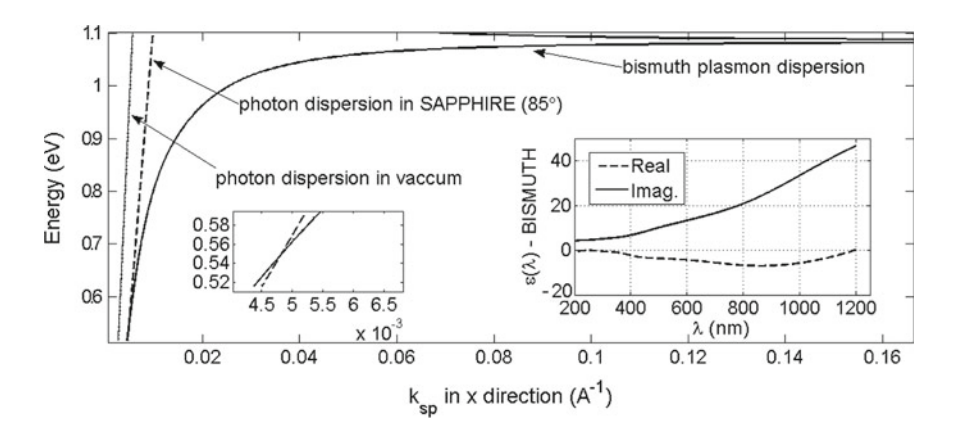


Fig. 10.21 Photon and SPP-dispersion curves of Bismuth at the metal-water interface (*solid-line*), calculated for a Sapphire substrate (*dashed-line*) and incident angle of 85°. The related intersection point and resonance appears near 0.58 eV at very low k-values. *Right inset* reveals the real and imaginary fractions of the CDK; as function of wavelength

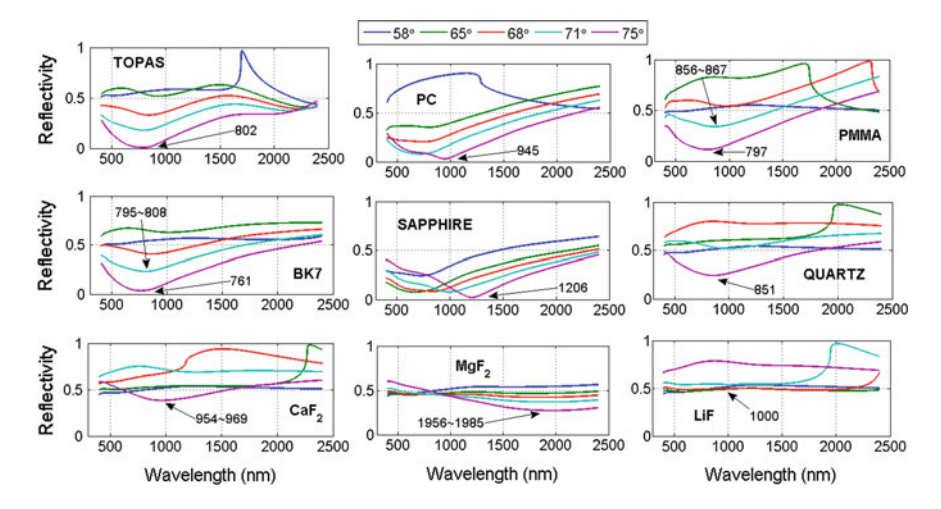


Fig. 10.22 Reflectance curves under WIM-conditions, calculated for different substrate materials, as indicated in the plots. Incident angles are: 58° , 65° , 68° , 71° and 75° for the wavelength range $300 \, \mathrm{nm} < \lambda < 2,500 \, \mathrm{nm}$. The Bi-film thickness is $25 \, \mathrm{nm}$, in contact with water as the liquid dielectric

The reflectance under AIM conditions is shown in Fig. 10.23, indicating that all substrates, exhibit high resonance angles, which are difficult to realize technically. The SP-line broadening parameters $\Delta \lambda_{res}$ and $\Delta \theta_{res}$ is consistently very high for all substrate materials.

A compilation of achievable SPR sensor performance is displayed in Table 10.5.

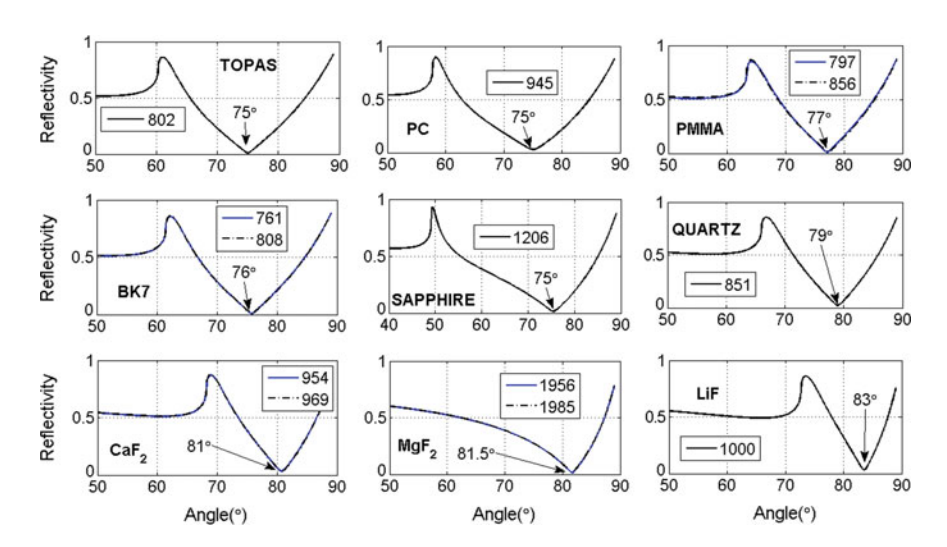


Fig. 10.23 Reflectance curves under AIM-conditions for different substrate materials, as indicated in the *plots*, and different incident wavelengths for the angle range $40^{\circ} < \theta < 90^{\circ}$. Bi-film thickness is 25 nm, in contact with water

Table 10.5 SP-sensor performance and figures of merit for thin Bi-films at metal-water interface: BK7-substrate

Top To Cont Stone	isor performance and ne	ace of medical control	there are a sound performance and upon the first of the performance and the performanc	aco, Diei Baconia	2	
Operation mode	Suited/best substrate	Optical responsivity	Linear dynamic range	SPR width	Optimum film thickness	Remarks
AIM	TOPAS/BK7/Quartz	65°/RIU	$< 4.5 \times 10^{-2} \mathrm{RIU}$	$14 \pm 2^{\circ}$	25 nm	
WIM	TOPAS/BK7/Quartz	2000 nm/RIU	$<3 \times 10^{-2} \mathrm{RIU}$	$950 \pm 50 \mathrm{nm}$ 25 nm	25 nm	Poor SP-sensing

References 157

References

 Golovashkin, A.I., Levchenko, I.S., Motulevich, G.P., Shubin, A.A.: Optical properties of indium. Sovi. Phys. JETP 24(6), 1093–1100 (1967)

- Gaspari, G.D., Das, T.P.: Band structure, fermi surface, and knight shift of indium metal. Phys. Rev. 167, 660–669 (1968)
- 3. The Indium Corporation of America, Application Notes on native oxide removal. http://www.indium.com/inorganic-compounds/indium-compounds/indiumtin-oxide/
- 4. MacRae, R.A., Arakawa, T.: Optical properties of vacuum-evaporated white tin. Phys. Rev. **162**(3), 615–620 (1967)
- Pedersen, T.G., Modak, P., Pedersen, K., Christensen, N.E., Kjeldsen, M.M., Nylandsted-Larsen, A.: Ab initio calculation of electronic and optical properties of metallic tin. J. Phys. Condens. Matter 21, 1–5 (2009)
- 6. Boggs, W.E., Trozzo P.S., Pellissier, G.E.: The oxidation of tin: the morphology and mode of growth of oxide films on pure tin. J. Electrochem. Soc. **108**, 13–24 (1961)
- 7. Yarovaya, R.G., Shklyarevskii, I.N., EI-Shazly, A.F.A.: Temperature dependence of the optical properties and the energy spectrum of zinc. Sov. Phys. JETP **38**(2), 331–334 (1974)
- 8. Stark, R.W., Falicov, L.M.: Band structure and Fermi surface of zinc and cadmium. Phys. Rev. Lett. 19, 795–799 (1967)
- 9. Zuo, J., Erbe, A.: Optical and electronic properties of native zinc oxide films on polycrystalline Zn. Phys. Chem. Chem. Phys. **12**, 11467–11476 (2010)
- Ordal, M.A., Bell, R.J., Alexander Jr., R.W., Long, L.L., Querry, M.R.: Optical properties of Au, Ni, and Pb at submillimeter wavelengths. Appl. Opt. 26, 744–752 (1987)
- Horn, K., Reihl, B., Zartner, A., Eastman, D.D., Hermann, K., Noffke, J.: Electronic energy bands of lead: angle-resolved photoemission and band-structure calculations. Phys. Rev. B 30, 1711–1720 (1984)
- Thompson, J.G.: Properties of lead-bismut, lead-tin, type metal, and fusible alloys. Bur. Stan. J. Res. 5, 1085–1107 (1930)
- 13. Hagemann, H.-J. et al.: Optical constants from the far infrared to the x-ray region: Mg, Al, Cu, Ag, Au, Bi, C, and Al₂O₃. J. Opt. Soc. Am. **65**(6), 742–744 (1975)
- 14. Heine, V.: The band structure of bismuth. Proc. Phys. Soc. A. **69**, 513–519 (1956)
- Golin, S.: Band structure of bismuth: pseudopotential approach. Phys. Rev. 166, 643–651 (1968)

Chapter 11 SPR Active Metal-Type Compounds

11.1 Thin Indium-Tin-Oxide (ITO) Films

ITO is an n-type degenerately doped, wide band gap (3-4eV) semiconductor. It is composed as a solid solution of In_2O_3 ($\approx 90\%$) with SnO_2 ($\approx 10\%$), alternatively considered as In_2O_3 , doped with Sn or off-stoichiometric $In_{2-x}Sn_xO_3$, comprising cubic NaCl structure. The complex optical constant $\varepsilon_{mr}(\lambda) = \varepsilon'_{mr}(\lambda) + j\varepsilon''_{mr}(\lambda)$ has been taken from Ref. [1] and is illustrated in the right inset of Fig. 11.1. Due to a very high concentration of free carriers >10²⁰ cm⁻³, the nonmagnetic, quasi-metallic material exhibits moderate electrical dc-conductivity $> 10^5 (\Omega \text{ m})^{-1}$, sensitively depending on deposition conditions. The CDK largely agrees with the DA. Band-structure calculations for un-doped In_2O_3 are provided in Ref. [2]. At wavelengths $\lambda > 1,450$ nm, $\varepsilon'_{mr}(\lambda)$ drops steadily to negative values. $\varepsilon''_{mr}(\lambda)$ -values are low positive within the spectral range of interest. For the Sapphire substrate at 71°, the SP- dispersion appears undistorted, and exhibits a distinct resonant cross-over point at around 0.57 eV. The SP-energy at high k for the metaloxide-water interface is 0.7 eV. ITO-films are readily produced by reactive magnetron sputtering from In_2O_3/SnO_2 pellet targets in low pressure Ar/O_2 -atmosphere (Ref. [2]), by laser ablation, electron beam and by thermal evaporation. Thin ITO-films typically are polycrystalline, or amorphous, depending on thermal annealing and deposition conditions and the substrate material. The material is highly corrosion resistant. Experimental and theoretical SP-properties of ITO at the metaloxide-air interface are also reported in Ref. [3].

Related spectral features of the reflectance $R_{WIM}(\lambda)$ in the WIM are shown in Fig. 11.2 for the substrate materials under consideration. Similar to the optical properties of Ta and W-films, depicted before, virtually all dielectric substrates, except LiF and MgF_2 , exhibit moderately broadened SP-resonances. ITO-films are thus suited for SP-sensing applications in the WIM.

Reflectance under AIM conditions is shown in Fig. 11.3, again indicating angularly broadened resonances and suited angles $<75^{\circ}$, except MgF_2 and LiF substrates. For the BK7 substrate, the SP-energy (eV) varies with the incident angle within the range $65^{\circ} < \theta < 75^{\circ}$ weakly non-linear as: $E_{SP}(\theta) = -0.0001\theta^2 + 0.097\theta - 2.24$.

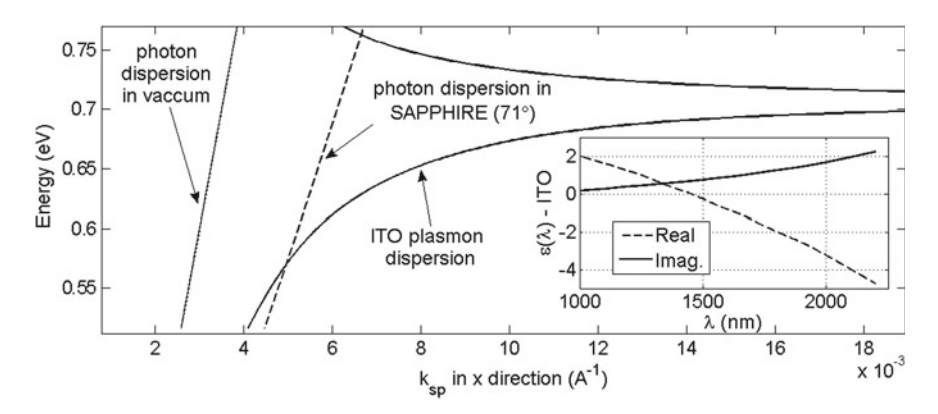


Fig. 11.1 Photon and SPP-dispersion curves of ITO at the solid-water interface (*solid-line*), calculated for Sapphire substrate (*dashed-line*) and incident angle of. The *upper* dispersion curve belongs to the quasi-bound SPP. *Right inset* reveals the real and imaginary fractions of the CDK as function of wavelength

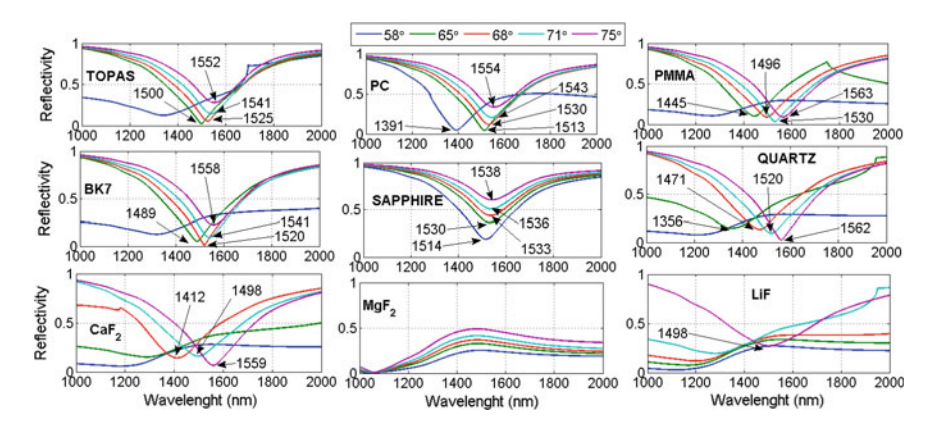


Fig. 11.2 Reflectance curves under WIM-conditions for different substrate materials, as indicated in the *plots*, and incident angles of 58°, 65°, 68°, 71° and 75° for the wavelength range 1,000 nm $< \lambda < 2,000$ nm. The ITO-film thickness is 30 nm, in contact with water as the liquid dielectric

The sensing characteristic in the WIM is shown in Fig. 11.4 for BK7, comprising an initial wavelength of 1,500 nm. The displacement of the resonance position as function of the refractive index (RIU) of the liquid analyte n_{an} is shown in the upper right inset and decreases with n_{an} . The depth/contrast does not vary with an increase of the RIU-value of the analyte, the SPR dip appears undistorted. The associated sensor responsivity R_{WIM} is illustrated in the lower left inset; its magnitude is low and increases approximately linear with n_{an} . The moderate SPR-line broadening parameter (at FWHM) is depicted in the upper left inset and increases with n_{an} .

The SPR-sensing characteristic in the AIM is shown in Fig. 11.5, comprising an initial resonance angle of 68° and wavelength of 1,520 nm. The depth of the

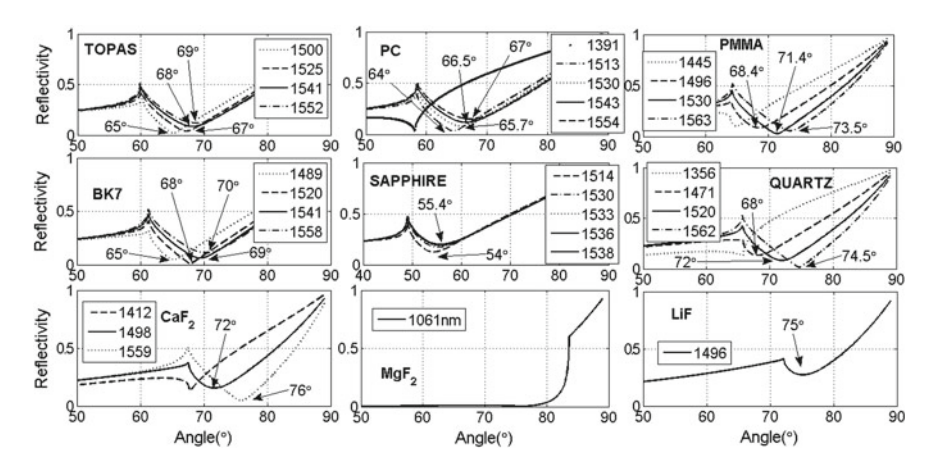


Fig. 11.3 Reflectance curves under AIM-conditions for different substrate materials, as indicated in the *plots*, and different incident wavelengths for the angle range $50^{\circ} < \theta < 90^{\circ}$. ITO-film thickness is 30 nm, in contact with water

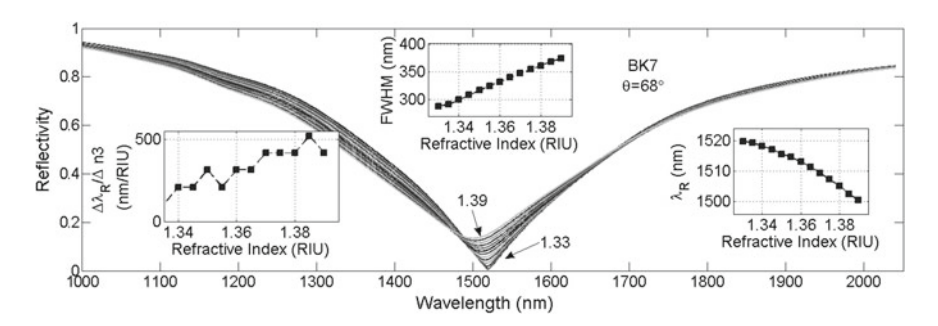


Fig. 11.4 WIM-sensor properties and spectral reflectance $R(\lambda)$ for different RIU-values of the aqueous analyte 1.33 < n_{an} < 1.39. Substrate is BK7, incident angle is 68°. *Upper inset* show the line broadening $\Delta\theta_{res}(n_{an})$. *Lower left* and *right insets* show responsivity $R_{WIM}(n_{an})$ and resonance displacement $\theta_{res}(n_{an})$ respectively

SP-resonance does not vary significantly with the RIU of the analyte. A linear increase of both, resonance angle $\theta_{res}(n_{an})$ and line broadening parameter $\Delta\theta_{res}(n_{an})$ with the RIU of the analyte are resolved in the two upper two sub-figures. SPR sensor responsivity R_{AIM} is shown for four different wavelengths below; their values are low and do not vary with n_{an} .

Eventually, the influence of film thickness for the AIM is outlined in Fig. 11.6. This data set indicates that the ITO-film thickness for optimum SPR sensor operation would be placed at 30 nm.

A compilation of achievable SPR sensor performance is displayed in Table 11.1.

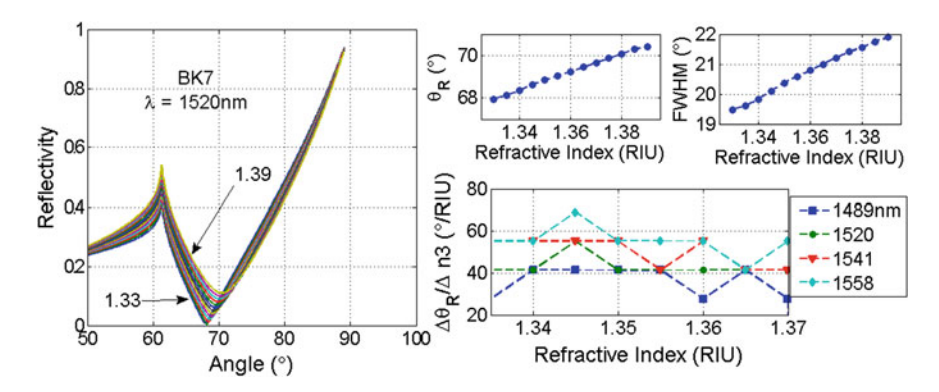


Fig. 11.5 AIM-sensor properties: angular reflectance $R(\theta)$ for different RIU-values of an aqueous analyte 1.33 $< n_{an} < 1.39$. Substrate is BK7, incident wavelength 1,520 nm. *Upper right* two sub-figures show resonance displacements $\theta_{res}(n_{an})$, SP-line broadening $\Delta\theta_{res}$ at FWHM and responsivity R_{AIM} below for four wavelengths

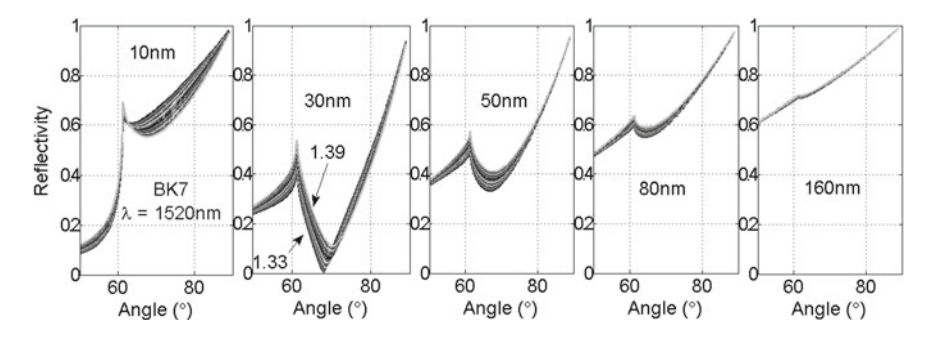


Fig. 11.6 AIM-reflectance at the SP-resonance for different ITO-film thickness values of 10, 30, 50, 80 and 160 nm

11.2 Thin Titanium-Nitride (TiN) Films

TiN is considered as a ceramic material, comprising mainly a cubic NaCl type crystallographic structure. The complex optical constant $\varepsilon_{mr}(\lambda) = \varepsilon'_{mr}(\lambda) + j\varepsilon''_{mr}(\lambda)$ been taken from Ref. [4] and is illustrated in the right inset of Fig. 11.7. The nonmagnetic material exhibits a rather low electrical dc-conductivity at ambient T around $10^4~(\Omega~m)^{-1}$ that sensitively depends on deposition conditions. The CDK approximately agrees with the DA. The band-structure is reported in Ref. [5], indicating that TiN is a correlated metal in the vicinity of a Mott transition. At wavelengths $\lambda > 300~\text{nm}$, $\varepsilon'_{mr}(\lambda)$ drops steadily to negative values. $\varepsilon''_{mr}(\lambda)$ -values are low positive within the spectral range of interest. For the BK7 substrate at 75°, the SP-dispersion appears undistorted, and exhibits a diffuse resonant cross-over at around 1.3 eV. The SP-energy at high k for the solid-water interface is 2.15 eV. Stoichiometric or non-stoichiometric TiN_{1-x} -films can be deposited by reactive magnetron sputtering

Table II.1 SP-ser	isor performance and figures c	ormance and figures of merit for thin ITO-films at solid-water interface	s at solid-water interface			
Operation mode	Suited/best substrate	Optical responsivity	Linear dynamic range	SPR width	Optimum film thickness	Remarks
AIM	All except MgF2 and LiF	$40 \pm 20^{\circ}$ /RIU	$>6 \times 10^{-2} \text{ RIU}$	$21 \pm 1^{\circ}$	30 nm	
WIM	All except MgF ₂ and LiF 200–500 nm/RIU	200-500 nm/RIU	None	$350 \pm 50 \mathrm{nm}$	30 nm	

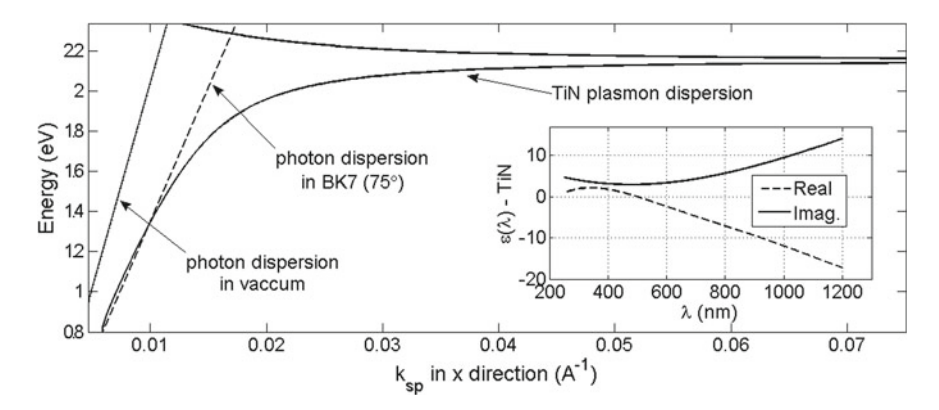


Fig. 11.7 Photon and SPP-dispersion curves of TiN at the solid-water interface (*solid-line*), calculated for BK7 substrate (*dashed-line*) and incident angle of 75°. The *upper* dispersion curve belongs to the quasi-bound SPP. *Right inset* reveals the real and imaginary fractions of the CDK as function of wavelength

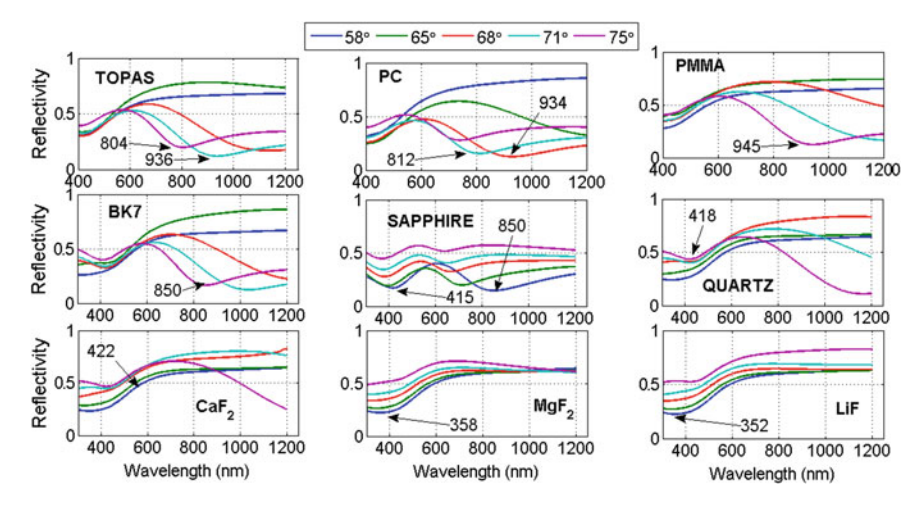


Fig. 11.8 Reflectance curves under WIM-conditions for different substrate materials, as indicated in the plots, and incident angles of 58° , 68° , 68° , 71° and 75° for the wavelength range $400 \text{ nm} < \lambda < 1,200 \text{ nm}$. TiN-film thickness is 45 nm, in contact with water

from a massive Ti target in low pressure Ar/N_2 -atmosphere (Ref. [6]). Sputtered thin TiN-films typically are polycrystalline, or amorphous, depending on thermal annealing, thermal deposition conditions and the substrate material. The material is highly corrosion resistant. Native oxide formation is not reported.

Related spectral features of the reflectance $R(\lambda)$ in the WIM are shown in Fig. 11.8 for the substrate materials under consideration. Only few dielectrics as the polymers and Sapphire exhibit clear, albeit broadened SP-resonances at suited angles. TiN-films are thus poorly suited for SP-sensing applications in the WIM.

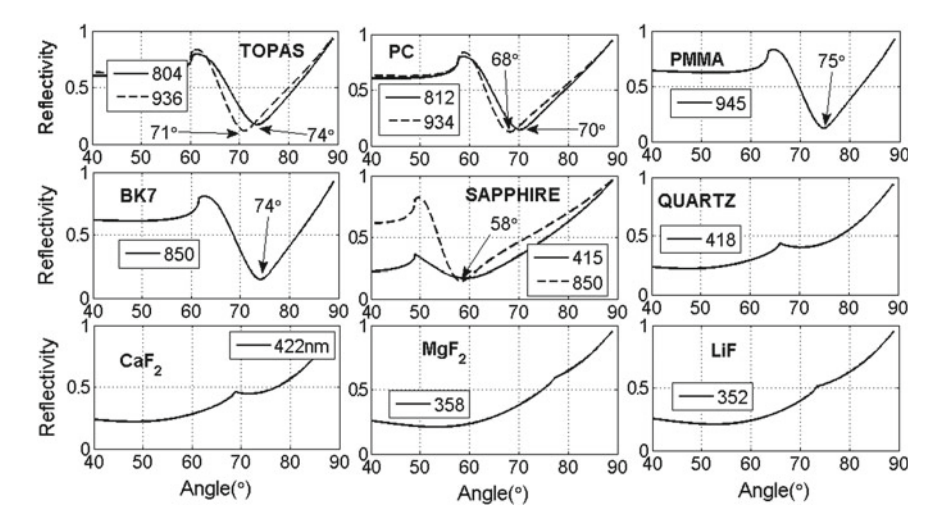


Fig. 11.9 Reflectance curves under AIM-conditions for different substrate materials, as indicated in the plots, and different incident wavelengths for the angle range $40^{\circ} < \theta < 90^{\circ}$. TiN-film thickness is 45 nm, in contact with water

Reflectance under AIM conditions is shown in Fig. 11.9, again indicating angularly broadened resonances and suited angles <75° for TOPAS, PC, PMMA, BK7 and Sapphire substrates.

The sensing characteristic in the WIM is shown in Fig. 11.10 for BK7, comprising an initial wavelength of 850 nm. The displacement of the resonance position as function of the refractive index of the liquid analyte n_{an} is shown in the lower left inset. The SP depth/contrast is small and decreases further with an increase of n_{an} , the SPR-dip is poorly resolved. The associated sensor responsivity R_{WIM} is illustrated

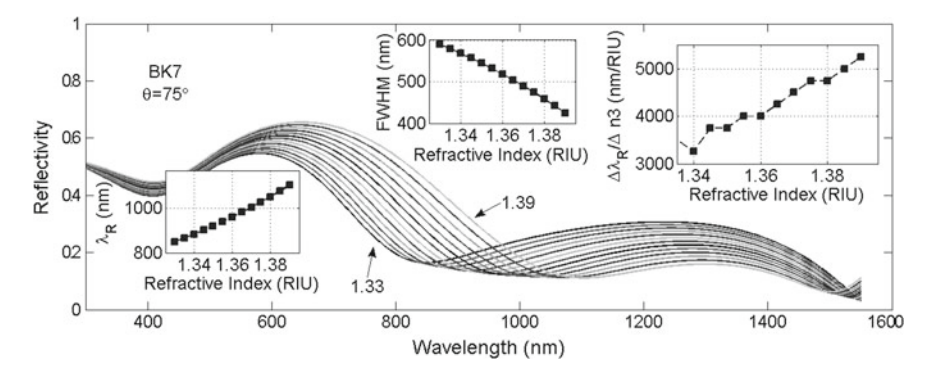


Fig. 11.10 WIM-sensor properties and spectral reflectance $R_{WIM}(\lambda)$ for different RIU-values of the aqueous analyte 1.33 < n_{an} < 1.39. Substrate is BK7, incident angle is 75°. Upper right and left insets show and responsivity $R_{WIM}(n_{an})$ and line broadening $\Delta\theta_{res}(n_{an})$, respectively, resonance displacement $\theta_{res}(n_{an})$; at lower left

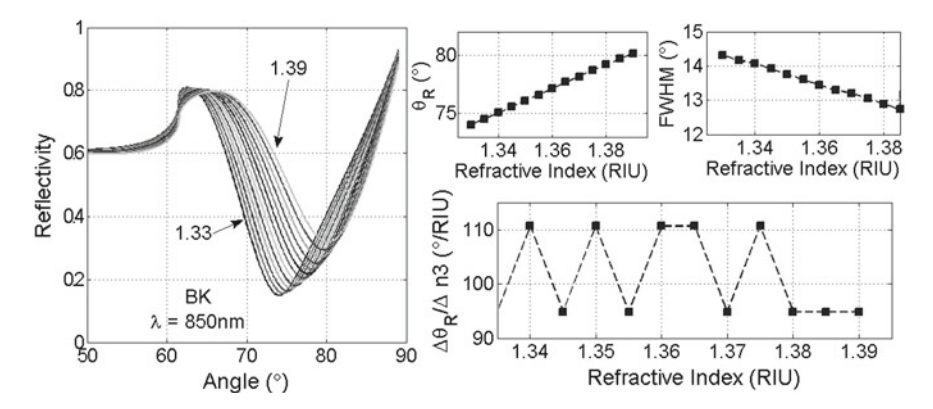


Fig. 11.11 AIM-sensor properties: angular reflectance $R(\theta)$ for different RIU-values of the aqueous analyte 1.33 < n_{an} < 1.39. Substrate is BK7, incident wavelength 850 nm. *Upper right* two sub-figures show resonance displacements $\theta_{res}(n_{an})$, SP-line broadening $\Delta\theta_{res}$ at FWHM and responsivity R_{AIM} below for single wavelength of 850 nm

in the upper right inset; its magnitude is moderate and increases linearly with n_{an} . The moderate SPR-line broadening parameter (at FWHM) is depicted in the upper left inset and decreases with n_{an} .

The SPR-sensing characteristic in the AIM is shown in Fig. 11.11, comprising an initial resonance angle of 74° and wavelength of 850 nm. The depth of the SP-resonance decreases with the RIU of the analyte. A linear increase of resonance angle $\theta_{res}(n_{an})$ and decrease of the line broadening parameter $\Delta\theta_{res}(n_{an})$ with the RIU of the analyte are resolved in the right upper two sub-figures. SPR sensor responsivity R_{AIM} is shown for wavelengths of 850 nm below; the value is high and does not vary with the RIU of the analyte.

Eventually, the influence of film thickness for the AIM is outlined in Fig. 11.12. This data set indicates that the TiN-film thickness for optimum SPR sensor operation would be placed at 45 nm.

A compilation of achievable SPR sensor performance is displayed in Table 11.2.

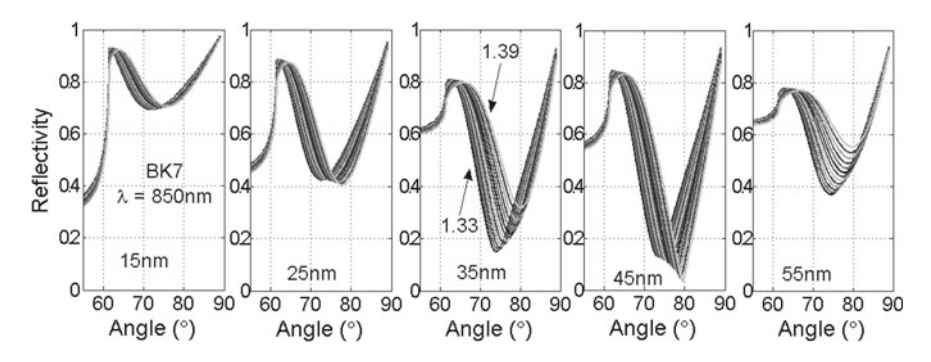


Fig. 11.12 AIM-reflectance at the SP-resonance for different TiN-film thickness values of 15, 25, 35, 45 and 55 nm

Table 11.2 SP-sensor performance and figures of merit for thin TiN-films at the solid-water interface

			The second secon			
Operation mode	Suited/best substrate	Optical responsivity	Linear dynamic range	SPR width	Optimum film thickness	Remarks
AIM	TOPAS/PC/PMMA/BK7/Sapphire $100 \pm 10^{\circ}$ /RIU	$100 \pm 10^{\circ}/\text{RIU}$	$>6 \times 10^{-2} \text{RIU}$ $13 \pm 1^{\circ}$	$13 \pm 1^{\circ}$	45 nm	
WIM	TOPAS/PC/PMMA/BK7/Sapphire	PMMA/BK7/Sapphire $ 4,500 \pm 1,000 \mathrm{nm/RIU} $ None	None	$500 \pm 100 \mathrm{nm}$ 45 nm	45 nm	SP-split for Sapphire

References

- Erhart, P., Klein, A., Egdell, R.G., Albe, K.: Band structure of indium oxide: indirect versus direct gap. Phys. Rev. B 75, 153205 (2007)
- 2. Kerkache, L., Layadi, A., Mosser, A.: Effect of oxygen partial pressure on the structural and optical properties of dc sputtered ITO thin films. J. Alloy. Compd. **485**, 46–50 (2009)
- Rhodes, C., Franzen, S., Maria, J.P., Losego, M., Leonard, D.N., Laughlin, B., Duscher, G., Weibel, S.: Surface plasmon resonance in conducting metal oxides. J. Appl. Phys. 100, 054905 (2006)
- Roux, L., Hanus, J., Fracois, J.C., Sigrist, M.: The optical properties of titanium nitrides and carbides: spectral selectivity and photothermal conversion of solar energy. Sol. Energy Mater. 7, 299–312 (1982)
- 5. Allmaier, H., Chioncel, L., Arrigoni, E.: Titanium nitride: a correlated metal at the threshold of a Mott transition. Phys. Rev. B **79**, 235126 (2009)
- 6. Meng, L.-J., Azevedo, A., dos Santos, M.P.: Deposition and properties of titanium nitride films produced by dc reactive magnetron sputtering. Vacuum 46, 233–239 (1995)

Chapter 12 Artificial Metal-Insulator Multi-layer Structures

12.1 Silver-Al₂O₃-Silver Multilayer Structures

Metal-Insulator multi-layer structures that exhibit a manifold of internal interfaces are artificial materials, and also known as meta-materials. Their optical SPR properties are experimentally yet not explored. Here, the confinement of thin Ag films, embedded between identical and 300 nm thick dielectric Al₂O₃ films (in Sapphire structure) has been explored by FA. The number of metal films varies and increases from a single up to 4 metal layers. The exact geometrical layer arrangement is outlined in the individual plots. These configurations approach the ideal case that would be required for optimum excitation of the LRSPP. Comparable data, shown before in Chap. 7 for 50 nm thin Cu, Ag and Au-layers, were obtained for the BK7-Teflonmetal-water configuration. However, this earlier layer system does not fully meet the precise LRSPP- resonance conditions, since the CDK's of the dielectric materials are not exactly identical. Two co-existing, i.e. split-off SP-modes, appeared in Figs. 7.29 and 7.30, and were assigned to co-existing symmetric and anti-symmetric SPP-states, along with superior SP-sensing properties. This situation does not apply to the layer configurations under consideration. Due to the relatively thick Al₂O₃ layer in contact with the adjacent aqueous analyte, changes of its refractive index remain virtually undetected. Nevertheless, a manifold of SP resonances is resolved in the Fresnel data set for this type of a meta-material.

The reflectance under AIM conditions for a single embedded Ag-layer is depicted in Fig. 12.1, and exhibits now four co-existing, sharp SP-modes, placed at 366.1, 446.4, 584.1 and 858.3 nm.

A split-off resonance also is resolved for the short wavelength of 366.1 nm, through presence of a further broadened SP feature at 80°. SP-splitting is absent for the three longer wavelengths. The related WIM situation is shown in Fig. 12.2. A manifold of four SP-resonances with exceptionally narrow spectral broadening

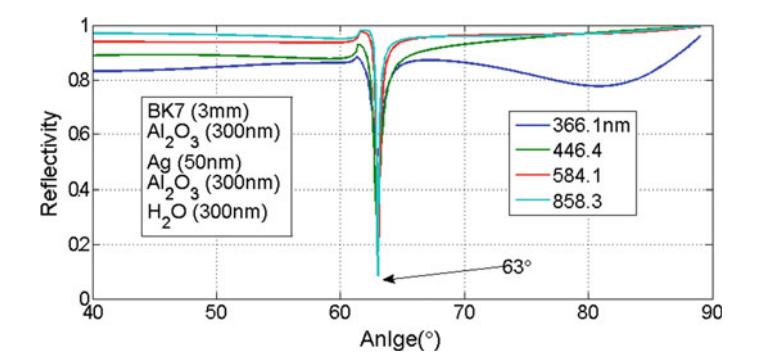


Fig. 12.1 AIM-reflectance, calculated for exact LRSPP-conditions at four selected wavelength for a 50 nm Ag-film, confined between $300 \, \text{nm}$ thin Al_2O_3 layers. The sandwich structure is placed onto a 3 mm thick BK7 substrate, and in contact with a $300 \, \text{nm}$ thin water film at the opposite site. The film geometry is indicated in the *left inset*

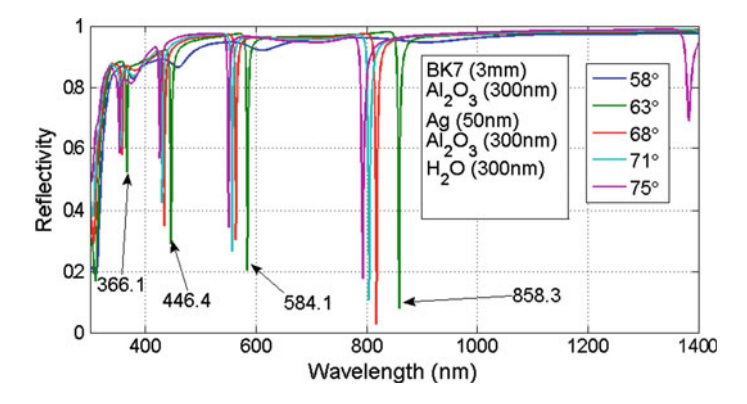


Fig. 12.2 WIM-reflectance for the same film configuration as Fig. 12.1 for 5 different incident angles

at these specific wavelengths is resolved. Most likely, these multiple resonances are related to interference effects, involving four different interfaces in the structure and require incident angles $>58^{\circ}$. The dip at the shortest wavelength around 320 nm belongs to the bulk Plasmon.

As the number of Ag-layers increases, the SP-dips become broader and the resonance at low angle of 58° becomes more pronounced, see Fig. 12.3. With three Ag-layers (Fig. 12.3), those resonances within the wavelength region $500 \text{ nm} < \lambda < 900 \text{ nm}$ begin to diminish. For the 4 layer configuration of Fig. 12.4, a clear spectral gap opens, without presence of SP-resonances. Comparison with Fig. 7.29 ultimately suggests presence of a plasmonic bandgap, which separates the symmetric (S) at short wavelength around 500 nm and anti-symmetric (AS) SPP mode that is centered at longer wavelength around 900 nm.

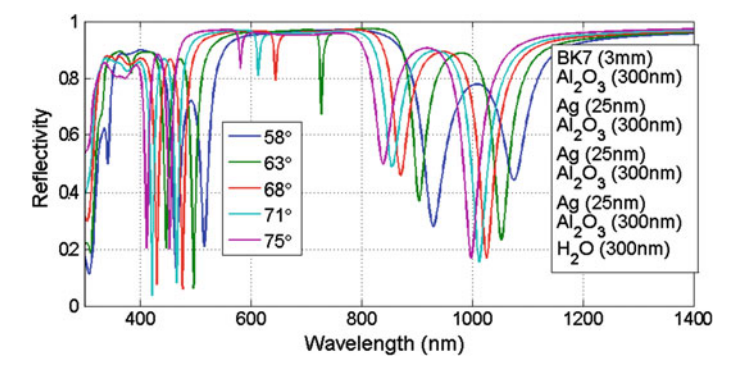


Fig. 12.3 WIM reflectance of a multi-layer arrangement, comprising: three 25 nm thin Ag-layers, confined between $300 \, \text{nm}$ thick identical Al_2O_3 films, calculated for 5 incident angles, as indicated in the *left inset*

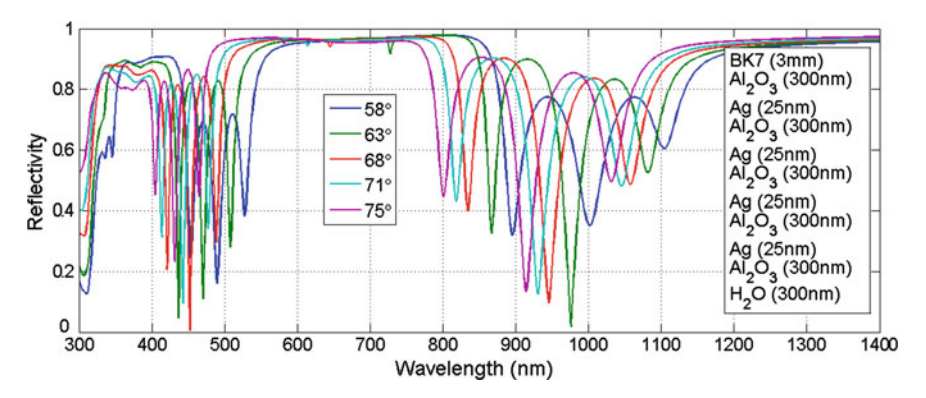


Fig. 12.4 IM reflectance of a multi-layer arrangement, comprising: four 25 nm thin Ag-layers, confined between $300\,\mathrm{nm}$ thick identical $\mathrm{Al_2O_3}$ films, calculated for 5 incident angles, as indicated in the *left inset*

Both, the S-and AS modes split into further sub-modes, as the number of Ag-layers increases. For three Ag-layers, displayed in Fig. 12.3, two sub-modes are resolved. For four Ag-layers, revealed in Fig. 12.4, three equidistant sub-modes appear for the S and AS states, at each angle.

Chapter 13 Conclusions

The manifold of SPR-sensor features, as outlined in Chaps. 6–12 for the WIM and AIM operation modes, and a broad variety of metal films with their respective substrate materials are qualitatively summarized in the matrix display from Table 13.1. The vertical axis exhibits the 30 different SP-active metal and metal like films, the horizontal axis is assigned to the related 10 dielectric substrates thereof. Green marked symbols account for decent/good SP sensing properties, blue symbols correspond to moderate and red colored symbols indicate rather poor SP-sensing performance.

The table assigns MgF₂ substrates largely as not suited, whilst LiF exhibits appropriate SPR sensor properties for only few metals. Evidently, BK7 glass, and most of the polymers, especially TOPAS are favorable substrate materials. Furthermore, the classical noble metals and two of the free electron metals exhibit decent SPR properties, whilst most of the transition metals, except Osmium and Rhodium, display rather poor SP-sensing characteristics.

Figure 13.1 illustrates the sensor performance for the various metals, employing the relation $E_{sp} \approx \sigma_0^{0.5}$. Presence of the exponent 0.5 is considered here as a criterion that confirms the validity of the Drude approximation. E_{sp} is the SP energy for the metal-aqueous solution interface at large k-values and saturation, respectively, and σ_0 is the electrical dc-conductivity of the metal. Both physical quantities are connected by the DA, as was briefly outlined earlier in Chap. 1.

Three separated regions can be identified, and the exponent for the best fit is attached to each curve: in principle, those metals marked with green colored symbols and placed within the low energy range $E_{sp} < 3.4$ eV, will exhibit good SP-sensor performance and pronounced SP-dips, respectively. Within this interval, the exponent is 0.5 and these metals largely obey the DA. Those metal films, comprising SP-energies within the range $2.5 < E_{sp} < 4.5$ eV exhibit somewhat degraded SP-sensor properties, indicated by blue colored symbols. The associated exponent of 0.361 suggests reduced agreement with the DA. Eventually, metals with red colored symbols at SP-energies >5 eV mostly exhibit poor SP-sensor performance, the a.m. exponential $E_{sp} - \sigma_0$ relation for the DA is not applicable.

174 13 Conclusions

 Table 13.1
 SP-sensing properties for all metals and dielectric substrate materials

		8 F F-										
	Dielectric										BK7-	
Metal	Dielectric	TOPAS	PC	PMMA	BK7	Sapphire	Quartz	CaF ₂	MgF ₂	LiF		
											LRSPP	
	Ag	W	W	W	W	W	W	W	W	W	W	(A)
	8	A	4	A	4	4	4	4	A	4	4	T.
	Al	W	Ø	W	W	W	W	W	W	Ø	W	
		4	4	4	4	A	A	4	4	4	a	_
	Au	W	W	W	W	W	W	W	W	W	W	(FR
	7 LU	4	4	4	4	A	A	4	A	4	4	
	Bi	W	Ø	W	W	W	W	W	W	Ø	-	
	Di	4	4	4	4	A	A	A	4	4	_	_
	Cr	W	Ø	W	W	W	W	W	W	W		
	Cr	A	4	a	4	A	A	4	4	4	-	-
	Со	W	Ø	W	W	W	W	W	W	W		
	Co	a	4	4	4	A	A	4	A	4	-	-
	C	W	W	W	W	W	W	W	W	Ø	W	
	Cu	a	3	4	4	a	4	4	A	4	4	PR
	T.	D	Ø	W	W	W	D	Ø	W	Ø		歸
	Fe	4	4	A	4	A	A	4	4	4	-	PR
		W	Ø	W	W	W	W	W	W	Ø		
	In	a	4	4	4	A	4	4	A	4	-	-
		D	Ø	W	Ø	W	W	W	W	Ø		(Ks
	Ir	A	4	4	4	A	4	A	4	a	-	
		D	Ø	W	Ø	W	W	W	W	Ø		
	Li	A	4	a	4	4	A	A	A	4	-	-
		W	W)	W	W	W	D	W	W	Ø		
	Mg	4	4	4	4	A	A	4	A	a	-	-
		W	W	W	W	W	w.	W	D	D		
	Mo	4	4	4	4	A	4	A	A	4	-	-
		D	W)	₩.	W	W.	D	W.	D	Ø		
	Ni	4	4	4	4	4	A	4	A	4	-	-
		W	W)	W	W	D	W	W	D	Ø		
	Nb	A	4	4	3	4	4	4	A	4	-	-

(continued)

Table 13.1 (continued)

Table 13.1 (continu										BK7-	
Dielectric	TOPAS	PC	PMMA	BK7	Sapphire	Quartz	CaF ₂	MgF ₂	LiF	Teflon	Np's
Metal										LRSPP	
Os	W	W	W	W	W	W	W	W	W	W	歸
Os	4	4	4	4	4	4	4	4	4	A	
Pb	W	W	W	W	W	W	W	W	W	W	6
	4	4	4	4	a	4	4	A	4	A	
Pd	W	W	W	W	W	D	W	W	W	_	_
T u	4	A	A	4	A	A	4	A	4		
Pt	W	W	W	W	W	D	W	W	W	_	_
	4	4	4	4	A	4	A	4	4		
Rh	D	W	W	W	W	D	W	W	W	_	_
	4	A	4	4	A	4	4	4	4		
Ru	D	W	W	W	W	D	W	W	Ø	_	_
- Ku	4	4	4	4	A	4	4	4	4		
Sn	W	Ø	W	W	W	D	W	W	W	_	_
511	a	4	4	4	A	A	4	4	4		
Ta	W		W	W	W	W	W	W	W		_
14	4	4	4	4	A	4	4	A	4		
Ti	W	3	W	W	W	W.	W	W	Ø	_	_
11	4	A	a	4	A	4	A	4	4	-	-
v	W	Ø	W	W	W	W	W	W	W	_	_
•	4	4	4	4	A	4	4	4	4	-	-
W	W	W	D	W	W	W	W	W	Ø	_	
**	4	4	4	4	A	4	4	A	4	_	-
Zn	W	W	W	W	W	W	W	W	Ø		
ΔII	4	4	4	4	A	4	4	A	4	-	-
Zr	D	Ø	W	W	W	D	W	W	Ø	_	
ZΓ	4	4	4	4	4	A	4	A	4	-	-
ITO	W	W	W	W	W	W	W	D	Ø		
ITO	4	4	a	4	A	4	4	4	4	-	-
/press.t	W	W	W	W	W	W.	Ø	W	Ø		
TiN	4	4	4	4	4	A	A	A	A	-	-

Green decent/good, blue moderate/or difficult instrumentation and red poor SP-performance for spectral (W), angular (A) and localized (LSPR) modes

176 13 Conclusions

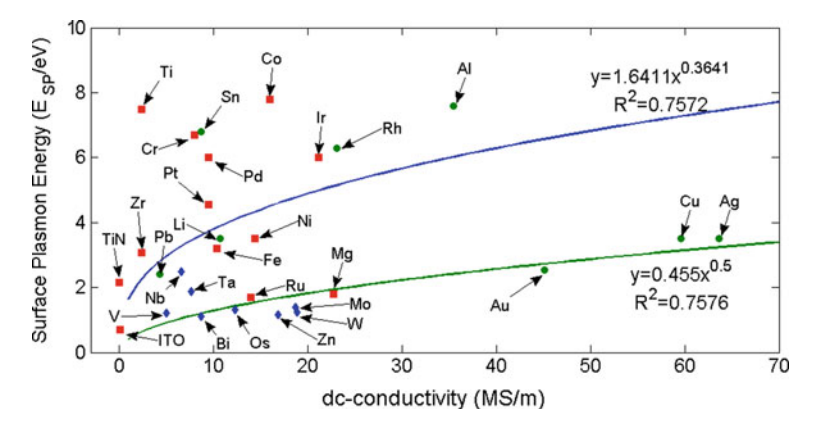


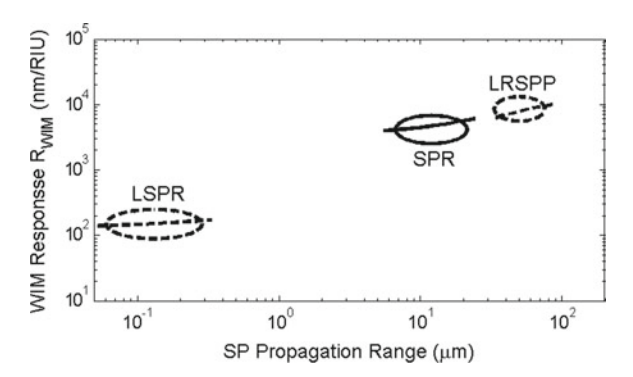
Fig. 13.1 Classification of various metals for their SP-sensing characteristics and the agreement with the DA. *green circle* decent/good, *blue diamond* moderate/or difficult instrumentation and *red square* poor SP-performance (Color figure online)

However, this simplified approach certainly does not represent a general rule: Aluminum and Rhodium films reveal high SP-energies, but both metals exhibit useful SP sensor properties. Indium exhibits the highest E_{SP} -value >19 eV of all metals under consideration, but is not included in this analysis. In-films exhibit moderate SP sensor properties at the metal-water interface for some substrate materials, as outlined in Table 13.1 and Chap. 10, despite of the high SP-energy. The trend, however, still holds and implies that the best sensing characteristic is found at low SP-energies. Good examples are the classical noble metals Au, Ag and Cu. There are considerable differences between the different operation modes: a major drawback for the WIM in comparison with the AIM for almost all metal films, is its pronounced nonlinear variation of the sensor responsivity $R_{WIM}(n_{an})$ with the refractive index of the aqueous analyte n_{an} . This results in a limited linear sensing range and thus makes a quantitative data analysis and accurate determination of n_{an} a difficult task.

The operation modes under consideration differ by several orders of magnitude. A further comparison of this figure of merit is also illustrated in Fig. 13.2, where the range of values $R_{WIM}(\lambda_{res})$ for the localized SPR, the common SPR and the long range SPP modes, is plotted as function of the SP-propagation lengths. This figure illustrates that LSPR operation exhibits the lowest responsivity, with $50 < R_{WIM} < 200$, whilst the propagation length corresponds to the particle size. The conventional SPR mode exhibits good performance, with $3,000 < R_{WIM} < 5,000$, especially for the classical noble metals Ag, Au and Cu. Excellent sensor properties can be expected for thin Cu-films in the LRSPP mode, with R_{WIM} approaching 12,000 nm/RIU. Use of thin Al-films certainly is an alternative to the noble metals, since the Al-water interface exhibits appealing SP-sensing properties. Although the native oxide film that forms

13 Conclusions 177

Fig. 13.2 Classification of three SP-operation modes as function of propagation range



on Al-surfaces in plain aqueous solution remains sufficiently stable, it is not fully clear whether this also holds in presence of reactive anions in case of electrolytic solutions. Use of thin Ta and Sn-films certainly is a further option, since their SP-resonances are located below 1,000 nm wavelength and favorable angle <75°.

Glossary

AIM Angular Interrogation Mode.

CCD Charge-coupled Device.

CDK Complex Dielectric Constant.

CMOS Complementary Metal-Oxide-Semiconductor.

DA Drude approximation is the application of kinetic theory to explain the

transport properties of electrons in materials.

FA Fresnel Analysis.FEM Finite Element Method.

FPGA Field Programmable Gate Array.FWHM Full Width at Half Medium.

IM Intensity Mode.LOD Limit of detection.

LRSPP Long Range Surface Plasmon Polaritons.LSPR Localized Surface Plasmon Resonance.

LW Long Wavelength.NP Nano-Particle.OB Ouasi-bound mode.

Qtz Quartz.

RIU Refractive Index Unit.

RPP Radiative Surface Plasmon Polariton.

SERS Surface-enhanced Raman spectroscopy or surface-enhanced Raman scat-

tering is a surface-sensitive technique that enhances Raman scattering by molecules adsorbed on rough metal surfaces or by nanostructures such

as plasmonic-magnetic silica nanotubes.

SP Surface Plasmon.

SPP Surface plasmon polaritons, are infrared or visible-frequency electromag-

netic waves, which travel along a metal-dielectric or metal-air interface.

SPR Surface plasmon resonance is the collective oscillation of electrons in a

solid or liquid stimulated by incident light.

180 Glossary

SW Short Wavelength.TFb Teflon bilayer.

TIR Total Internal Reflection.
TM Transverse Magnetic.

WIM Wavelength Interrogation Mode.

Index

A Aluminum films, 33 AIM-conditions, see Angular Interrogation Mode Al-water interface, 34 LRSPP, 36 responsivity, 36 WIM-conditions, see Wavelength Interrogation Mode Angular Interrogation Mode, 12 AIM, 20	-Fe-particles, 107 -Ir-particles, 72 -Os-particles, 77 -Pb-particles, 152 -Pt-particles, 85 Complex dielectric constant, 2 Copper films, 47 AIM-conditions, 49 AIM-responsivity, 49 Cu-water interface, 48 LRSPP, 51 WIM-conditions, 48 WIM-responsivity, 49
В	Cs-films, 39
Bandgap, 170 Bismuth-films, 154	,
AIM-conditions, 155	D
Bi-water interface, 154	Drude approximation, 1, 14
WIM-conditions, 155	Tr,
BK7-Teflon-metal-water configuration, 169	
	\mathbf{F}
	FEM, 31, 109
C	Finite Element Method, 31
Chromium films, 97	
AIM-conditions, 99	
Cr-water interface, 98	\mathbf{G}
WIM-conditions, 98	Gold films, 54
Cobalt films, 99	AIM-conditions, 55
AIM-conditions, 102	AIM-responsivity, 56
Co-water interface, 101	Au-water interface, 54
WIM-conditions, 101	LRSPP, 57
Colloidal particles, 38, 51, 57, 65, 72, 77, 85,	WIM-conditions, 55
107, 152	WIM-responsivity, 55
-Ag-particles, 65	
-Al-particles, 38	
-Au-particles, 57	I
-Cu-particles, 51	Indium films, 139
© The Author(s) 2015 L.C. Oliveira et al., <i>Surface Plasmon Resonance</i>	Sensors,

SpringerBriefs in Physics, DOI 10.1007/978-3-319-14926-4

181

182 Index

AIM conditions, 141 AIM-responsivity, 140 In-water interface, 140 WIM-condictions, 140 Intensity Mode, 15 IM, 20 Iridium films, 69 AIM-conditions, 71	Magnesium-cyclohexane interface, 44 WIM-conditions, 44 Mie theory, 5, 30 Molybdenum films, 110 AIM-conditions, 111 Mo-water interface, 110 WIM-conditions, 111 WIM-responsivity, 110
Ir-water interface, 70	
WIM-conditions, 70	N
WIM-responsivity, 71	Na-films, 39, 42
Iron films, 104	Nickel films, 112
AIM-conditions, 105	AIM-conditions, 115
AIM-responsivity, 106 Fe-water interface, 104	Ni-water interface, 114
	WIM-conditions, 114
WIM responsivity, 104	Niobium films, 115
WIM-responsivity, 104 ITO films, 159	AIM-conditions, 118
AIM-conditions, 161	AIM-responsivity, 119
AIM-responsivity, 161	Nb-water interface, 117
ITO-solid-water interface, 160	WIM-conditions, 117
WIM-conditions, 160	
WIM-responsivity, 160	
Will responsively, 100	0
	Optical spectroscopy with localized plas-
K	mons, 5
K-films, 39, 42	Osmium films, 74 AIM-conditions, 75
Kretschmann configuration, 4	LRSPP, 76
	Os-water interface, 74
	WIM-conditions, 75
L	WIM-responsivity, 75
Lead films, 147	Otto-configuration, 4
AIM-conditions, 150	oue comparation,
AIM-responsivity, 150	
LRSPP, 151	P
Pb-water interface, 149	Palladium films, 78
WIM-conditions, 149	AIM-conditions, 81
Limit of detection, 1, 16	Pd-water interface, 80
Lithium films, 39 AIM-conditions, 42	WIM-conditions, 80
Li-cyclo-hexane interface, 41	Photon wave-vector, 12
WIM-conditions, 41	Plasmon resonance, 12
WIM-responsivity, 41	Platinum films, 81
Localized surface plasmons, 4	AIM-conditions, 84
Long range surface plasmon polariton, 4, 29	Pt-water interface, 83
BK7-Teflon-metal-water configuration,	WIM responsibility 95
169	WIM-responsivity, 85
LSPR, 51, 57, 65, 72, 77, 85, 107, 152, see	
also Mie theory	R
•	Rhodium-films, 86
	AIM-conditions, 89
M	AIM-responsivity, 89
Magnesium films, 44	Rh-water interface, 88
AIM-conditions, 45	WIM-conditions, 88

Index 183

Ruthenium films, 92	AIM-conditions, 144
AIM-conditions, 93	Sn-water interface, 143
Ru-water interface, 92	WIM-conditions, 144
WIM-conditions, 93	Titanium films, 123
	AIM-conditions, 126
	Ti-water interface, 125
S	WIM-conditions, 125
Sellmeier equation, 7	Tungsten-films, 126
Silver films, 61	AIM-conditions, 129
Ag-water interface, 61	W-water interface, 128
AIM-conditions, 62	WIM-conditions, 128
AIM-responsivity, 63	
LRSPP, 64	
WIM-conditions, 62	V
WIM-responsivity, 62	Vanadium films, 129
Silver- <i>Al</i> ₂ <i>O</i> ₃ -Silver Multilayer, 169	AIM-conditions, 132
SPP wave-vector, 12	AIM-responsivity, 132
Superlattice structure, 5	V-water interface, 131
Silver-Al ₂ O ₃ -Silver Multilayer, 169	WIM-conditions, 131
Surface enhanced Raman scattering, 11	
Surface plasmon polariton, 1	
Surface plasmon resonance, 1	\mathbf{W}
	Wavelength Interrogation Mode, 12 WIM, 20
Т	W IIVI, 20
Tantalum-films, 119	
Ta-water interface, 121	Z
WIM-conditions, 121	Zinc films, 145
WIM-responsivity, 122	AIM-conditions, 147
TiN films, 164	WIM-conditions, 146
AIM-conditions, 165	Zn-water interface, 146
AIM-responsivity, 166	Zirconium films, 133
TiN-solid-water interface, 164	AIM-conditions, 136
	· · · · · · · · · · · · · · · · · · ·
WIM responsivity 165	AIM-responsivity, 136
WIM-responsivity, 165	WIM-conditions, 135
Tin films, 143	Zr-water interface, 135